UNIVERSITÉ CÔTE D'AZUR

ÉCOLE DOCTORALE
SCIENCES FONDAMENTALES ET APPLIQUÉES

THÈSE DE DOCTORAT

SIMULATION DE SUSPENSIONS NON-BROWNIENNES CONCENTRÉES FRICTIONNELLES ET ADHÉSIVES EN ÉCOULEMENT LINÉAIRE OU NON-LINÉAIRE

Michel ORSI
Institut de Physique de Nice

Présentée en vue de l'obtention du grade de docteur en Physique d'Université Côte d'Azur

Dirigée par : François Peters

Co-encadrée par : Laurent Lobry

Soutenue le : 2 Décembre 2022

Devant le jury, composé de :

Pascale Aussillous, *Professeure*, IUSTI Marseille

Eric Climent, *Professeur*, IMFT Toulouse

Romain Mari, *Chargé de Recherche*, LIPhy Grenoble

Jeffrey F. Morris, *Professor*, Levich Institute New York

Stany Gallier, *Ingénieur de Recherche*, ArianeGroup

SIMULATION DE SUSPENSIONS NON-BROWNIENNES CONCENTRÉES FRICTIONNELLES ET ADHÉSIVES EN ÉCOULEMENT LINÉAIRE OU NON-LINÉAIRE

Simulation of concentrated non-Brownian frictional and adhesive suspensions in linear and nonlinear flows

---

JURY :

Présidente

Pascale Aussillous, *Professeure des Universités*, Institut Universitaire des Systèmes Thermiques Industriels (IUSTI), CNRS, Aix Marseille Université

Rapporteurs

Eric Climent, *Professeur des Universités*, Institut de Mécanique des Fluides de Toulouse (IMFT), CNRS, Université de Toulouse

Romain Mari, *Chargé de Recherche*, Laboratoire Interdisciplinaire de Physique (LIPhy), CNRS, Université Grenoble Alpes

Examinateurs

Jeffrey F. Morris, *Professor*, Benjamin Levich Institute for Physico-Chemical Hydrodynamics and Department of Chemical Engineering, City College of New York

Stany Gallier, *Ingénieur de Recherche (HDR)*, ArianeGroup, Le Bouchet Research Center

Directeur de thèse

François Peters, *Maître de Conférences*, Institut de Physique de Nice (InPhyNi), CNRS, Université Côte d'Azur

Membre invité

Laurent Lobry, *Maître de Conférences*, Institut de Physique de Nice (InPhyNi), CNRS, Université Côte d'Azur

RÉSUMÉ

Nous présentons une méthode de simulation à l'échelle des particules pour les écoulements de suspensions non-Browniennes à faible nombre de Reynolds, basée sur la méthode des domaines fictifs et complétée par des corrections de lubrification de sous-maille. Dans leur forme habituelle, ces corrections font intervenir l'écoulement linéaire ambiant. Dans ce travail, nous déterminons les conditions requises pour éviter de considérer cet écoulement ambiant tout en conservant l'invariance par changement de référentiel, et nous construisons une matrice de correction de sorte que ces conditions soient intrinsèquement présentes. Cette procédure étend l'utilisation correcte de ces corrections aux écoulements non-linéaires. La méthode est validée pour diverses configurations d'écoulement de particules, impliquant quelques particules dans des écoulements linéaires et non-linéaires avec diverses conditions aux limites, ou des suspensions concentrées dans un écoulement de cisaillement simple. Ensuite, nous étudions le rôle des forces d'adhésion dans les suspensions frictionnelles, en faisant varier à la fois l'intensité de l'adhésion et la fraction volumique : après avoir présenté les difficultés liées à la déplétion aux parois et aux bandes de cisaillement, nous montrons que la viscosité relative de la suspension est fonction à la fois de la fraction volumique ϕ et de la contrainte de cisaillement Σ_{12}. La variation de la viscosité en fonction de ces deux paramètres est bien décrite via une fraction volumique de blocage à condition que celle-ci dépende de la contrainte sans dimension σ^* qui s'exprime en fonction de la force d'adhésion entre les particules. La variation de la fraction volumique de blocage en fonction de la contrainte peut être interprétée comme la variation de la contrainte seuil en fonction de la fraction volumique. Cette courbe sépare le plan (ϕ, σ^*) en deux régions : une dans laquelle la suspension s'écoule et l'autre dans laquelle elle est bloquée. Dans une dernière partie, nous étudions la migration des particules induite par le cisaillement dans un écoulement de Poiseuille. Dans un tel système, les particules migrent vers le centre du canal, ce qui entraîne le développement d'un gradient de concentration avec l'apparition d'une région centrale où la fraction volumique de blocage, mesurée dans un écoulement de cisaillement simple, peut être dépassée. Le profil de vitesse est donc hautement non-linéaire, à la fois en raison du gradient de pression et du gradient de concentration variant dans le temps, ce qui justifie l'utilisation de la méthode numérique présentée. Nous comparons les résultats à une version modifiée du *Suspension Balance Model*, confirmant les limites bien connues de ce modèle dans la région centrale. Enfin, nous montrons que les contraintes calculées obéissent à la loi de conservation de quantité de mouvement dans le canal. Ceci confirme le bon comportement de la méthode numérique pour des écoulements non-linéaires.

Mots-clés :

RHÉOLOGIE – SUSPENSIONS – SIMULATIONS – OPENFOAM – ADHÉSION – ÉCOULEMENTS NON-LINÉAIRES – CORRECTIONS DE SOUS-MAILLE – LUBRIFICATION – MIGRATION – MÉTHODE DE DOMAINE FICTIF

ABSTRACT

We present a particle-scale simulation method for non-Brownian suspension flows at low Reynolds number, based on the Fictitious Domain Method and supplemented by sub-grid lubrication corrections. In their usual form, sub-grid corrections involve the underlying linear flow. In the present work, the conditions required to avoid considering this ambient flow while keeping frame indifference are determined, and a sub-grid correction matrix is built for the particle-particle and particle-wall hydrodynamic interactions such that the mentioned conditions inherently hold. This procedure extends the correct use of such sub-grid corrections to nonlinear flows. The method is validated against various particle-flow configurations, involving a few particles in linear and nonlinear flows with various boundary conditions, or concentrated suspensions in simple shear flow. Then, we study the role of adhesive forces in frictional suspensions, by varying both the intensity of adhesion and the volume fraction: after presenting the difficulties of simulating adhesive suspensions at low volume fractions due to particle depletion at the wall and shear-banding, we show that the relative viscosity of the suspension is a function of both volume fraction ϕ and shear stress Σ_{12}. The variation of the viscosity with these two parameters may be understood in the usual frame of suspension jamming provided that the jamming volume fraction now depends on the dimensionless suspension stress σ^* that involves the adhesive force between particles. The variation of the jamming volume fraction with stress may be interpreted as the variation of the yield stress with volume fraction. This curve separates the plane (ϕ, σ^*) into two regions: one in which the suspension flows and the other in which it jams. We continue by investigating the shear-induced particle migration in a pressure-driven channel suspension flow. In such a system, particles are driven toward the channel center, resulting in a volume fraction gradient across the channel and a plug region where the jamming volume fraction as measured in shear flow may be exceeded. The flow profile is thus highly nonlinear, both due to the pressure gradient and the time-varying concentration gradient, which justifies the use of the present numerical method. We compare the results to a modified version of the Suspension Balance Model, confirming the well-known limits of such a model in the plug region. Finally, we show that the computed stresses obey the usual momentum balance in the channel: the tangential stress is indeed driven by the pressure gradient as predicted by theory and the second normal stress (parallel to the velocity gradient) does not vary over the channel width, although contact and hydrodynamic contributions significantly do over both time and space. This confirms the good behavior of the present numerical method when nonlinear flows are tackled.

Key-words:

RHEOLOGY – SUSPENSIONS – SIMULATIONS – OPENFOAM – ADHESION – FICTITIOUS DOMAIN METHOD – LUBRICATION – NONLINEAR FLOWS – SUB-GRID CORRECTIONS – PARTICLE MIGRATION

ACKNOWLEDGMENTS

I thank the members of the jury for reading, appreciating, and criticizing my work. I will treasure the discussions I have been fortunate enough to share with you.

François, choisir les bons mots pour te remercier est très difficile. Je pense de tout cœur que t'avoir eu comme directeur de thèse a été l'une des plus grandes fortunes de ma vie. "Encadrant" est un mot qui n'existe pas en italien dans ce sens, mais c'est exactement ce que tu as été pour moi pendant ces trois années : un mentor, un guide, un exemple. Merci de m'avoir accompagné avec patience, rigueur et honnêteté. Le café du matin, frapper à ta porte pour te poser des questions, rester tard le soir devant le tableau, les blagues, tes leçons sur la matrice de résistance... ce ne sont que quelques exemples de moments qui vont me manquer. Merci de m'avoir accompagné dans cette aventure, et de m'avoir transmis les bonnes valeurs avec lesquelles je vais bâtir ma vie de chercheur. Il y a tellement de choses à dire, je suis sûr que j'oublie quelque chose, je conclue donc par un simple et sincère, immense, MERCI. Je garderai précieusement tes enseignements.

Laurent, ton grand sourire m'a accompagné tout au long de ces années. De toi, j'ai appris à être sérieusement léger et jamais superficiel : tes observations et raisonnements pointus ont été un élément fondamental dans mes travaux de thèse. J'ai aussi appris que, de temps en temps, il vaut mieux laisser les mouches tranquilles... Un grand MERCI à toi.

Élisabeth, Fred, merci de m'avoir accueilli à bras ouverts dans l'équipe et de m'avoir donné le sentiment de faire partie d'une grande famille dès le début. En plus des discussions scientifiques, je remercie Élisabeth pour m'avoir initié avec passion à la politique française et Fred pour les mémorables soirées sévillanes. Vous avez contribué à faire de mon doctorat une expérience positive et inoubliable, et je vous en remercie infiniment.

Ensuite, je souhaite remercier,

Guillaume, l'une des personnes les plus intéressantes et belles que j'aie jamais rencontrées. C'est grâce à toi que j'ai découvert (en bois) les jeux de mots en français. Après trois ans, je commence enfin à les comprendre tout de suite (ou presque). Tu es un ami très cher.

Jordy, le roublard, pour ton inépuisable générosité. Et pour le vin portugais ! Un jour, peut-être, tu n'arriveras plus à me persuader... Tu es un ami incroyable sur lequel je peux toujours compter.

Christophe, collègue de bureau ayant les mêmes problèmes mentaux que moi avec l'ordre. Merci pour tes discussions sur la politique, l'actualité et la culture, pour les mille passages et pour tes desserts-bombes ! Si un jour, j'ai un quelconque problème administratif, tu seras le premier que j'appellerai. Tu es un grand ami.

Marjorie, la personne la plus gentille et instable (physiquement, dans le sens que tu trébuches toujours) que je connaisse. Merci pour ta bonté extraordinaire. Je te laisse mes plantes, je suis sûr que tu en prendras mieux soin que moi.

Thibaut, maître de donjon, pour m'avoir initié aux jeux de rôle et pour les apéritifs. On t'as appelé Adrien, puis Thomas, quand tu coupes les cheveux tu n'es plus la même personne... Mais rappelle-toi : un Caterpie peut se transformer en un Butterfree, mais le cœur qui bat à l'intérieur reste le même.

Duncan, *ma cheee* ! Un jour, je t'apprendrai à faire l'accent italien (et pas celui espagnol). Tu m'as fait sentir que je faisais partie du groupe avant même que j'arrive. Merci pour ton honnêteté, les gros rires au bureau et les dîners chez toi et Caro.

Lorenzo et Alek, pour avoir partagé avec moi la passion pour les mangas et les animes, et pour m'avoir fait découvrir Jojo !

Amandine, pour ton sourire constant. Je te laisserai la recette du limoncello parfait.

Antoine, pour ton humour, ta sympathie, et pour l'énorme quantité de fromage que tu ramènes quand on fait des dîners !

Enzo, pour les blagues interminables et pour m'avoir accueilli dans l'équipe.

Maeva, pour ta sympathie, ton support technique, et pour m'avoir toujours accordé des millions et des millions d'heures de calcul sur le cluster.

Bernard et Jerôme, pour votre support technique indispensable et votre patience.

Tous les doctorants, post-doctorants et stagiaires avec qui j'ai partagé cette aventure, ainsi que toutes les personnes du laboratoire INPHYNI pour la bonne ambiance et le soutien.

Infine, ci tengo a ringraziare,

Greta, per la tua bontà e per essere rimasta sempre al mio fianco. Insieme, abbiamo scoperto Nizza ed i suoi dintorni, in giro sulla mitica Shadow! La tua presenza ha reso questi tre anni indimenticabili, spensierati, e leggeri. La prima convivenza (in un monolocale!), i confinamenti chiusi in casa, le cene fuori, il nostro primo albero di Natale insieme, le tue torte, i film durante i quali mi addormento sempre... questi e altri mille nostri ricordi rimarranno per sempre legati al mio dottorato e a questi luoghi. Quindi uno speciale grazie a te che hai reso questi momenti ancora più preziosi.

I miei genitori, mio fratello Gianfi, e Giulia, per essere fondamenta e pilastri portanti della mia vita, e un supporto costante sul quale posso contare ad occhi chiusi. Grazie di avermi sempre messo nelle condizioni di poter fare ciò che ho voluto, e per aver costruito i miei valori e reso di me la persona che sono oggi. Crescere in una famiglia come la nostra è stata la mia fortuna più grande.

To conclude, I just want to thank all the amazing people I have met over the past few years. It has been a heck of an adventure.

Cheers!

If I'd had only one CPU,
my PhD would have lasted 571 years.

CONTENTS

INTRODUCTION (FR)

Que signifie “rhéologie” ? Le terme vient des mots grecs ῥέο̄ (*rhéo* : “écoulement”) et −λογία (*-logia* : “étude de”). Nous appliquons cette étude aux suspensions, donc nous voulons **étudier l’écoulement des suspensions**. Le terme “rhéologie” a été inventé par Eugene C. Bingham en 1920 et s’inspire de l’aphorisme du philosophe grec Héraclite πάντα ῥεῖ (*panta rhei* : “tout coule”), qui a vécu entre c. 535 BCE et c. 475 BCE. Ce qu’Héraclite suggère, c’est que tout est en constant devenir, et que rien ne reste jamais identique. Partons donc de ses précieuses paroles et allons plus loin : Comment les suspensions coulent-elles ? Quels sont les mécanismes moteurs ? Quels sont les paramètres de contrôle ? Et aussi, les suspensions coulent-elles vraiment *toujours* ? Ce sont des questions très complexes, et cela fait maintenant plus d’un siècle que les chercheurs du monde entier cherchent des réponses. Certaines questions ont reçu des réponses, d’autres seulement partiellement, certaines réponses se sont révélées incomplètes ou même fausses. Ce qui est sûr, c’est qu’il s’agit d’un sujet très stimulant. Notre espoir est de faire un pas en avant précieux avec le présent travail.

Les suspensions sont partout autour de nous : dans l’industrie sous la forme de béton frais, dans le transport des aliments, dans le carburant des fusées Ariane, dans les peintures et les cosmétiques ; dans la nature, la boue, la lave, les glissements de terrain sous-marins, le transport de sédiments dans les rivières ou le sang dans nos veines sont tous des suspensions complexes. Il est donc très important de comprendre leur rhéologie afin de prédire le comportement de ces systèmes omniprésents. La nature même de ces matériaux peut introduire une multitude de paramètres (taille et forme des particules solides, degré de polydispersité, propriétés rhéologiques du fluide en suspension, différence de densité entre les deux phases, etc.) et générer une abondance de comportements rhéologiques complexes : thixotropie, rhéofluidification, rhéoépaississement, contrainte seuil, pour n’en citer que quelques-uns. Cependant, même une suspension extrêmement simple de particules rigides, sphériques et non colloïdales immergées dans un liquide Newtonien présente une physique très riche et complexe qui continue à soulever de nombreuses questions.

Depuis les travaux fondateurs de Einstein (1909, 1911), diverses études théoriques, expérimentales et numériques ont permis une meilleure compréhension en mettant en évidence des propriétés communes aux suspensions telles que l’augmentation de la viscosité avec la concentration en particules solides jusqu’à la divergence pour une certaine fraction volumique appelée *“fraction de blocage”* pour laquelle la suspension se bloque. La compréhension d’autres propriétés importantes, telles que la structuration des particules dans le cœur ou au voisinage de parois solides, qui conduit probablement au glissement, ou la localisation du cisaillement, est également de première importance. Enfin, la migration des particules induite par le cisaillement est également un enjeu majeur pour la compréhension de la rhéologie des suspensions d'un point de vue fondamental, mais aussi pour l'optimisation des procédés industriels qui nécessitent souvent de telles suspensions.

On sait aujourd'hui que l'on peut distinguer deux types d'interactions jouant un rôle dans l'écoulement des suspensions non-Browniennes concentrées : les interactions hydrodynamiques et les interactions non-hydrodynamiques. L'hydrodynamique comprend les interactions à longue portée et les interactions à courte portée sous forme de forces de lubrification. Les interactions non-hydrodynamiques sont essentiellement liées au contact direct entre particules solides, longtemps considéré comme impossible à cause des forces de lubrification qui divergent lorsque deux particules entrent en contact. En réalité, ces contacts sont rendus possibles par la présence de rugosités qui tapissent la surface des particules réelles. La littérature souligne aujourd'hui le rôle majeur que jouent ces contacts directs dans la rhéologie des suspensions concentrées : ils augmentent drastiquement la viscosité de la suspension, et peuvent être à l'origine de phénomènes de rhéofluidification et de migration. En particulier, le *Suspension Balance Model* (SBM) de Morris & Boulay (1999), qui est un modèle biphasique, établit que la migration des particules est proportionnelle à la divergence des contraintes normales particulaires. Plus tard, Lhuillier (2009) et Nott et al. (2011) ont modifié le SBM en introduisant l'idée que seules les contraintes des particules dont l'origine est le contact solide entre les particules jouent un rôle dans la migration. Ceci a motivé de nombreuses études numériques et expérimentales visant à déterminer les contraintes particulaires impliquées dans la migration.

De manière générale, il existe actuellement un besoin de proposer des lois constitutives pour les suspensions non-Browniennes afin de pouvoir décrire ou prédire leur écoulement. Ainsi, si des modèles tels que le SBM semblent prometteurs pour décrire le comportement rhéologique des suspensions, ils souffrent cruellement d'un manque de mesures expérimentales pour étayer leur théorie. Dans ce cadre, les simulations numériques à l'échelle des particules entièrement résolues constituent un terrain fertile : ayant un accès complet à toutes les informations relatives au fluide et aux particules, elles jouent un rôle clé pour fournir toutes les quantités d'intérêt.

Dans ce travail, après avoir rappelé les généralités des écoulements de suspension dans Chapter 1, nous employons la méthode des domaines fictifs (FDM) : cette méthode numérique permet le calcul de l'écoulement de suspension à l'échelle de la particule en utilisant un maillage Cartésien fixe. D'un côté, cela introduit des difficultés dans la résolution de l'interface particule-fluide, mais d'un autre côté cela réduit les énormes coûts de calcul qu'un remaillage exigerait, ce qui donne à la FDM un fort attrait. L'approche numérique, les idées de base de la méthode et son implémentation dans OpenFOAM, ainsi que les techniques numériques nécessaires, sont entièrement détaillées dans Chapter 2.

Comme un maillage régulier fixe est utilisé, des corrections sous-maille sont nécessaires pour prendre en compte correctement le flux de lubrification qui se produit entre les particules à une distance proche. L'implémentation standard de ces corrections de sous-maille n'est valable que pour les flux linéaires. Dans Chapter 3, nous développons une version invariante par changement de référentiel de ces corrections de sous-maille, permettant leur utilisation correcte également dans des écoulements non-linéaires et, ainsi, s'ouvrant à une grande variété d'investigations telles que les suspensions dans un écoulement de Poiseuille. Les détails concernant la théorie de la lubrification, la forme générale des tenseurs de résistance, les matrices théoriques, la façon dont ces matrices ont été mesurées dans ce travail, et la façon dont l'invariance par changement de référentiel est obtenue, sont donnés dans Appendices A to D.

Dans Chapter 4, de nombreuses validations de la méthode numérique et des corrections de sous-maille sont proposées, où de multiples configurations de particules et d'écoulement sont étudiées et comparées à la littérature existante : en partant de configurations de une à trois particules, le chapitre se termine par des suspensions frictionnelles concentrées bidisperses dans un écoulement de cisaillement simple. Des détails sur la façon dont les erreurs de mesure sont estimées sont donnés dans Appendix G.

Dans Chapter 5, nous étudions le rôle des forces adhésives entre les particules dans des suspensions bidisperses frictionnelles modérément concentrées et concentrées subissant un écoulement de cisaillement simple : nous étudions trois valeurs du coefficient de friction en faisant varier l'intensité des forces adhésives et la fraction volumique, et nous montrons que la viscosité relative de la suspension dépend à la fois de la fraction volumique et de la contrainte de cisaillement. Pour introduire les forces attractives, nous utilisons un modèle très simple, qui est comparé à un modèle plus complet dans Appendix E.

Enfin, dans Chapter 6, la migration des particules induite par le cisaillement est étudiée dans des écoulements de suspension en canal sous pression : en considérant des suspensions frictionnelles bidisperses avec trois fractions volumiques différentes, nous étudions le comportement des profils de fraction volumique locale et de de vitesse des particules, ainsi que l'équilibre des contraintes dans la suspension. Les résultats sont comparés à une version modifiée du SBM proposée par Badia et al. (2022) et dérivée dans Appendix F.

Un long voyage nous attend, et nous espérons savoir satisfaire la curiosité du lecteur.

INTRODUCTION (EN)

What does "rheology" mean? The term comes from the greek words ῥέō (*rhéo*: "flow") and −λογία (*-logia*: "study of"). We apply this study to suspensions, so we want to **study the flow of suspensions**. The term "rheology" was coined by Eugene C. Bingham in 1920 and was inspired by the aphorism by the Greek philosopher Heraclitus πάντα ῥεῖ (*panta rhei*: "everything flows"), who lived between c. 535 BCE and c. 475 BCE. What Heraclitus was suggesting is that everything is a constant becoming, and nothing ever stays the same. So let us start from his precious words and go further: How do suspensions flow? What are the driving mechanisms? What are the control parameters? And also, do suspensions *always* flow? These are very complex questions, and it has been now more than a century that researchers all over the world are hunting for answers. Some of the questions have been answered, others only partially, and some answers have proved to be incomplete or even wrong. What is sure is that this is a very challenging topic. We hope to make a valuable step forward with the current work.

Suspensions are all around us: in the industry in the form of fresh concrete, in food transportation, in Ariane rockets fuel, in paints and cosmetics; in nature, mud, lava, underwater landslides, sediment transport in rivers or blood in our veins are all complex suspensions. It is therefore very important to understand their rheology to predict the behavior of such ubiquitous systems. The very nature of the constituents of these materials can introduce a multitude of parameters (size and shape of the solid particles, degree of polydispersity, rheological properties of the suspending fluid, density difference between the two phases, etc.) and generate an abundance of complex rheological behaviors: thixotropy, shear-thinning, shear-thickening, threshold stress, to mention a few. However, even an extremely simple suspension of rigid, spherical, non-colloidal particles immersed in a Newtonian liquid presents a very rich and complex physics that continues to raise many questions.

Since the seminal work of Einstein (1909, 1911), various theoretical, experimental, and numerical studies have led to a better understanding by highlighting properties common to suspensions such as the increase of viscosity with the concentration of solid particles up to the divergence for a certain volume fraction called *"jamming fraction"* for which the suspension jams. The understanding of other important properties, such as the structuring of the particles in the bulk or in the vicinity of solid walls which probably leads to wall-slip, or the localization of shear, is also of primary importance. Finally, shear-induced particle migration is also a major issue in the understanding of suspension rheology from a fundamental point of view, but also for the optimization of industrial processes that often require such suspensions.

Today, we know that two types of interactions playing a role in the flow of concentrated non-Brownian suspensions can be distinguished: hydrodynamic and non-hydrodynamic. Hydrodynamics includes long-range interactions and short-range interactions in the form of lubricating forces. The non-hydrodynamic interactions are essentially related to the direct contact between solid particles, which was considered impossible for a long time because of the lubrication forces that diverge when two particles come into contact. In reality, these contacts are made possible by the presence of roughness which lines the surface of real particles. The literature now emphasizes the major role that these direct contacts play in the rheology of concentrated suspensions: they drastically increase the viscosity of the suspension and can be at the origin of shear-thinning and migration phenomena. In particular, the Suspension Balance Model (SBM) by Morris & Boulay (1999), which is a two-phase model, establishes that the migration of particles is proportional to the divergence of the particle's normal stresses. Later, Lhuillier (2009) and Nott et al. (2011) modified the SBM by introducing the idea that only particle stresses whose origin is solid contact between particles play a role in migration. This has motivated numerous numerical and experimental studies aimed at determining the particle stresses involved in particle migration.

In general, there is currently a need to propose constitutive laws for non-Brownian suspensions to be able to describe or predict their flow. Thus, if models such as the SBM seem promising to describe the rheological behavior of suspensions, they cruelly suffer a lack of experimental measurements to support their theory. In this framework, fully-resolved particle-scale numerical simulations have fertile soil: having complete access to all the information related to both fluid and particles, they play a key role in furnishing all the quantities of interest.

In this work, after recalling the generalities of suspension flows in Chapter 1, we employ the Fictitious Domain Method (FDM): this numerical method allows the computation of the suspension flow at the particle scale employing a fixed Cartesian mesh. The latter, on the one hand, introduces difficulties in the resolution of the particle-fluid interface, but on the other hand, it reduces the enormous computational costs that a re-meshing would require, giving the FDM a strong appeal. The numerical approach, the basic ideas of the method, and its implementation in OpenFOAM, together with necessary numerical technicalities, are fully detailed in Chapter 2.

As a fixed regular mesh is used, sub-grid corrections are needed to correctly take into account the lubrication flow arising between particles at a close distance. The standard implementation of such sub-grid corrections is valid only in linear flows. In Chapter 3, we develop a frame-invariant version of such sub-grid corrections, allowing their correct use also in nonlinear flows and, thus, opening up to a wide variety of investigations such as suspensions in a Poiseuille flow. Details about the lubrication theory, the general form of the resistance tensors, the theoretical matrices, how such matrices have been measured in this work, and how the frame indifference is achieved, are given in Appendices A to D.

In Chapter 4, numerous validations of both the numerical method and the frame-invariant sub-grid corrections are proposed, where multiple particles and flow configurations are investigated and compared to existing literature: starting from one-to-three-particles configurations, the chapter concludes with bidisperse concentrated frictional suspensions in simple shear flow. Details about how systematic measurement errors are estimated are given in Appendix G.

In Chapter 5, we investigate the role of adhesive forces between particles in bidisperse frictional moderately-concentrated and concentrated suspensions undergoing simple shear flow: we study three values of the friction coefficient by varying the intensity of adhesive forces and the volume fraction, and we show that the relative viscosity of the suspension depends on both volume fraction and shear stress. To introduce the attractive forces, we employ a very simple model, which is compared to a more complete one in Appendix E.

Finally, in Chapter 6, the shear-induced particle migration is studied in pressure-driven channel suspension flows: by considering bidisperse frictional suspensions at three values of the volume fraction, we investigate the behavior of the local volume fraction and particle velocity profiles, as well as the suspension stress balance. The results are compared to a modified version of the SBM proposed by Badia et al. (2022) and derived in Appendix F.

A long journey awaits, and we hope to gratify the reader's curiosity.

1

GENERALITIES

Before dealing with the methodology employed and discussing the results obtained, it is certainly useful to define the context of the current work: we are going to see **why** it is so interesting to study the rheology of particulate suspensions, then we are going to see **what** are the physical quantities to measure to understand the behaviors of these complex fluids, and finally we are going to see **how** the investigation is performed.

Particular attention is given to what directly concerns the current dissertation, while more complete reviews can be found in the literature, e.g. Denn & Morris (2014), Maxey (2017), É. Guazzelli & Pouliquen (2018), and Ness et al. (2021), to cite a few.

1.1 CONTEXT

The context is defined in the title of the current work: *"Simulation of concentrated non-Brownian frictional and adhesive suspensions in linear and nonlinear flows"*. So, let us analyze it:

- a **suspension** is a mixture of particles and fluid; they are omnipresent in natural phenomena (e.g., blood, mud, lava, river beds, etc.) and industrial processes (e.g., fresh concrete, cosmetics, food, solid rocket fluid, etc.);
- we deal with **non-Brownian** particles, meaning that the suspended particles are sufficiently large (i.e., with a radius much larger than a micrometer) for random thermal fluctuations of the positions of the particles to be neglected;
- we are interested in **concentrated** suspensions, meaning that there is a high density of suspended particles (in the current work, the terms "dense" and "concentrated" are used with the same meaning); in such systems, direct interactions between particles (and between particles and walls) play a central role in the rheology;
- we consider **frictional** particles, meaning that, as soon as there is contact, there is also a tangential force; in Chapter 5, an **adhesive** (i.e. attractive) normal force is added to the elastic contact force; we want to investigate the effects these direct interactions have on the rheological properties of particulate suspensions;
- we investigate both **linear** (e.g., simple shear) and **nonlinear** (e.g., Poiseille) Stokes **flows**, as very interesting and variegate behaviors are observed in these two types of flow (e.g., shear jamming, shear-induced particle migration);
- we choose to perform such an investigation by the means of numerical **simulations**, and we want to do that the hard way, i.e. by writing from scratch our code.

1.2 RHEOPHYSICS OF NON-BROWNIAN DENSE SUSPENSIONS

We consider non-inertial, non-colloidal, neutrally buoyant, and non-Brownian rigid spherical particles suspended in an incompressible and Newtonian fluid. In this case, the Reynolds number (defined as the ratio of inertial forces to viscous ones) is zero, while the Péclet number (defined as the ratio of advection to diffusion fluxes) is infinity:

- $\mathrm{Re} = \dfrac{\text{inertial forces}}{\text{viscous forces}} = \dfrac{\rho_f u L}{\eta} = 0$
- $\mathrm{Pe} = \dfrac{\text{advection}}{\text{diffusion}} = \dfrac{6\pi a^3 \dot{\gamma} \eta}{kT} = \infty$

where ρ_f is the density of the fluid, u is the typical fluid velocity, L is the typical length scale of the flow, η is the dynamic viscosity of the fluid, a is the particle radius, $\dot{\gamma}$ is the shear rate, and kT is the Boltzmann energy.

Even in such a – *seemingly!* – simple case, physics can be complex and non-Newtonian behaviors may arise. Before proceeding, let us define the two following central quantities:

- relative viscosity $= \eta^s = \dfrac{\text{viscosity of the suspension}}{\text{viscosity of the suspending fluid}} = \dfrac{\eta_{susp}}{\eta}$
- volume fraction $= \phi = \dfrac{\text{volume occupied by the particles}}{\text{total volume}}$

1.2.1 MACROSCOPIC BEHAVIORS

Adding suspended particles to a fluid increases the effective viscosity of the mixture above that of the suspending fluid. This has been known for a Newtonian fluid since the work of Einstein (1909, 1911), who determined the expression of the viscosity of a dilute suspension: $\eta\,(1+5\phi/2)$. However, this linear dependence of the suspension viscosity with the solid volume fraction is valid only in very dilute suspensions (up to $\phi \approx 0.05$). Probably the most famous of the striking behaviors of particulate suspensions is that the relative viscosity is found to drastically increase with the volume fraction and to diverge when approaching the so-called jamming volume fraction ϕ_J, the latter being defined as the volume fraction at which the suspension flow stops and the corresponding shear rate $\dot{\gamma}$ is equal to zero. Other models have been developed to correctly take into account this behavior, and one of them is the Maron-Pierce correlation:

$$\eta^s = \frac{\alpha}{(1-\phi/\phi_J)^2} \tag{1.1}$$

where α and ϕ_J are fitting parameters. This model will be widely used in the current work.

It is also striking that the value of the jamming volume fraction is not a universal constant, even for quite large reasonably monodisperse spherical particles. For instance, in Fig. 1.1, where several viscosity curves from experimental and numerical studies have been gathered, the experimental jamming volume fraction ranges from 0.58 to 0.605. As will be explained in the following, the reason for such variations may be found in the particular interaction forces between particles, including contact forces.

Another important behavior is that of the existence of normal-stress differences, i.e. normal stresses are no longer isotropic under shear. What are the normal-stress differences? Since the suspension is incompressible, the pressure (i.e., the trace of the total suspension stress tensor $\mathbf{\Sigma}$) is of no rheological interest, and the two relevant quantities are the first and second normal-stress differences defined as $N_1 = \Sigma_{11} - \Sigma_{22}$ and $N_2 = \Sigma_{22} - \Sigma_{33}$, respectively, where flow, velocity gradient, and vorticity directions are labeled 1, 2, and 3. Since normal stresses do not depend on the sign of the shear stress, the normal-stress differences are proportional to the shear stress modulus $|\tau|$ via some coefficients which are solely a function of the volume fraction ϕ. In addition, these coefficients do not diverge at ϕ_J, meaning that normal stress differences and shear stress present the same divergence when approaching the jamming volume fraction and do not diverge (Morris & Boulay, 1999).

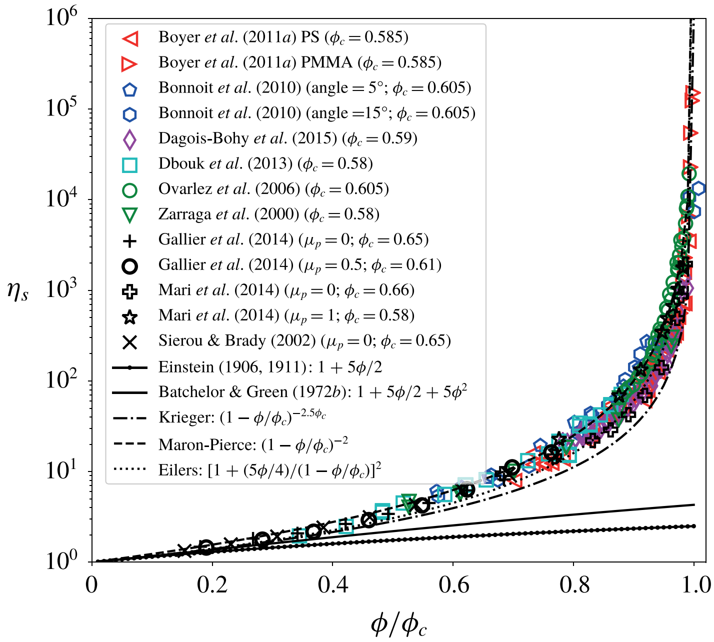

Figure 1.1
Relative viscosity η^s versus the reduced volume fraction ϕ/ϕ_c: experimental and numerical results, and models (see É. Guazzelli & Pouliquen (2018) for more details).

Moreover, Boyer et al. (2011) unified particulate suspension and dry granular rheology under the same framework. They employed an original experimental setup, consisting of an annular shear cell in which pressure-imposed measurements are performed, which is well suited to explore very high values of the volume fraction. They showed that in the highly concentrated range $0.45 \leqslant \phi \leqslant 0.58$ the behavior of a suspension can be fully described by the macroscopic friction coefficient and the volume fraction, both quantities being a unique function of the viscous number $J = \eta\dot{\gamma}_0/P^p$ (being $\dot{\gamma}_0$ and P^p the imposed shear rate and particle pressure, respectively).

1.2.2 MICROSCOPIC MECHANISMS

The above-mentioned macroscopic phenomena result from mechanisms occurring at the particle scale. The microstructure of the particle phase shows very interesting behaviors. When a suspension of neutrally buoyant hard spheres is sheared, particles follow the mean motion imposed by shear but also interact with each other, leading to random motion. However, a certain organization exists in the averaged position of the particles relative to each other. To investigate the behavior of the microstructure, the pair distribution function (PDF) can be computed, indicating how the particle density varies as a function of the distance from a reference particle at the origin and of the angle between the two particles. This pair distribution function is expected to be independent of the shear rate and to depend only on the volume fraction. The first attempt at obtaining the PDF was made Gadala-Maria & Acrivos (1980), who measured the relative arrangement of particles located near the top

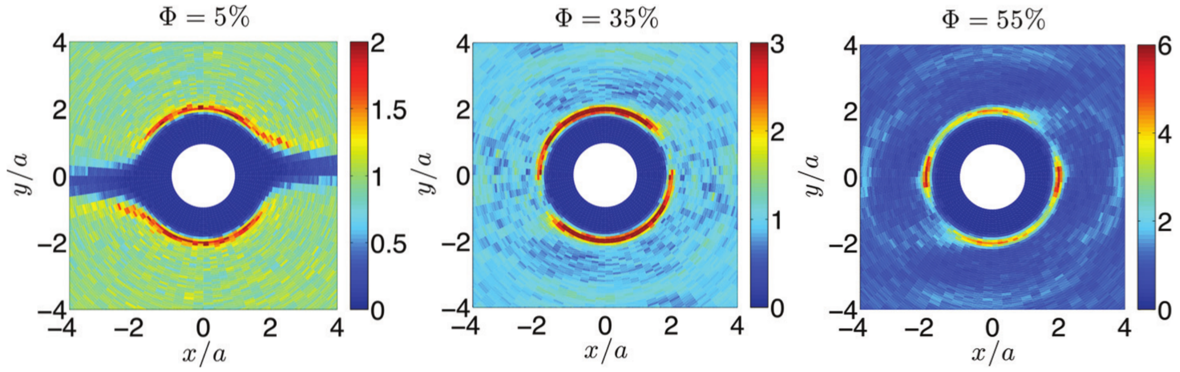

Figure 1.2
Experimental PDF in the plane of the shear for different ϕ, data from Blanc et al. (2013).

layer of a concentrated suspension sheared in a Couette cell. Recent experiments (Parsi & Gadala-Maria, 1987; Rampall et al., 1997; Blanc et al., 2011a) and simulations (Sierou & Brady, 2002; Drazer et al., 2004; Yeo et al., 2010; Gallier et al., 2014a), concerning non-Brownian suspensions ranging from dilute to dense regimes, show that the microstructure loses isotropy (see Fig. 1.2), establishing a preferred direction for finding the close-contact pairs that control the observed rheology of concentrated suspensions (Blanc et al., 2013). The shape of such PDF (Blanc et al., 2011a) as well as measurements of individual particles trajectories (Pham et al., 2015) allowed to connect the microscale motion of the particles to direct contact between surface asperities, highlighting the importance of direct contact forces, in addition to the usual hydrodynamic interactions. Both types of interaction are addressed in the following.

1.3 HYDRODYNAMICS

The hydrodynamic interactions are of great interest in the current work. That is also why, as we will see in the following, a numerical method that solves the Navier-Stokes equations for the flow is chosen. The presence of a particle modifies the flow around itself, and this perturbation is transferred from the fluid to other surrounding particles, modifying their dynamics. These hydrodynamic interactions also contribute to the increase of the suspension viscosity and have a long-range influence as they decrease very slowly with the distance from the considered particle (typically with $1/r$ or $1/r^2$): that is why it is fundamental to take them into account in dilute and moderately dense suspensions. Also, when studying systems with few particles, the size of the domain (i.e., the distance between the particles and the walls) plays a central role.

Short-range hydrodynamic interactions are also present: when two particles approach each other at a small distance, a lubrication flow that resists the relative motion arises, leading to lubrication forces acting on both particles. These forces are one of the central interests in the current work and will be deeply discussed in Chapter 3.

1.4 DIRECT INTERACTIONS

In the last decade, the role played by frictional contact in the rheology of dense suspensions has been widely acknowledged. Thanks to numerical simulations, it is very easy to measure interactions between particles and the influence they have on microstructure (Abbas et al., 2007), and then estimate the relative importance of the stresses carried by contacts and those due to hydrodynamic forces to determine which contribution controls the rheological behaviors observed in experiments.

In Fig. 1.3, the numerical results for the relative viscosity of a sheared suspension from Gallier et al. (2014b) for different friction coefficients μ are compared to the experimental measurements by Zarraga et al. (2000) and Dbouk et al. (2013). It can be noticed that the friction coefficient has to be increased up to 0.5 to recover the values of the viscosity observed in experiments. This behavior is explained by the variation of the jamming volume fraction ϕ_J with the friction coefficient μ. Several studies (Gallier, 2014; Mari et al., 2014; Peters et al., 2016) have indeed shown that the higher the friction coefficient the lower the jamming volume fraction: in particular, in bidisperse suspensions, the jamming volume fraction ϕ_J can be decreased from ≈ 0.64 for $\mu = 0$ down to ≈ 0.55 for $\mu = \infty$.

As we notice in Fig. 1.4 [a], for frictional suspensions the contribution of contacts remains negligible for $\phi \lesssim 0.25$. For larger volume fractions, the contact contribution rapidly increases and becomes dominant for $\phi \gtrsim 0.4$. The hydrodynamic contribution increases too, but at a lower rate, showing that in the jamming transition the rheology is practically dominated only by contacts. In Fig. 1.4 [a] and [b], the same analysis can be carried out for the normal-stress differences: for α_1 the hydrodynamics have always a negative contribution, whereas the contact contribution changes sign at $\phi \approx 0.40$, so that for larger volume fractions the two contributions are of the same order of magnitude; the scenario strongly differs for α_2, which is dominated by contacts with a negative contribution.

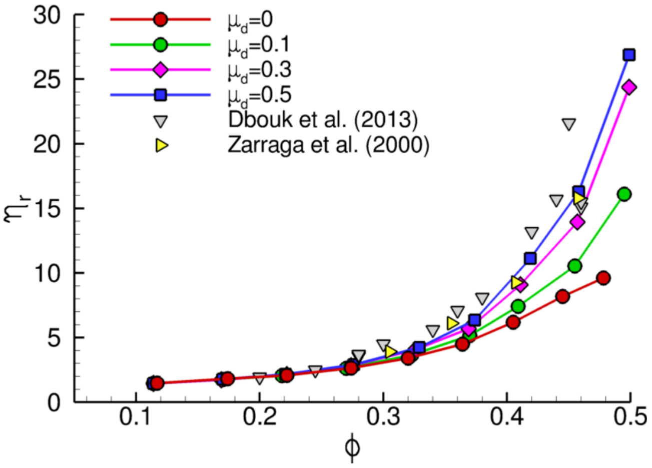

Figure 1.3
Relative viscosity as a function of the volume fraction for different values of the friction coefficient μ: comparison between the numerical results by Gallier et al. (2014b) and the experimental measurements by Zarraga et al. (2000) and Dbouk et al. (2013) (figure from Gallier (2014)).

Peculiar mechanisms arise when investigating the role of friction on the transient of shear-reversed suspensions. Studying the re-organization of the microstructure and the relaxation of contact forces during the transient by varying the contact law parameters (surface roughness height and friction coefficient), it can be shown that in the long-time transient the difference between the steady viscosity and the minimum one is proportional to the contact contribution to the steady viscosity, allowing in principle easy determination of the latter in experiments (Peters et al., 2016).

What happens when the friction coefficient is allowed to depend on suspension stress? Frictional contact forces are essential to reproduce the experimentally observed shear-thickening behavior. The lubricated-to-frictional transition provides a coherent mechanistic basis for shear-thickening, confirmed by numerical simulations (Wyart & Cates, 2014; Morris, 2018; Abhinendra Singh et al., 2018).

Moreover, a load-dependent inter-particle friction coefficient has arisen as a plausible explanation of the shear-thinning behavior of non-Brownian suspensions (Lobry et al., 2019): rough particles come into solid contact through one or few asperities. In such a few-asperities elastoplastic contact, the friction coefficient is expected to decrease when increasing the normal load. This model has been experimentally validated (Arshad et al., 2021), showing that the inter-particle friction coefficient decreases with the load, contrary to what is expected for macroscopic contacting bodies.

Other peculiar direct interactions are the adhesive (i.e., attractive) forces between particles and between particles and walls. Adhesion can lead to very interesting behaviors. This problem will be tackled in Chapter 5, where the role of adhesion in frictional suspensions undergoing simple shear flow will be investigated.

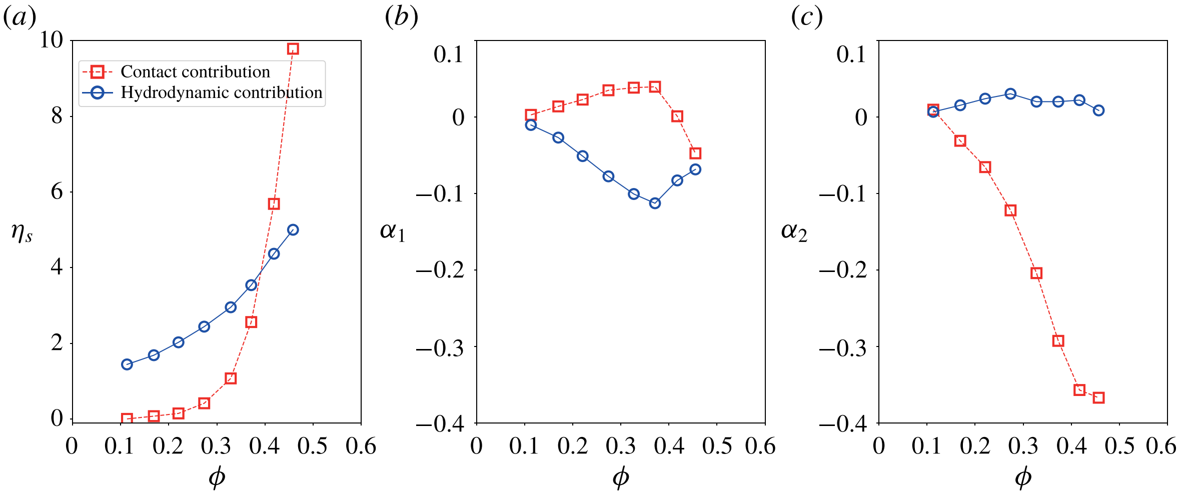

Figure 1.4
Relative contribution of the frictional contact (red squares) and the hydrodynamic (blue circles) stresses to (a) the viscosity, and (b) first and (c) second normal-stress differences $\alpha_1 = N_1/|\tau|$ and $\alpha_2 = N_2/|\tau|$, respectively, as a function of the volume fraction ϕ (figure from É. Guazzelli & Pouliquen (2018), data from the numerical simulations of Gallier et al. (2014b) including particle roughness as well as frictional contacts with friction coefficient $\mu = 0.5$).

1.5 NONLINEAR FLOWS

The previously presented behaviors arise also in very simple flows, like linear flows with a constant shear rate. The situation seems already quite complicated. As we are doing the job, let us add some more complications and consider nonlinear flows. As we are going to see in the following, nonlinear flows are of central interest in the current work. But why is it interesting to investigate nonlinear flows? Nonlinear flows, i.e. flows with a spatially variable shear rate (e.g., a pressure-driven flow), can give life to mechanisms that are not present in linear flows. However, the nature of these mechanisms still has to be enlightened.

One of the mechanisms in question is the viscous resuspension, first discovered by Gadala-Maria & Acrivos (1980) while measuring the rheological properties of suspensions of heavy non-Brownian particles in viscous Newtonian fluids using a parallel-plate device. The initially-settled particles were observed to resuspend under shear and the flowing suspension was seen to achieve a non-uniform concentration profile. Later, Leighton & Acrivos (1987b) showed that the equilibrium resuspension height could be modeled as a diffusive process balancing the downward gravitational flux of particles, both fluxes acting in the shear-gradient direction. This mechanism has been recently investigated by d'Ambrosio et al. (2021), who performed local measurements of both velocity and volume fraction of spherical particles dispersed in a lighter Newtonian fluid sheared in a vertical Couette cell. We can easily observe in Fig. 1.5 the variation of the resuspension height with the rotor rotation speed, and the corresponding volume fraction profiles.

In the case of a planar Poiseuille flow, the shear rate (defined as the absolute value of the derivative of the velocity profile) is not spatially constant and varies across the channel width, reaching its maximum value at the walls and its minimum value (i.e., zero) at the

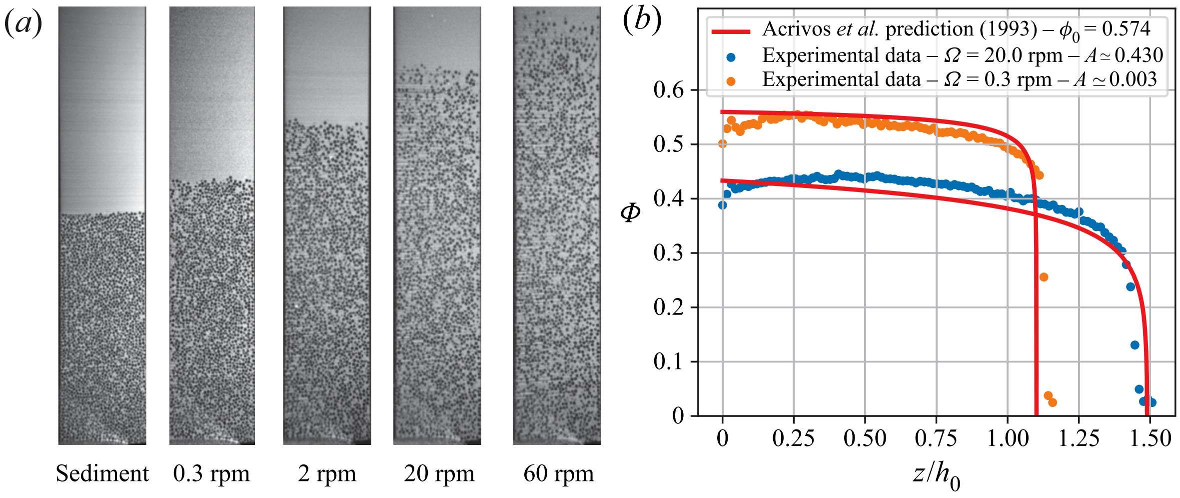

Figure 1.5
(a) Typical images recorded for different rotor rotation speeds; we can observe the variation of the resuspension height with the rotation speed. (b) Examples of the vertical concentration profiles for two rotation speeds, and comparison with the model proposed by Acrivos (1993). Data and figures from d'Ambrosio et al. (2021).

channel center. In this case, we can see at play one of the most common behaviors of nature: laziness. In this case, particles are lazy. So lazy that they tend to migrate toward regions where the shear rate is smaller than the one in which they are. The actual mechanisms are much more complicated and rely on the shear-induced particle migration (Gadala-Maria & Acrivos, 1980; Leighton & Acrivos, 1987a,b; Nott & Brady, 1994; Mills & Snabre, 1995; Miller & Morris, 2006; Lhuillier, 2009; Yeo & Maxey, 2011; Abbas et al., 2014). In concentrated regimes, migration can also lead to a volume fraction at the channel center that exceeds the jamming one! How is that possible? Is the suspension *really* jammed in that region? What are the driving mechanisms? These problems will be deeply treated in Chapter 6. However, it has to be stressed that simulations of suspensions in nonlinear flows require special care, as explained in the following.

1.6 NUMERICAL METHODS

In the understanding of the complex physics behind suspension flows, numerical simulations have been demonstrated to be a fundamental tool that can provide details not easily available in experiments, helping to identify which factors are most significant in determining the intricate behaviors observed in the rheology of particulate suspensions. For instance, in the specific field of non-Brownian suspensions, hydrodynamic interactions, both long- and short-range, direct interaction, and external potential forces have a prominent influence. Their relative influence depends on the nature of the fluid, the flow type, the particle volume fraction, the density mismatch between particles and fluid, and the velocity gradient intensity. During the last century, many different numerical approaches have been presented, each one having its advantages and downsides. Therefore, choosing the most suited approach can be very challenging, and defining the questions to be answered and the applications to aim for becomes fundamental. The spatial length scale, the computational complexity, and the available resources are the earliest considerations to tackle.

If the suspended particles are very small compared to the typical length scale of a flow and the volume fraction is very low, it may be feasible to treat each particle as a point and determine the fluid force on it from theoretical models or empirical correlations. Point particle methods typically present a low computational cost – at least for the particle sub-problem – making it possible to simulate a very large number of particles. These methods are useful in giving a first answer to how particle transport will develop in a flow and can be very useful in finite-Reynolds-number applications. However, there is an inherent ambiguity because the point force and momentum coupling of a particle to the fluid locally alter the underlying flow, and this in turn modifies the estimated particle velocity (Squires, 2007). For gas-solid flows with many small particles, this may not be an issue, but may well be in other contexts (Maxey, 2017).

On the opposite end of the spectrum in terms of particle resolution, we found the full Arbitrary Lagrangian Eulerian (ALE) simulations, in which the motion of each particle is

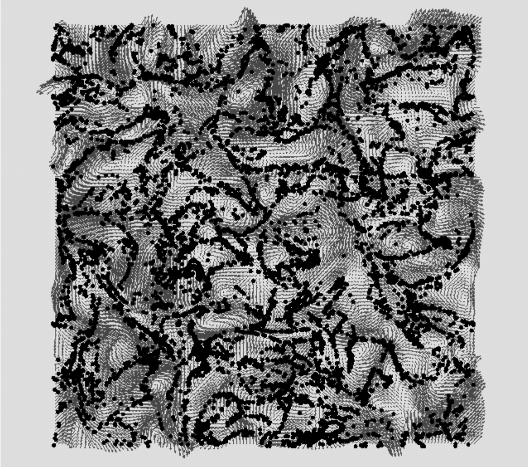

Figure 1.6
Example from a computation of particle-laden isotropic turbulence (Squires, 2007).

determined by the fluid force acting on it, as given by the fluid stress tensor integrated over the particle surface together with any external forces and non-hydrodynamic interactions between the particles. A key feature is a need to update the mesh as particles move (Hughes et al., 1981). Important factors are selecting the velocity of the mesh nodes, updating the mesh, periodically regenerating a new mesh to maintain the resolution, and interpolating the flow variables between the meshes. ALE simulations are incredibly effective for high-resolution studies, as the flow between particles and the particle-particle interactions are perfectly resolved. However, they present a monolithic computational cost, which makes them attractive only for a limited number of particles.

A primary tool for investigating the dynamics of both dilute and dense suspensions of spherical particles in a Stokes flow is the Stokesian Dynamics (SD) approach (Brady, 1988, 2001). This has been a widely employed fruitful method, which has given throughout the years the majority of the numerical results on the rheology of dense suspensions. The method is based on a low-order multipole representation of the far-field flow induced by a particle, including Stokeslet, rotlet, and stresslet terms and associated degenerate multipoles. These are calculated by pairwise sum and reflection methods to obtain a mobility matrix for the particle system (Bossis & Brady, 1984). Lubrication corrections for the viscous forces and torques, when particles are close to contact, are added in a pairwise manner for the resistance matrix (Durlofsky et al., 1987). SD is a meshless scheme, similar in style to molecular dynamics simulations, and is used to evaluate the velocities based on a specific particle configuration from which an updated configuration is obtained. Until the 2000s, SD has been employed only for two-dimensional simulations (to be more precise, a mono-layer of particles), mostly due to the high computational cost related to the inversion of the resistance matrix for the computation of the velocities of the particles. Works in the last 20 years have obtained a significant reduction of this computational cost, reaching simulations of up to thousands of particles (Sierou & Brady, 2001, 2002, 2004; Ouaknin et al., 2021). This approach is only suited for the case of a Newtonian suspending fluid. It has been mainly implemented for spherical particles, although it can tackle ellipsoidal particles as

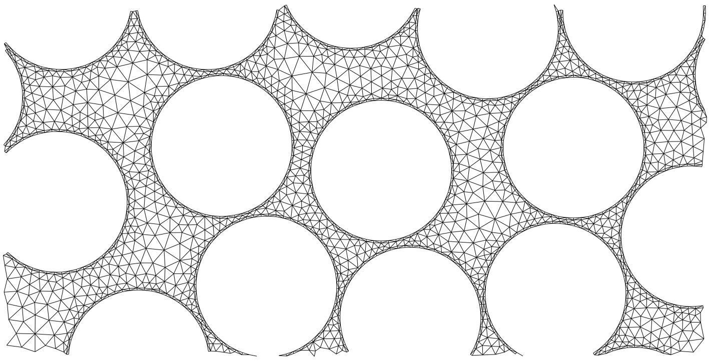

Figure 1.7
Example of a 2D mesh for ALE simulations (Lefebvre & Maury, 2005). High-resolution studies can be performed. However, as re-meshing – a very expensive operation – has to be done for each time step, a limited number of particles is typically employed.

well (Claeys & Brady, 1993). Periodic shear flow is usually implemented, but the method has been upgraded so that plane boundary walls may be tackled (Swan & Brady, 2011).

The lattice Boltzmann method (LBM) has become established as a mesoscopic simulation tool. The LBM is a weakly compressible flow solver based on the kinetic theory of gases and the evolution of a molecular distribution function on a lattice. The Navier-Stokes equations are not solved directly, but the fluid flow is computed using as the primary quantity the one-particle discrete-velocity distribution function discretized at the nodes of a lattice (Ladd, 1994; Nguyen & Ladd, 2002). The method has a simple structure that easily scales for parallel computation. However, the time steps are short. One approach is to use the LBM as a flow solver in combination with an immersed boundary method for the particle phase.

The Smooth Particle Hydrodynamics is an example of lagrangian meshless methods where flow fields are represented using co-moving fluid volumes interacting via pairwise forces. Particles and walls are modeled as frozen sets of particles similar to fluid ones. Both Brownian (Bian et al., 2012) and non-Brownian spherical particles in Newtonian (Vázquez-Quesada & Ellero, 2016) or non-Newtonian (Vázquez-Quesada & Ellero, 2017) fluids may be tackled, as well as arbitrary particle shape.

A method that aims at reducing the costs of ALE simulations but maintaining the full resolution of the flow is the Fictitious Domain Method (FDM). The determination of the force may involve a Lagrange multiplier (Glowinski, 1999; Glowinski et al., 2001), or not (N. Patankar et al., 2000). Lagrange-multiplier-free FDMs have been applied to tackle spherical (Gallier et al., 2014a) or non-spherical particles (Wu et al., 2020). The key feature of the FDM is that the Navier-Stokes equations for an incompressible flow are solved for the full domain, and a fixed computational mesh is specified for the whole domain $\mathcal{D}$, including the volume $\mathcal{D}_p$ occupied by the particles, and a force density field $\boldsymbol{\lambda}$ is set so that the (fictitious) fluid inside each particle responds as if it were in rigid-body motion. The force density field is defined throughout the particle volume. Inevitably, the transition from a viscous flow outside a particle to an equivalent rigid-body motion for the fluid inside leads to a sharp change in the velocity gradient, even if the velocity field itself is continuous. Therefore, particle tracking is a primary issue to tackle.

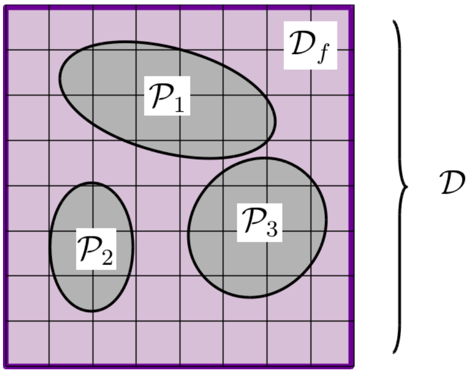

Figure 1.8
Example of a fixed Cartesian mesh for the FDM (Gallier, 2014).

The Force Coupling Method (FCM) is based on a low-order, finite force multipole representation of the effect particles have on the surrounding fluid (Maxey & Patel, 2001). It serves as a bridge between methods for Stokes flow and low-Reynolds-number conditions (Abbas et al., 2014). The force monopole corresponds to the force a particle transmits to the fluid if it were replaced by a rigid particle with the same density as the fluid. The force dipole is a combination of a symmetric stresslet and a torque that acts on the fluid. The torque is set similarly to the force monopole in terms of the angular momentum of the particle, which of the displaced fluid, and any external torques on the particles. The stresslet is chosen to ensure that the average rate of strain is zero within each particle. The aim is to create a flow outside the particle that matches the actual flow within a short distance from the surface. The fluid inside the particle volume satisfies the same integral moments as a rigid particle. This interior flow is an active part of the simulation. Finally, short-range hydrodynamic interactions are tackled using sub-grid corrections. The FCM gives results that are equivalent to those of SD. It is well suited for neutrally buoyant particles in Couette and Poiseuille flows, for both spheres (Yeo & Maxey, 2010a,b) and ellipsoids (Liu et al., 2009). The FCM has also been used to examine the particle-induced modulation of forced homogeneous turbulence (Yeo et al., 2010) and the dynamics of finite-Reynolds-number suspensions in homogeneous shear (Yeo & Maxey, 2013).

Another method involving the actual computation of the suspending fluid flow is the Immersed Boundary Method (Uhlmann, 2005; Breugem, 2012), in which point forces are exerted on the fluid in the vicinity of the surface defining the solid boundaries to enforce the particle rigid body motion.

Finally, the Discrete Element Method (DEM) has emerged as a powerful numerical method. Originally developed in the field of dry granular material (Pöschel & Schwager, 2005), it accounts for direct contact interactions, including friction. To allow suspension simulations, it must be supplemented with short-range lubrication interactions. In the last decade, it allowed outstanding progress in the understanding of the discontinuous shear-thickening (DST) in non-Brownian suspensions (Seto et al., 2013; Mari et al., 2014) and of the stress-induced transition from frictionless to frictional particle interactions (see Morris (2018) for a review). The influence of various particle contact behaviors on DST has been also evidenced, such as adhesion and rolling friction (Abhinendra Singh et al., 2020). Apart from DST, the effect of adhesive forces in highly concentrated suspensions on jamming has been probed (Jones & Ness, 2018). The rheology of suspensions in extensional flows has been also studied (Cheal & Ness, 2018). The main drawback of the method is that it does not account for long-range hydrodynamics, which seems not that important for straining flows, except maybe when shear-induced diffusion is addressed (Gallier et al., 2018). However, problems are expected for flows where particle settling is relevant since long-range interactions are known to have primary effects (E. Guazzelli et al., 2011). However, long-range hydrodynamic interactions may be introduced using a pore pressure (Catalano et al., 2014). Another drawback of DEM is that the underlying flow is needed to compute the drag, making it difficult to simulate problems where the latter is not prescribed.

1.6.1 OUR CHOICE

In the current work, we aim to build an efficient and precise tool for the simulation of particulate suspensions: we want to investigate the physics at a microscopic level, but we want a reasonable computational cost to simulate a great number of particles. We want to resolve the flow around the particles and take into account all the particle interactions. Yes, we have a lot of demands. That is why we have chosen the FDM as the method to be employed here. A highly detailed presentation of the method, its implementations, its performances, and its limitations, can be found in Gallier (2014)'s doctoral dissertation, as well as in his papers (Gallier et al., 2014a,b, 2016, 2018).

Here, we take inspiration from Gallier's work and build up a new tool. It should be stressed again that most of the methods mentioned above need specific treatment to be able to account for short-range hydrodynamic interactions as particles are at a distance that is smaller than the smallest length scale specified by the method (mesh size or fluid particle size). One of the most interesting and challenging developments we performed is a frame-invariant formulation of the sub-grid corrections needed to correctly take into account the lubrication forces: this feature makes the current method well suited to the simulation of non-homogeneous flows. More details will be presented in Chapters 3 and 6. We also take care of the optimization of the code, using a message-passing standard (MPI) and multi-threading (OpenMP). The method has been implemented in the OpenFOAM toolbox, making it cross-platform and easy to use.

In the following chapter, we start by presenting the equations that govern the fluid flow and the ones that dictate the dynamics of the particles; then, we present the numerical implementation of the method and we split the fluid sub-problem from the particle one, giving particular attention to the contact model. After showing the algorithm of the approach, we will go into important numerical details, explaining the challenges we had to address and how we tackled them. In the end, the reader will have a complete overview of the code and its functioning. Numerous validations of the code will be provided in Chapter 4.

2

NUMERICAL APPROACH

We start by presenting the equations governing the systems considered in the current work. We want to simulate rigid particles suspended in a Newtonian fluid. Therefore, the Navier-Stokes equations for an incompressible fluid flow are used, modified by adding a forcing term λ that reflects the forces and torques acting on the particles and enforces a rigid body motion inside their domain. Also, the flow equations are coupled to the particle dynamics via the forcing term (which is also used to compute the hydrodynamic interactions), for which the classic Newton's laws for motion are employed. We can start to seize the difficulties of the numerical procedure that have to be tackled.

Then, after showing in detail how the hydrodynamic interactions are computed, we are going to see that sub-grid corrections for lubrication are needed: when particles approach at a distance smaller than the spatial resolution (i.e., the mesh cell size), the solver cannot correctly compute the squeezing flow arising between their surfaces. The sub-grid corrections depend on the velocities and positions of the particles, and a linear system that takes into account all the forces and torques acting on the particles needs to be solved to obtain the velocities of the particles. Albeit these sub-grid corrections will be deeply treated in the next chapter, we need to introduce them here to have a wide and complete vision and understanding of the numerical approach and its algorithm.

Thereafter, the fluid sub-problem can be split from the particle sub-problem. We start by discussing the finite volume method and why it is so widely employed in CFD; we continue by presenting the numerical implementation of the governing equations in OpenFOAM: we discuss in detail the discretization of the different terms as well as the schemes involved, and we display the numerical procedure proposed by OpenFOAM and how it is employed in the framework of the current work. We use the SIMPLEC algorithm, which is characterized by two steps: the first one is the *prediction* step, in which the (compressible) momentum equation is solved by using the previous pressure field, obtaining a velocity field that is not fully divergence-free; then, the *correction* step follows, in which a pressure field that satisfies the continuity equation is sought, and the velocity field is accordingly corrected.

Then, the particle sub-problem is treated, and we enhance how it is coupled to the fluid sub-problem: the difficulty here is to determine the correct forcing term $\boldsymbol{\lambda}$ to get the right particle dynamics. To achieve this, the two sub-problems need to proceed simultaneously until convergence: first, the fluid problem is solved using the previous forcing term; then, the velocities of the particles are computed, always using the previous forcing term; finally, rigid body motion is imposed inside the particles domain and the forcing term is consequently corrected. This is repeated until the forcing term is no longer evolving.

After presenting the algorithm, we approach the end of the chapter by talking about some – *very important!* – numerical details, such as particle tracking, boundary conditions, parallelization of both the problems, and convergence control, the former being a very delicate issue. We also present the model employed for the contact forces, both the normal (using Hertz law) and the tangential (using Amontons-Coulomb friction law) components.

Details about the computational performances will be given at the end of Chapter 4 when simulations of concentrated suspensions with a high number of particles in a simple shear flow will be presented.

We conclude the current chapter by defining how the rheological quantities of interest such as the particle stresslet, the local volume fraction and stresses, and the relative viscosity, are computed.

This is a long, dense, heavy, but fundamental chapter. We recommend keeping a cup of coffee, tea, or anything useful to relieve the reading, nearby.

2.1 GOVERNING EQUATIONS

In the Fictitious Domain Method (FDM), the fluid flow is computed in the whole simulation domain $\mathcal{D}$ including the particles. A Newtonian fluid is assumed, with dynamic viscosity η and density ρ_f.

The particles are rigid spheres whose density is denoted by ρ_p, which can be different from the fluid one; their rigidity is enforced using a force density $\rho_f \boldsymbol{\lambda}$ that acts only in the volume of each particle $\mathcal{D}_p$. As a consequence, the fluid obeys modified incompressible Navier-Stokes equations:

$$\begin{aligned} &\rho_f \left(\frac{\partial \mathbf{u}}{\partial t} + \mathbf{u} \cdot \boldsymbol{\nabla} \mathbf{u} \right) = \boldsymbol{\nabla} \cdot \boldsymbol{\sigma} + \rho_f \boldsymbol{\lambda} \\ &\boldsymbol{\nabla} \cdot \mathbf{u} = 0 \end{aligned} \tag{2.1}$$

$$\boldsymbol{\sigma} = -p\boldsymbol{\delta} + \eta \left(\boldsymbol{\nabla} \mathbf{u} + \boldsymbol{\nabla} \mathbf{u}^T \right) \tag{2.2}$$

with the constraint that the fluid inside the particle undergoes rigid body motion:

$$\mathbf{u}(\mathbf{x}) = \mathbf{U}_p + \boldsymbol{\Omega}_p \times (\mathbf{x} - \mathbf{x}_p) \qquad \text{for} \quad \mathbf{x} \in (\mathcal{D}_p) \tag{2.3}$$

where $\mathbf{x}_p$ denotes the position of the particle (p) center. Then, Newton's equations read for each particle (p):

$$\begin{aligned} &M_p \frac{d\mathbf{U}_p}{dt} = \frac{\rho_p - \rho_f}{\rho_p} M_p \mathbf{g} + \mathbf{F}_p^h + \mathbf{F}_p^c + \mathbf{F}_p^{ext} \\ &\mathbf{J}_p \cdot \frac{d\boldsymbol{\Omega}_p}{dt} + \boldsymbol{\Omega}_p \times (\mathbf{J}_p \cdot \boldsymbol{\Omega}_p) = \mathbf{T}_p^h + \mathbf{T}_p^c + \mathbf{T}_p^{ext} \end{aligned} \tag{2.4}$$

where M_p and $\mathbf{J}_p$ are the particle mass and moment of inertia respectively, $\mathbf{F}_p^h$, $\mathbf{F}_p^c$, and $\mathbf{F}_p^{ext}$ respectively stand for the hydrodynamic, contact and additional external forces exerted on the particle (p), and $\mathbf{T}_p^h$, $\mathbf{T}_p^c$, and $\mathbf{T}_p^{ext}$ are the corresponding torques. Further details about the contact model will be given in Section 2.6.

Since the gravity force on the fluid has been absorbed in the pressure (Eqs. (2.1) and (2.2)), the hydrodynamic force $\mathbf{F}_p^h$ does not include the buoyancy force on the particle, consistent with Eq. (2.4).

On the one hand, the momentum equations for the fluid (Eq. (2.1)) and the particles (Eq. (2.4)) are coupled, since the particles (p) and the fluid inside the particles domain $\mathcal{D}_p$ share the same velocity field (Eq. (2.3)), and on the other hand, the hydrodynamic force and torque exerted on any particle originate in the stress on the particle surface.

Eq. (2.1) and its counterpart for the angular momentum may be integrated over the volume of each particle, which, with the help of Eq. (2.3), leads to:

$$\begin{aligned}
&\frac{\rho_f}{\rho_p} M_p \frac{d\mathbf{U}_p}{dt} = \int_{\partial \mathcal{D}_p} \boldsymbol{\sigma} \cdot \mathbf{n} \, d\mathcal{S} + \rho_f \int_{\mathcal{D}_p} \boldsymbol{\lambda} \, d\mathcal{V} \\
&\frac{\rho_f}{\rho_p} \left(\mathbf{J}_p \cdot \frac{d\boldsymbol{\Omega}_p}{dt} + \boldsymbol{\Omega}_p \times (\mathbf{J}_p \cdot \boldsymbol{\Omega}_p) \right) = \int_{\partial \mathcal{D}_p} (\mathbf{x} - \mathbf{x}_p) \times \boldsymbol{\sigma} \cdot \mathbf{n} \, d\mathcal{S} + \rho_f \int_{\mathcal{D}_p} (\mathbf{x} - \mathbf{x}_p) \times \boldsymbol{\lambda} \, d\mathcal{V}
\end{aligned} \tag{2.5}$$

As a consequence, the hydrodynamic force and torque exerted on each particle (p) as computed by the fluid flow solver read:

$$\begin{aligned}
\mathbf{F}_p^{FDM} &= \int_{\partial \mathcal{D}_p} \boldsymbol{\sigma} \cdot \mathbf{n} \, d\mathcal{S} = \frac{\rho_f}{\rho_p} M_p \frac{d\mathbf{U}_p}{dt} - \rho_f \int_{\mathcal{D}_p} \boldsymbol{\lambda} \, d\mathcal{V} \\
\mathbf{T}_p^{FDM} &= \int_{\partial \mathcal{D}_p} (\mathbf{x} - \mathbf{x}_p) \times \boldsymbol{\sigma} \cdot \mathbf{n} \, d\mathcal{S} = \frac{\rho_f}{\rho_p} \left(\mathbf{J}_p \cdot \frac{d\boldsymbol{\Omega}_p}{dt} + \boldsymbol{\Omega}_p \times (\mathbf{J}_p \cdot \boldsymbol{\Omega}_p) \right) - \rho_f \int_{\mathcal{D}_p} (\mathbf{x} - \mathbf{x}_p) \times \boldsymbol{\lambda} \, d\mathcal{V}
\end{aligned} \tag{2.6}$$

As already mentioned, the fluid flow solver cannot compute the flow at a scale smaller than the spatial resolution, i.e. the mesh size Δ. The lubrication flow arising between particles approaching at a small distance generates strong hydrodynamic forces that heavily influence the particle dynamics and, therefore, have to be correctly taken into account. Thus, sub-grid (SG) corrections have to be added to the force and torque on each particle. The implementation of these sub-grid corrections needs particular attention: a full explanation and many more details will be presented in Chapter 3. By defining the vector of translational and rotational velocities:

$$\mathcal{U} = (\mathbf{U}_1, \mathbf{U}_2, \ldots, \boldsymbol{\Omega}_1, \boldsymbol{\Omega}_2, \ldots) \tag{2.7}$$

the sub-grid corrections for forces and torques read:

$$\begin{aligned}
\mathbf{F}_p^{SG} &= -\mathcal{R}_{F\mathcal{U}}^{SG} \cdot \mathcal{U} \\
\mathbf{T}_p^{SG} &= -\mathcal{R}_{T\mathcal{U}}^{SG} \cdot \mathcal{U}
\end{aligned} \tag{2.8}$$

where $\mathcal{R}_{F\mathcal{U}}^{SG}$ and $\mathcal{R}_{T\mathcal{U}}^{SG}$ are the sub-grid correction resistance matrices that link the sub-grid correction forces and torques acting on the particles to their velocities and are a function of the distance between the particles. In particular, the linearity of the relations in Eq. (2.8) is related to the low Reynolds number flow at the particle scale that is considered in the current work. The total hydrodynamic force and torque in Eq. (2.4) finally read:

$$\begin{aligned}
\mathbf{F}_p^h &= \mathbf{F}_p^{FDM} + \mathbf{F}_p^{SG} \\
\mathbf{T}_p^h &= \mathbf{T}_p^{FDM} + \mathbf{T}_p^{SG}
\end{aligned} \tag{2.9}$$

From Eqs. (2.4), (2.6) and (2.9) the equations that govern the constraint on the force density $\boldsymbol{\lambda}$ are derived, and are written in Eq. (2.10) together with the fluid equations:

$$\rho_f \left(\frac{\partial \mathbf{u}}{\partial t} + (\mathbf{u} \cdot \boldsymbol{\nabla})\, \mathbf{u} \right) = \eta \boldsymbol{\Delta} \mathbf{u} - \boldsymbol{\nabla} p + \rho_f \boldsymbol{\lambda} \tag{2.10a}$$

$$\boldsymbol{\nabla} \cdot \mathbf{u} = 0 \tag{2.10b}$$

$$\mathbf{u} = \mathbf{U}_p + \boldsymbol{\Omega}_p \times (\mathbf{x} - \mathbf{x}_p) \quad \text{in} \quad \mathcal{D}_p \tag{2.10c}$$

$$\frac{\rho_p - \rho_f}{\rho_p} M_p \frac{d\mathbf{U}_p}{dt} = \frac{\rho_p - \rho_f}{\rho_p} M_p \mathbf{g} - \rho_f \int_{\mathcal{D}_p} \boldsymbol{\lambda}\, d\mathcal{V} + \mathbf{F}_p^{SG} + \mathbf{F}_p^{c} + \mathbf{F}_p^{ext} \tag{2.10d}$$

$$\frac{\rho_p - \rho_f}{\rho_p} \left(\mathbf{J}_p \cdot \frac{d\boldsymbol{\Omega}_p}{dt} + \boldsymbol{\Omega}_p \times (\mathbf{J}_p \cdot \boldsymbol{\Omega}_p) \right) = -\rho_f \int_{\mathcal{D}_p} (\mathbf{x} - \mathbf{x}_p) \times \boldsymbol{\lambda}\, d\mathcal{V} + \mathbf{T}_p^{SG} + \mathbf{T}_p^{c} + \mathbf{T}_p^{ext} \tag{2.10e}$$

In the following, inertia at particle scale is neglected, both for the fluid and the particles, so that the LHS of Eqs. (2.10a), (2.10d) and (2.10e) can be discarded. It should be stressed that this step is not mandatory and that the method is also convenient for finite-Reynolds-number flows (Gallier et al., 2014a). Finally, the simplified equations are:

$$0 = \nu \boldsymbol{\Delta} \mathbf{u} - \frac{\boldsymbol{\nabla} p}{\rho_f} + \boldsymbol{\lambda} \tag{2.11a}$$

$$\boldsymbol{\nabla} \cdot \mathbf{u} = 0 \tag{2.11b}$$

$$\mathbf{u} = \mathbf{U}_p + \boldsymbol{\Omega}_p \times (\mathbf{x} - \mathbf{x}_p) \quad \text{in} \quad \mathcal{D}_p \tag{2.11c}$$

$$0 = \frac{\rho_p - \rho_f}{\rho_p} M_p \mathbf{g} - \rho_f \int_{\mathcal{D}_p} \boldsymbol{\lambda}\, d\mathcal{V} + \mathbf{F}_p^{SG} (\mathbf{U}_p, \boldsymbol{\Omega}_p) + \mathbf{F}_p^{c} + \mathbf{F}_p^{ext} \tag{2.11d}$$

$$0 = -\rho_f \int_{\mathcal{D}_p} (\mathbf{x} - \mathbf{x}_p) \times \boldsymbol{\lambda}\, d\mathcal{V} + \mathbf{T}_p^{SG} (\mathbf{U}_p, \boldsymbol{\Omega}_p) + \mathbf{T}_p^{c} + \mathbf{T}_p^{ext} \tag{2.11e}$$

where the unknowns have been put in red and $\nu = \eta / \rho_f$ is the kinematic viscosity. Eqs. (2.11a) and (2.11b) correspond to the fluid sub-problem, while Eqs. (2.11d) and (2.11e) correspond to the particle sub-problem. Eq. (2.11c) links the two sub-problems, imposing rigid body motion inside each particle domain $\mathcal{D}_p$.

The above equations are solved simultaneously and iteratively with a predictor-corrector method: the fluid sub-problem is solved using the previous forcing term $\boldsymbol{\lambda}^{n-1}$, obtaining $\mathbf{u}^{**}$ which does not fully comply with a rigid body motion inside the particles; then, the velocities of the particles $\mathbf{U}^n$ and $\boldsymbol{\Omega}^n$ are computed using $\mathbf{u}^{**}$ and $\boldsymbol{\lambda}^{n-1}$; finally, the forcing term and velocity fields are corrected imposing the rigid body motion inside the particles domain, obtaining $\boldsymbol{\lambda}^n$ and $\mathbf{u}^n$. More details are given in the following, together with a full explanation of the numerical procedure.

2.2 FLUID SUB-PROBLEM

2.2.1 FINITE VOLUME METHOD

Here, only what concerns the current work is dealt with. A deep and full description of the finite volume method and its implementation in OpenFOAM can be found in the marvelous book by Moukalled et al. (2016).

The finite volume method is a numerical technique that transforms the partial differential equations representing conservation laws over differential volumes into discrete algebraic equations over finite volumes. This method is strictly conservative, which makes it the preferred method in CFD (Moukalled et al., 2016). Its popularity (Blazek, 2001; Ferziger & Perić, 2002) stems also from the high flexibility that comes from the discretization carried out directly in the physical space.

First, a discretization of the physical domain is needed, i.e. a mesh providing a range of information both geometric and topological, on which the governing equations are solved. In general, a structured or unstructured grid system can be generated. In the current work, only structured grids are employed. In this case, three-dimensional elements are defined by their local indices (i, j, k) in the (x, y, z) coordinate directions, and every interior cell in the domain is connected to the same number (six) of neighboring cells, which can be identified using their indices (see Fig. 2.1). As the size of the elements tends to zero, the numerical solution is expected to be the exact one; however, the discretized equations must possess some properties to ensure a meaningful solution field.

From a physical point of view, it is fundamental for the transported variables to be conserved in the discretized solution domain too, results may be unrealistic otherwise. It is important to stress that this property is inherent to the finite volume method because the fluxes (obtained by transforming the volume integrals into surface ones via the Gauss theorem) integrated at an element face are based on the values of the elements sharing the face; thus, for any surface common to two elements, the flux leaving the face of one element will be exactly equal to the flux entering the other element through that same face. The cell-centered variable arrangement is currently the most popular type of variable arrangement used with the finite volume method: the variables are stored at the centroids of grid cells or elements. Thus, the elements are identical to the discretization elements. This results in a set of equations with the values of the dependent variables at the cell centers as unknowns. The way these unknowns are organized and solved classifies the adopted computational approach.

An example of a mesh cell and its neighbors is given if Fig. 2.1, with both a three-dimensional and a two-dimensional representation for the sake of clarity.

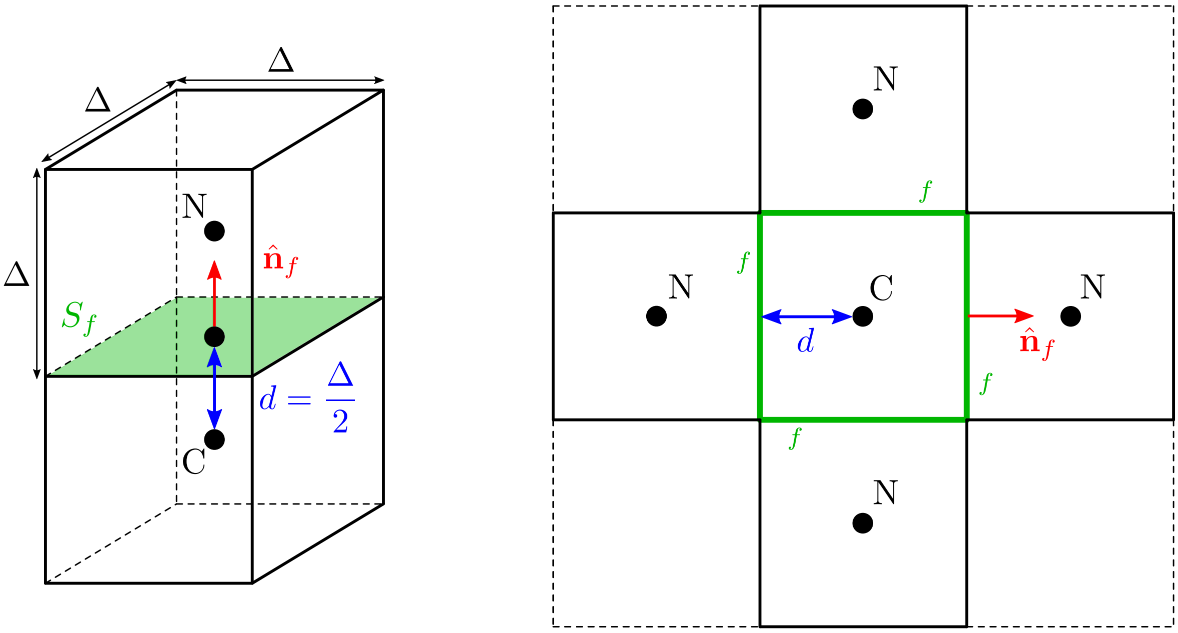

Figure 2.1
We employ an isotropic mesh, where Δ is the mesh size. Considering a mesh cell, the distance from its center C and a face f is then $d = \Delta/2$. The surface of a face is S_f, and the outward-pointing unity vector is $\hat{\mathbf{n}}_f$. Each cell has six neighboring cells N. (left) 3D representation of a cell and one of its neighbors; (right) 2D representation of a cell and its neighbors.

OPENFOAM

OpenFOAM (Open source Field Operation And Manipulation) is an object-oriented C++ framework that includes several utilities that can be directly used. An important characteristic is its use of operator overloading that allows algorithms to be expressed naturally, as it will be presented hereafter. We implemented the Fictitious Domain Method in OpenFOAM because it is an established free open-source CFD toolbox – *and not a black-box software!* – with a rich and expanding community – *thank you, CFD-online*.

Numerous namespaces and operators are available, but the namespaces `fvm` and `fvc` are surely the most significant ones and allow for the evaluation of the operators implicitly and explicitly, respectively: the explicit operator `fvc`, named "finite volume calculus", returns an equivalent field based on the actual field values; the `fvm` implicit operator, instead, defines the implicit finite volume discretization in terms of matrices of coefficients. The role of these two operators is to construct the right-hand side and the left-hand side, respectively, of a system of equations representing the discretized form of the governing equations over each element in the mesh. The discretization process yields a system of equations that can be represented in the matrix form. The source or the right-hand side is stored under a specific vector called "source". Let us now see the numerical procedure used to solve the fluid sub-problem.

2.2.2 SIMPLEC

The discretization of the Navier-Stokes equations for an incompressible flow is a standard procedure in OpenFOAM (Jasak, 1996; Moukalled et al., 2016). As clearly explained by Moukalled et al. (2016), the main difficulty comes from the unavailability of an explicit equation for the pressure field in the momentum equation. So, in addition to the discretized velocity equation from Eq. (2.11a), a pressure equation whose solution guarantees the incompressibility of the velocity field needs to be derived. A cell-centered collocated grid is used for the pressure and velocity fields, and the pressure equation is built using a Rhie-Chow interpolation to prevent checkerboard instability (Rhie & Chow, 1983). The pressure-momentum coupling is addressed using the SIMPLEC (Semi Implicit Method for Pressure Linked Equations – Consistent) method, a modified version proposed by Van Doormaal & Raithby (1984) of the SIMPLE method of S. V. Patankar & Spalding (1972) and S. V. Patankar (1980, 1981). The discretized implicit velocity equation is first solved, using the forcing term of the previous time step and the pressure of the previous iteration. In a further step, the pressure equation is solved and the velocity field is corrected according to the new pressure. The latter step is performed twice to improve consistency between pressure and velocity.

For the sake of clarity, we recall here the notation employed: $(\cdot)^n$ and $(\cdot)^{n-1}$ respectively indicate values at the current and at the previous iterations; $\mathbf{u}^*$ is the velocity field obtained at the end of the prediction phase, it is not fully divergence-free and does not comply a rigid body motion inside the particles domain; $\mathbf{u}^{**}$ is the velocity field resulting from the correction phase, it is divergence-free but still does not comply a rigid body motion inside the particle domain.

PREDICTION

Here, we consider incompressible flows. However, in OpenFOAM we have to start from Eq. (2.11a) re-written for a compressible fluid flow with zero bulk viscosity:

$$-\nu\boldsymbol{\nabla}\cdot\left(\boldsymbol{\nabla}\mathbf{u}+\boldsymbol{\nabla}\mathbf{u}^{\mathsf{T}}\right)+\nu\boldsymbol{\nabla}\cdot\left(\frac{2}{3}\boldsymbol{\nabla}\cdot\mathbf{u}\delta\right)-\boldsymbol{\lambda}=-\frac{\boldsymbol{\nabla}p}{\rho_f} \tag{2.12}$$

We recall that:

$$\begin{aligned}
(\boldsymbol{\nabla}\mathbf{u})_{ij} &= \frac{\partial u_i}{\partial x_j} & \left(\boldsymbol{\nabla}\mathbf{u}^{\mathsf{T}}\right)_{ij} &= \frac{\partial u_j}{\partial x_i} \\
(\boldsymbol{\nabla}\cdot(\boldsymbol{\nabla}\mathbf{u}))_i &= \partial_j\frac{\partial u_i}{\partial x_j} & \left(\boldsymbol{\nabla}\cdot\left(\boldsymbol{\nabla}\mathbf{u}^{\mathsf{T}}\right)\right)_i &= \partial_j\frac{\partial u_j}{\partial x_i} \\
\boldsymbol{\nabla}\cdot\mathbf{u} &= \operatorname{tr}(\boldsymbol{\nabla}\mathbf{u}) = \operatorname{tr}(\boldsymbol{\nabla}\mathbf{u})^{\mathsf{T}} \\
(\boldsymbol{\nabla}\cdot\mathbf{T})_i &= \partial_j T_{ij}
\end{aligned} \tag{2.13}$$

The term $\boldsymbol{\nabla}\cdot(\boldsymbol{\nabla}\cdot\mathbf{u}\delta)$ vanishes for an incompressible flow. However, it is kept for stability reasons, but the factor may be changed from $2/3$ to $1/3$ via the operators `dev` and `dev2`, respectively, to increase the convergence rate. Choosing the $1/3$ factor, we can define:

$$\operatorname{dev}\left(\boldsymbol{\nabla}\mathbf{u}^{\mathsf{T}}\right)=\boldsymbol{\nabla}\mathbf{u}^{\mathsf{T}}-\frac{1}{3}\operatorname{tr}\left(\boldsymbol{\nabla}\mathbf{u}^{\mathsf{T}}\right)\delta \tag{2.14}$$

Finally, we can write Eq. (2.12) again as:

$$-\nu\boldsymbol{\nabla}\cdot\boldsymbol{\nabla}\mathbf{u}-\nu\boldsymbol{\nabla}\cdot\operatorname{dev}\left(\boldsymbol{\nabla}\mathbf{u}^{\mathsf{T}}\right)-\lambda=-\frac{\boldsymbol{\nabla}p}{\rho_f} \tag{2.15}$$

We integrate now Eq. (2.15) and, as previously introduced, we consider the fluxes at the element faces transforming the volume integrals into surface ones via the Gauss theorem. Let us see the discretization of each term. As we are going to see, we will often need to evaluate some values from the cell centers to the cell faces: we employ a linear interpolation, a simple scheme that guarantees conservation and second-order accuracy. For the first term, which is the only one treated implicitly, the component i reads:

$$\begin{aligned}\left[[\boldsymbol{\nabla}\cdot(\boldsymbol{\nabla}\mathbf{u})]_i\right]_C&=\frac{1}{V_c}\int_{V_C}[\boldsymbol{\nabla}\cdot(\boldsymbol{\nabla}\mathbf{u})]_i\,d\mathcal{V}=\frac{1}{V_C}\int_{V_C}\partial_j\frac{\partial u_i}{\partial x_j}\,d\mathcal{V}=\frac{1}{V_C}\oint_{\partial V_C}\frac{\partial u_i}{\partial x_j}n_j\,d\mathcal{S}\\&=\frac{1}{V_C}\sum_f\boldsymbol{\nabla}u_i\cdot\hat{n}_jS_f=\frac{S_f}{2dV_C}\sum_N\left(u_N^i-u_C^i\right)=\frac{1}{2d^2}\sum_N\left(u_N^i-u_C^i\right)\end{aligned} \tag{2.16}$$

where u_C and u_N are the values of the velocity field at the considered cell center and its neighbors' centers, respectively, and $\sum_f$ is the summation over the cell faces, and the gradient is computed as $\boldsymbol{\nabla}u_{i,f}\cdot n_{j,f}S_f=1/(2d)\left(u_N^i-u_C^i\right)$, for which no explicit interpolation is needed. As we employ cubic mesh cells $V_C=S_f2d$, and each cell has 6 faces, so:

$$-\nu\left[[\boldsymbol{\nabla}\cdot(\boldsymbol{\nabla}\mathbf{u})]_i\right]_C=\nu\left(\frac{6}{d^2}u_C^i-\sum_N\frac{1}{d^2}u_N^i\right) \tag{2.17}$$

For the second term, we need to perform two consecutive discretizations. Let us start from $\boldsymbol{\nabla}\mathbf{u}^{\mathsf{T}}$. In the same line as in Eq. (2.16), its value at the cell center is computed as:

$$\left[\boldsymbol{\nabla}\mathbf{u}^{\mathsf{T}}\right]_C=\frac{1}{V_C}\sum_f\hat{\mathbf{n}}_f\otimes\mathbf{u}_fS_f \tag{2.18}$$

for which an interpolation at the cell faces is needed. Its deviatoric part (Eq. (2.14)) reads:

$$\left[\operatorname{dev}\left(\boldsymbol{\nabla}\mathbf{u}^{\mathsf{T}}\right)\right]_C=\frac{1}{V_C}\sum_f\operatorname{dev}\left(\hat{\mathbf{n}}_f\otimes\mathbf{u}_f\right)S_f \tag{2.19}$$

We have to take its divergence, getting back a vector:

$$\left[\boldsymbol{\nabla}\cdot\left(\operatorname{dev}\left(\boldsymbol{\nabla}\mathbf{u}^{\mathsf{T}}\right)\right)\right]_C=\frac{1}{V_C}\oint_{\partial V_C}\left(\operatorname{dev}\left(\boldsymbol{\nabla}\mathbf{u}^{\mathsf{T}}\right)\cdot\hat{\mathbf{n}}\right)\,d\mathcal{S}=\frac{1}{V_C}\sum_f\operatorname{dev}\left(\boldsymbol{\nabla}\mathbf{u}^{\mathsf{T}}\right)\Big|_f\cdot\hat{\mathbf{n}}_fS_f \tag{2.20}$$

for which a second interpolation at the faces is needed.

The forcing term is needed at the cells' centers, and we suppose that its value varies linearly with the position. So, its discretization simply reads:

$$\frac{1}{V_C}\int_{V_C}\lambda\,d\mathcal{V}\cong\lambda_C \tag{2.21}$$

The last term (i.e., the pressure gradient) needs particular attention and will be treated in the following; in particular, it will be discretized in two different manners. Then, the semi-discretized momentum equation is obtained:

$$-\frac{\nu}{V_C}\sum_f \nabla\mathbf{u}|_f\cdot\hat{\mathbf{n}}_f S_f-\frac{\nu}{V_C}\sum_f \mathrm{dev}\left(\nabla\mathbf{u}^T\right)\Big|_f\cdot\hat{\mathbf{n}}_f S_f-\lambda_C=-\frac{\nabla p}{\rho_f} \tag{2.22}$$

We recall here that the first term is the only one treated implicitly and, therefore, computed at the iteration n; all the other terms except for ∇p, are treated explicitly and their values at the iteration $n-1$ is needed. Eq. (2.22) is written under the form:

$$\underbrace{a_C\mathbf{u}_C^*+\sum_N a_N\mathbf{u}_N^*-b_C}_{a_C\mathbf{u}_C^*-H(\mathbf{u}^*)}=-\frac{\nabla p^{n-1}}{\rho_f} \tag{2.23}$$

where $\mathbf{u}^{n-1}$ is needed for b_C. We have already seen in Eq. (2.16) that $a_C=6\nu/d^2$ and $a_N=-\nu/d^2$, so, keeping in mind that we employ an isotropic domain for which each cell has 6 neighbors, we notice that:

$$a_C+\sum_N a_N=0 \tag{2.24}$$

We finally have the equation to be solved for the predictor phase:

$$a_C\mathbf{u}_C^*=H(\mathbf{u}^*)-\frac{\nabla p^{n-1}}{\rho_f} \tag{2.25}$$

For this phase, the pressure gradient is discretized explicitly with a Gauss linear scheme:

$$\nabla p^{n-1}=\frac{1}{V_C}\sum_f p_f^{n-1}\hat{\mathbf{n}}_f S_f \tag{2.26}$$

In order to get $\mathbf{u}^*$, the linear system resulting from Eq. (2.25) needs to be solved.

It should be noted here that because of Eq. (2.24) we need to perform under-relaxation of Eq. (2.23), which results in the modification of operator H as explained below. The reason why this step must be executed will be clearly shown in the following. Replacing $a_C\mathbf{u}_C+\sum_N a_N\mathbf{u}_N$ by $b_C-\nabla p/\rho_f$, leads to:

$$\mathbf{u}_C^*=\frac{1}{a_C}\left(-\sum_N a_N\mathbf{u}_N^*+b_C-\frac{\nabla p_C^{n-1}}{\rho_f}\right) \tag{2.27}$$

We now make a weighted average of $\mathbf{u}_C^*$ and $\mathbf{u}_C^{n-1}$:

$$\mathbf{u}_C^* = \alpha \frac{1}{a_C} \left(-\sum_N a_N \mathbf{u}_N^* + b_C - \frac{\nabla p_C^{n-1}}{\rho_f} \right) + (1-\alpha)\, \mathbf{u}_C^{n-1} \tag{2.28}$$

We finally get:

$$\frac{1}{\alpha} a_C \mathbf{u}_C^* + \sum_N a_N \mathbf{u}_N^* = b_C - \frac{\nabla p_C^{n-1}}{\rho_f} + \frac{1-\alpha}{\alpha} \mathbf{u}_C^{n-1} \tag{2.29}$$

This modifies the diagonal coefficients and the source term of the linear system, allowing using SIMPLEC in the case without inertia. This corresponds exactly to an under-relaxation: this is also needed to improve the convergence of nonlinear problems but also to avoid divergence when starting with a guessed initial field that could be far from the solution. The under-relaxation method promotes convergence by "slowing down" the changes made to the values of the considered variable during the solution. $\alpha = 1$ means no under-relaxation. We use $\alpha = 0.9$, which allows a fast convergence rate with the right amount of stability. Since Eq. (2.29) takes the same form as Eq. (2.23) with a modified operator H, the expression of Eq. (2.23) is adopted for the relaxed equation.

OPENFOAM PHRASING

Finally, the momentum equation in OpenFOAM reads:

```
fvVectorMatrix UEqn (
  - fvm::laplacian(nu,U)
  - fvc::div(nu*dev(T(fvc::grad(U))))
  - lambda
);
UEqn.relax();
solve(UEqn == - fvc::grad(p));
```

where the pressure p in OpenFOAM is divided by the fluid density ρ_f by default. Regarding the Laplacian operator, it is built to account for space-varying viscosity, which would then be interpolated to the cell faces. Again, we notice that only the Laplacian term goes into the matrix (`fvm`, implicit), while all the other terms go into the source term (`fvc`, explicit). It is worth noting here that the equation for the fluid flow (Eq. (2.11a)) is quite different from the standard equations usually tackled in OpenFOAM: no inertia is accounted for so that the lack of convective momentum transport is not a source of nonlinearity. In addition, only steady equations are considered, so that, except for the force density $\boldsymbol{\lambda}$ inside the particles, the equations are linear. However, the main difficulty is the determination of the distribution of $\boldsymbol{\lambda}$ so that Eqs. (2.11c) to (2.11e) are fulfilled.

The reader can now take a break before dealing with the correction phase.

CORRECTION

Following an iterative solution strategy, the momentum equation is solved using the velocity and pressure values of the preceding iteration. The velocity obtained is in general not divergence-free: a pressure-momentum coupling is needed to construct an equation for the pressure, aiming at obtaining a pressure field which, if inserted in the momentum equation, delivers a divergence-free velocity field. We seek new velocity and pressure fields $\mathbf{u}^{**}$ and p^n such that:

$$a_C \mathbf{u}_C^{**} = H\left(\mathbf{u}^{**}\right) - \frac{\nabla p^n}{\rho_f} \tag{2.30}$$

where we note that in $H\left(\mathbf{u}^{**}\right)$ there are some explicit terms (that depend on $\mathbf{u}_N^{n-1}$). We add now a "perturbation" to the velocity and pressure fields, and we define:

$$\mathbf{u}^{**} = \mathbf{u}^* + \mathbf{u}' \,, \quad p^n = p^{n-1} + p' \quad \Rightarrow \quad \mathbf{u}_C^{**} = \frac{H\left(\mathbf{u}^* + \mathbf{u}'\right)}{a_C} - \frac{\nabla p^{n-1}}{a_C \rho_f} - \frac{\nabla p'}{a_C \rho_f} \tag{2.31}$$

For the moment, $\nabla p'$ is still not discretized, and:

$$H\left(\mathbf{u}^* + \mathbf{u}'\right) = -\sum_N a_N \left(\mathbf{u}_N^* + \mathbf{u}_N'\right) + b_C = H\left(\mathbf{u}^*\right) - \sum_N a_N \mathbf{u}_N' \tag{2.32}$$

The SIMPLEC algorithm assumes the following simplification:

$$-\sum_N a_N \mathbf{u}_N' \approx -\sum_N a_N \mathbf{u}_C' = -\mathbf{u}_C' \sum_N a_N = H_1 \mathbf{u}_C' \tag{2.33}$$

with $H_1 = -\sum_N a_N$. By consequence:

$$H\left(\mathbf{u}^* + \mathbf{u}'\right) \approx H\left(\mathbf{u}^*\right) + H_1 \mathbf{u}_C' \tag{2.34}$$

Getting back to Eq. (2.31), we obtain:

$$\mathbf{u}_C^{**} = \mathbf{u}_C^* + \mathbf{u}_C' = \frac{H\left(\mathbf{u}^*\right)}{a_C} + \frac{H_1 \mathbf{u}_C'}{a_C} - \frac{\nabla p^{n-1}}{\rho_f a_C} - \frac{\nabla p'}{\rho_f a_C} \tag{2.35}$$

and with Eq. (2.25):

$$\mathbf{u}_C' = -\frac{1}{a_C - H_1} \frac{\nabla p'}{\rho_f} \tag{2.36}$$

where $a_C - H_1 = 0$ in the case without inertia, so that as mentioned above, under-relaxation of the velocity equation is needed (Eq. (2.29)). This last equation relates the two unknowns $\mathbf{u}_C'$ and p'. From Eqs. (2.31) and (2.36) we get:

$$\mathbf{u}_C^{**} = \frac{H\left(\mathbf{u}^*\right)}{a_C} - \frac{\nabla p^{n-1}}{\rho_f a_C} - \frac{\nabla p'}{\rho_f a_C} \left(1 + \frac{H_1}{a_C - H_1}\right) \tag{2.37}$$

We directly search for $\nabla p^n = \nabla p^{n-1} + \nabla p'$, so:

$$\mathbf{u}_C^{**} = \frac{H(\mathbf{u}^*)}{a_C} - \frac{\nabla p^{n-1}}{\rho_f}\left(\frac{1}{a_C} - \frac{1}{a_C - H_1}\right) - \frac{\nabla p^n}{\rho_f}\frac{1}{a_C - H_1} \tag{2.38}$$

By searching for a divergence-free velocity field:

$$\nabla \cdot \mathbf{u}^{**} = 0 \qquad \Rightarrow \qquad \frac{1}{V_C}\sum_f \mathbf{u}_f^{**} \cdot S_f = 0 \tag{2.39}$$

we finally get to the equation for the correction phase:

$$\begin{aligned} \frac{1}{V_C}\Bigg\{ \sum_f \frac{H(\mathbf{u}^*)}{a_C}\bigg|_f \cdot S_f - \sum_f \left(\frac{1}{a_C}\bigg|_f - \frac{1}{a_C - H_1}\bigg|_f\right)\frac{\nabla p_f^{n-1}}{\rho_f} \cdot S_f \\ - \sum_f \frac{1}{a_C - H_1}\bigg|_f \frac{\nabla p_f^n}{\rho_f} \cdot S_f \Bigg\} = 0 \end{aligned} \tag{2.40}$$

The last term is a Laplacian and is treated implicitly, for which the unknowns are the pressures at the cells' centers. All the other terms are treated explicitly and are computed either by interpolation (first term) or by computing the gradient in the direction normal to the faces (second term). It should be noted here that if the hypothesis introduced (Eq. (2.33)) was correct, only one correction step would be needed, but it is not exactly the case, and, therefore, we make two correction steps. After computing the new pressure field p^n with Eq. (2.40), the velocity field $\mathbf{u}^*$ has to be corrected accordingly with Eq. (2.38), obtaining $\mathbf{u}^{**}$.

OPENFOAM PHRASING

The pressure-momentum coupling equation in OpenFOAM reads:

```
volScalarField     rAU  = 1.0 / UEqn.A();
volScalarField     rAtU = rAU-UEqn.H1();
volVectorField     HbyA(constrainHbyA(rAU*UEqn.H(), U, p));
surfaceScalarField phiHbyA("phiHbyA", fvc::flux(HbyA));

adjustPhi(phiHbyA, U, p);
phiHbyA += fvc::interpolate(rAtU-rAU)*fvc::snGrad(p)*mesh.magSf();
HbyA    -= (rAU-rAtU)*fvc::grad(p);

constrainPressure(p, U, phiHbyA, rAtU);
fvScalarMatrix pEqn (fvm::laplacian(rAtU, p) == fvc::div(phiHbyA));
pEqn.setReference(pRefCell, pRefValue);
pEqn.solve();

phi = phiHbyA - pEqn.flux();
U   = HbyA - rAtU*fvc::grad(p);
U.correctBoundaryConditions();
```

where:

- `rAU = 1.0 / UEqn.A()` computes the field of the reciprocal of the diagonal entries of the momentum equation required later to solve the pressure equation so that the division is done once and then it is multiplied where required (multiplication is computationally cheaper than division);
- `phiHbyA("phiHbyA", fvc::flux(HbyA))` performs $\left(H\left[u\right]/a_P\right) \cdot S_f|_f$, explicitly interpolating the field $H\left[u\right]/a_P$ at the cell faces and making the scalar product of the interpolated field with the surface vector S_f;
- `phiHbyA += fvc::interpolate(rAtU-rAU)*fvc::snGrad(p)*mesh.magSf()` and `HbyA -= (rAU-rAtU)*fvc::grad(p)` computes the explicit fields required for the SIMPLEC method and adds the velocity correction to the field `HbyA`;
- `constrainHbyA(rAU*UEqn.H(), U, p)` ensures that Eq. (2.31) is satisfied also at the boundary faces;
- `adjustPhi(phiHbyA, U, p)` ensures that the global balance is satisfied if one sets a reference pressure;
- `constrainPressure(p, U, phiHbyA, rAtU)` updates the pressure gradient for the patches where a `fixedFluxPressure` boundary condition is employed.

In the pressure-momentum coupling step, the previous forcing term λ^{n-1} has been used. Therefore, at the end of the SIMPLEC step, the velocity field denoted by $\mathbf{u}^{**}$ is divergence-free but not perfectly rigid inside the particles. The velocities of the particles $\mathbf{U}_p^n$ and $\boldsymbol{\Omega}_p^n$ must be determined, and rigid body motion enforced inside the particles and the force density accordingly corrected.

2.3 PARTICLE SUB-PROBLEM

In the following, the particles are assumed spherical, so that the inertia tensor amounts to a scalar quantity. The latter quantity is not explicitly part of the equations at this stage but will be reintroduced in the course of the resolution.

As previously explained, the fluid velocity $\mathbf{u}^{**}$ is computed by solving Eqs. (2.11a) and (2.11b) using the forcing term λ^{n-1} from the previous iteration, and so it does not comply a rigid body motion inside the particles. However, the particles velocities $\mathbf{U}_p^n$ and $\boldsymbol{\Omega}_p^n$ are still unknown at this stage. We assume that the correction of the force density field λ reads (Gallier et al., 2014a):

$$\lambda^n = \lambda^{n-1} + \frac{\mathbf{U}_p^n + \boldsymbol{\Omega}_p^n \times (\mathbf{x} - \mathbf{x}_p) - \mathbf{u}^{**}}{\alpha_\lambda} \qquad \text{inside} \quad \mathcal{D}_p \tag{2.41}$$

where α_λ has the dimension of time and it is given by the value of the momentum diffusion time at the scale of the mesh cell Δ: $\alpha_\lambda = \Delta^2/\nu$. We have observed that this parameter drives the convergence speed and behavior of $\boldsymbol{\lambda}$: a too-small value speeds up convergence but introduces strong instabilities, while a big value slows down convergence.

Using Eq. (2.41) into Eqs. (2.11d) and (2.11e) yields the following equations that must be solved for $\mathbf{U}_p^n$ and $\boldsymbol{\Omega}_p^n$:

$$\begin{aligned}
\frac{\rho_f}{\rho_p}\frac{M_p}{\alpha_\lambda}\mathbf{U}_p^n &= \frac{\rho_p-\rho_f}{\rho_p}M_p\mathbf{g} + \rho_f\int_{\mathcal{D}_p}\left(\frac{\mathbf{u}^{**}}{\alpha_\lambda} - \boldsymbol{\lambda}^{n-1}\right)\,d\mathcal{V} + \mathbf{F}_p^{SG} + \mathbf{F}_p^c + \mathbf{F}_p^{ext} \\
\frac{\rho_f}{\rho_p}\frac{J_p}{\alpha_\lambda}\boldsymbol{\Omega}_p^n &= \rho_f\int_{\mathcal{D}_p}(\mathbf{x}-\mathbf{x}_p)\times\left(\frac{\mathbf{u}^{**}}{\alpha_\lambda} - \boldsymbol{\lambda}^{n-1}\right)\,d\mathcal{V} + \mathbf{T}_p^{SG} + \mathbf{T}_p^c + \mathbf{T}_p^{ext}
\end{aligned} \tag{2.42}$$

Computing the velocities of the particles requires particular attention: as already mentioned, sub-grid corrections are needed to correctly take into account the lubrication forces between particles at a close distance.

Replacing Eq. (2.8) in Eq. (2.42), a set of coupled equations involving the translational and angular velocities of the particles, $\mathbf{U}_p$ and $\boldsymbol{\Omega}_p$, is obtained, which must be solved to get the particle motion, together with Eqs. (2.1) and (2.2). From Eq. (2.42), the set of linear equations that must be solved for the velocities of the particles reads:

$$\left[\frac{\rho_f}{\rho_p}\frac{\mathcal{J}}{\alpha_\lambda} + \mathcal{R}_{F,T}^{SG}\right]\cdot\mathcal{U}^n = \mathcal{F}^{tot} \tag{2.43}$$

where $\mathcal{J}$ is the diagonal matrix accounting for the particles masses and inertia moments, $\mathcal{R}^{SG}$ is the sub-grid resistance matrix for lubrication correction ($\mathcal{R}_{F,T}^{SG} = \left[\mathcal{R}_{F\mathcal{U}}^{SG};\mathcal{R}_{T\mathcal{U}}^{SG}\right]$), $\mathcal{U}^n$ is the vector of the particles translational and angular velocities, and $\mathcal{F}^{tot}$ is the generalized force vector that reads:

$$\mathcal{F}^{tot} = \begin{pmatrix}
\frac{\rho_p-\rho_f}{\rho_p}M_1\mathbf{g} + \rho_f\int_{\mathcal{D}_1}\left(\frac{\mathbf{u}^{**}}{\alpha_\lambda} - \boldsymbol{\lambda}^{n-1}\right)\,d\mathcal{V} + \mathbf{F}_1^c + \mathbf{F}_1^{ext} \\
\frac{\rho_p-\rho_f}{\rho_p}M_2\mathbf{g} + \rho_f\int_{\mathcal{D}_2}\left(\frac{\mathbf{u}^{**}}{\alpha_\lambda} - \boldsymbol{\lambda}^{n-1}\right)\,d\mathcal{V} + \mathbf{F}_2^c + \mathbf{F}_2^{ext} \\
\cdots \\
\cdots \\
\rho_f\int_{\mathcal{D}_1}(\mathbf{x}-\mathbf{x}_p)\times\left(\frac{\mathbf{u}^{**}}{\alpha_\lambda} - \boldsymbol{\lambda}^{n-1}\right)\,d\mathcal{V} + \mathbf{T}_1^c + \mathbf{T}_1^{ext} \\
\rho_f\int_{\mathcal{D}_2}(\mathbf{x}-\mathbf{x}_p)\times\left(\frac{\mathbf{u}^{**}}{\alpha_\lambda} - \boldsymbol{\lambda}^{n-1}\right)\,d\mathcal{V} + \mathbf{T}_2^c + \mathbf{T}_2^{ext}
\end{pmatrix} \tag{2.44}$$

Once the velocities of the particles have been computed, an explicit forcing of the rigid body motion is thus possible:

$$\begin{aligned} \mathbf{u}^n &= \mathbf{U}_p^n + \boldsymbol{\Omega}_p^n \times (\mathbf{x} - \mathbf{x}_p) && \text{inside } \mathcal{D}_p \\ \mathbf{u}^n &= \mathbf{u}^{**} && \text{outside } \mathcal{D}_p \end{aligned} \tag{2.45}$$

and the force density is corrected according to Eq. (2.41).

Again, we notice a lag between the velocity field and the forcing term: the velocity field $\mathbf{u}^n$ and the velocities of the particles $\mathbf{U}_p^n$ and $\boldsymbol{\Omega}_p^n$ are first computed using the previous forcing term λ^{n-1}, and only then the forcing term is corrected (Eq. (2.41)) obtaining λ^n, together with imposing rigid body motion of the particles (Eq. (2.45)). Therefore, this procedure is repeated until convergence of λ, i.e. until the field λ is no longer evolving (see Section 2.5.5).

2.4 ALGORITHM

Here follows the numerical algorithm implemented in OpenFOAM:

1. Update the particle positions $\mathbf{x}_p$: move the particles using the Adams-Bashforth method.
2. Set the force density field $\lambda = 0$ outside the particles.
3. Solve the fluid sub-problem (Section 2.3): solve the pressure-momentum coupling problem using the previous forcing term λ^{n-1}, obtaining $\mathbf{u}^{**}$ and p^n.
4. Solve the particle sub-problem using Eq. (2.43), obtaining the particles velocities $\mathbf{U}_p^n$ and $\boldsymbol{\Omega}_p^n$ (more details about the sub-grid corrections in Chapter 3).
5. Compute the new forcing term λ^n using Eq. (2.41).
6. Compute the new velocity field $\mathbf{u}^n$: correct the velocity field $\mathbf{u}^{**}$ by enforcing rigid body motion in the particle domain (Eq. (2.45)).
7. Repeat steps 3, 4, 5 and 6 until convergence of λ.
8. Proceed to the next time step and repeat.

The reader should note that steps 5 and 6 are independent and switchable. Step 2 is needed to guarantee the absence of the force density λ outside the particles; alternatively, λ could be advected using the velocity field $\mathbf{u}$. This is at the cost of too much numerical diffusion so the advection step has been discarded.

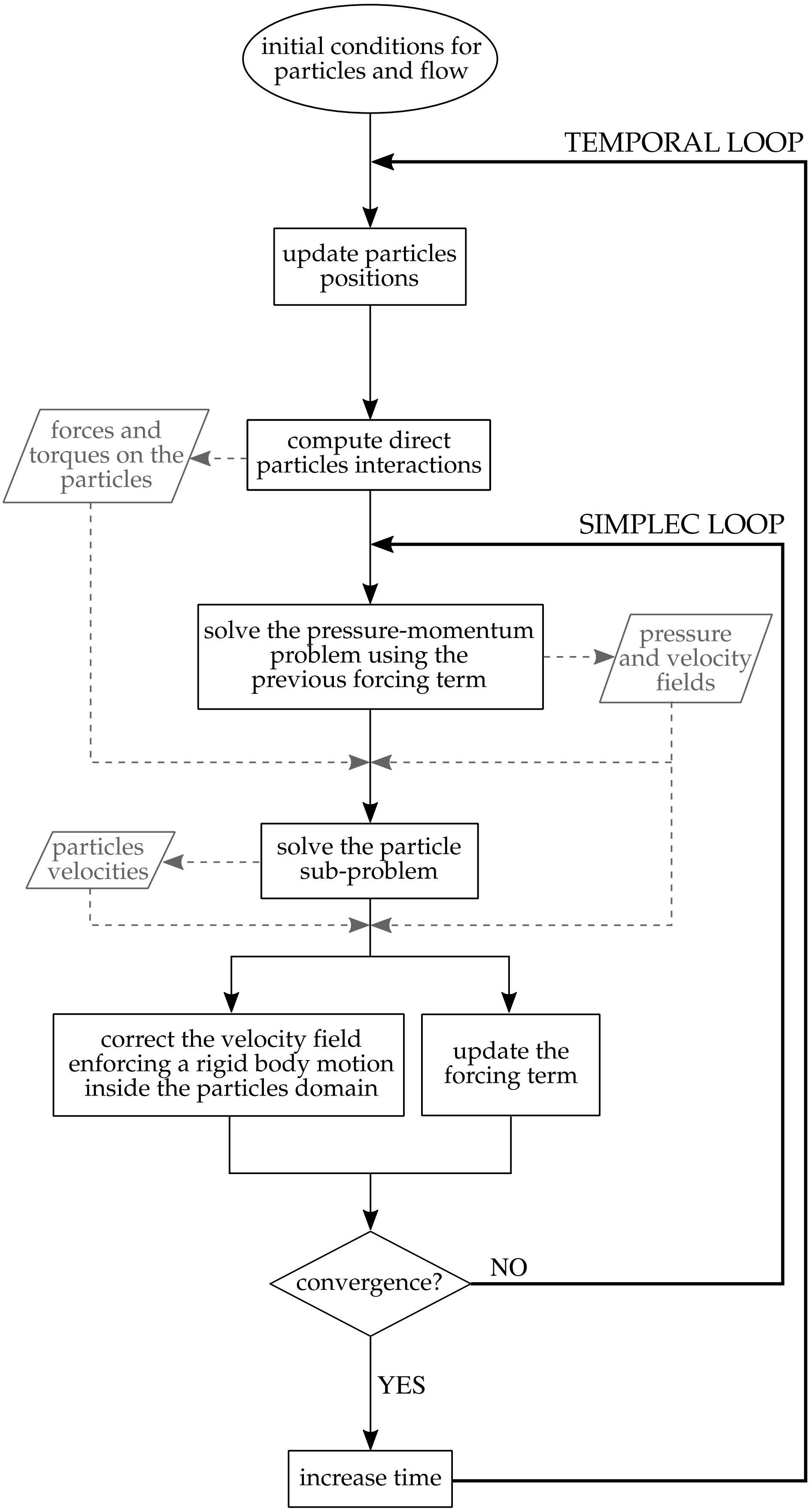

Figure 2.2
Flowchart of the numerical procedure. The SIMPLEC loop is repeated until convergence. Details about convergence criteria are given in Section 2.5.5.

2.5 NUMERICAL DETAILS

2.5.1 SOLVING THE ALGEBRAIC LINEAR SYSTEMS

FLUID SUB-PROBLEM

Numerous methods are proposed in OpenFOAM. For the prediction step (Eq. (2.25)), we have found that the most efficient method is the Preconditioned Conjugate Gradient method (PCG), using an Incomplete Cholesky Decomposition (DIC). While for the solution of the linear system coming from the pressure-momentum coupling equation, i.e. the correction step (Eq. (2.40)), we have seen a different behavior when changing the number of mesh cells per processor: if each processor has less than 100k mesh cells, the PCG/DIC method is the most efficient one; but if there are more than 100k cells per processor, the PCG/DIC method is less efficient and a Geometric agglomerated Algebraic Multigrid (GAMG) solver coupled with a Gauss-Seidel smoother is the most efficient one.

PARTICLE SUB-PROBLEM

For the solution of the linear system of Eq. (2.43), which solutions are the velocities of the particles, we employ a PCG/DIC method by using the Eigen library, which is a very versatile toolbox that makes it easy to use sparse matrices, the latter being a fundamental feature for memory optimization.

RESIDUALS IN OPENFOAM

For a matrix system $A\mathbf{x} = \mathbf{b}$ the residual is defined as:

$$\mathbf{r} = \mathbf{b} - A\mathbf{x} \tag{2.46}$$

Then, residual scaling is applied using the following normalization procedure:

$$n = \sum \left(|A\mathbf{x} - A\bar{\mathbf{x}}| + |\mathbf{b} - A\bar{\mathbf{x}}| \right) \tag{2.47}$$

where $\bar{\mathbf{x}}$ is the average of the solution vector. The scaled residual is finally given by:

$$r = \frac{1}{n} \sum |\mathbf{b} - A\mathbf{x}| \tag{2.48}$$

This form leads to a normalized residual of 1 for uniform systems, i.e. where $\mathbf{x} = \bar{\mathbf{x}}$. However, this also shows that if the initial solution changes the normalization also changes, leading to a different convergence history. In any case, in the current work, we never are in the conditions for which $\mathbf{x} = \bar{\mathbf{x}}$.

2.5.2 PARALLELIZATION

Parallelization is handled via the domain decomposition method proposed in OpenFOAM: the principle is to break up the domain – geometry and fields – and allocate each part to a different CPU. Information (namely the velocity and pressure fields $\mathbf{u}$ and p) are then shared using the MPI standard. An example of a decomposed domain is given in Fig. 2.3.

Building up from this method, we carry out the parallelization of the particles following the same concept: each process manages the particles inside the corresponding domain together with the particles in the neighboring domains that may interact with them so that part of the particles is shared by multiple processes.

Lubrication and contact interactions require listing the particle pairs: each process performs this task for the particles hosted in its domain and builds the local resistance matrix. Finally, the local matrices are collected by the master process for the inversion of the linear system obtained for the computation of the velocities of the particles. For the systems investigated in the current work, delegating this operation to the master process using the Eigen library was found faster than solving it in parallel using the local matrices with message-passing between the interacting processes. Further speedup of the latter part can be obtained by exploiting the multi-threading (OpenMP) available in Eigen.

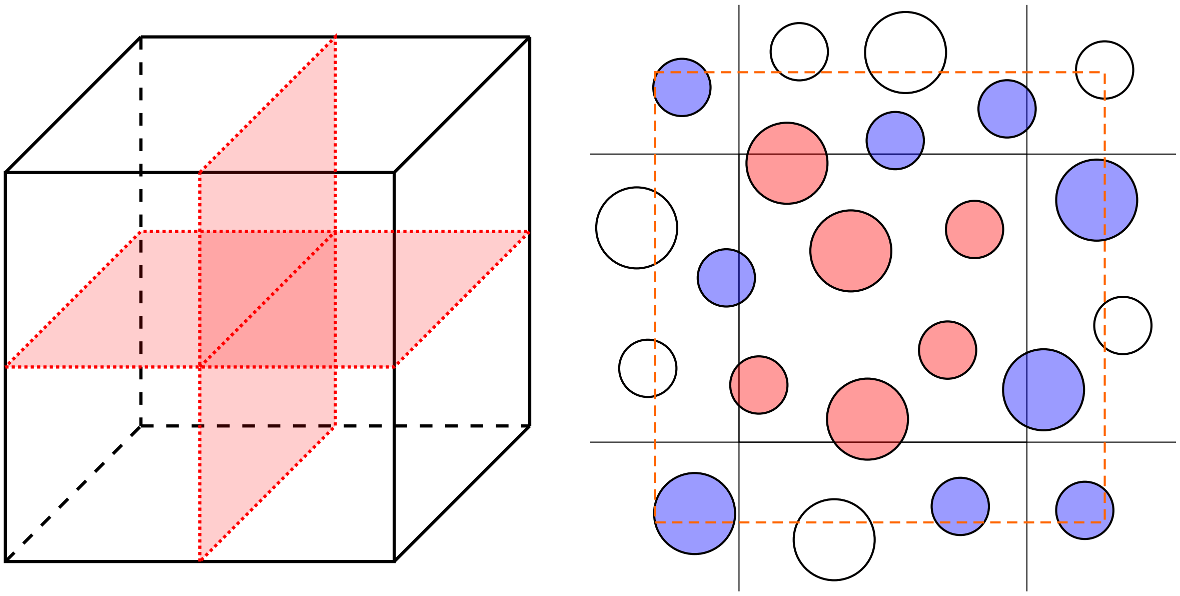

Figure 2.3
(left) Example of a domain decomposed in four identical sub-domains. (right) Example of how particles are treated: (red) particles owned by the current process; (blue) neighboring particles that may interact with the red ones; (white) particles of other processes not interacting.

2.5.3 BOUNDARY CONDITIONS

OpenFOAM proposes various built-in conditions. We use the `cyclic` condition in the case of periodic boundary conditions for the pressure and velocity fields. If a wall is present, we use a Dirichlet (`fixedValue`) condition for $\mathbf{u}$ imposing a value for the velocity, and the `fixedFluxPressure` condition for p, which sets the pressure gradient for the volume flux on the boundary to be consistent with the velocity boundary condition. Another condition that can be used in the presence of a wall is the `slip` condition, which for a vector sets to zero the component normal to the wall and uses a `zeroGradient` condition for the tangential ones (i.e., zero normal gradient); for a scalar, it is equivalent to the `zeroGradient` condition. For all pressure boundary conditions in the current work, pressure is given a reference value (0) at a single point in the simulation domain.

2.5.4 PARTICLE TRACKING: CHOICE OF THE INDICATOR FUNCTIONS

We present here the choice of the indicator functions used to compute the required integrals over the volume of the particles. Regarding the particle dimensions, we employ two radius lengths (with $a_2/a_1 = 1.4$), to avoid particle ordering usually observed in concentrated mono-disperse systems (**yeo2010c**; Gallier et al., 2014a, 2016); all lengths are normalized by a_1. As for the influence of the mesh size Δ compared to the particle radius, it has been studied before by Gallier et al. (2014a), and in the following the value $\Delta = a_1/5$ will not be changed.

Non-boundary-fitted Eulerian methods are attractive since a fixed mesh avoids any re-meshing difficulties and computational costs. However, the interface between fluid and particles is critical and must be properly defined. This issue is made simpler here because only rigid particles are considered, and their shape consequently remains unchanged. The tracking of the particles is needed to define and distinguish the particle region $\mathcal{D}_p$ from the fluid one $\mathcal{D}_f$. The chosen method rests on the level-set approach, which considers a level-set function $\mathcal{I}_{\mathcal{P}}(\mathbf{x})$ equal to 1 inside the particles and 0 outside, with a smeared interface:

$$\mathcal{I}_{\mathcal{P}}(\mathbf{x}) = \frac{1}{2}\left[1 - \tanh\left(b\frac{s}{\Delta}\right)\right] \tag{2.49}$$

where $s = \|\mathbf{x} - \mathbf{x}_p\| - a_p$, Δ is the grid spacing and b is a free parameter controlling the smearing on a typical size $\sim \mathcal{O}(\Delta/b)$. The level-set function $\mathcal{I}_{\mathcal{P}}(s)$ is then used to compute the particle mass, volume, and inertia tensor as well as any integral of a quantity ϕ on the particle volume $\mathcal{D}_p$:

$$\int_{\mathcal{D}_p} \phi \, d\mathcal{V} = \int_{\mathcal{D}} \mathcal{I}_{\mathcal{P}}(\mathbf{x})\phi(\mathbf{x}) \, d\mathcal{V} \tag{2.50}$$

The correction of the force density field $\boldsymbol{\lambda}$ (Eq. (2.41)) and the forcing of the rigid body motion of the particles (Eq. (2.45)) require an indicator function as well. Finally, we use two different indicator functions:

- $\mathcal{I}_u(\mathbf{x})$ is used to impose rigid body motion inside the particles, to compute the integrals in which the velocity field is involved, and to compute M_p and J_p;
- $\mathcal{I}_\lambda(\mathbf{x})$ is used to increment the force density field $\boldsymbol{\lambda}$ and to compute the integrals in which the force density $\boldsymbol{\lambda}$ is involved.

We find that the best choice for $\mathcal{I}_\lambda$ is a steep Heaviside function, and for $\mathcal{I}_u$ a smooth indicator function is chosen:

$$\mathcal{I}_\lambda(\mathbf{x}) = \begin{cases} 1 & \text{if } \|\mathbf{x}-\mathbf{x}_p\| \leqslant a_p + c\Delta \\ 0 & \text{if } \|\mathbf{x}-\mathbf{x}_p\| > a_p + c\Delta \end{cases} \tag{2.51}$$

$$\mathcal{I}_u(\mathbf{x}) = \begin{cases} \frac{1}{2}\left[1-\tanh\left(b\frac{s}{\Delta}\right)\right] & \text{if } \|\mathbf{x}-\mathbf{x}_p\| \leqslant a_p + c\Delta \\ 0 & \text{if } \|\mathbf{x}-\mathbf{x}_p\| > a_p + c\Delta \end{cases} \tag{2.52}$$

See Fig. 2.4 for an example of the indicator functions.

Using these indicator functions, Eqs. (2.41), (2.42) and (2.45) write:

$$\begin{aligned}
&\frac{\rho_f}{\rho_p}\frac{M_p}{\alpha_\lambda}\mathbf{U}_p^n = \frac{\rho_p-\rho_f}{\rho_p}M_p\mathbf{g} + \rho_f\int_{\mathcal{D}}\left[\mathcal{I}_u\frac{\mathbf{u}^{**}}{\alpha_\lambda} - \mathcal{I}_\lambda\boldsymbol{\lambda}^{n-1}\right]\,d\mathcal{V} + \mathbf{F}_p^{SG} + \mathbf{F}_p^c + \mathbf{F}_p^{ext} \\
&\frac{\rho_f}{\rho_p}\frac{J_p}{\alpha_\lambda}\boldsymbol{\Omega}_p^n = \rho_f\int_{\mathcal{D}}(\mathbf{x}-\mathbf{x}_p)\times\left[\mathcal{I}_u\frac{\mathbf{u}^{**}}{\alpha_\lambda} - \mathcal{I}_\lambda\boldsymbol{\lambda}^{n-1}\right]\,d\mathcal{V} + \mathbf{T}_p^{SG} + \mathbf{T}_p^c + \mathbf{T}_p^{ext} \\
&\boldsymbol{\lambda}^n = \boldsymbol{\lambda}^{n-1} + \mathcal{I}_\lambda\frac{\mathbf{U}_p^n + \boldsymbol{\Omega}_p^n\times(\mathbf{x}-\mathbf{x}_p) - \mathbf{u}^{**}}{\alpha_\lambda} \\
&\mathbf{u}^n = \mathbf{u}^{**} + \mathcal{I}_u\left[\mathbf{U}_p^n + \boldsymbol{\Omega}_p^n\times(\mathbf{x}-\mathbf{x}_p) - \mathbf{u}^{**}\right]
\end{aligned} \tag{2.53}$$

Mainly, the indicator function $\mathcal{I}_u$ controls to what extent the velocity inside the particle is set to rigid body motion at the particle boundary, and connects the particle velocity and angular velocity to the underlying liquid velocity field. The indicator function $\mathcal{I}_\lambda$ allows the force density felt by the liquid to be properly transmitted to the particles. Some comments on the choice of the form of the different indicator functions may be useful:

- due to the small parameter $c > 0$, the actual size of the particle is slightly larger than the theoretical size a_p. Should it not be the case, the hydrodynamic resistance coefficients on a sphere would be underestimated, as shown below in the particular case of the drag on a cubic lattice of particles. The parameters b and c in Eqs. (2.51) and (2.52) have to be tuned, as explained in the following;

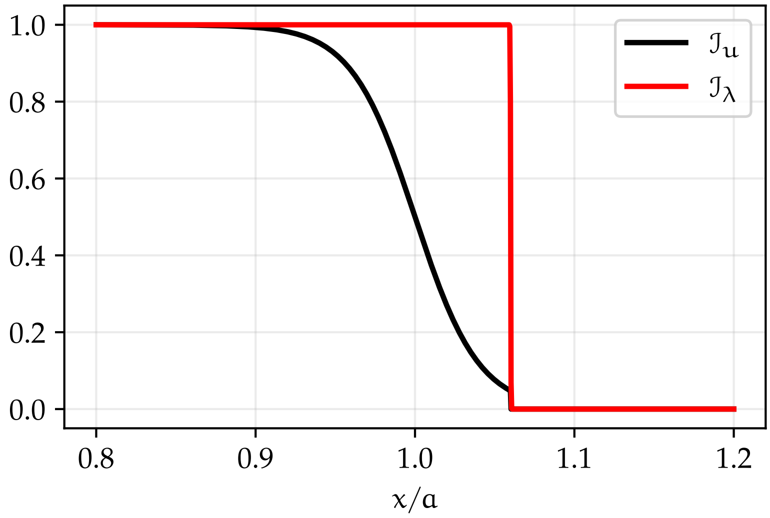

Figure 2.4
Indicator functions $\mathcal{I}_\lambda$ and $\mathcal{I}_u$ from Eqs. (2.51) and (2.52) with $b = 5$ and $c = 0.3$.

- the integral of the force density over each particle directly defines the force and torque felt by the particle due to the stress as computed by the flow solver(Eq. (2.6)). From Eqs. (2.10d) and (2.10e), the linear and angular momentum balance for each particle is fulfilled. In addition, the integral of the force density over a volume enclosing a single particle without any indicator function (i.e., related to the force exerted on the fluid by the particle) must be equal to the integral involved in Eqs. (2.10d) and (2.10e), in agreement with Newton's third law. This is the reason for using a steep Heaviside function for the integration of $\boldsymbol{\lambda}$;

- for the same reason, when two particles are at a close distance their indicator functions $\mathcal{I}_\lambda$ are both given the value 0.5 at the overlapping positions (only two particles at a time can overlap);

- the indicator function $\mathcal{I}_u$ used in the computation of M_p, J_p, $\int \mathbf{u}^*(\mathbf{x})\, d\mathcal{V}$ has been given a smooth shape to limit the oscillations due to the finite mesh-size Δ;

- choosing a smooth $\mathcal{I}_\lambda$ results in a decrease of the convergence rate.

DETERMINATION OF b AND c

We can now tune the parameters b and c that determine the shape of the indicator functions $\mathcal{I}_u$ and $\mathcal{I}_\lambda$ (Eqs. (2.51) and (2.52)). To this purpose, we measure the drag coefficient of a translating periodic array of spheres (a case that will be treated in Section 4.1.1) over 64 positions evenly distributed inside a single mesh cell in a domain of size $L/a = 8$ by varying b and c. The main advantage of choosing this particular flow is that a theoretical solution is available for a finite-size (periodic) domain. Also, in this special case, no sub-grid correction is needed as particles are far from each other and, therefore, the fluid flow solver can correctly compute the hydrodynamic interactions between particles.

The different tolerances for the resolution of the algebraic linear systems defined in Section 2.5.1 are now set to $\text{tol}_p = 5 \cdot 10^{-6}$, $\text{tol}_u = 10^{-6}$, and $\text{tol}_\lambda = 10^{-4}$ except for the first position for which we set $\text{tol}_\lambda = 10^{-5}$. This choice is justified in the next section.

The parameter c seems to have the most important role, as it sets the actual size of the particle, i.e. the precise spatial zone where $\boldsymbol{\lambda}$ is computed. On the contrary, the parameter b sets the smoothness of the indicator function $\mathcal{I}_u$, and has a role of *smoother* of some of the quantities as the particle moves through the mesh; in addition, we recall that the indicator function $\mathcal{I}_\lambda$ used to increment $\boldsymbol{\lambda}$ is a discontinuous Heaviside function for which only c is relevant. We first let b vary while keeping $c = 0.3$: as we can observe in Table 2.1, the drag coefficient K keeps nearly constant, and so does its standard deviation σ_K. This is at first sight surprising since the role of a smooth indicator function is to limit the oscillations of particle quantities as it moves across the mesh. However, although not shown here, other quantities such as the particle mass do oscillate, and the oscillations are all the more intense as the indicator function $\mathcal{I}_u$ is steep. On the other hand, too smooth an indicator function is not convenient either. Indeed, $\mathcal{I}_u$ is forced to vanish at $\|\mathbf{x} - \mathbf{x}_p\| = a_p + c\Delta$ (Eq. (2.52) and Fig. 2.4), so that a smaller value of b induces a larger discontinuity of $\mathcal{I}_u$. $b = 5$ turns out to be a satisfactory compromise and is also the value that has been used in previous works (Gallier et al., 2014a).

The influence of the parameter c is now probed while keeping $b = 5$ fixed. As displayed in Table 2.2, $c = 0.3$ yields the value of $\langle K \rangle$ closest to the theoretical value. In Fig. 2.4 we represent the indicator function with the optimal parameters.

Table 2.1
Drag coefficient of a translating periodic array of spheres for different values of the parameter b for the indicator function $\mathcal{I}_u$ (average over 64 positions in a single mesh cell and standard deviation).

b $(c = 0.3)$	$\langle K \rangle$	σ_K
2	1.532135	0.014381
5	1.532059	0.014380
7	1.532041	0.014387
10	1.532030	0.014399

Table 2.2
Drag coefficient of a translating periodic array of spheres for different values of the parameter c of the indicator functions, mean over 64 positions in a single mesh cell.

c $(b = 5)$	$(\langle K \rangle - K_{th}) / K_{th}$ [%]
0.10	-5.69
0.20	-3.01
0.25	-1.27
0.30	0.11
0.35	1.47
0.40	3.25
0.50	6.09

2.5.5 CONVERGENCE CONTROL

The purpose of the current section is to explain and explore the control of the convergence of the numerical procedure. Four tolerances have to be defined: one for each of the three fields p, $\mathbf{u}$, and $\boldsymbol{\lambda}$, and one for the resolution of the linear system for the computation of the velocities of the particles $\mathcal{U}^{n+1}$. The tolerances for p, $\mathbf{u}$, and $\mathcal{U}^{n+1}$ control the inversion of the corresponding linear systems of equations (steps 3 and 4 of the algorithm in Section 2.4, Eqs. (2.25), (2.40) and (2.43)).

The linear systems are solved using iterative methods: the inversion procedure is iterated until the normalized residual falls under the prescribed tolerance. The convergence of the whole algorithm for a time step is reached when the value of the force density at step $n+1$ is sufficiently close to the value at step n, i.e.:

$$\frac{\|\boldsymbol{\lambda}^{n+1}-\boldsymbol{\lambda}^{n}\|}{\|\boldsymbol{\lambda}^{n}\|} < \mathrm{tol}_{\lambda} \quad \text{where:} \quad \|\boldsymbol{\lambda}\| = \sum_{\text{cells } c_i} \sqrt{\sum_k \lambda_k(c_i)^2} \tag{2.54}$$

As previously mentioned, the main nonlinearity of the equations lies in the force density $\boldsymbol{\lambda}$, which is recursively modified as the fluid problem is solved. As a consequence, it is difficult to address separately the resolution of the fluid sub-problem from the particle sub-problem. In the following, the choice of the value of the different tolerances is explained.

As the solution of the linear system associated with the velocities of the particles is a task that is a lot cheaper than the flow solution, the tolerance for $\mathcal{U}^{n+1}$ is not investigated here, and we fix it to 10^{-6}. Hence, we present the investigation of the tolerances for p, $\mathbf{u}$, and $\boldsymbol{\lambda}$, hereafter denoted respectively by tol_p, tol_u and tol_{λ}. To this purpose, we choose the special

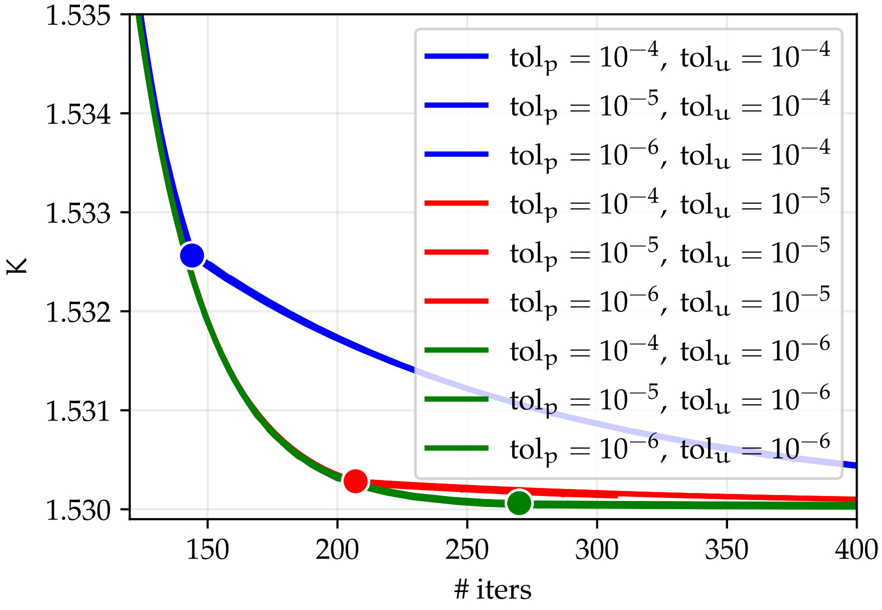

Figure 2.5
Drag coefficient of a translating periodic array of spheres: convergence history for different values of tol_p and tol_u.

case of a translating periodic array of spheres. It should be noted that tol_p and tol_u are compared to the absolute residuals computed as in Section 2.5.1, while tol_λ is compared to the relative residuals computed as in Eq. (2.54).

Fig. 2.5 displays the convergence behavior of the drag coefficient K. We observe that tol_p has no effect either on the value of K or on the convergence history. It seems that the value of tol_u has an insignificant influence on the converged solution. However, it determines a point in the convergence history, i.e. a value of K and a number of iterations (highlighted in Fig. 2.5), from which the convergence slows down. The smaller the tolerance, the higher the number of iterations before convergence slowdown.

We turn now to the convergence history of the residual for λ (Fig. 2.6 (top)). At the same moment as the convergence of K slows down (the points highlighted in Fig. 2.5), the residual for λ starts to oscillate. Moreover, in this case, we appreciate an effect caused by tol_p: the oscillation amplitude of the residual of λ increases with tol_p, and the oscillations propagate earlier in the convergence. They most probably are responsible for the convergence slowdown.

Finally, the data in Figs. 2.5 and 2.6 (top) are recast in Fig. 2.6 (bottom), where the convergence history of the error between K and its final value K_0 is displayed as a function of the residual of λ for different values of tol_u and tol_λ. Again, two regimes are evidenced,

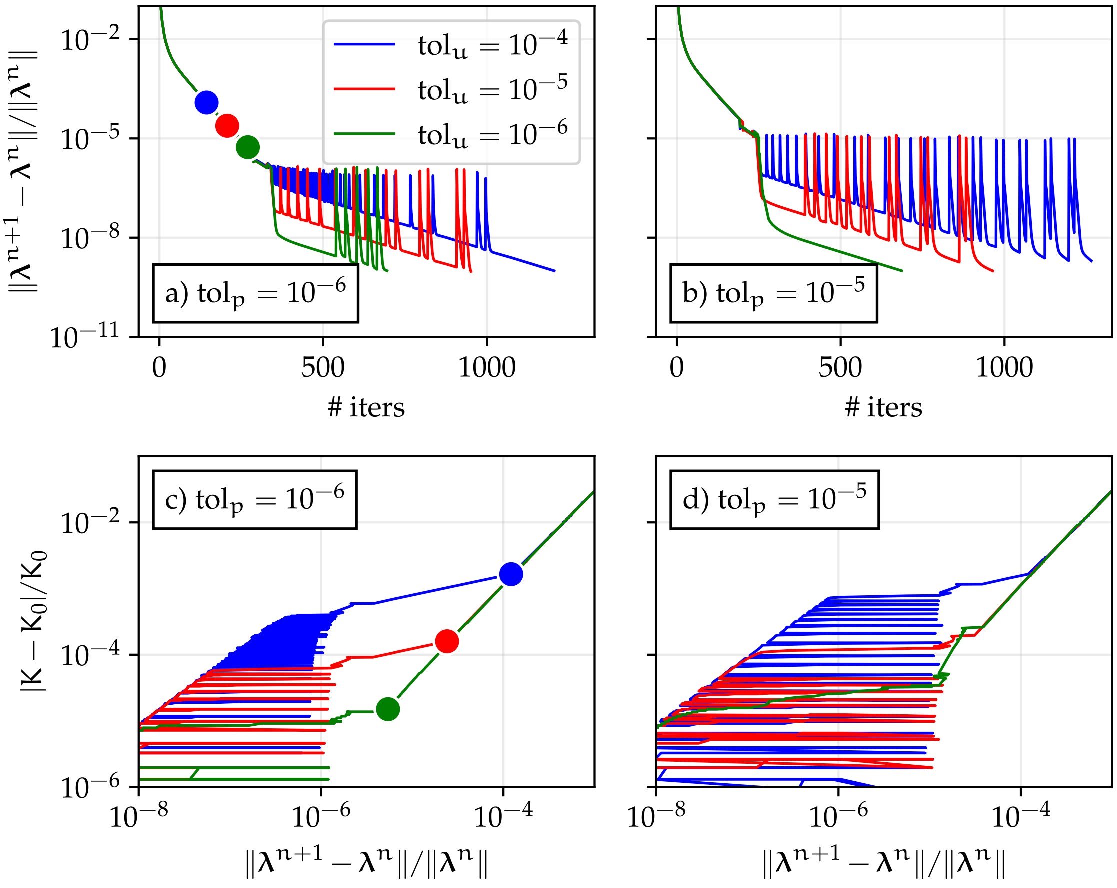

Figure 2.6
(top) Relative residual for λ: convergence history for different values of tol_p and tol_u. (bottom) Error of the drag coefficient w.r.t. the value at convergence for different values of tol_p and tol_u.

corresponding respectively to the fast and slow convergence rates. In the fast convergence regime, the value of the residual for λ determines the difference between the actual value of K and the converged value. In the slow one, large oscillations of the residual of λ occur, with a weak effect on the value of K, which slowly tends to the converged value. The transition between the two regimes is mainly controlled by tol_u, which sets the minimum value of the residual for $\boldsymbol{\lambda}$ for which the convergence still has a good behavior (i.e., the oscillations are not important and the convergence is not too slow). Again we observe that tol_p plays a role in the amplitude of these oscillations and lets them propagate earlier.

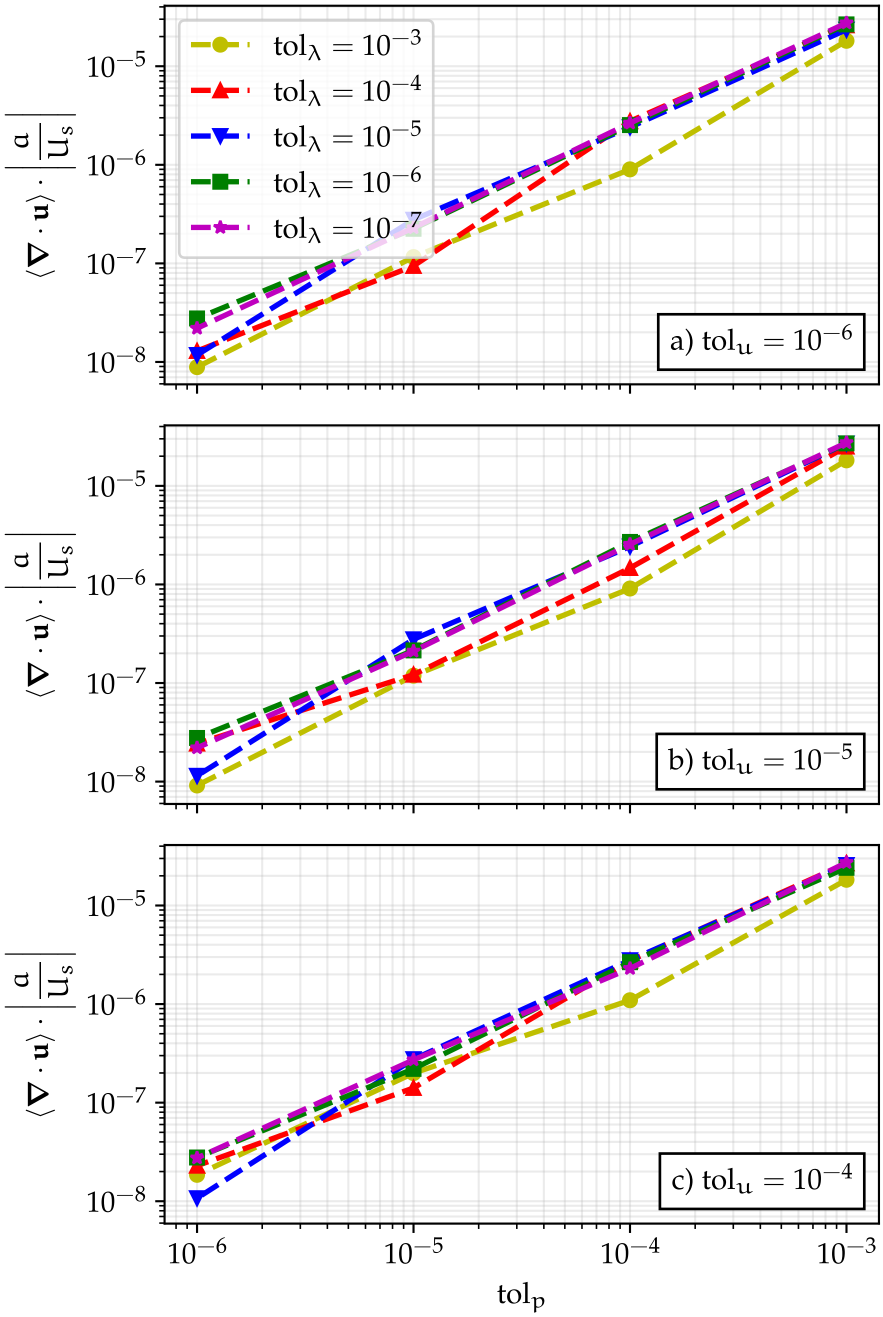

Figure 2.7
Measures of the fractional rate of expansion for a translating periodic array of spheres (see Chapter 4 for more details about the simulation setup).

As a last check, again in the case of a translating periodic array of spheres, we measured the fractional rate of expansion $\langle \mathbf{u} \rangle$ of the converged velocity field obtained for different values of tol_p, tol_u and tol_λ. As we can notice in Fig. 2.7, the tolerances for $\mathbf{u}$ and $\boldsymbol{\lambda}$ do not play a role, while $\langle \boldsymbol{\nabla} \cdot \mathbf{u} \rangle a / |U_s|$ (where $U_s = \frac{1}{V_0} \int_{\mathcal{D}} \mathbf{u} \, d\mathcal{V}$ is the slip velocity) decreases linearly with tol_p. This last check simply shows that the pressure-velocity coupling of the momentum equation is conveniently tackled by OpenFOAM.

From the data shown, we can draw some guiding ideas about the choice of the values of the different tolerances: tol_λ is the stopping criterion and sets the distance of the solution from the value at convergence; tol_u influences the minimal value of the residual of $\boldsymbol{\lambda}$ for which a good convergence behavior is still maintained; tol_p influences the oscillations of the residual of $\boldsymbol{\lambda}$ and sets the fractional rate of expansion.

The purpose of the current chapter is the presentation of the method and its numerical implementation. In Chapter 4 we are going to concentrate on its validation and, as a consequence, low tolerances are chosen for the different quantities, keeping in mind that, depending on the required computation speed and precision, less demanding tolerances could be chosen. Therefore, for all the validations concerning one, two, or three particles, we will set $\mathrm{tol}_u = 10^{-6}$ and $\mathrm{tol}_p = 5 \cdot 10^{-6}$; as for $\boldsymbol{\lambda}$, we set $\mathrm{tol}_\lambda = 10^{-5}$ for the first time step (to correctly compute the initial solution) and $\mathrm{tol}_\lambda = 10^{-4}$ for the next time steps.

2.6 ELASTIC CONTACT MODEL

Some important points should be recalled concerning the interaction forces. During the last decade, it has been shown that contact forces between particles play a major influence on the rheological properties of non-Brownian suspensions: even in the case of model spheres, contact occurs due to micro-asperities on the particle surface (Blanc et al., 2011a; Pham et al., 2015). In particular, friction between particles significantly enhances the suspension viscosity (Gallier, 2014; Peters et al., 2016; Abhinendra Singh et al., 2018).

Here, both surface roughness and friction are taken into account using a simple contact model (see Peters et al. (2016)). Contact occurs between particles as soon as the distance between their surface is smaller than the roughness height h_r, resulting in elastic interaction forces, both normal ($\mathbf{F}_n$) and tangential ($\mathbf{F}_t$). Sliding is not allowed until the tangential force reaches the value $\|\mathbf{F}_t\| = \mu \|\mathbf{F}_n\|$, where μ stands for the static friction coefficient. As long as sliding occurs, the latter relation between normal and tangential forces holds, meaning that no difference is made here between static and dynamic friction coefficients.

The influence of the roughness height is quite moderate as long as its value is kept under $10^{-2} a_1$ (Gallier, 2014). In the following, the value $h_r / a_1 = 5 \cdot 10^{-3}$ is chosen, which is consistent with experimental data (Blanc et al., 2011a). In contrast, friction induces a strong increase of the suspension viscosity (Gallier, 2014; Peters et al., 2016; Abhinendra Singh et al., 2018) as μ increases in the range $[0; 2]$. In the following, the friction coefficient value is chosen constant and equal to $\mu = 0.5$.

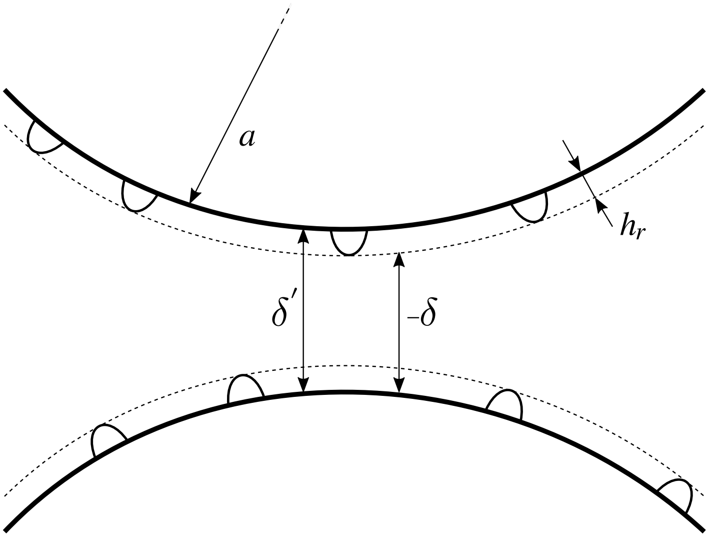

Figure 2.8
Sketch of roughness modeling: δ' is the actual separation distance, h_r the roughness height and contact occurs when $\delta = h_r - \delta' \geqslant 0$.

For a pair of spherical particles (p_i) and (p_j) undergoing contact, the contact force $\mathbf{F}^c$ exerted by particle (p_j) on particle (p_i) is classically decomposed into its normal $\mathbf{F}^c_n$ and tangential $\mathbf{F}^c_t$ components:

$$\mathbf{F}^c = \mathbf{F}^c_n + \mathbf{F}^c_t \tag{2.55}$$

We consider homogeneously distributed asperities all over the surface of the particles. Considering the roughness height h_r, particles radii a_i and a_j, positions $\mathbf{x}_i$ and $\mathbf{x}_j$ and distance $\mathbf{r}_{ij} = \mathbf{x}_j - \mathbf{x}_i$, we define the overlap distance as $\delta = h_r - \left[\|\mathbf{r}_{ij}\| - (a_i + a_j)\right]$. Contact occurs whenever $\delta \geqslant 0$ (Fig. 2.8). The normal contact force is modeled using a Hertz law:

$$\mathbf{F}^c_n = -k_n \delta^{3/2} \mathbf{n} \tag{2.56}$$

where $\mathbf{n}$ is the unitary normal vector $\mathbf{n} = \mathbf{r}/\|\mathbf{r}\|$.

This expression is for instance well adapted to the contact between a single asperity and a smooth part of another particle or of a bounding wall. In that case, the normal stiffness k_n depends on the Young modulus and Poisson ratio of the particle material, together with the curvature radius of one asperity (Peters et al., 2016). However, the stiffness computed for the relevant particle properties turns out to be quite high and may be tackled only at the price of significant time step reduction. For numerical reasons, the stiffness may be reduced. To tune its actual value, the average roughness deformation $\bar{\epsilon} = |\bar{\delta}|/h_r$ is estimated. Balancing contact and hydrodynamic forces (in dilute regimes) yields $6\pi\eta\dot{\gamma}a_c^2 = k_n \left(\bar{\epsilon}h_r\right)^{3/2}$ (here, $a_c = 1.0$) from which the expression of k_n follows. Parametric simulations on $\bar{\epsilon}$ (and so k_n) have shown that there are weak effects on rheology as long as it is sufficiently small, typically below 0.2 (Gallier et al., 2014b). We also note that other studies have considered a linear spring force instead of the nonlinear Hertz law, with similar results for stiff contact (Mari et al., 2014; Chèvremont et al., 2019). Usually, the stiffness is tuned to keep low deformation in the course of the simulation.

However, due to the softness of the normal force, and the high level of contact forces at a high solid volume fraction, particles may sometimes overlap, meaning that the asperity is fully flattened out, and the distance between surfaces may become negative. To avoid this, a threshold (10^{-5}) is imposed on the reduced distances $\xi = 2\|\mathbf{r}_{ij}\|/(a_i + a_j) - 2$ and $\varepsilon = \|\mathbf{r}_{pw}\|/a - 1$ for the contact between particles and between a particle and a wall, respectively, and a multiplying function is included, which goes to infinity for $\delta' = \hat{\delta}'_\infty \cdot h_r$, so that the distance between the surfaces of the particles, δ', is kept larger than $\hat{\delta}'_\infty \cdot h_r$, with $\hat{\delta}'_\infty = 10^{-5}\left(a_i + a_j\right) / \left(2h_r\right)$ for a particle pair and $\hat{\delta}'_\infty = 10^{-5} a/h_r$ for a particle in contact with a wall. Finally, the normal contact force reads:

$$\mathbf{F}_n^c = -k_n \delta^{3/2} \left[\frac{1 - \exp\left[10\left(\hat{\delta}'_\infty - 1\right)\right]}{1 - \exp\left[10\left(\hat{\delta}'_\infty - \dfrac{\delta'}{h_r}\right)\right]} \right] \mathbf{n} \tag{2.57}$$

When a force scale for the particle interactions F_0 is relevant (e.g., when adhesion forces or load-dependent friction takes place), the dimensionless shear rate $\dot{\Gamma}$ measures the strength of hydrodynamic forces in dilute suspensions compared to this force scale:

$$\dot{\Gamma} = \frac{6\pi\eta\dot{\gamma}a_c^2}{F_0} \tag{2.58}$$

When no other force scale is relevant, the force necessary to achieve the roughness deformation $\bar{\varepsilon}h_r$ may be chosen as the force scale, yielding the particular value $\dot{\Gamma} = 1$.

The tangential force is given by:

$$\mathbf{F}_t^c = -k_t \boldsymbol{\mathcal{Y}} \tag{2.59}$$

where k_t is the stiffness of the tangential spring. A classic choice for k_t is (Peters et al., 2016)

$$k_t = \frac{2}{7}\frac{|\mathbf{F}_n|}{\delta} \tag{2.60}$$

$\boldsymbol{\mathcal{Y}}$ is the relative tangential displacement of the surfaces of the two particles and it is calculated by integrating the slip velocity $\mathbf{U}_s$ during the contact:

$$\boldsymbol{\mathcal{Y}} = \int_0^t \mathbf{U}_s \, dt \tag{2.61}$$

where $\mathbf{U}_s$ is the slip velocity:

$$\mathbf{U}_s = \mathbf{U}_i - \mathbf{U}_j - \left[\left(\mathbf{U}_i - \mathbf{U}_j\right) \cdot \mathbf{n}\right] \cdot \mathbf{n} + \left(a_i \boldsymbol{\Omega}_i + a_j \boldsymbol{\Omega}_j\right) \times \mathbf{n} \tag{2.62}$$

According to the classic Amontons-Coulomb law of friction, sliding occurs if the tangential force exceeds the friction limit $\mu|\mathbf{F}_n^c|$, where μ is the friction coefficient. The tangential force is then given by:

$$\mathbf{F}_t^c = \mu \, |\mathbf{F}_n^c| \frac{\mathbf{F}_t^c}{|\mathbf{F}_t^c|} \tag{2.63}$$

In particular, no difference is made in this model between static and dynamic friction coefficients.

Finally, the corresponding contact torques are:

$$\mathbf{T}_i^c = \frac{a_i}{a_i + a_j} \mathbf{x}^{(ij)} \times \mathbf{F}_{t,i}^c \qquad \mathbf{T}_j^c = \frac{a_j}{a_i + a_j} \mathbf{x}^{(ji)} \times \mathbf{F}_{t,j}^c \tag{2.64}$$

where $\mathbf{x}^{(ij)} = \mathbf{x}_j - \mathbf{x}_i$ and, obviously, $\mathbf{F}_{t,j}^c = -\mathbf{F}_{t,i}^c$ and $\mathbf{x}^{(ji)} = -\mathbf{x}^{(ij)}$.

2.7 RHEOLOGY

The computation of the relevant rheological quantities is addressed. The computation of the volume fraction, the stresses, and the viscosity needs particular attention: as we will show in Chapter 4, and even though we employ two particle sizes $a_2/a_1 = 1.4$, particle ordering is observed close to the walls. This separates a *core* region from a wall one: in the wall region, the local volume fraction varies over a few particle sizes, while in the core region, the volume fraction is practically constant.

The relevant rheological quantities, such as the stresses (and therefore the viscosity), can have quite different values if computed in the whole domain or the core region exclusively. Also, it is important to average them over multiple deformation units in the stationary regime to avoid time-related oscillations.

2.7.1 PARTICLE STRESSLET

HYDRODYNAMIC MOMENT

To compute the effective stress in a suspension of solid particles, the first moment of the hydrodynamic surface stress acting on each particle $\mathbf{D}_p$ (Batchelor, 1970; Jeffrey et al., 1993) is needed:

$$\mathbf{D}_p = \int_{\partial \mathcal{D}_p} \boldsymbol{\sigma} \cdot \mathbf{n} \otimes (\mathbf{x} - \mathbf{x}_p) \, d\mathcal{S} \tag{2.65}$$

The anti-symmetric part of the force dipole $\mathbf{D}_p$ is related to the hydrodynamic torque exerted on the particle, while the symmetric part – the stresslet – determines the contribution of the particle to the effective stress. The latter is split into the deviatoric stresslet $\mathbf{S}_p$ and the isotropic part $s_p/3\,\boldsymbol{\delta}$, where s_p stands for the trace of the force dipole. Both $\mathbf{S}_p$ and s_p are computed from the FDM contribution and the sub-grid correction. The FDM contribution of the dipole moment is computed from the force density $\boldsymbol{\lambda}$ and the solver pressure p. In more detail, using the divergence theorem, Eq. (2.65), together with Eq. (2.11a) yields:

$$\mathbf{D}_p^{FDM} = -\rho_f \int_{\mathcal{D}_p} \boldsymbol{\lambda} \otimes (\mathbf{x} - \mathbf{x}_p)\, d\mathcal{V} + \int_{\mathcal{D}_p} \boldsymbol{\sigma}\, d\mathcal{V} \tag{2.66}$$

The strain rate vanishes inside the particle so that the stress $\boldsymbol{\sigma}$ written in Eq. (2.2) reduces to the isotropic pressure component and the FDM traceless stresslet and stresslet trace write:

$$\begin{aligned} \mathbf{S}_p^{FDM} &= -\rho_f \int_{\mathcal{D}_p} \left\{ \frac{1}{2} [\boldsymbol{\lambda} \otimes (\mathbf{x} - \mathbf{x}_p) + (\mathbf{x} - \mathbf{x}_p) \otimes \boldsymbol{\lambda}] - \frac{1}{3} \boldsymbol{\lambda} \cdot (\mathbf{x} - \mathbf{x}_p)\, \boldsymbol{\delta} \right\} d\mathcal{V} \\ s_p^{FDM} &= -\int_{\mathcal{D}_p} [\rho_f \boldsymbol{\lambda} \cdot (\mathbf{x} - \mathbf{x}_p) + 3p]\, d\mathcal{V} \end{aligned} \tag{2.67}$$

As mentioned previously, a sub-grid correction must be added to the FDM force dipole on the particles, so that:

$$\begin{aligned} \mathbf{S}_p^h &= \mathbf{S}_p^{FDM} + \mathbf{S}_p^{SG} \\ s_p^h &= s_p^{FDM} + s_p^{SG} \end{aligned} \tag{2.68}$$

It should be noted that in such an incompressible flow the overall pressure level is arbitrary so a reference pressure must be defined. This reference pressure is chosen at each time step as the mean pressure in the simulation domain, and the relevant pressure is the difference between the pressure and this reference value.

CONTACT MOMENT

Contact forces also induce an additional stresslet which is given by:

$$\begin{aligned} \mathbf{S}_i^c &= \frac{1}{2} \frac{a_i}{a_i + a_j} \left(\mathbf{F}^c \otimes \mathbf{x}^{(ij)} + \mathbf{x}^{(ij)} \otimes \mathbf{F}^c \right) \\ \mathbf{S}_j^c &= \frac{1}{2} \frac{a_j}{a_i + a_j} \left(\mathbf{F}^c \otimes \mathbf{x}^{(ij)} + \mathbf{x}^{(ij)} \otimes \mathbf{F}^c \right) \end{aligned} \tag{2.69}$$

This stresslet is not traceless and its trace determines the contribution of contact to the particle pressure. Also note that since $\langle \mathbf{F}^c \otimes \mathbf{x}^{(ij)} \rangle$ may not be symmetric, i.e. there may exist an antisymmetric contact contribution to the particle stress due to contact torques. However, due to the lack of particle inertia, this contribution is balanced by its hydrodynamic counterpart, so that the total torque exerted on each particle vanishes.

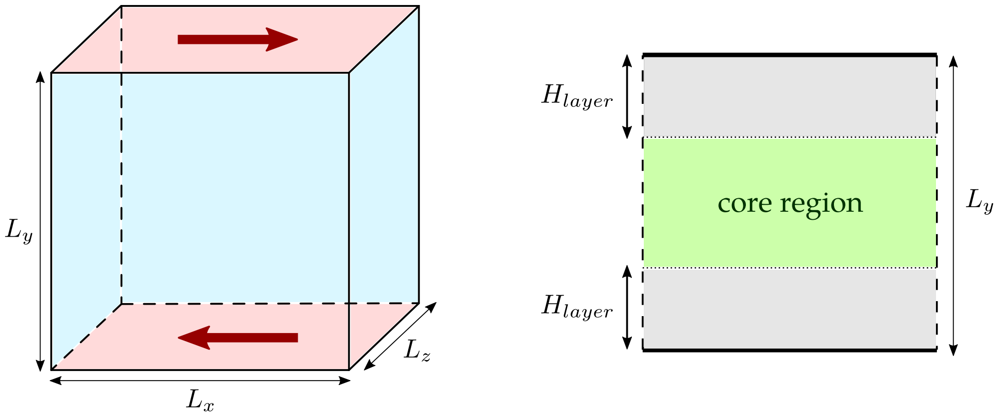

Figure 2.9
Example of the system adopted for simulating a simple shear flow. On the right, the separation of the core region from wall one is represented, being H_{layer} the distance from the wall at which particle ordering is observed and the volume fraction profile is not constant.

2.7.2 MATERIAL FUNCTIONS IN LINEAR FLOWS

As pointed out at the beginning of this section, particle ordering is observed close to the walls, and a *core* region can be identified. Rheological quantities can have quite different values if computed in the whole domain or the core region exclusively. Let us see how to define them in a simple shear flow as in Fig. 2.9.

VOLUME FRACTION

The suspensions investigated in this work are composed of bidisperse particles to reduce the strength and extension of the wall layering. However, a local ordering is still observed in the vicinity of the walls, over a shorter extension though. Following (Yeo & Maxey, 2011), the local volume fraction is computed using the surface averaging procedure:

$$\phi(y) = \frac{1}{L_x \times L_z} \iint_{\{\text{plane } y\}} \sum_{p \in \mathcal{D}} \chi_p(\mathbf{x}) \, dx \, dz \tag{2.70}$$

where $\chi_p(\mathbf{x})$ is the particle indicator function and the integration is performed over the plane of constant height y. From Eq. (2.70), the mean volume fraction may be computed as $\phi_0 = (1/L_y) \int_{-L_y/2}^{+L_y/2} \phi(y) \, dy$. Based on the variation of the local volume fraction, the simulation domain may be split into a wall region and a core region. In the former region, the time-averaged volume fraction varies with the distance to the wall H_{layer} with a typical length scale $a_1 + a_2$, while in the latter region, the volume fraction is approximately constant, and the particle velocity profile is nearly linear. The core volume fraction is computed as the average of the local volume fraction from Eq. (2.70):

$$\phi_{core} = \frac{1}{L_y - 2H_{layer}} \int_{-L_y/2+H_{layer}}^{L_y/2-H_{layer}} \phi(y) \, dy \tag{2.71}$$

STRESSES AND VISCOSITY

The stress in the suspension is usually defined as:

$$\boldsymbol{\Sigma} = -P\boldsymbol{\delta} + \eta\dot{\gamma}\left(\mathbf{e}_x \otimes \mathbf{e}_y + \mathbf{e}_y \otimes \mathbf{e}_x\right) + \boldsymbol{\Sigma}^{h_p} + \boldsymbol{\Sigma}^{c} \tag{2.72}$$

where the last two terms stand respectively for the hydrodynamic and contact contributions to the particle stress and are respectively computed from the hydrodynamic stresslet (Eqs. (2.67) and (2.68)) and contact forces on the particles in the core region:

$$\boldsymbol{\Sigma}^{h_p} = \frac{1}{V_{core}} \sum_{p \in \mathcal{D}_{core}} \left(\mathbf{S}_p^{FDM} + \mathbf{S}_p^{SG} + \frac{s_p^{FDM} + s_p^{SG}}{3} \boldsymbol{\delta} \right) = \frac{1}{V_{core}} \sum_{p \in \mathcal{D}_{core}} \mathbf{S}_p^{H} \tag{2.73}$$

$$\begin{aligned} \boldsymbol{\Sigma}^{c} &= \frac{1}{V_{core}} \sum_{p \in \mathcal{D}_{core}} \sum_{p' \in \mathcal{D}_{core}} \frac{1}{2} \frac{a_p}{a_p + a'_p} \left(\mathbf{F}^{p' \to p} \otimes \mathbf{x}^{(pp')} + \mathbf{x}^{(pp')} \otimes \mathbf{F}^{p' \to p} \right) \\ &= \frac{1}{V_{core}} \sum_{p \in \mathcal{D}_{core}} \mathbf{S}_p^{c} \end{aligned} \tag{2.74}$$

where $\mathbf{S}_p^H = \mathbf{S}_p^h + s_p^h \boldsymbol{\delta}/3$, and $\mathbf{x}^{(pp')} = \mathbf{x}^{(p')} - \mathbf{x}^{(p)}$. It should be stressed that $\mathbf{S}_p^H$ and $\mathbf{S}_p^c$ are now both not traceless. The pressure in Eq. (2.72) is the contribution of the mean pressure in the liquid to the suspension stress (Batchelor, 1970).

In the current work, in line with the computation of the volume fraction, and following Yeo & Maxey (2011), the local particle contribution to the stress is computed with the assumption that the particle stresslet is homogeneously distributed over the particle domain with volume V_p:

$$\boldsymbol{\Sigma}^{h_p,c}(y) = \frac{1}{L_x \times L_z} \iint_{\{\text{plane } y\}} \sum_p \frac{\mathbf{S}_p^{H,c}}{V_p} \chi_p(\mathbf{x}) \, dx \, dz \tag{2.75}$$

The local stress is then averaged over the core region in the same way as the volume fraction in Eq. (2.71), yielding the core stress. The reduced bulk viscosity reads:

$$\eta^s_{core} = \frac{\langle \Sigma^{core}_{xy} \rangle}{\eta \langle \dot{\gamma}_{core} \rangle} = 1 + \frac{\left\langle \Sigma^{h_p,core}_{xy} \right\rangle + \left\langle \Sigma^{c,core}_{xy} \right\rangle}{\eta \langle \dot{\gamma}_{core} \rangle} \tag{2.76}$$

where $\langle \cdot \rangle$ denotes time-averaging over the steady flow, and $\dot{\gamma}_{core}$ is defined by performing a linear regression of the velocity of the centers of the particles in the core region (usually $\dot{\gamma}_{core} < \dot{\gamma}_0$, being $\dot{\gamma}_0$ the imposed shear rate).

3

SUB-GRID CORRECTIONS

Sub-grid corrections are classically implemented for linear flows (e.g., a simple shear flow); in principle, it would be difficult to use them in nonlinear flows (e.g., a pressure-driven flow). We developed a new formulation and obtained frame-invariant sub-grid corrections that do not need to take into account the terms related to the ambient flow, making it possible to employ them also in heterogeneous flows.

We start by recalling the standard sub-grid corrections. Then, we show how to determine the resistance matrix as measured by the solver. Finally, we demonstrate how to get a frame-invariant sub-grid correction matrix for both the cases of two close particles and a particle close to a wall, by isolating and evaluating the ambient flow contributions.

Many more details about practical ways for measuring the resistance coefficients as well as their general forms and theoretical expressions are given in Appendices A to D.

3.1 STANDARD SUB-GRID CORRECTIONS

Sub-grid corrections aim at supplying the system with the contribution of the short-scale flow that occurs between close solid surfaces (particle-particle or particle-wall) that is missed by the fluid flow solver. Since low-Reynolds-number flows at particle scale are considered, the governing equations for the flow are linear (Stokes equations), resulting in linear relations between the stress moments exerted on the particles (force, torque, and stresslet), and the particles and flow velocities (Kim & Karrila, 1991). Such relations hold for the total stress moment as well as for the sub-grid corrections. As just mentioned, in their usual form they involve both the particles and the ambient flow velocities. If the length scales of the flow variations are bigger than the particle size, we may assume the local linearity of the flow at particle scale, i.e. that the following expression holds for the ambient flow:

$$\mathbf{u}_\infty(\mathbf{x}) = \mathbf{U}_0 + \mathbf{\Omega}_\infty \times \mathbf{x} + \mathbf{E}_\infty \cdot \mathbf{x} \tag{3.1}$$

where $\mathbf{U}_0$, $\mathbf{\Omega}_\infty$ and $\mathbf{E}_\infty$ are respectively the translational and angular velocities, and the strain tensor of the suspension. The three of them are constant, i.e. do not depend on the position $\mathbf{x}$. The linear relation between sub-grid forces, torques, and stresslets on the one hand, and the velocities of the particles, on the other hand, may be written as:

$$\begin{aligned}
\mathcal{F}^{SG} &= -\mathcal{R}^{SG}_{\mathcal{F}\mathcal{U}} \cdot (\mathcal{U} - \mathcal{U}_\infty) + \mathcal{R}^{SG}_{\mathcal{F}E} : \mathbf{E}_\infty \\
\mathcal{S}^{SG} &= -\mathcal{R}^{SG}_{\mathcal{S}\mathcal{U}} \cdot (\mathcal{U} - \mathcal{U}_\infty) + \mathcal{R}^{SG}_{\mathcal{S}E} : \mathbf{E}_\infty \\
\mathbf{s}^{SG} &= -\mathcal{R}^{SG}_{s\mathcal{U}} \cdot (\mathcal{U} - \mathcal{U}_\infty) + \mathcal{R}^{SG}_{sE} : \mathbf{E}_\infty
\end{aligned} \tag{3.2}$$

where the tensors $\mathcal{R}^{SG}_{\dots}$ depend on the sizes and positions of the particles, and $\mathcal{F}^{SG}$ is the vector of sub-grid forces and torques exerted on the particles, $\mathcal{S}^{SG}$ is the vector of the sub-grid traceless stresslets, and $\mathbf{s}^{SG}$ is the vector of the sub-grid traces of the force dipoles:

$$\begin{aligned}
\mathcal{F}^{SG} &= \left(\mathbf{F}^{SG}_1, \mathbf{F}^{SG}_2, \dots, \mathbf{T}^{SG}_1, \mathbf{T}^{SG}_2, \dots\right) \\
\mathcal{S}^{SG} &= \left(\mathbf{S}^{SG}_1, \mathbf{S}^{SG}_2, \dots,\right) \\
\mathbf{s}^{SG} &= \left(s^{SG}_1, s^{SG}_2, \dots,\right)
\end{aligned} \tag{3.3}$$

$\mathcal{U}$ is the vector of the particle translational and angular velocities, and $\mathcal{U}_\infty$ is the vector of the ambient flow velocities at the center of each particle:

$$\mathcal{U} = (\mathbf{U}_1, \mathbf{U}_2, \dots, \mathbf{\Omega}_1, \mathbf{\Omega}_2, \dots) \qquad \mathcal{U}_\infty = (\mathbf{u}_\infty(\mathbf{x}_1), \mathbf{u}_\infty(\mathbf{x}_2), \dots, \mathbf{\Omega}_\infty, \mathbf{\Omega}_\infty, \dots) \tag{3.4}$$

The corrections are built as the superposition of the individual contributions of the pairs of close particles, and the particles close to the bounding walls. Both types of contribution are detailed in the next two sections.

3.1.1 TWO-PARTICLE RESISTANCE MATRIX

The building block of the former contribution is the two-particle resistance matrix $\mathcal{R}_{2p}^{SG}$, which allows writing the stress moments vector $\mathcal{M}^{SG}$ as:

$$
\begin{aligned}
\mathcal{M}^{SG} = \begin{pmatrix} \mathbf{F}_1^{SG} \\ \mathbf{F}_2^{SG} \\ \mathbf{T}_1^{SG} \\ \mathbf{T}_2^{SG} \\ \mathbf{S}_1^{SG} \\ \mathbf{S}_2^{SG} \\ s_1^{SG} \\ s_2^{SG} \end{pmatrix} &= -\mathcal{R}_{2p}^{SG} \cdot \begin{pmatrix} \mathbf{U}_1 - \mathbf{u}_\infty(\mathbf{x}_1) \\ \mathbf{U}_2 - \mathbf{u}_\infty(\mathbf{x}_2) \\ \mathbf{\Omega}_1 - \mathbf{\Omega}_\infty \\ \mathbf{\Omega}_2 - \mathbf{\Omega}_\infty \\ -\mathbf{E}_\infty \\ -\mathbf{E}_\infty \end{pmatrix} \\
&= -\eta \begin{pmatrix}
\mathbf{A}_{11} & \mathbf{A}_{12} & \tilde{\mathbf{B}}_{11} & \tilde{\mathbf{B}}_{12} & \tilde{\mathbf{G}}_{11} & \tilde{\mathbf{G}}_{12} \\
\mathbf{A}_{21} & \mathbf{A}_{22} & \tilde{\mathbf{B}}_{21} & \tilde{\mathbf{B}}_{22} & \tilde{\mathbf{G}}_{21} & \tilde{\mathbf{G}}_{22} \\
\mathbf{B}_{11} & \mathbf{B}_{12} & \mathbf{C}_{11} & \mathbf{C}_{12} & \tilde{\mathbf{H}}_{11} & \tilde{\mathbf{H}}_{12} \\
\mathbf{B}_{21} & \mathbf{B}_{22} & \mathbf{C}_{21} & \mathbf{C}_{22} & \tilde{\mathbf{H}}_{21} & \tilde{\mathbf{H}}_{22} \\
\mathbf{G}_{11} & \mathbf{G}_{12} & \mathbf{H}_{11} & \mathbf{H}_{12} & \mathbf{M}_{11} & \mathbf{M}_{12} \\
\mathbf{G}_{21} & \mathbf{G}_{22} & \mathbf{H}_{21} & \mathbf{H}_{22} & \mathbf{M}_{21} & \mathbf{M}_{22} \\
\mathbf{P}_{11} & \mathbf{P}_{12} & 0 & 0 & \mathbf{Q}_{11} & \mathbf{Q}_{12} \\
\mathbf{P}_{21} & \mathbf{P}_{22} & 0 & 0 & \mathbf{Q}_{21} & \mathbf{Q}_{22}
\end{pmatrix} \cdot \begin{pmatrix} \mathbf{U}_1 - \mathbf{u}_\infty(\mathbf{x}_1) \\ \mathbf{U}_2 - \mathbf{u}_\infty(\mathbf{x}_2) \\ \mathbf{\Omega}_1 - \mathbf{\Omega}_\infty \\ \mathbf{\Omega}_2 - \mathbf{\Omega}_\infty \\ -\mathbf{E}_\infty \\ -\mathbf{E}_\infty \end{pmatrix}
\end{aligned}
\tag{3.5}
$$

Where the elementary blocks $\mathbf{A}_{\alpha\beta}$, $\mathbf{B}_{\alpha\beta}, \ldots$ are tensors of different ranks depending on the quantities that they connect and the superscript $(\cdot)^{SG}$ has been removed for the sake of clarity. Their physical meaning is straightforward: as an example, the tensor $\mathbf{A}_{12}$ defines the sub-grid force exerted on particle (p_1) in the case where particle (p_1) is at rest and particle (p_2) undergoes a translational motion with velocity $\mathbf{U}_2$ in a liquid at rest ($\mathbf{u}_\infty(\mathbf{x}) = 0$) with $\mathbf{F}_1^{SG} = -\eta \mathbf{A}_{12} \cdot \mathbf{U}_2$. In the case of spherical particles of interest in the present study, these elementary tensors are simply written as a function of the radii of the particles, the distance between the centers of the particles, and the unit vector along the centerline. In addition, they obey symmetry relations that originate either from geometric symmetry argument or from Lorentz reciprocal theorem (Kim & Karrila, 1991). The general form of the different tensors, together with the symmetry relations that they obey, are recalled in Appendix A. It should be noted here that the matrix $\mathcal{R}_{2p}^{SG}$ is computed as the difference between the theoretical matrix from Stokes flow theory (Jeffrey & Onishi, 1984; Jeffrey, 1992; Jeffrey et al., 1993) and the matrix as seen by the Fictitious Domain Method solver:

$$
\mathcal{R}_{2p}^{SG} = \mathcal{R}_{2p}^{th} - \mathcal{R}_{2p}^{FDM} \tag{3.6}
$$

3.1.2 PARTICLE-WALL RESISTANCE MATRIX

The particle-wall resistance matrix reflects the linear relation between the stress moments on a particle (p) close to a wall and the generalized relative velocity of the particle. In the following, the wall is supposed to have zero angular velocity for the sake of simplicity. Any point of the wall moves with the velocity $\mathbf{U}_w$. A (linear) simple shear flow parallel to the wall is assumed in the vicinity of the wall, so that the undisturbed velocity reads:

$$\mathbf{u}_\infty(\mathbf{x}) = \mathbf{U}_w + \mathbf{\Omega}_\infty \times \mathbf{x} + \mathbf{E}_\infty \cdot \mathbf{x} \tag{3.7}$$

where the origin of the frame lies on the wall, and the usual relation between $\mathbf{\Omega}_\infty$ and $\mathbf{E}_\infty$ for a simple shear flow is assumed. The hydrodynamic stress moments on the particle read:

$$\mathcal{M}_p^{SG} = \begin{pmatrix} \mathbf{F}_p^{SG} \\ \mathbf{T}_p^{SG} \\ \mathbf{S}_p^{SG} \\ s_p \end{pmatrix} = -\mathcal{R}_w^{SG} \cdot \begin{pmatrix} \mathbf{U}_p - \mathbf{u}_\infty(\mathbf{x_p}) \\ \mathbf{\Omega}_p - \mathbf{\Omega}_\infty \\ -\mathbf{E}_\infty \end{pmatrix} = -\eta \begin{pmatrix} \mathbf{A}_w & \tilde{\mathbf{B}}_w & \tilde{\mathbf{G}}_w \\ \mathbf{B}_w & \mathbf{C}_w & \tilde{\mathbf{H}}_w \\ \mathbf{G}_w & \mathbf{H}_w & \mathbf{M}_w \\ \mathbf{P}_w & 0 & 0 \end{pmatrix} \cdot \begin{pmatrix} \mathbf{U}_p - \mathbf{u}_\infty(\mathbf{x_p}) \\ \mathbf{\Omega}_p - \mathbf{\Omega}_\infty \\ -\mathbf{E}_\infty \end{pmatrix} \tag{3.8}$$

Due to the symmetry of the simple shear flow, the matrix $\mathbf{Q}_w$ yields no force dipole trace so that it has been removed in Eq. (3.8). The standard sub-grid particle-wall correction matrix $\mathcal{R}_w^{SG}$ is defined in the same way as the two-particle one.

3.2 DETERMINATION OF THE SOLVER RESISTANCE MATRIX

In the case of two particles at a close distance, the whole set of resistance functions is deduced from the computation of 8 particular arrangements of the positions and velocities of the particles and ambient flows (shown and detailed in Appendix C). Each arrangement was tackled for 64 positions of the pair with respect to a mesh cell to avoid oscillations due to the spatial discretization and for 4 sizes of a cubic domain $(L/(a_1 = 1.0) = 20, 30, 40, 50)$. Then, the asymptotic values for an infinite domain size were estimated, to get rid of long-range hydrodynamic interactions with the bounding walls. This procedure was repeated for multiple reduced distances $\xi = 2\|\mathbf{x}_2 - \mathbf{x}_1\|/(a_1 + a_2) - 2$ of interest.

In Fig. 3.1, an example of the fit obtained for two resistance functions is shown. In the case of a particle close to a wall, the same procedure was followed, except that fewer arrangements – namely 5 – were requested to build the whole matrix as written in Eq. (3.8). In that case, each arrangement was tackled for 16 positions of the particle in the plane

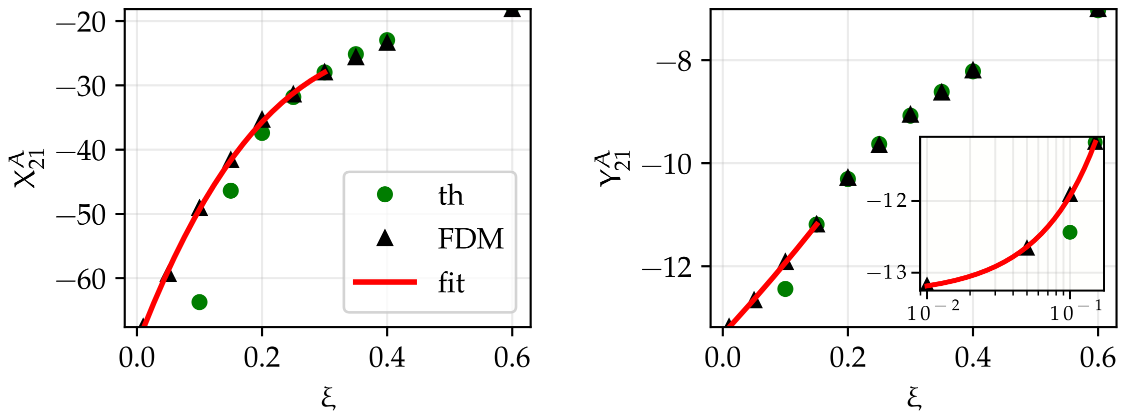

Figure 3.1
Measured FDM values, theoretical values, and fits of the resistance functions X_{21}^A and Y_{21}^A for a particle pair as a function of the reduced distance $\xi = 2\|\mathbf{x}_2 - \mathbf{x}_1\|/(a_1 + a_2) - 2$.

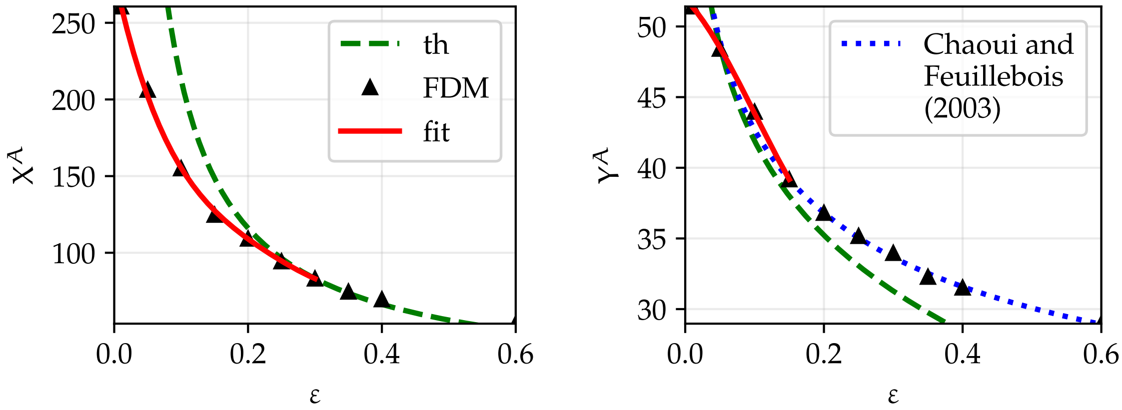

Figure 3.2
Measured FDM values, theoretical (lubrication approximation) values gathered by Yeo & Maxey (2010b), and fits of the resistance functions X^A and Y^A for a particle close to a wall as a function of the reduced distance $\varepsilon = d/a - 1$. In blue, the expansion proposed by Chaoui & Feuillebois (2003).

parallel to the wall, again for the same 4 domain sizes, and repeated for multiple reduced distances $\varepsilon = d/a - 1$ of interest (with d the distance between the particle center and the wall). In Fig. 3.2 we show as an example the measurement of X^A and Y^A, respectively.

In both figures, the values measured by the fluid flow solver (FDM) are compared to theoretical expressions and tabulated values (more details can be found in Appendix B). As we can observe in Fig. 3.1, the X resistance functions need to be corrected earlier (i.e., starting from a greater ξ) than the Y resistance functions: we choose to correct the X functions for $\xi \leqslant 0.3$ and the Y ones for $\xi \leqslant 0.15$. In Fig. 3.2 we study for Y^A the difference between the expressions gathered by Yeo & Maxey (2010b) and the expansions proposed by Chaoui & Feuillebois (2003). Using the latter (for Y^A, Y^B and Y^C) allows us to precisely determine the ε-range for which the sub-grid corrections are needed, i.e. starting from $\varepsilon < 0.3$ for the X terms and from $\varepsilon < 0.15$ for the Y terms.

3.3 TWO-PARTICLE FRAME-INVARIANT SUB-GRID CORRECTION MATRIX

The expression of the sub-grid correction as written in Eq. (3.2) is well suited to homogeneous linear flows obeying Eq. (3.1). However, it is not possible to easily implement it when the ambient flow is not prescribed but evolves in the course of the simulation. It seems mandatory to locally measure the ambient flow properties ($\mathbf{U}_0$, $\mathbf{\Omega}_\infty$ and $\mathbf{E}_\infty$), which raises some practical problems. As explained in detail in the following, this may be unnecessary. The purpose of the following section is to explain under which conditions the influence of the ambient flow $\mathbf{u}_\infty(\mathbf{x})$ may be ignored in the computation of the sub-grid corrections. In the next section, a fully frame-invariant correction matrix is built.

3.3.1 AMBIENT FLOW CONTRIBUTION

The expression of the two-particle stress moments in Eq. (3.5) may be rearranged to separate the contribution of the velocities of the particles and the contributions of the ambient flow:

$$-\mathcal{R}^{SG}_{2p}\cdot\begin{pmatrix}\mathbf{U}_1-\mathbf{u}_\infty(\mathbf{x}_1)\\ \mathbf{U}_2-\mathbf{u}_\infty(\mathbf{x}_2)\\ \mathbf{\Omega}_1-\mathbf{\Omega}_\infty\\ \mathbf{\Omega}_2-\mathbf{\Omega}_\infty\\ -\mathbf{E}_\infty\\ -\mathbf{E}_\infty\end{pmatrix} = -\mathcal{R}^{SG}_{2p}\cdot\begin{pmatrix}\mathbf{U}_1\\ \mathbf{U}_2\\ \mathbf{\Omega}_1\\ \mathbf{\Omega}_2\\ 0\\ 0\end{pmatrix} - \mathcal{R}^{SG}_{2p}\cdot\begin{pmatrix}-\mathbf{u}^{RBM}_\infty(\mathbf{x}_1)\\ -\mathbf{u}^{RBM}_\infty(\mathbf{x}_2)\\ -\mathbf{\Omega}_\infty\\ -\mathbf{\Omega}_\infty\\ 0\\ 0\end{pmatrix} - \mathcal{R}^{SG}_{2p}\cdot\begin{pmatrix}-\mathbf{E}_\infty\cdot\mathbf{x}_1\\ -\mathbf{E}_\infty\cdot\mathbf{x}_2\\ 0\\ 0\\ -\mathbf{E}_\infty\\ -\mathbf{E}_\infty\end{pmatrix} \tag{3.9}$$

where $\mathbf{u}^{RBM}_\infty(\mathbf{x}) = \mathbf{U}_0 + \mathbf{\Omega}_\infty\times\mathbf{x}$ denotes the rigid body motion (RBM) component of the ambient flow. The contributions of the ambient flow to the sub-grid correction are thus constituted by the second and third terms of the RHS of Eq. (3.9). The necessary condition for those terms to be omitted is that they would vanish, or that they would be far smaller than the first term. Fortunately, rapid analysis of those terms shows that they are expected to be small by construction. The second term in the RHS of Eq. (3.9) is the sub-grid correction for a particle pair that moves according to the RBM velocity $-\mathbf{u}^{RBM}_\infty(\mathbf{x})$ in a liquid at rest far away from the pair. In such a motion, no lubrication flow is expected to occur between the surfaces of the particles, so the flow from the solver should be close to the theoretical flow everywhere, and the stress moments should not need significant corrections. Regarding the third term in the RHS, the same trends are expected: it corresponds to corrections to the stress moments for two particles at rest in a liquid in pure straining motion. Again, no lubrication flow is expected, and weak sub-grid corrections may be needed.

In conclusion, it seems possible at first sight to only keep the first term of the RHS of Eq. (3.9) as the expression of the sub-grid corrections. We thus propose to omit the second and third terms and to write the sub-grid corrections for the stress moments as:

$$\mathcal{M}^{SG} = -\mathcal{R}^{SG} \cdot \begin{pmatrix} \mathbf{U}_1 \\ \mathbf{U}_2 \\ \mathbf{\Omega}_1 \\ \mathbf{\Omega}_2 \end{pmatrix} \tag{3.10}$$

where $\mathcal{R}^{SG}$ is identical to $\mathcal{R}^{SG}_{2p}$, except for the two last columns that were removed.

However, it turns out that the expression in Eq. (3.10) has more fundamental implications. We seek a general relation between stress moments and velocities, which would be valid as is in any reference frame, i.e. a frame-invariant relation. Since the stress moments do not depend on a particular reference frame, the second term of Eq. (3.10) should be frame-invariant. This is indeed the case of the general relation in Eq. (3.9), which involves the velocities of the particles in the reference frame attached to the liquid in rigid body motion (first and second terms of the RHS), together with the strain rate tensor $\mathbf{E}_\infty$ of the ambient flow. We recall here that the strain rate tensor of any flow is a frame-invariant quantity (Rivlin & Ericksen, 1955; Saramito, 2016). However, the relation in Eq. (3.10) may not be invariant to change of reference frame, which cannot be allowed, as a very simple and intuitive following example shows: considering a particle pair at rest in a liquid at rest, the flow solver yields a resting system, which is also the theoretical solution, and no sub-grid correction is needed for the particles at rest, in agreement with Eq. (3.10); considering the same system in the reference frame that translates with the velocity $\mathbf{U}_0$ with respect to the initial frame, the flow solver now yields the velocities $-\mathbf{U}_0$ for both particles, as well as for the liquid far away from the particles, and the stress moments vector from the solver vanishes again. The sub-grid stress moments vector $\mathcal{M}^{SG}$ is now:

$$\mathcal{M}^{SG} = -\mathcal{R}^{SG} \cdot \begin{pmatrix} -\mathbf{U}_0 \\ -\mathbf{U}_0 \\ 0 \\ 0 \end{pmatrix} \tag{3.11}$$

Obviously, the stress moments vector in Eq. (3.11) must vanish, which imposes constraints on the components of the matrix $\mathcal{R}^{SG}$. Should this not be the case, the sub-grid correction would introduce fake forces proportional to the frame velocity. The general condition for the relation in Eq. (3.10) to be frame-invariant can be easily expressed as follows. Assuming that the particles move with velocities $(\mathbf{U}_1, \mathbf{U}_2)$ and angular velocities $(\mathbf{\Omega}_1, \mathbf{\Omega}_2)$ with respect to a reference frame, any other frame may be characterized by a translational velocity $\mathbf{U}_0$ and an angular velocity $\mathbf{\Omega}_0$ such that any point $\mathbf{x}$ at rest in this second reference frame moves with respect to the initial frame with the velocity $\mathbf{u}_{ref}(\mathbf{x}) = \mathbf{U}_0 + \mathbf{\Omega}_0 \times \mathbf{x}$. The condition for the relation in Eq. (3.10) to be frame-invariant is that for any value of $\mathbf{U}_0$ and $\mathbf{\Omega}_0$:

$$-\mathfrak{R}^{SG} \cdot \begin{pmatrix} \mathbf{U}_1 \\ \mathbf{U}_2 \\ \mathbf{\Omega}_1 \\ \mathbf{\Omega}_2 \end{pmatrix} = -\mathfrak{R}^{SG} \cdot \begin{pmatrix} \mathbf{U}_1 - \mathbf{u}_{ref}(\mathbf{x}_1) \\ \mathbf{U}_2 - \mathbf{u}_{ref}(\mathbf{x}_2) \\ \mathbf{\Omega}_1 - \mathbf{\Omega}_0 \\ \mathbf{\Omega}_2 - \mathbf{\Omega}_0 \end{pmatrix} \tag{3.12}$$

and then, due to linearity:

$$-\mathfrak{R}^{SG} \cdot \begin{pmatrix} \mathbf{U}_0 + \mathbf{\Omega}_0 \times \mathbf{x}_1 \\ \mathbf{U}_0 + \mathbf{\Omega}_0 \times \mathbf{x}_2 \\ \mathbf{\Omega}_0 \\ \mathbf{\Omega}_0 \end{pmatrix} = 0 \tag{3.13}$$

This last relation is equivalent to the vanishing of the second term in Eq. (3.9). As a consequence, it should be constrained to vanish. In this respect, neglecting the third term in Eq. (3.9) is not of equal importance: it may induce a quantitatively imperfect computation of the sub-grid forces in straining flow, but it does not imply a violation of fundamental principles. On the contrary, neglecting the second term without caution may induce spurious frame-dependent forces, torques, etc., which would alter the dynamics of the particles.

Returning to Eq. (3.9), the ambient flow contribution to the sub-grid correction can be split into three independent contributions, each of which should ideally vanish, or at least be weak for any value of $\mathbf{U}_0'$, $\mathbf{\Omega}_\infty$, and $\mathbf{E}_\infty$.:

$$\mathfrak{R}^{SG}_{2p} \cdot \begin{pmatrix} \mathbf{U}_0' \\ \mathbf{U}_0' \\ 0 \\ 0 \\ 0 \\ 0 \end{pmatrix} + \mathfrak{R}^{SG}_{2p} \cdot \begin{pmatrix} -\mathbf{\Omega}_\infty \times \frac{r\mathbf{d}}{2} \\ \mathbf{\Omega}_\infty \times \frac{r\mathbf{d}}{2} \\ \mathbf{\Omega}_\infty \\ \mathbf{\Omega}_\infty \\ 0 \\ 0 \end{pmatrix} + \mathfrak{R}^{SG}_{2p} \cdot \begin{pmatrix} -\mathbf{E}_\infty \cdot \frac{r\mathbf{d}}{2} \\ \mathbf{E}_\infty \cdot \frac{r\mathbf{d}}{2} \\ 0 \\ 0 \\ \mathbf{E}_\infty \\ \mathbf{E}_\infty \end{pmatrix} = 0 \tag{3.14}$$

where $\mathbf{U}_0' = \mathbf{U}_0 + \mathbf{\Omega}_\infty \times \frac{\mathbf{x}_1 + \mathbf{x}_2}{2} + \mathbf{E}_\infty \cdot \frac{\mathbf{x}_1 + \mathbf{x}_2}{2}$, $r = \|\mathbf{x}_2 - \mathbf{x}_1\|$ and $r\mathbf{d} = \mathbf{x}_2 - \mathbf{x}_1$.

The various terms in Eq. (3.14) correspond to the sub-grid corrections for, respectively, a translation of the particle pair with velocity $-\mathbf{U}_0'$ in an otherwise resting liquid, a rigid body rotation of the pair with angular velocity $-\mathbf{\Omega}_\infty$, and a particle pair at rest in a straining flow with strain rate tensor $\mathbf{E}_\infty$. We note that the decomposition in Eq. (3.14) is not unique, since the particular point $(\mathbf{x}_1 + \mathbf{x}_2)/2$ is arbitrary. However, it allows easier algebra while, due to the linearity of the different relations (see Section 3.3.3), the various expressions that are

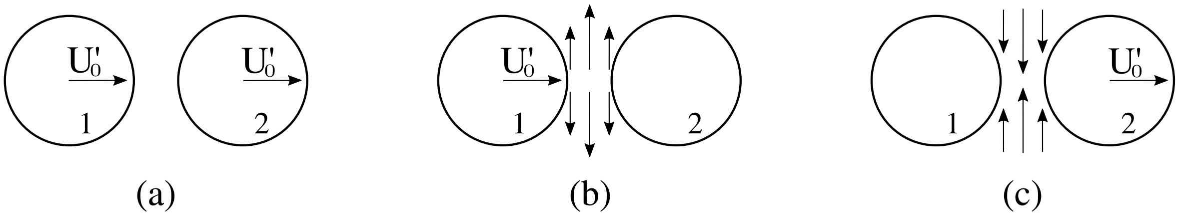

Figure 3.3
Sketch of a particle pair translating with velocity $\mathbf{U}_0'$. (a) Translation of the whole pair. Decomposition in (b) (respectively (c)) a translation of particle 1 (resp. 2) while particle 2 (resp. 1) is at rest.

deduced in the following do not depend on this particular point. Systematic cancellation of each term yields a set of linear equations with the matrix coefficients as unknowns. As an example of such relations, the sub-grid force exerted on particle (p_1) due to a translation along the centerline with velocity $\mathbf{U}_0'$ should vanish (Fig. 3.3a):

$$\mathbf{F}_1^{SG} = -\eta \left(X_{11}^{A,SG} + X_{12}^{A,SG} \right) \mathbf{U}_0' = 0 \tag{3.15}$$

where the scalar coefficients $X_{11}^{A,SG}$ and $X_{12}^{A,SG}$ only depend on the distance between the particles and their radii. Since the two-particle sub-grid resistance matrix is the difference between the theoretical and the FDM solver ones, Eq. (3.15) may be written as:

$$X_{11}^{A,FDM} + X_{12}^{A,FDM} = X_{11}^{A,th} + X_{12}^{A,th} \tag{3.16}$$

which means that the solver should properly account for the force due to the translation of the pair without the need for any correction.

Thus, the validity of Eq. (3.15) is checked by comparing the two sides of Eq. (3.16). In Fig. 3.4 [a], the LHS of Eq. (3.16) (FDM resistance coefficient) is displayed as a function of the reduced distance between particle surfaces ξ for a pair of particles of the same radius $a_1 = 1$, together with its theoretical counterpart. The agreement is very good, as also shown in Fig. 3.4 [b] where the relative difference between the two terms is displayed. It should be stressed here that any of the resistance coefficients, X_{11}^A or X_{12}^A, takes very different values in the low distance range, whether the FDM coefficient or the theoretical one is considered.

Indeed, in Fig. 3.4 [c], $X_{11}^{A,th}$ is shown to diverge as $\xi \to 0$. Since $X_{11}^{A,th}$ accounts for the force exerted on particle (p_1) as it moves while particle (p_2) is kept at rest, its high value reflects the lubrication flow occurring between the particles (Fig. 3.3 [b]). The corresponding FDM coefficient $X_{11}^{A,FDM}$ takes values very close to $X_{11}^{A,th}$ as soon as ξ exceeds a distance typically equal to the mesh size Δ, but does not diverge at contact. This was indeed expected since the solver cannot account for the lubrication flow between the particle surfaces. The same discrepancy is observed for the coefficient X_{12}^A (Fig. 3.4 [d]) due to a lubrication flow in the opposite direction to the former as only particle (p_2) moves (Fig. 3.3 [c]). Despite these large discrepancies, the sum of the coefficients $X_{11}^A + X_{12}^A$ from the FDM computations or the theory yields very close values. This agreement may be qualitatively understood considering that no lubrication flow develops between the surfaces of the particles as the particles move as a rigid pair (Fig. 3.3 [a]). For that reason, the sum of the theoretical resistance

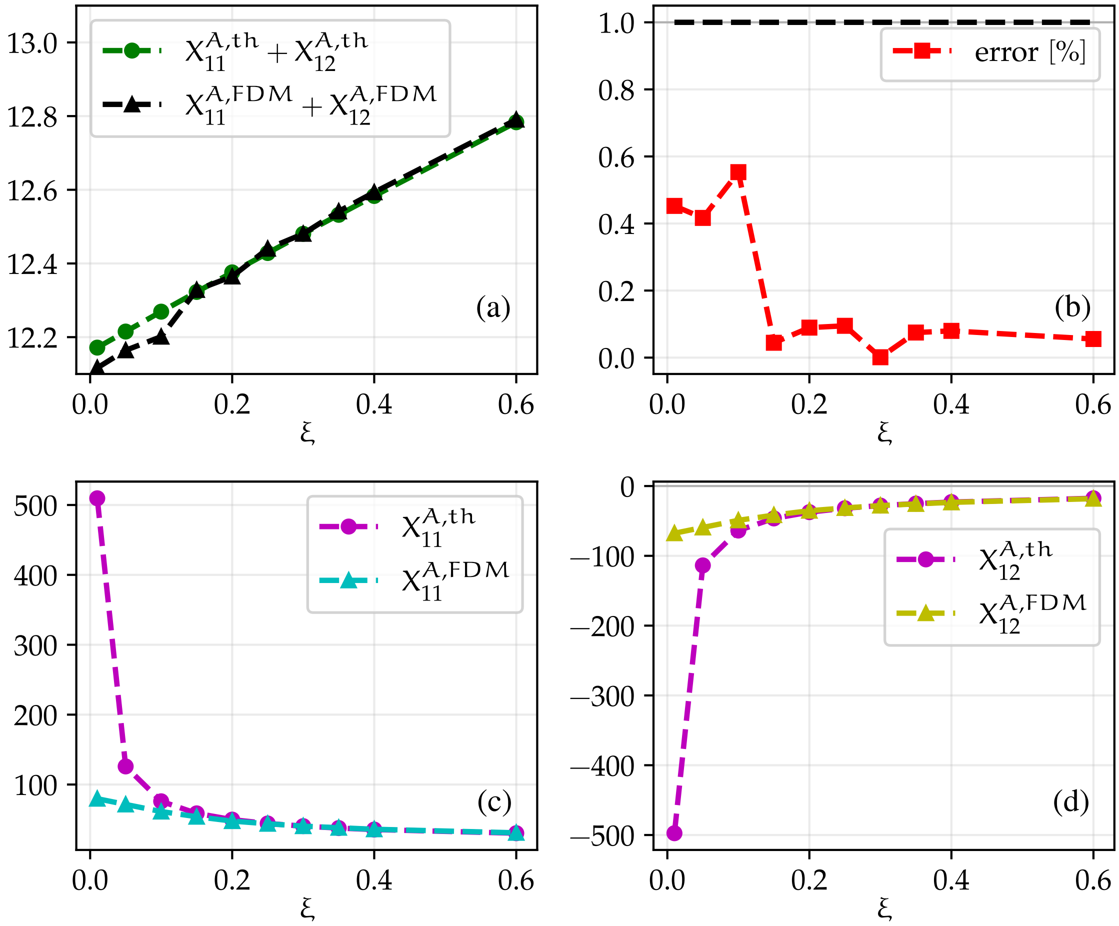

Figure 3.4
Comparison between the FDM and theoretical resistance coefficients $X_{11}^{A} + X_{12}^{A}$ for the force exerted on particle (p_1) when the particles pair moves rigidly along the center line, as a function of the distance between the surfaces ξ. (b) shows the relative difference between the two quantities in (a).

coefficients, which accounts for the viscous force on particle (p_1), does not diverge as $\xi \to 0$, but smoothly decreases (Fig. 3.4 [a]). In the same line, since the flow between particles is weak, most of the force exerted on particle (p_1) originates in the flow outside the gap, which is correctly computed by the FDM solver, and the sub-grid corrections are not needed. Nevertheless, considering that the theoretical values of X_{11}^{A} or X_{12}^{A} are very large compared to their FDM counterpart in the low range of ξ and that their sum is quite small compared to the individual FDM values, keeping also in mind that $X_{11}^{A,FDM}$ and $X_{12}^{A,FDM}$ have been computed separately, the agreement between $X_{11}^{A,FDM} + X_{12}^{A,FDM}$ and $X_{11}^{A,th} + X_{12}^{A,th}$ is remarkable and highlights the great quality of the method.

The symmetry of the FDM resistance matrix following the Lorentz reciprocal theorem has been checked in the same way. Each relation has been found to hold to within a few percent. For this reason, the third term of the RHS in Eq. (3.9) is simply removed. For the second terms to be removed and the sub-grid corrections to be written as in Eq. (3.10), the matrix $\mathcal{R}^{SG}$ must be modified in such a way that the relations quoted in Section 3.3.3 rigorously hold. This is explained in the following.

3.3.2 BUILDING A FRAME-INVARIANT SUB-GRID CORRECTION MATRIX

The idea of a frame-invariant resistance matrix is not new. Such a property has been indeed sought in earlier works from the literature.

Ball and Melrose (Ball & Melrose, 1997) performed molecular dynamic simulations of Brownian suspensions. They compute the total resistance matrix of hydrodynamic interactions as the superposition of two-particle resistance matrices that obey Eq. (3.10). To this purpose, the motion of the particles is computed in the co-rotational frame, i.e. the frame attached to the line that joins the centers of the particles. Doing this, they only consider the internal motion modes corresponding to lubrication flow, i.e. squeeze, shear, pump, and twist, and they pick the relevant matrix coefficients from the lubrication theory. It should be noted here that choosing a sub-grid correction matrix that obeys Eq. (3.14) is formally equivalent to correct only for the above-mentioned internal motion modes. Their model has been extensively used, and it has been implemented in the molecular dynamics toolbox LAMMPS (Plimpton, 1995; Ness & Sun, 2015). The computation of the hydrodynamic forces in Ball & Melrose (1997) does not involve any ambient flow. It neither explicitly accounts for the many-body long-range hydrodynamic interactions between particles.

In the frame of the Stokesian Dynamics method (Brady, 1988; Sierou & Brady, 2001), the long-range hydrodynamic interactions are accounted for using a multipole expansion, supplemented by lubrication corrections in the form of a correction matrix, in the same general way as in the method presented here. Cichocki et al. (1999) note that a correction matrix in the form of Eq. (3.10) may not only involve the relative motion of the particles inside a particle pair, which is responsible for the so-called lubrication interactions, but also the collective motion of the particles. To get rid of the latter, they build a modified correction matrix using a convenient projection. It should be noted here that their purpose is very similar to the one followed here since our objective is to modify the matrix $\mathcal{R}^{SG}$ so that a particle pair in rigid body motion, i.e. undergoing collective motion, may yield no sub-grid corrections. Then, only the deviation of the motion of the particles from a rigid body motion will induce sub-grid corrections. Finally, Cichocki et al. (1999) show that using a correction matrix where the collective motion is not projected out results in an erroneous computation of the three-particle contribution to the translational short-time self-diffusion in Brownian suspensions, leading to the divergence of the latter. The explanation that they provide is akin to the simple example that was given in Section 3.3.1: the translation of a close particle pair results in a spurious lubrication force, which induces a slow decaying stokeslet flow proportional to the inverse of the distance from the pair.

In the present study, the raw sub-grid matrix is modified differently compared to the method explained by Cichocki et al. (1999). It should first be recalled that the matrix $\mathcal{R}^{SG}$ in Eq. (3.10) is identical to the matrix $\mathcal{R}^{SG}_{2p}$ in Eq. (3.5), except for the two last columns that were suppressed. As a consequence, we are mainly interested in the functions defining the tensors $\mathbf{A}$, $\mathbf{B}$, $\mathbf{C}$, $\mathbf{G}$, $\mathbf{H}$ and $\mathbf{P}$, but $\tilde{\mathbf{G}}$ and $\tilde{\mathbf{H}}$ have to be tackled as well due to the symmetry relations resulting from the Lorentz's reciprocal theorem. The corresponding part of the matrix involves 52 resistance functions. There are 20 symmetry relations between these functions due to Lorentz's reciprocal theorem; now there are 26 linear relations involving the functions of interest imposed by the cancellation of each of the independent terms of Eq. (3.14), but they are not linearly independent from the previous ones. In conclusion, we expect only 10 independent resistance functions for the frame-invariant sub-grid correction matrix. We choose one function among each group of similar functions: X^A_{21}, Y^A_{21}, Y^B_{21}, X^C_{21}, Y^C_{11}, X^G_{11}, Y^G_{11}, Y^H_{21}, X^P_{21}, X^P_{12}. The remaining ones are expressed as a function of the 10 base functions. It should be noted here that the strong reduction in the number of independent functions is consistent with the approaches developed by Ball & Melrose (1997) and Cichocki et al. (1999): since such a frame-invariant correction matrix only accounts for the internal motion mode to the exclusion of collective (rigid body) motion, fewer functions are needed.

3.3.3 FINAL RELATIONS

CONSTRAINTS

The whole set of relations that follow from Eq. (3.9), which are required for the relation between the sub-grid forces and torques and the velocities of the particles to be fully frame-invariant, are developed in Appendix D. They yield a set of linear relations that the resistance functions must obey. Those relations are quoted below. The relations for the $(\cdot)_{11}$ and $(\cdot)_{12}$ terms are shown: the remaining ones are obtained by simply replacing $(\cdot)_{11}$ by $(\cdot)_{21}$ and $(\cdot)_{12}$ by $(\cdot)_{22}$. The superscript "SG" has been omitted for the sake of simplicity. It should be noted that all resistance functions are dimensioned quantities.

$$
\begin{array}{ll}
X^A_{11} + X^A_{12} = 0 & \frac{r}{2}\left(Y^A_{11} - Y^A_{12}\right) - \left(Y^{\tilde{B}}_{11} + Y^{\tilde{B}}_{12}\right) = 0 \\
Y^A_{11} + Y^A_{12} = 0 & \frac{r}{2}\left(Y^B_{11} - Y^B_{12}\right) + \left(Y^C_{11} + Y^C_{12}\right) = 0 \\
Y^B_{11} + Y^B_{12} = 0 & \frac{r}{2}\left(Y^G_{11} - Y^G_{12}\right) - \left(Y^H_{11} + Y^H_{12}\right) = 0 \\
X^C_{11} + X^C_{12} = 0 & \frac{r}{2}\left(-X^A_{11} + X^A_{12}\right) + \left(X^{\tilde{G}}_{11} + X^{\tilde{G}}_{12}\right) = 0 \\
X^G_{11} + X^G_{12} = 0 & \frac{r}{2}\left(-Y^B_{11} + Y^B_{12}\right) - 2\left(Y^{\tilde{H}}_{11} + Y^{\tilde{H}}_{12}\right) = 0 \\
Y^G_{11} + Y^G_{12} = 0 & \frac{r}{2}\left(-Y^A_{11} + Y^A_{12}\right) + 2\left(Y^{\tilde{G}}_{11} + Y^{\tilde{G}}_{12}\right) = 0 \\
X^P_{11} + X^P_{12} = 0 & \frac{r}{2}\left(-Y^G_{11} + Y^G_{12}\right) + \left(Y^M_{11} + Y^M_{12}\right) = 0 \\
\frac{1}{2}\left(Z^M_{11} + Z^M_{12}\right) = 0 & \frac{r}{2}\left(-X^G_{11} + X^G_{12}\right) + \frac{3}{2}\left(X^M_{11} + X^M_{12}\right) = 0 \\
 & \frac{r}{2}\left(-X^P_{11} + X^P_{12}\right) + \left(X^Q_{11} + X^Q_{12}\right) = 0
\end{array}
$$

EXPRESSIONS

Putting together the previous constraints and imposing the symmetry that originates from Lorentz's reciprocal theorem, we can get a list of relations between the different resistance functions. We need to choose only ten independent resistance functions: X^A_{21}, Y^A_{21}, Y^B_{21}, X^C_{21}, Y^C_{11}, X^G_{11}, Y^G_{11}, Y^H_{21}, X^P_{12}, X^P_{21}. The expressions of the remaining ones are (the superscript "SG" has been omitted for the sake of simplicity):

$$\begin{aligned} X^A_{11} &= -X^A_{21} \\ X^A_{12} &= X^A_{21} \\ X^A_{22} &= -X^A_{21} \end{aligned}$$

$$\begin{aligned} X^C_{11} &= -X^C_{21} \\ X^C_{12} &= X^C_{21} \\ X^C_{22} &= -X^C_{21} \end{aligned}$$

$$\begin{aligned} Y^B_{11} &= -Y^B_{21} + rY^A_{21} \\ Y^B_{12} &= Y^B_{21} - rY^A_{21} \\ Y^B_{22} &= -Y^B_{21} \end{aligned}$$

$$\begin{aligned} X^P_{11} &= -X^P_{12} \\ X^P_{22} &= -X^P_{21} \end{aligned}$$

$$\begin{aligned} X^G_{12} &= -X^G_{11} \\ X^G_{21} &= -X^G_{11} - rX^A_{21} \\ X^G_{22} &= X^G_{11} + rX^A_{21} \end{aligned}$$

$$\begin{aligned} Y^G_{12} &= -Y^G_{11} \\ Y^G_{21} &= -Y^G_{11} - \frac{1}{2}rY^A_{21} \\ Y^G_{22} &= Y^G_{11} + \frac{1}{2}rY^A_{21} \end{aligned}$$

$$\begin{aligned} Y^H_{11} &= -Y^H_{21} - \frac{1}{2}r^2Y^A_{21} + \frac{1}{2}rY^B_{21} \\ Y^H_{12} &= Y^H_{21} + \frac{1}{2}r^2Y^A_{21} + rY^G_{11} - \frac{1}{2}rY^B_{21} \\ Y^H_{22} &= -Y^H_{21} - \frac{1}{2}r^2Y^A_{21} - rY^G_{11} \end{aligned}$$

$$\begin{aligned} Y^A_{11} &= -Y^A_{21} \\ Y^A_{12} &= Y^A_{21} \\ Y^A_{22} &= -Y^A_{21} \end{aligned}$$

$$\begin{aligned} Y^C_{12} &= -Y^C_{11} + rY^B_{21} - r^2Y^A_{21} \\ Y^C_{21} &= -Y^C_{11} + rY^B_{21} - r^2Y^A_{21} \\ Y^C_{22} &= Y^C_{11} - 2rY^B_{21} + r^2Y^A_{21} \end{aligned}$$

$$\begin{aligned} Y^{\tilde{B}}_{11} &= Y^B_{21} - rY^A_{21} \\ Y^{\tilde{B}}_{12} &= -Y^B_{21} \\ Y^{\tilde{B}}_{21} &= -Y^B_{21} + rY^A_{21} \\ Y^{\tilde{B}}_{22} &= Y^B_{21} \end{aligned}$$

$$\begin{aligned} X^{\tilde{G}}_{11} &= X^G_{11} \\ X^{\tilde{G}}_{12} &= -X^G_{11} - rX^A_{21} \\ X^{\tilde{G}}_{21} &= -X^G_{11} \\ X^{\tilde{G}}_{22} &= X^G_{11} + rX^A_{21} \end{aligned}$$

$$\begin{aligned} Y^{\tilde{G}}_{11} &= Y^G_{11} \\ Y^{\tilde{G}}_{12} &= -Y^G_{11} - \frac{1}{2}rY^A_{21} \\ Y^{\tilde{G}}_{21} &= -Y^G_{11} \\ Y^{\tilde{G}}_{22} &= Y^G_{11} + \frac{1}{2}rY^A_{21} \end{aligned}$$

$$\begin{aligned} Y^{\tilde{H}}_{11} &= -Y^H_{21} - \frac{1}{2}r^2Y^A_{21} + \frac{1}{2}rY^B_{21} \\ Y^{\tilde{H}}_{12} &= Y^H_{21} \\ Y^{\tilde{H}}_{21} &= Y^H_{21} + \frac{1}{2}r^2Y^A_{21} + rY^G_{11} - \frac{1}{2}rY^B_{21} \\ Y^{\tilde{H}}_{22} &= -Y^H_{21} - \frac{1}{2}r^2Y^A_{21} - rY^G_{11} \end{aligned}$$

3.4 PARTICLE-WALL FRAME-INVARIANT SUB-GRID CORRECTION MATRIX

The sub-grid correction matrix as written in Eq. (3.8) is simplified in the same line as the two-particle matrix in Section 3.3, and stress moments are split into two contributions:

$$\begin{pmatrix} \mathbf{F}_p^{SG} \\ \mathbf{T}_p^{SG} \\ \mathbf{S}_p^{SG} \\ s_p^{SG} \end{pmatrix} = -\mathcal{R}_w^{SG} \cdot \begin{pmatrix} \mathbf{U}_p - \mathbf{U}_w \\ \mathbf{\Omega}_p \\ 0 \end{pmatrix} - \mathcal{R}_w^{SG} \cdot \begin{pmatrix} -\mathbf{\Omega}_\infty \times \mathbf{x}_p - \mathbf{E}_\infty \cdot \mathbf{x}_p \\ -\mathbf{\Omega}_\infty \\ -\mathbf{E}_\infty \end{pmatrix} \tag{3.17}$$

The first term of the RHS is the stress moments vector on the moving particle as the liquid far from the wall moves at the same velocity $\mathbf{U}_w$ as the wall. Concerning the second term, we recall here that $\mathbf{\Omega}_\infty$ and $\mathbf{E}_\infty$ are not independent: they define a simple shear flow parallel to the wall. The whole term stands for the stress moment on a particle at rest when the wall is also at rest and the liquid far from it experiences a simple shear flow. The latter contribution does not involve any lubrication flow so that the corresponding resistance functions do not diverge as the distance from the wall $\varepsilon = d/a - 1$ goes to zero. It is thus expected to be well accounted for by the FDM without the need for specific sub-grid corrections.

We check that the ambient flow contribution to the sub-grid corrections can be neglected. To this purpose, a particle is placed at rest in a simple shear flow close to a fixed wall (same ambient flow as in Fig. 4.3), and the force and torque friction factors $\hat{F}^{\dot{\gamma}}$ and the $\hat{T}^{\dot{\gamma}}$, as defined below, are computed without any sub-grid correction.

$$\begin{aligned} \hat{F}^{\dot{\gamma}} &= \frac{F_x}{6\pi\eta a^2(1+\varepsilon)\dot{\gamma}} = \frac{(1+\varepsilon)aY^A - (1/2)\,Y^{\tilde{B}} - Y^{\tilde{G}}}{6\pi a^2(1+\varepsilon)} \\ \hat{T}^{\dot{\gamma}} &= -\frac{T_z}{4\pi\eta a^3\dot{\gamma}} = \frac{(1+\varepsilon)aY^B + (1/2)\,Y^C + Y^{\tilde{H}}}{4\pi a^3} \end{aligned} \tag{3.18}$$

The computed values are compared to the data from Chaoui & Feuillebois (2003), who performed precise computations of the quantities of interest, in Fig. 3.5. A very good agreement is observed, although weak oscillations of the quantities with the position due to the finite mesh size may be noted (we recall that in this case, we averaged over "only" 16 positions inside a mesh-cell-sized plane parallel to the wall). This explicitly shows that no sub-grid correction is requested for the ambient flow contribution. In addition, the symmetry of the FDM particle-wall matrix has been checked, meaning that $Y^{B,SG} = -Y^{\tilde{B},SG}$, $Y^{G,SG} = Y^{\tilde{G},SG}$ and $Y^{H,SG} = Y^{\tilde{H},SG}$. Finally, the following expressions are deduced:

$$\begin{aligned} Y^{G,SG} &= \quad (1+\varepsilon)aY^{A,SG} + (1/2)\,Y^{B,SG} \\ Y^{H,SG} &= -(1+\varepsilon)aY^{B,SG} - (1/2)\,Y^{C,SG} \end{aligned} \tag{3.19}$$

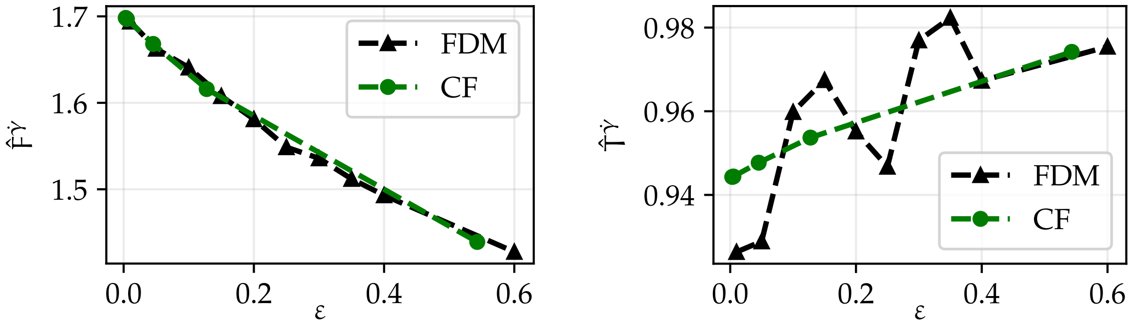

Figure 3.5
Force and torque friction factors $\hat{F}^{\dot\gamma}$ and $\hat{T}^{\dot\gamma}$ for a particle held fixed near a wall: (▲) measured FDM values, (●) Chaoui & Feuillebois (2003).

which are the counterpart for the particle-wall corrections of the expressions quoted in Section 3.3.3 for two particles: $Y^{G,SG}$ and $Y^{H,SG}$ may be directly computed from $Y^{A,SG}$, $Y^{B,SG}$, $Y^{C,SG}$. This presents the particular advantage that the latter quantities may be computed with a better precision due to the high quality of the theoretical expressions proposed by Chaoui & Feuillebois (2003) for Y^A, Y^B and Y^C (Appendix B.2). The stresslet was also computed, and it is related to the resistance functions through:

$$\hat{S}^{\dot\gamma} = \frac{S_{xy}}{(10/3)\,\pi a^3 \eta \dot\gamma} = \frac{-(1+\varepsilon)aY^G + (1/2)\,Y^H + (1/2)\,Y^M}{(10/3)\,\pi a^3} \qquad \hat{s}^{\dot\gamma} = 0 \tag{3.20}$$

The lubrication approximation of the resistance functions (presented in Appendix B.2) confirms that no divergence takes place for the stresslet. In addition, the FDM solver yields a very low value for the trace $\hat{s}^{\dot\gamma,FDM}$ in agreement with Eq. (3.20), and the value of the stresslet for the smallest distance probed ($\varepsilon = 10^{-2}$) is close to the asymptotic limit from the lubrication approximation ($\lim_{\varepsilon\to 0}\hat{S}^{\dot\gamma} = 0.5325$). However, a more detailed comparison is difficult, since the lubrication approximation for $\hat{S}^{\dot\gamma}$ cannot be used as soon as $\varepsilon \geqslant 10^{-2}$. Finally, the sub-grid stress moments vector reduces to the first term of the RHS of Eq. (3.17):

$$\begin{pmatrix} \mathbf{F}_p^{SG} \\ \mathbf{T}_p^{SG} \\ \mathbf{S}_p^{SG} \\ s_p^{SG} \end{pmatrix} = -\eta \begin{pmatrix} \mathbf{A}_w^{SG} & \tilde{\mathbf{B}}_w^{SG} \\ \mathbf{B}_w^{SG} & \mathbf{C}_w^{SG} \\ \mathbf{G}_w^{SG} & \mathbf{H}_w^{SG} \\ \mathbf{P}_w^{SG} & 0 \end{pmatrix} \cdot \begin{pmatrix} \mathbf{U}_p - \mathbf{U}_w \\ \mathbf{\Omega}_p \end{pmatrix} \tag{3.21}$$

Eq. (3.21) does not depend on a specific reference frame, since it precisely involves the velocity and angular velocity of the particle in the reference frame attached to the translating wall. As a consequence, it may be used without further caution. As a conclusion, the sub-grid resistance functions needed are $X^{A,SG}$, $Y^{A,SG}$, $Y^{B,SG}$, $X^{C,SG}$, $Y^{C,SG}$, $X^{G,SG}$, $X^{P,SG}$, while $Y^{G,SG}$ and $Y^{H,SG}$ are computed using Eq. (3.19) and $Y^{M,SG}$ is not needed. As we can notice, we finally save only three resistance functions.

4

VALIDATIONS

In this chapter, multiple validations of the numerical method and the new formulation of the frame-invariant sub-grid corrections are presented. We start by checking the numerical methods against the computation of flows involving a few particles. The particles may be either close or far from bounding walls, and when there are several of them, they may be close or far from each other. Both the cases of a simple shear flow and a pressure-driven flow are investigated. The computed quantities are compared to either analytical, semi-analytical, or very accurate numerical computations from the literature. In the second part of the chapter, the case of particulate suspensions in a simple shear flow is studied and the computed material functions are compared to earlier computations from the literature. In all considered flows, the densities of the liquid and the particles are equal.

4.1 UP TO THREE SPHERES IN A STOKES FLOW

4.1.1 STOKES FLOW THROUGH A PERIODIC ARRAY OF SPHERES

We consider here the slow flow of a Newtonian liquid through a simple cubic periodic array of spheres, and we focus on the drag force exerted on the array. This problem has been solved by Hasimoto (1959) using the Fourier series and by Zick & Homsy (1982) using a collocation method. The direction of the flow is parallel to one of the lattice basis vectors and, in the cited papers, the spheres are kept stationary. In this geometry, the slip velocity is defined as the mean velocity over a unit cell:

$$\mathbf{U}_s = \frac{1}{V_0}\int_{\mathcal{D}_{\mathtt{fluid}}} \mathbf{u}\,d\mathcal{V} = \frac{1}{V_0}\int_{\mathcal{D}} \mathbf{u}\,d\mathcal{V} \tag{4.1}$$

where V_0 is the volume of the unit cell $\mathcal{D}$. The drag force exerted on each sphere of the array is given by:

$$\mathbf{F} = 6\pi\eta a K \mathbf{U}_s \tag{4.2}$$

where K is the drag coefficient. Hasimoto (1959) derives the following expression for K for a simple cubic lattice:

$$K = \frac{1}{1 - 1.7601\sqrt[3]{\phi} + \phi - 1.5593\phi^2 + \dots} \tag{4.3}$$

where ϕ is the solid volume fraction of the array:

$$\phi = \frac{4\pi a^3}{3V_0} \tag{4.4}$$

The numerical computations by Zick & Homsy (1982) showed that Eq. (4.3) is valid up to volume fraction values of approximately 0.06. In the present work, we consider volume fraction lower than 0.0082, i.e. inside the validity range of Eq. (4.3).

In Fig. 4.1 we show the numerical setup that allows measurement of the drag coefficient K, i.e. a single sphere in a cubic domain of side length L with periodic boundary conditions for the velocity $\mathbf{u}$ and the pressure p on all boundaries. A uniform pressure gradient in the x-direction is added to the periodic pressure to induce fluid flow. To stick to the usual algorithm, the particle velocity $\mathbf{U}$ is left as a free parameter, but an external force is exerted on the particle to counterbalance the hydrodynamic force (Eq. (2.42)). This force is deduced from the fluid momentum balance Eq. (2.1):

$$0 = \boldsymbol{\nabla}\cdot\boldsymbol{\sigma} - \boldsymbol{\nabla}P_0 + \rho_f\boldsymbol{\lambda} \tag{4.5}$$

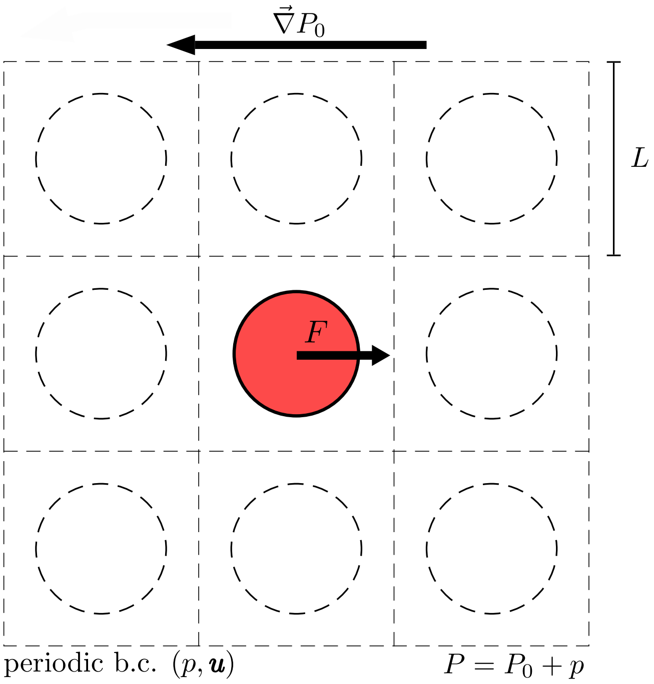

Figure 4.1
Stokes flow through a periodic array of particles. **F** denotes the hydrodynamic drag force exerted on the particle.

where the stress is split into the periodic component $\boldsymbol{\sigma}$ and the uniform pressure tensor $-P_0\boldsymbol{\delta}$. Eq. (4.5) is integrated over the simulation domain and, since the periodic component does not contribute to the integral, the total hydrodynamic force exerted on the particle reads:

$$\mathbf{F} = -\rho_f \int_{\mathcal{D}_p} \boldsymbol{\lambda}(\mathbf{x})\, d\mathcal{V} = -V_0 \boldsymbol{\nabla} P_0 \tag{4.6}$$

Finally, the slip velocity $\mathbf{U}_s$ is computed:

$$\mathbf{U}_s = \frac{1}{V_0} \int_{\mathcal{D}} \mathbf{u}(\mathbf{x})\, d\mathcal{V} - \mathbf{U} \tag{4.7}$$

The drag coefficient K follows from Eq. (4.2), averaging over 64 positions inside a single mesh cell to get rid of the oscillations due to the mesh. As previously explained in Section 2.5.4, this simulation allows to tune the parameters b and c involved in the indicator functions $\mathcal{I}_u(\mathbf{x})$ and $\mathcal{I}_\lambda(\mathbf{x})$ (Eqs. (2.51) and (2.52)).

The computed values of K are shown for the best values $(b, c) = (5, 0.3)$ in Fig. 4.2 and Table 4.1 for different values of the ratio L/a, or equivalently for different values of the solid volume fraction ϕ, in very good agreement with the theoretical predictions of Hasimoto (1959) (Eq. (4.3)). It should be noted here that the long-range hydrodynamic interactions between the particles in the lattice are always important or at least significant, i.e. $K \neq 1$, including the case of the largest unit cell considered ($L/a = 50$), and that they are properly accounted for by the FDM.

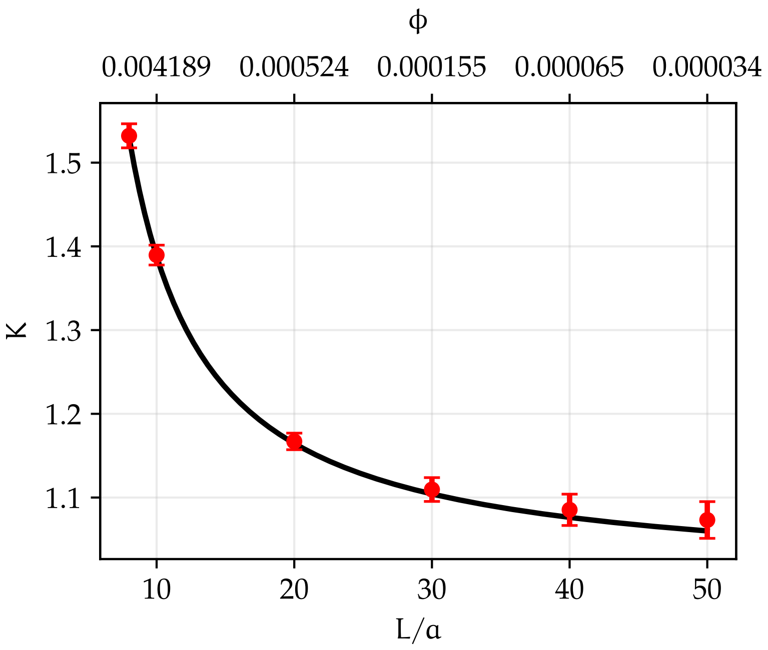

Figure 4.2
Drag coefficient K as a function of the reduced size of the cubic cell, or equivalently as a function of the solid volume fraction ϕ: red dots: simulation results; plain line: Hasimoto (1959) predictions.

Table 4.1
Comparison between our simulations and the values predicted by Hasimoto (1959).

L/a	ϕ	K_H	K	σ_K	$\lvert K - K_H \rvert / K_H$ [%]
8	0.00818	1.53041	1.532059	0.014381	0.11
10	0.00419	1.38805	1.389611	0.011877	0.11
20	0.000524	1.16461	1.167027	0.009899	0.21
30	0.000155	1.10427	1.109563	0.014221	0.48
40	0.0000654	1.07627	1.085323	0.018710	0.84
50	0.0000335	1.06012	1.073184	0.021934	1.23

4.1.2 A FREE SPHERE IN THE PRESENCE OF WALLS

In the present section, the FDM is tested against various shear flows past a single free sphere in the presence of solid walls. The first two examples address the case of a simple shear flow, bounded by either one (in theory) or two planes. It is shown that such flows are conveniently tackled, whether the particle is close to the wall and sub-grid corrections are needed, or not. In the latter two-plane configuration, the flow may be strongly confined leading to strong hydrodynamic interactions with both walls, and it is still suitably computed. Finally, the case of a single sphere in a confined nonlinear (Poiseuille) flow is addressed.

A SPHERE IN A SIMPLE SHEAR FLOW CLOSE TO A WALL

A free single particle with radius a is suspended in a simple shear flow close to a wall with $\varepsilon = d/a - 1$, where d is the distance between the particle center and the wall (Fig. 4.3). The simulation domain is a square hexahedron with dimension $(L_x/a_1, L_y/a_1, L_z/a_1) = (50, 50, 50)$. On the top and bottom boundaries (respectively $y = L_y$ and $y = 0$), the velocity is prescribed (respectively $\mathbf{u} = \dot{\gamma} L_y \mathbf{e}_x$ and $\mathbf{u} = 0$). The pressure and velocity fields on the other boundaries ($x = \pm L_x/2$, $z = \pm L_z/2$) obey cyclic boundary conditions.

The quantities of interest, namely the particle velocity, angular velocity, and stresslet, are computed for different values of the distance to the lower wall d, and both particle radius values a_1 and a_2. For each value of the distance to the wall and each particle radius, the quantities of interest are averaged over 16 different positions of the particle center evenly distributed in a single mesh cell. The standard deviation is computed to evaluate the accuracy of the computation and is shown in the following figures as error bars.

Since the size of the simulation box is much larger than the particle radius, the simulation data may be compared to the case of a free particle close to a single wall in an otherwise unbounded liquid. Chaoui & Feuillebois (2003) have performed highly accurate computations of the velocity and angular velocity of the particles in that case. They provide also a fitting polynomial expansion in $\log(\varepsilon)$ for both quantities:

$$U_x = \left[\sum_j u_j \, (\log \varepsilon)^j \right]^{-1} \qquad \Omega_z = \left[\sum_j \omega_j \, (\log \varepsilon)^j \right]^{-1} \tag{4.8}$$

where the coefficients u_j and ω_j are given in their paper (Chaoui & Feuillebois, 2003). They show for instance that the expansion gives a precision better than 10^{-11} for the velocity for $\varepsilon \leqslant 0.4$. The data from the present simulations are compared to the values from their expansion in Fig. 4.4. The agreement is very good, in particular for values of ε lower than 0.15 for which the sub-grid corrections (here, the relevant functions are Y^A, Y^B, Y^C) are

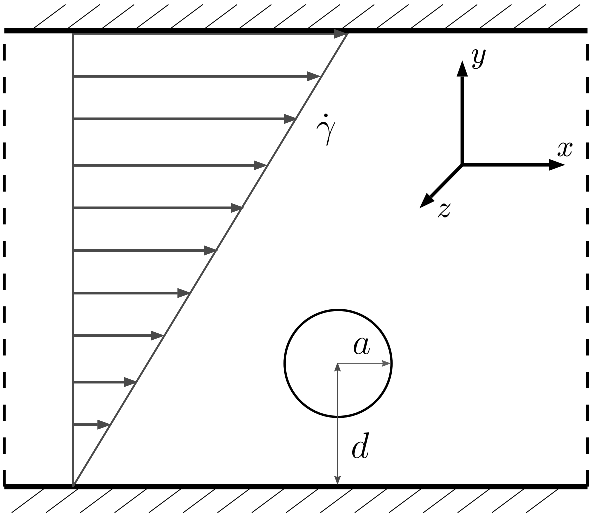

Figure 4.3
Free sphere in simple shear flow close to a wall.

activated. It should be recalled here that, according to the lubrication approximation, both the velocity and the angular velocity of the sphere slowly approach 0 as the reduced distance ε goes to 0 (Chaoui & Feuillebois, 2003).

Sangani et al. (2011) have performed computations of the stresslet in the same flow conditions. They use a semi-analytical method based on Lamb's multipoles. They also show that their data for the normalized stresslet $\hat{S}^{\dot{\gamma}} = S_{xy} / \left[(10/3)\,\pi\eta a^3 \dot{\gamma}\right]$ are well approximated by the expressions given below (with $Y = 1 + \varepsilon$):

$$\hat{S}^{\dot{\gamma}} = \begin{cases} \left[1 - \dfrac{15}{16Y^3} + \dfrac{1}{Y^5} - \dfrac{0.65}{Y^7}\right]^{-1} & \text{for } 0 < 1/Y \leqslant 0.85 \\ \dfrac{0.847 \ln \varepsilon^{-1} - 0.41 + 1.44\varepsilon \ln \varepsilon^{-1} - 0.3\varepsilon}{0.2 \ln \varepsilon^{-1} + 0.6376} & \text{for } 0.85 < 1/Y \leqslant 1 \end{cases} \tag{4.9}$$

The data from the present simulations are displayed in Fig. 4.4. Again, a very good agreement is found between the simulation data and the fitting function Eq. (4.9) over the

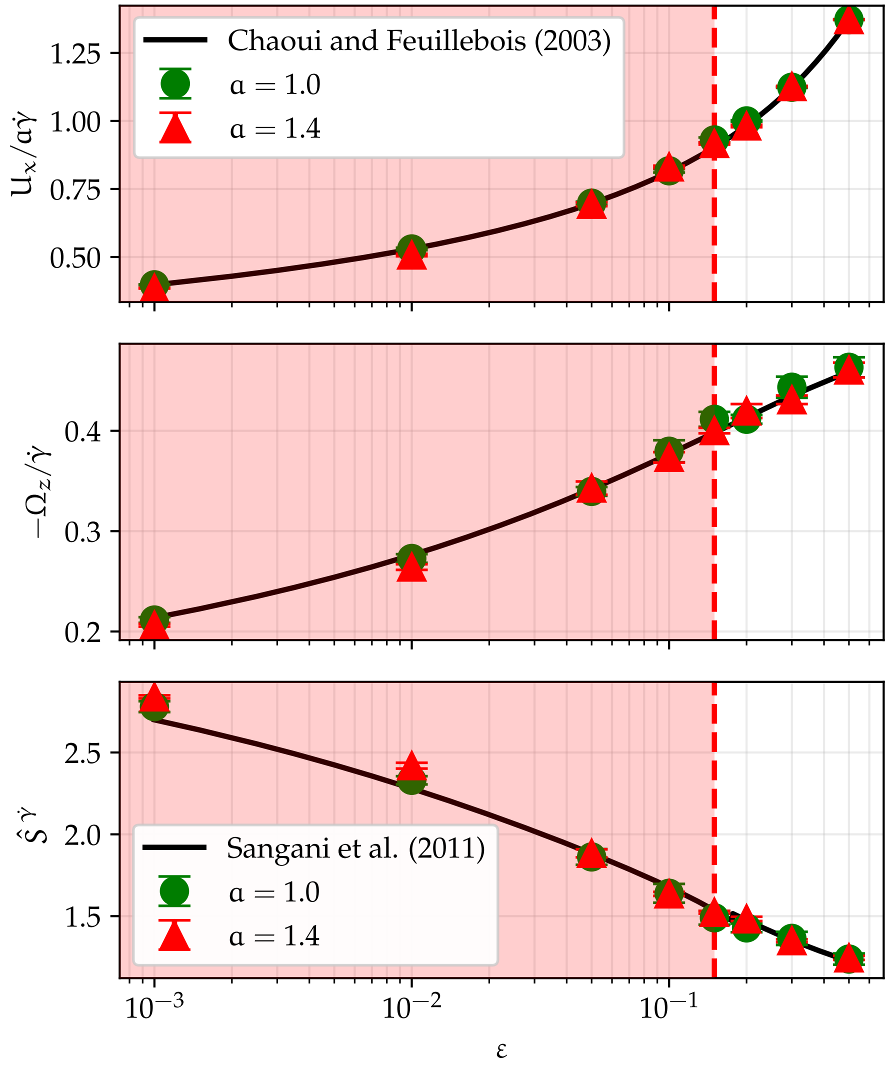

Figure 4.4
Normalized translational (top) and rotational (center) velocities and stresslet (bottom) for a free sphere in a simple shear flow close to a wall as a function of the distance ε from the wall. Red region: sub-grid corrections needed.

whole range of the distance to the wall, including the low distance range where the sub-grid corrections (here, the relevant resistance functions are Y^A, Y^B, Y^C, Y^G, Y^H) are needed.

In conclusion, the interaction between a sphere and a single wall in a simple shear flow is conveniently tackled by the fictitious domain method supplemented by the frame invariant sub-grid corrections. Since the underlying shear flow is not explicitly taken into account in the computation of the sub-grid corrections, this confirms that the FDM solver without sub-grid correction can capture the specific contribution of the ambient shear flow, as explained in Section 3.4. Then, this good agreement was indeed expected, since the particle-wall sub-grid corrections have been built so that this particular flow would be conveniently tackled. In the following sections, more complicated flows are addressed to further check the validity of the method.

A SPHERE IN A SIMPLE SHEAR FLOW AT THE CENTER OF A CHANNEL

A free sphere is placed at the center of a channel. The upper and lower walls move with equal and opposite velocities, inducing a simple shear flow (Fig. 4.5). On the other boundaries, periodic conditions are applied for the pressure and velocity fields. The flow is computed, together with the particle angular velocity Ω_z and the normalized stresslet $\hat{S}^{\dot{\gamma}}$ for different values of the reduced distance between the walls H/a. The translational velocity of the sphere is zero due to the symmetry of the flow. The dimensions of the bounding walls have been chosen large enough to mimic infinite planes $(L_x \times L_y) = (60a \times 40a)$.

Again, for each value of H, both particle radii $a_1 = 1.0$ and $a_2 = 1.4$ are considered and the quantities are averaged over 16 different positions of the particle center evenly distributed within a single mesh cell.

This case may appear a bit different from that addressed in the previous section, due to the significant hydrodynamic interactions between the walls. More precisely, in the more

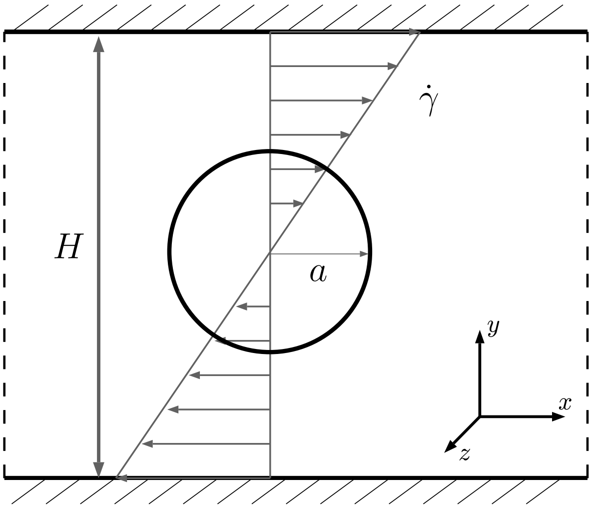

Figure 4.5
Free sphere in a simple shear flow at the center of a channel.

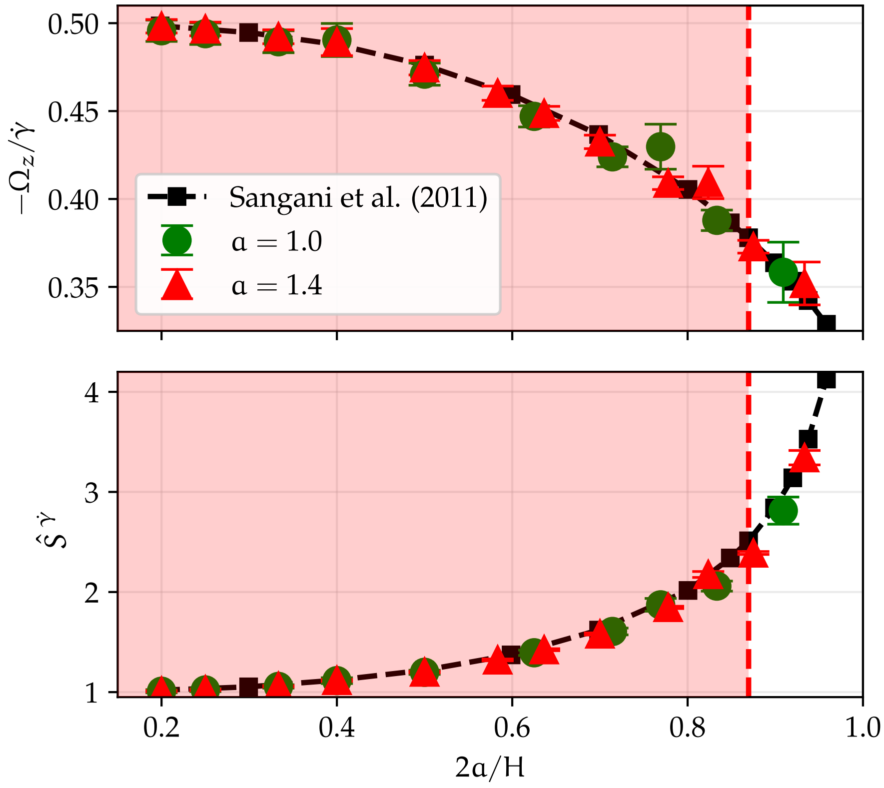

Figure 4.6
Normalized rotational velocity (top) and stresslet (bottom) for a free sphere in a simple shear flow at the center of the channel as a function of the reduced distance between the walls $2a/H$. Red region: sub-grid corrections needed. The lines are a guide to the eye.

confined geometry where $H \sim 2a$, besides the small scale flow between the sphere surface and the plane that makes the sub-grid corrections necessary, vortices develop in front of the sphere and behind it, with a typical dimension of the channel width, or equivalently of the sphere radius (Sangani et al., 2011). The computed angular velocity and normalized stresslet are displayed in Fig. 4.6 together with the computational data obtained by Sangani et al. (2011). The agreement is again satisfactory, still with small oscillations of the angular velocity (at most 3%). This shows that the present method can account for all components of the flow despite its complexity.

A FREE SPHERE IN A CHANNEL WITH A POISEUILLE FLOW

We turn now to the flow induced by a free-moving sphere in an ambient Poiseuille flow. The purpose of this section is to check the validity of the method for a single sphere in a nonlinear flow, including the sphere-wall sub-grid correction. The plane Poiseuille flow is bounded by two parallel walls separated by a distance H (see Fig. 4.7), and the unperturbed velocity reads:

$$\mathbf{u}_0(\mathbf{x}) = U_c \left(1 - \left(\frac{2y}{H}\right)^2\right) \mathbf{e}_x \tag{4.10}$$

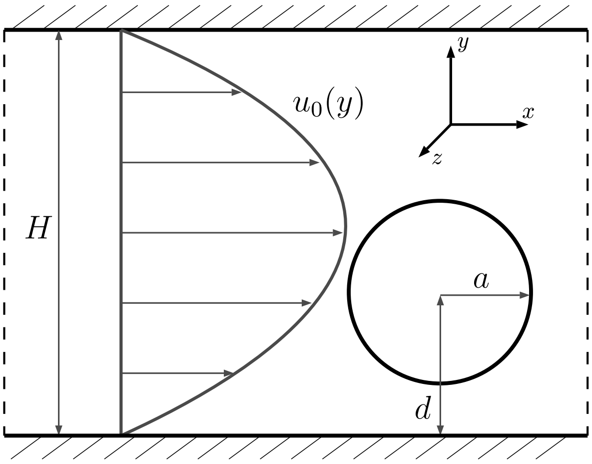

Figure 4.7
A free sphere in a plane Poiseuille.

A homogeneous pressure gradient is applied in the whole simulation domain:

$$\boldsymbol{\nabla} P_0 = -8\eta \frac{U_c}{H^2} \mathbf{e}_x \tag{4.11}$$

The particle translational U_x and rotational Ω_z velocities, as well as the stresslet S_{xy}, are computed for different values of the channel height H and of the distance between the particle center and the bottom wall d/a. Again, the computed quantities are averaged over 16 different positions inside the plane section of a single mesh cell. Two different values of the radius are considered for the sphere, $a = a_1 = 1.0$ and $a = a_2 = 1.4$. The channel height H is sampled in the range $[2.86a;\ 20a]$ and the dimensions of the bounding walls are chosen as $(L_x \times L_z) = (60a_1 \times 40a_1)$.

Using a boundary-integral method, Staben et al. (2003) computed the translational and angular velocities of the sphere in a similar flow geometry, with infinite planes though. The present computations are compared to their data in Fig. 4.8. The agreement is very good, whether the sphere is close to the wall or not, and for all values of $2a/H$, including the most confined case $2a/H = 0.7$.

The latter case is probably the most important for our purpose due to the strongly nonlinear variation of the unperturbed flow at the scale of the sphere: the shear-rate variation over the sphere diameter $16aU_c/H^2$ amounts to $8a/H \approx 1.6$ times the mean shear-rate of the flow $2U_c/H$, making difficult the definition of a single value for the shear-rate as seen by the particle. For that reason, the formulation of the particle-wall sub-grid corrections in Eq. (3.21) is better suited to the present flow geometry than the general expression in Eq. (3.8), and, as shown in Fig. 4.8, its accuracy is very satisfactory.

Ghalya et al. (2020) computed the stresslet for the ratio of the diameter to the channel height $2a/H = 0.4$ using a bipolar coordinates method (infinite planes). Their results for the normalised stresslet $S^* = S_{xy}/\left(4U_c\eta a^3/H\right)$ are displayed in Fig. 4.8, together with the values from the present method. Both sets of values are in close agreement, including the smallest value of the distance to the wall $d/a = 1.1$, which requires sub-grid corrections.

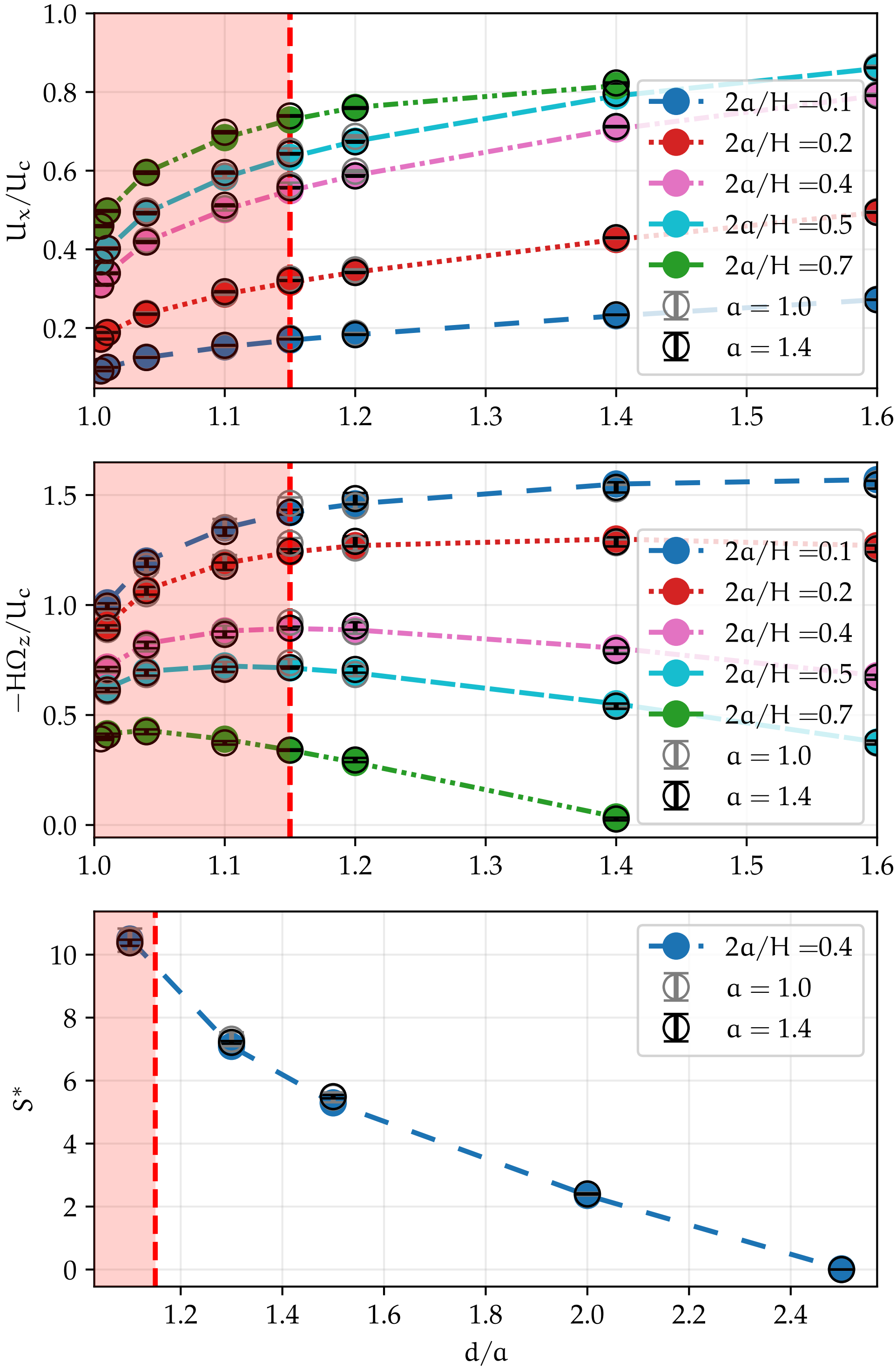

Figure 4.8
Normalized translational and rotational velocities and stresslet for a free sphere in a plane Poiseuille flow for different channel heights H as a function of the distance from the bottom wall d/a. (●): Staben et al. (2003) (top and center) and Ghalya et al. (2020) (bottom), the lines are a guide to the eye. (◯): present computations. Red region: sub-grid corrections needed.

4.1.3 A PARTICLE PAIR IN A SIMPLE SHEAR FLOW

The emblematic case of two particles in a simple shear flow is treated here. The flow is the same as in Section 4.1.2, with $L_x = L_y = L_z = 40a_1$. The particles are placed in the same shear plane $z = 0$, at initial positions $x/a_1 = \pm 3$, $y = \mp r_y^0/2$, where r_y^0 is the impact parameter, and the relative trajectory is computed ($r_x = x_1 - x_2$, $r_y = y_1 - y_2$). We let vary the radii ratio a_2/a_1 and the impact parameter r_y^0. Two different cases are considered: either the particles move only due to hydrodynamic interactions, or an additional force is applied to mimic contact between particles as they are close enough (Section 2.6).

In the former case, the relative trajectory is expected to display fore-aft symmetry (Da Cunha & Hinch, 1996) due to the linearity of Stokes equations combined with the symmetry of the ambient flow. In addition, depending on the impact parameter, the trajectories may either be open ("large" impact parameter) or closed and periodic ("small" impact parameter). Zarraga & Leighton (2001) showed that for two particles with the same radius $a_2 = a_1$, the smallest distance between the surfaces for an open trajectory is very small, i.e. approximately $4 \cdot 10^{-5} a_1$, so that a quite short time step is required to obtain sufficient accuracy. The time step is $\dot{\gamma}_0 \Delta t = 10^{-4}$ in the following. In Fig. 4.9 (top), the trajectories for $a_2/a_1 = 1$ and different impact factors are showed. They display the expected fore-aft symmetry, suggesting

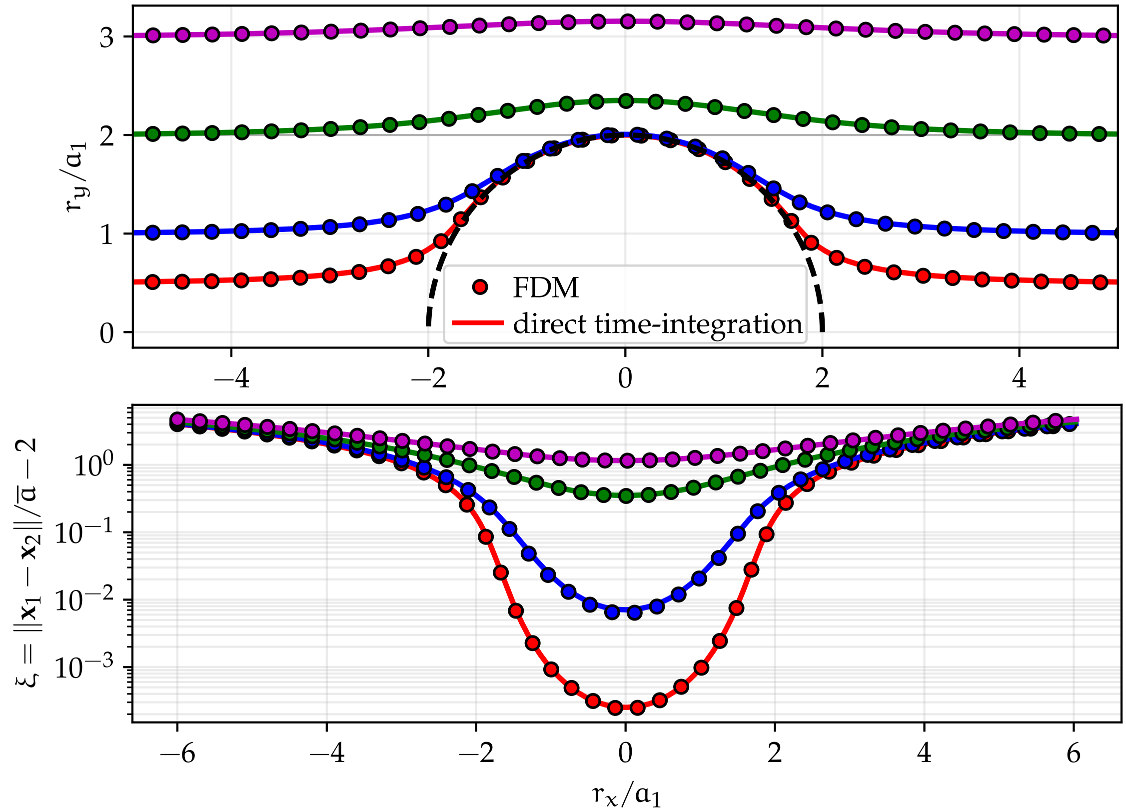

Figure 4.9
(top) Relative trajectories and (bottom) normalized distance between the particles surfaces of a particle pair in a simple shear flow without contact ($\overline{a} = (a_1 + a_2)/2$, $h_r = 0$, $a_2/a_1 = 1$), for different values of the impact factors r_y^0.

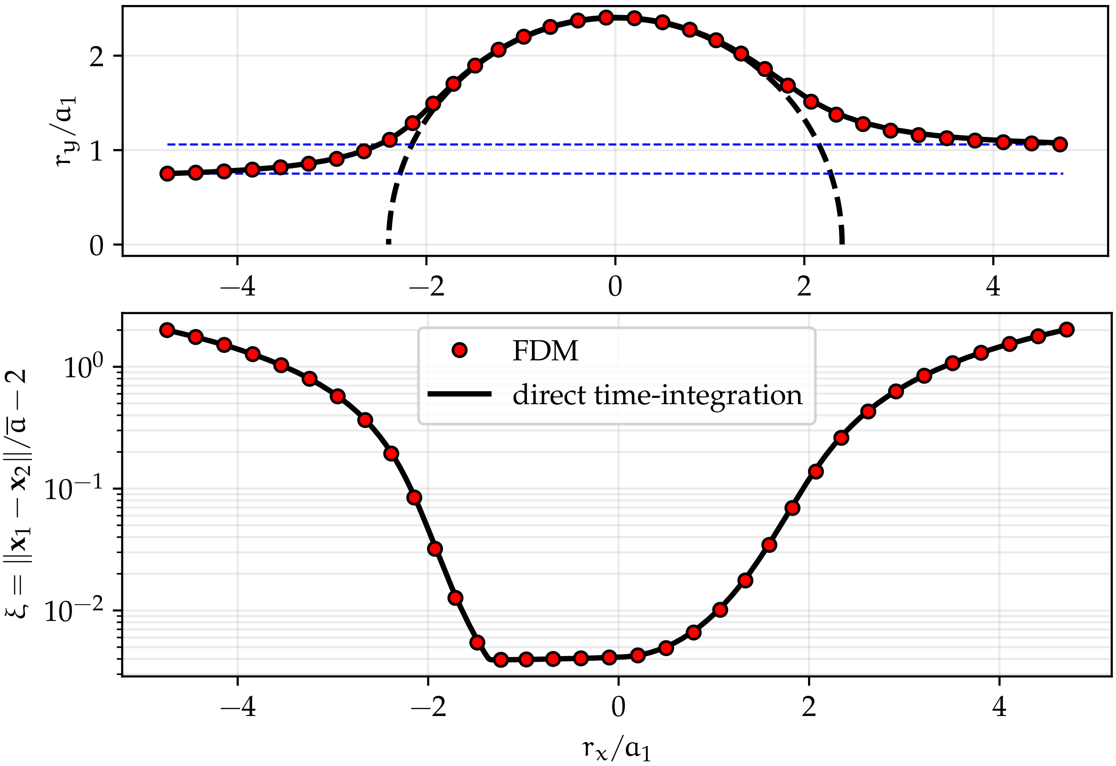

Figure 4.10
(top) Relative trajectories and (bottom) normalized distance between the particles surfaces of a particle pair in a simple shear flow with contact ($\overline{a} = (a_1 + a_2)/2$, $h_r = 5 \cdot 10^{-3} a_1$, $a_2/a_1 = 1.4$).

that the hydrodynamic interactions are properly tackled and that the time step is sufficiently small. The plain lines on the figure correspond to the direct time-integration of the velocity computed for a pair of free particles using the theoretical two-particle resistance matrix, in close agreement with the FDM computations. In Fig. 4.9 (bottom), the distance between the particles is displayed as a function of the relative x-position, r_x, of the particles for the same trajectories, together with its counterpart using direct integration of the theoretical velocity. Again, the good agreement validates the FDM computations. It should be stressed here that the cumulative error over $2 \cdot 10^5$ time steps is sufficiently small that fore-aft symmetry is preserved and that the trajectories from both methods are in close agreement.

On the other hand, the presence of non-hydrodynamic forces such as contact forces is known to induce asymmetry of the trajectory (Da Cunha & Hinch, 1996; Zarraga & Leighton, 2001). To validate the FDM against the computation of contacting-particles trajectories, a roughness height h_r is defined, and a contact force is triggered as the distance between the surfaces is smaller than h_r. As explained in Section 2.6, a standard contact model is used, also including constant friction (Gallier et al., 2014b). A typical trajectory is shown in Fig. 4.10 (top) for size ratio $a_2/a_1 = 1.4$, roughness $h_r = 5 \cdot 10^{-3}$ and friction coefficient $\mu_s = 0.5$. Fore-aft asymmetry is induced by contact between particles that occurs in the present trajectory for $-1.39 \lesssim r_x/a_1 \lesssim 0$ ($\xi \leqslant 2h_r/(a_1 + a_2) \approx 4.2\ 10^{-3}$). The simulations show good agreement with the direct time integration of the theoretical velocity. However, a slight discrepancy may be observed at the end of the trajectory: this is caused by the hydrodynamic interactions with the walls that are not accounted for by the theoretical two-particle matrix. Even though the domain is quite large compared to the particle sizes, the residual hydrodynamic interactions with the walls push the particles to the centerline, slowing them down and causing some delay. This discrepancy is more easily observed in the present case than in the former probably because one of the particles is larger and consequently induces stronger hydrodynamic interactions with the walls.

4.1.4 A PARTICLE PAIR IN A CONFINED POISEUILLE FLOW

The purpose of this section is to show that the present numerical method properly accounts for hydrodynamic interactions between two particles in a nonlinear flow, particularly when the small distance between the particle surfaces requires sub-grid corrections.

We consider two identical force- and torque-free particles with radius a suspended in a plane Poiseuille flow bounded by parallel planes Fig. 4.11. This particular flow has been numerically solved by Bhattacharya et al. (2006) for infinite walls with great accuracy. In the present study, the dimension of the stationary bounding walls is set to $(L_x \times L_z) = (60a_1 \times 40a_1)$, and the channel height is set to $H = 4a$. On the other bounding surfaces, periodic boundary conditions are applied. The unperturbed parabolic flow (Eq. (4.10)) is induced by an imposed pressure gradient (Eq. (4.11)). Both particles are in the same plane $(\mathbf{e}_x, \mathbf{e}_y)$. The first particle is placed at the center of the channel, while the second one is placed at a distance from the lower wall $d/a = 1.33$. The relevant particle translational and rotational velocities U_x, U_y and Ω_z are measured for values of the reduced lateral distance between the particles ρ_{12}/H ranging from 0.4714 to 1.5, which corresponds to a reduced distance $\xi = 2\|\mathbf{x}_2 - \mathbf{x}_1\|/(a_1 + a_2) - 2$ between the particle surfaces ranging from 10^{-5} to 4.04. As before, for each value of the lateral distance, the measured quantities are averaged over 16 different particle positions inside the plane section of a single mesh cell.

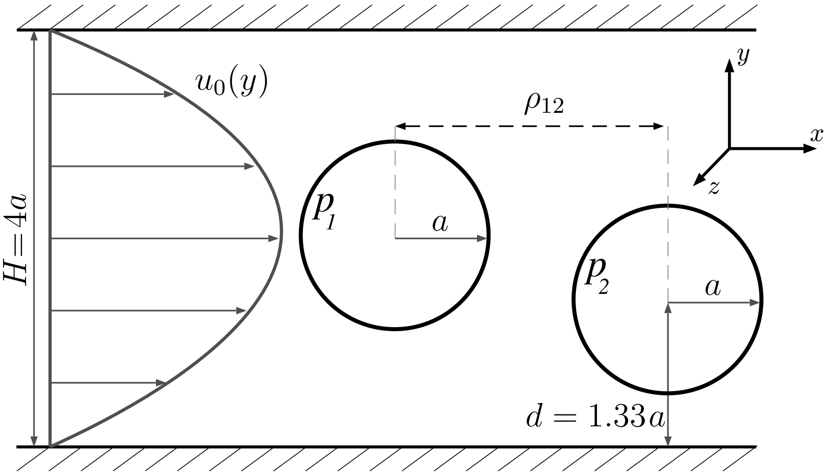

Figure 4.11
Two spheres in a plane Poiseuille.

The normalized velocities U_x/U_c, U_y/U_c and $2a\Omega_z/U_c$ from the FDM computations are displayed in Fig. 4.12 together with the results from Bhattacharya et al. (2006). As shown in the latter paper, the interactions between the particles and between the particles and the walls are quite strong in that arrangement of the particle positions, resulting in significant variations of the velocities as a function of ρ_{12}. We note a very good agreement between the present results and those from Bhattacharya et al. (2006), both in the near-contact and the far-field regions. In particular, the decay of the far-field flow, which is specific to the two-wall configuration (Bhattacharya et al., 2006), is properly accounted for by the FDM solver. We recall that the shortest distance between particle and wall is here $0.33a$, meaning that no sub-grid correction is needed for the particle-wall hydrodynamic interactions.

In the near-contact region, the velocities of the particles primarily depend on the lubrication flow between the surfaces of the particles. As shown in Fig. 4.12, the sub-grid corrections

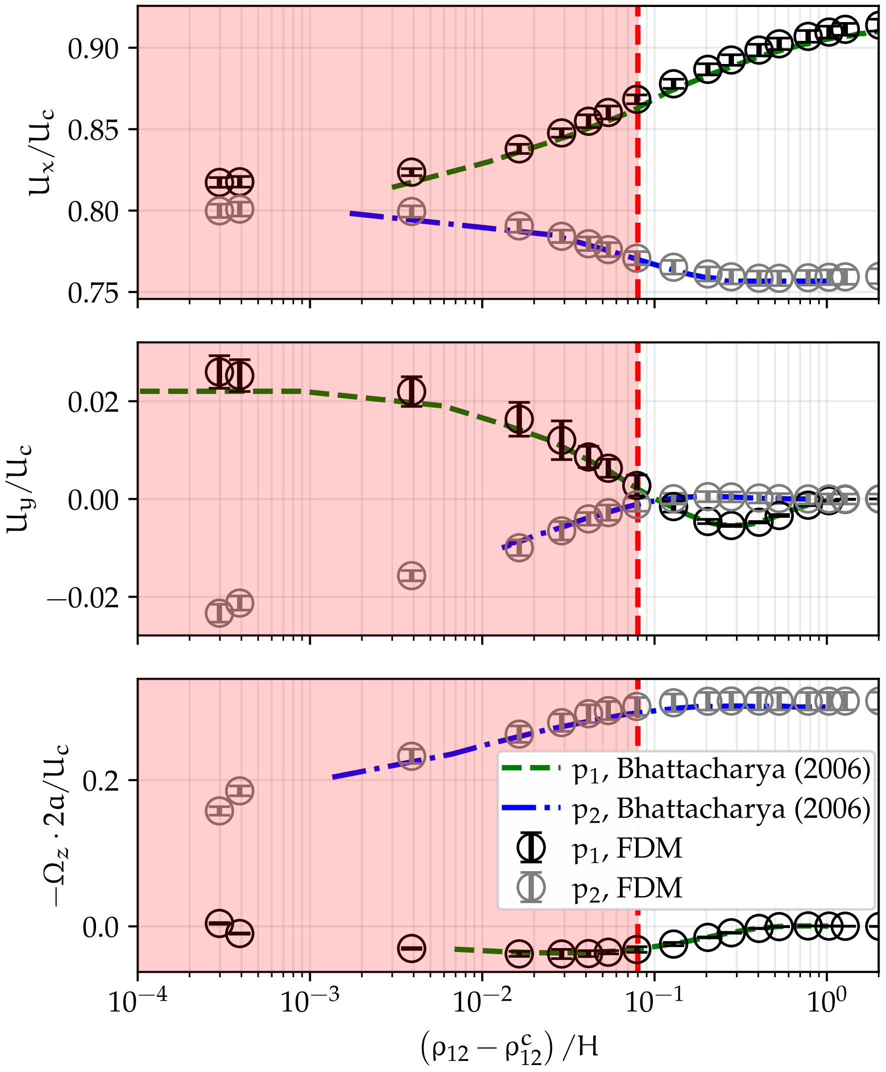

Figure 4.12
Normalized translational (top and center) and rotational (bottom) velocities for two free spheres in a plane Poiseuille as a function of the inter-particular distance ρ_{12}, where ρ_{12}^c is the longitudinal distance at which contact occurs between the two particles. The lines are a guide to the eye. Red region: sub-grid corrections needed.

allow accurate computation of the velocities in this distance range. The intermediate range is accurately described as well, with a sign change in the y-component of the translational velocities of the particles at $\rho_{12}/H \sim 0.6$. It should be stressed again that the expression of the sub-grid corrections in Eq. (3.10) does not require specifying any ambient strain rate tensor, which would be difficult to define in this particular case. The shear rate of the unperturbed flow indeed significantly varies at the scale of the particle, not to mention the strong influence of the walls on the flow around the particles.

It should be noted that the present case is a very strong validation of the sub-grid corrections proposed in Chapter 3: indeed, in such a confined Poiseuille flow the hypothesis introduced in Section 3.1 that we may assume local linearity of the flow at particle scale is not fulfilled; nevertheless, the agreement with the results obtained with the highly accurate method by Bhattacharya et al. (2006) is very good. The just-mentioned hypothesis is also not fulfilled in the case presented in Section 4.1.2 of a single free sphere in a confined pressure-driven flow which, therefore, is a strong validation of the sub-grid corrections between a particle and a wall.

4.1.5 THREE PARTICLES IN A LIQUID AT REST

We investigate the dynamics of three particles of the same radius a arranged in an equilateral triangle of side r in a quiescent fluid (see Fig. 4.13). Particle (p_1) is driven toward the triangle centroid with a force $F_x \mathbf{e}_x$ but no torque is exerted, while the two remaining particles are freely moving. The dimensions of the simulation domain are $(L_x, L_y, L_z) = (60, 40, 50)$. The plane $y = \pm L_y/2$ are rigid walls at rest, while the other boundaries $x = \pm L_x/2$ and $z = \pm L_z/2$ are applied periodic conditions. The velocity of all three particles is measured in the direction of the force (x) and the direction perpendicular to it (y), together with the angular velocity of particles (p_2) and (p_3) in the z-direction perpendicular to the plane of the particle centers. The velocities and angular velocities are made dimensionless using

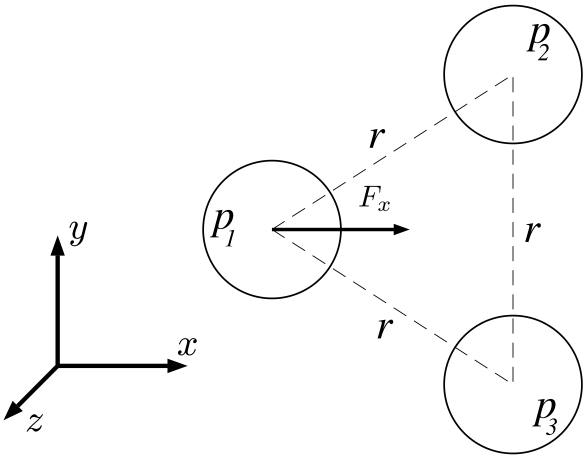

Figure 4.13
Three spheres arranged in an equilateral triangle of side r, one of which is driven toward the triangle centroid with a force F.

respectively $F_x/(6\pi\eta a)$ and $F_x/(6\pi\eta a^2)$. An important feature of the flow is that each particle is involved in the contribution of two particle-pair sub-grid corrections.

The triangle size, i.e., the distance between the particles, is varied over a range including both values for which sub-grid corrections are needed or not. For each distance, 64 different positions of the triangle centroid inside a single mesh cell are considered, and both the average quantities and their standard deviation are computed. The data are gathered in Tables 4.2 to 4.4 together with the reference solution provided by Wilson (2013), using a technique based on the Method of Reflections, for the case of a boundary-free system with an infinite extension of the fluid.

The velocities in the direction of the force (Table 4.2) from the FDM are significantly underestimated when compared to Wilson (2013). It was expected, since an external force parallel to the walls is applied on the triangle of particles, inducing a stokeslet flow far away from the particles. The latter is a slowly decreasing function of the distance, and thus induces significant hydrodynamic interactions, both with the walls and with the implied periodically repeated triangles. The discrepancy between the mean velocity of the three spheres from the FDM and the infinite size system amounts to 3.5% to 5.5%, which is roughly consistent with the discrepancy observed for the mobility of one sphere with radius $1.4a_1$ at the center of the simulation box driven by a force parallel to the walls compared to the theoretical sphere mobility in a fluid of infinite extension. However, the discrepancy is strongly reduced if the difference of velocity of particles (p_2, p_3) with respect to particle (p_1) is considered (Table 4.3). This was indeed expected, due to the small distance between the particles compared to the distance of the triangles to the walls. As for the velocity normal to the wall (y-component), the discrepancy between the data from the FDM and the infinite fluid case is very small (Table 4.4). This is probably because no stokeslet is produced in such

Table 4.2
Velocity components in the direction of the force parallel to the walls. The last two columns are the relative standard deviation from the 64 measurements (see text).

	Wilson (2013)		FDM (present work)			
r	$U_x^{p_1}$	$U_x^{p_{2,3}}$	$U_x^{p_1}$	$U_x^{p_{2,3}}$	$\frac{\sigma_{U_x^{p_1}}}{U_x^{p_1}}$ [%]	$\frac{\sigma_{U_x^{p_{2,3}}}}{U_x^{p_{2,3}}}$ [%]
2.01	0.65528	0.63461	0.61923	0.59857	2.3	2.4
2.10	0.73857	0.59718	0.70256	0.56129	2.2	2.7
2.50	0.87765	0.49545	0.83976	0.45889	1.7	3.1
3.00	0.93905	0.41694	0.90194	0.38084	1.6	3.7
4.00	0.97964	0.31859	0.94362	0.28491	1.4	4.6
6.00	0.99581	0.21586	0.96172	0.18428	1.4	6.6

a direction that the interactions with the walls are weaker. The angular velocities from the two methods (Table 4.4) are in better agreement as well.

In conclusion, except for the discrepancies induced by the hydrodynamic interactions with the walls due to the stokeslet originating in the external force, the results from the FDM are in good agreement with the accurate computations from Wilson (2013). In particular, the short-range hydrodynamic interactions are well tackled by the sub-grid corrections.

Table 4.3
Relative velocity components in the direction of the force parallel to the walls. The last column is the relative standard deviation from the 64 measurements (see text).

	Wilson (2013)	FDM (present work)	
r	$U_x^{p1} - U_x^{p2,3}$	$U_x^{p1} - U_x^{p2,3}$	$\frac{\sigma_{\Delta U_x^{p1,23}}}{\Delta U_x^{p1,23}}$ [%]
2.01	0.02067	0.02066	3.5
2.10	0.14139	0.14127	2.8
2.50	0.38220	0.38087	1.0
3.00	0.52211	0.52110	1.1
4.00	0.66105	0.65870	0.6
6.00	0.77995	0.77743	0.5

Table 4.4
Velocity components in the direction perpendicular to the force (left) and angular velocity component in the direction perpendicular to the force and parallel to the walls. The last column of each set is the relative standard deviation from the 64 positions measurements (see text).

	Wilson (2013)	FDM (present work)		Wilson (2013)	FDM (present work)	
r	$\lvert U_y^{p2,3}\rvert$	$\lvert U_y^{p2,3}\rvert$	$\frac{\sigma_{U_y^{p2,3}}}{\lvert U_y^{p2,3}\rvert}$ [%]	$\lvert \Omega_z^{p2,3}\rvert$	$\lvert \Omega_z^{p2,3}\rvert$	$\frac{\sigma_{\Omega_z^{p2,3}}}{\lvert \Omega_z^{p2,3}\rvert}$ [%]
2.01	0.00498	0.00501	8.9	0.037336	0.036476	5.0
2.10	0.03517	0.03514	5.5	0.052035	0.052299	8.3
2.50	0.07393	0.07372	1.5	0.045466	0.045646	7.2
3.00	0.07824	0.07830	1.1	0.035022	0.035065	5.9
4.00	0.06925	0.06893	0.7	0.021634	0.021648	6.8
6.00	0.05078	0.05003	0.3	0.010159	0.009992	8.7

4.1.6 THREE PARTICLES IN A SIMPLE SHEAR FLOW

We put three free particles in a simple shear flow in two configurations, as shown in Fig. 4.14: a) aligned in the compression axis with an inclination $\theta = 30°$ and b) with an L configuration. The distance between the surfaces of the particles is set to $a\xi = 10^{-2}$. As the particles are in the shear plane, the velocities U_z, Ω_x, Ω_y are zero and are not shown in the following tables. With these two configurations, particle B is involved in the contribution to the sub-grid corrections of two-particle pairs. Moreover, the interest of the L configuration is that the lubrication forces, in this case, are very small and the long-range hydrodynamic interactions are proportionally more important. Both particle radii $a_1 = 1.0$ and $a_2 = 1.4$ are tested, and the results shown are the averaged values over 16 positions on the same plane inside a single mesh cell to check the oscillations with respect to the relative position of the particles and the mesh. The domain size employed is $(L_x \times L_y \times L_z) = (30 \times 30 \times 30)a^3$.

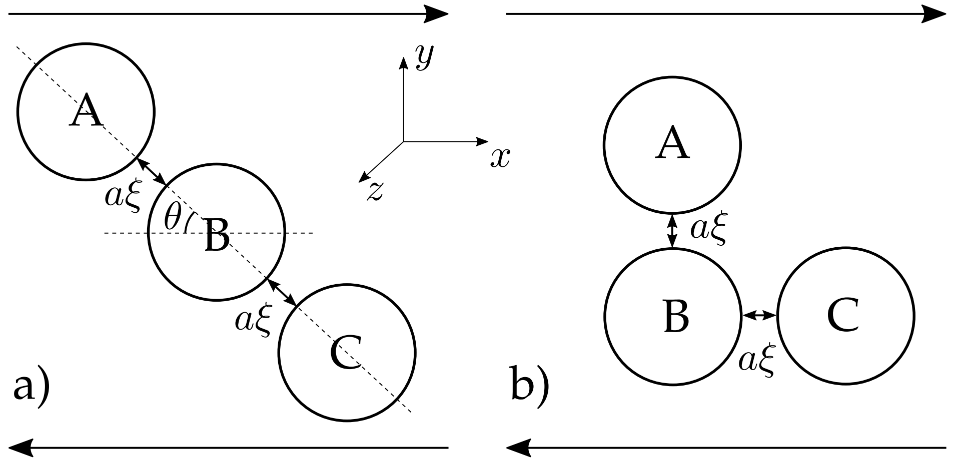

Figure 4.14
Three particles in a simple shear flow: a) aligned configuration with $\theta = 30°$; b) L configuration. The distance between the particles is fixed to $a\xi = 10^{-2}$.

We compare the results obtained for the velocities of the three particles with the ones proposed by Gallier (2014) and with the ones obtained with direct simulations done with the software COMSOL, where a very fine mesh is employed on the particles' surface and the interstitial lubrication flow is explicitly solved (i.e., no sub-grid correction is needed). As we can see in Tables 4.5 and 4.6, our results are in very good agreement with an average error of about ≈ 2%, showing that the sub-grid corrections are behaving correctly. Moreover, in the L configuration, our results seem to be in better agreement than the ones by Gallier (2014), showing that our formulation of the sub-grid corrections presented in Chapter 3 is more accurate.

Table 4.5
Particles velocities for the aligned configuration ($\theta = 30°$). Comparison between our results, COMSOL simulations, and Gallier (2014).

	COMSOL	Gallier (2014)	present work	
			$a_1 = 1.0$	$a_2 = 1.4$
U_x^A	0.322	0.321	0.323	0.324
U_y^A	0.463	0.467	0.466	0.466
Ω_z^A	-0.388	-0.389	-0.385	-0.387
U_x^B	0.000	<0.001	<0.001	<0.001
U_y^B	0.000	<0.001	<0.001	<0.001
Ω_z^B	-0.341	-0.339	-0.338	-0.338
U_x^C	-0.322	-0.323	-0.322	-0.323
U_y^C	-0.463	-0.463	-0.466	-0.467
Ω_z^C	-0.388	-0.380	-0.385	-0.387

Table 4.6
particles velocities for the L configuration. Comparison between our results, COMSOL simulations, and Gallier (2014).

	COMSOL	Gallier (2014)	present work	
			$a_1 = 1.0$	$a_2 = 1.4$
U_x^A	1.765	1.765	1.761	1.761
U_y^A	0.132	0.125	0.130	0.130
Ω_z^A	-0.669	-0.669	-0.676	-0.676
U_x^B	0.135	0.136	0.135	0.134
U_y^B	0.132	0.125	0.130	0.132
Ω_z^B	-0.500	-0.507	-0.506	-0.506
U_x^C	0.134	0.135	0.134	0.133
U_y^C	-0.246	-0.250	-0.245	-0.246
Ω_z^C	-0.329	-0.324	-0.327	-0.328

4.2 SUSPENSIONS IN A SIMPLE SHEAR FLOW

The geometry considered here is the same as in Fig. 4.5. We simulate moderately concentrated to concentrated ($0.27 \leqslant \phi_0 \leqslant 0.54$) frictional ($\mu = 0.5$) suspensions undergoing simple shear flow, with an imposed shear rate $\dot{\gamma}_0 = 1$. The particles are initially placed at random positions and, after a transient that occurs over a few strain units, the volume fraction profile (defined in Eq. (2.70)) and the particle velocity profile (that will be defined in Eq. (6.4)) reach steady profiles, from which the rheological quantities are extracted and time-averaged. The suspensions are made of particles of radii a_1 and $a_2 = 1.4a_1$ to reduce ordering, and the two populations occupy the same volume, i.e. $\phi_1 = \phi_2 = \phi_0/2$. All the quantities presented are averaged over a deformation of about $\approx 50t\dot{\gamma}_{\mathrm{core}}$.

4.2.1 NUMERICAL DETAILS

The domain size for each simulation is quoted in Table 4.7, together with the main simulation parameters, some of which will be explained in the following. Aiming at reducing the computational time, we increased the tolerances for p and $\mathbf{u}$ and we set them to $\mathrm{tol}_p = 10^{-3}$ and $\mathrm{tol}_u = 10^{-5}$. As already presented in Section 2.5, these values still present a good convergence behavior (fast and stable) and small errors. Also, by studying the residual of $\boldsymbol{\lambda}$ and the number of iterations needed for step 7 in the algorithm (i.e., the computation of the velocity and pressure fields and the update of the velocities of the particles, see Section 2.4), we decided to fix the number of iterations to limit the oscillations of the latter due to the mesh instead of requiring $\|\boldsymbol{\lambda}^{n+1} - \boldsymbol{\lambda}^n\|/\|\boldsymbol{\lambda}^n\| < \mathrm{tol}_\lambda$. As a consequence, the wall time is shortened at the cost of slight variations of the converged residual for $\boldsymbol{\lambda}$. In addition, the number of iterations required to have a small residual of $\boldsymbol{\lambda}$ varies with respect to the time step Δt employed. For example, for $\dot{\gamma}_0\Delta t = 10^{-4}$, ≈ 10 iterations are needed.

Table 4.7
Suspension in a Couette flow: simulations parameters.

ϕ_0	ϕ_{core}	$\dot{\gamma}_{\mathrm{core}}/\dot{\gamma}_0$	$\frac{L_{x,y}}{a_1}$	$\frac{L_z}{a_1}$	N_P	$\dot{\gamma}_0\Delta t$
0.27	0.303	0.923	20	20	350	10^{-4}
0.32	0.359	0.885	20	20	416	10^{-4}
0.37	0.405	0.873	20	20	481	10^{-4}
0.42	0.458	0.773	20	20	547	10^{-4}
0.47	0.493	0.745	25	20	956	10^{-4}
0.52	0.543	0.563	25	20	1057	10^{-4}
0.54	0.570	0.391	25	20	1098	$2 \cdot 10^{-5}$

4.2.2 MATERIAL FUNCTIONS

Experimental (Blanc et al., 2013; Sarabian et al., 2019; d'Ambrosio et al., 2021) and numerical (Yeo & Maxey, 2010b; Gallier, 2014; Gallier et al., 2016) studies have shown that, as a non-Brownian mono-disperse suspension is sheared between smooth walls, the particles near the walls form layers. Depending on the volume fraction, this local ordering may extend over several tenths of particle radii inside the suspension (Yeo & Maxey, 2010b; Gallier et al., 2016). In addition, the rheological properties are strongly affected in the layered region, leading, in particular, to significant wall slip.

In Fig. 4.15, the time-averaged volume fraction profile is displayed for a suspension with $\phi_0 = 0.42$. The particle ordering is observed close to the walls and decays over a length of a few particle radius units. The results shown in the following are averaged over the core region only (Eq. (2.71)), which is defined for all volume fractions as the positions farther from the wall than $H_{layer} = 5a_1$. The core shear rate $\dot{\gamma}_{core}$ is determined at each time step from a linear regression of the particle velocity distribution of the particles situated inside the core region (Table 4.7).

The computed viscosity (using Eq. (2.76)) is displayed as a function of the core volume fraction in Fig. 4.16. It is compared to results obtained by Lobry et al. (2019) using the Force Coupling Method, or by Gallier et al. (2018) using the FDM with standard sub-grid corrections. The different sets of data are in close agreement, with slight but significant discrepancy for the high volume fraction range ($\phi \geqslant 0.45$) where the viscosity from the present data set is a bit under the data from Gallier et al. (2018). This discrepancy might be explained by the different sizes of the simulation volume used in either of the two studies.

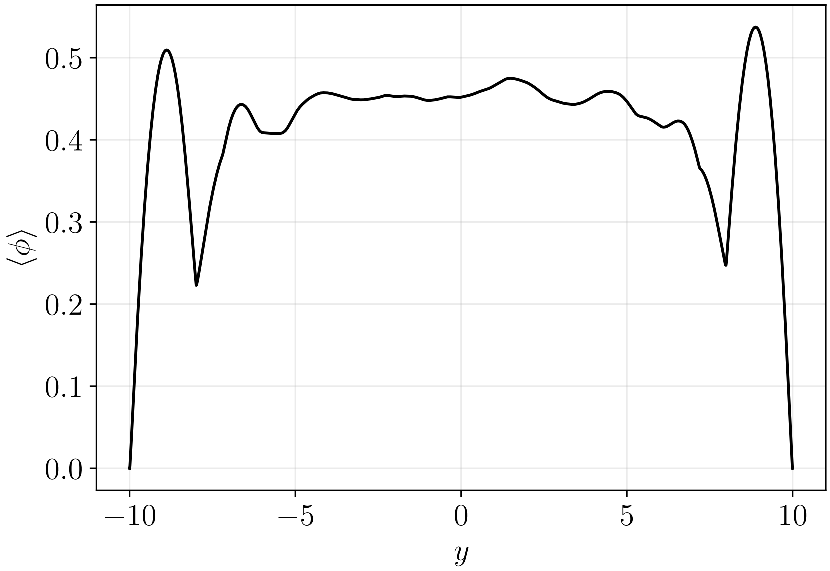

Figure 4.15
Steady volume fraction profile in a steady plane Couette flow for $\phi_0 = 0.42$.

While the channel width is at most $L_y = 25a_1$ for us, Gallier et al. (2018) chose a wider channel $L_y = 40a_1$. Thus, a slight residual ordering effect could be responsible for the lower viscosity in the present simulations.

A classic Maron-Pierce correlation law is fitted to the two FDM data sets:

$$\eta^s = \frac{\alpha}{(1 - \phi_{core}/\phi_J)^2} \tag{4.12}$$

where α and ϕ_J are fitting parameters. The jamming volume fraction ϕ_J is known to significantly depend on the friction coefficient μ, and takes decreasing values from 0.64 to approximately 0.55 as the μ increases from 0 to 10, although it hardly varies for $\mu \geqslant 2$ (Mari et al., 2014; Peters et al., 2016; Abhinendra Singh et al., 2018; Lobry et al., 2019). In the present work, the fitting procedure yields close values for the two FDM data sets, i.e. approximately 0.59, in good agreement with data from the literature for the same μ.

Normal and shear stresses, as well as their contact contribution, have been computed too. In the following, they are compared to the correlation laws proposed by Badia et al. (2022) that were obtained by a fitting procedure to the earlier numerical data mentioned above (Gallier et al., 2018; Lobry et al., 2019). They are displayed as normalized quantities:

$$\begin{aligned} \hat{N}_1 &= \frac{\Sigma_{11} - \Sigma_{22}}{\Sigma_{12}} & \hat{N}_2 &= \frac{\Sigma_{22} - \Sigma_{33}}{\Sigma_{12}} & \hat{\Sigma}^c_{12} &= \frac{\Sigma^c_{12}}{\Sigma_{12}} \\ \hat{\Sigma}^c_{11} &= \frac{\Sigma^c_{11}}{\Sigma_{12}} & \hat{\Sigma}^c_{22} &= \frac{\Sigma^c_{22}}{\Sigma_{12}} & \hat{\Sigma}^c_{33} &= \frac{\Sigma^c_{33}}{\Sigma_{12}} \end{aligned} \tag{4.13}$$

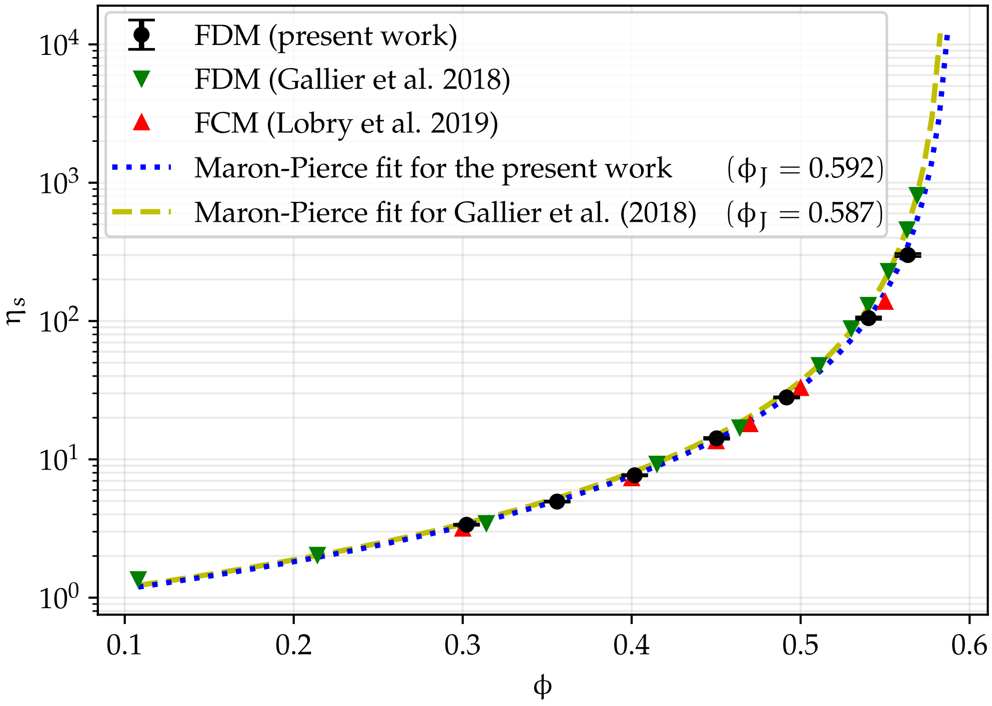

Figure 4.16
Suspension viscosity in the core region as a function of core volume fraction. Symbols: simulation data; dashed lines: Maron-Pierce fits. In the present work, $\alpha = 0.803$.

The first and second normal stress differences are displayed in Fig. 4.17 (top), together with the corresponding data from Gallier et al. (2018) and Lobry et al. (2019) and the correlation laws. Again, the agreement with earlier simulations is satisfactory, with a larger discrepancy for the first normal stress difference though. However, the latter quantity is smaller and subject to relatively higher fluctuations. Finally, the contact contribution to the shear and normal stresses are important quantities, since they are expected to play a key role in the shear-induced particle migration (Lhuillier, 2009; Nott et al., 2011). They are displayed in Fig. 4.17. Again, they stick to the correlation law from Badia et al. (2022).

As we can see, a very good agreement is observed between our results and the ones obtained by Gallier et al. (2018) by using the FDM with standard sub-grid corrections. The difference between the results, albeit small, increases with the volume fraction: some of it could come from the different sub-grid corrections employed. To check this, we can compare the slip velocity. By taking as an example $\phi_0 = 0.54$, we have a low shear rate equal to $\dot{\gamma}_{core} = 0.563\dot{\gamma}_0$, which is much lower than the one obtained by Gallier et al. (2018) ($\dot{\gamma}_{core}^{G.2018} = 0.801\dot{\gamma}_0$); however, the authors used a bigger domain ($L_x = L_y = L_z = 40a_1$). We can define the slip velocity as $u_s = (\dot{\gamma} - \dot{\gamma}_{core})\, L_y/2$: at $\phi_0 = 0.54$ we obtain $u_s = 5.46 = 9.7\dot{\gamma}_{core}a_1$, while Gallier et al. (2018) obtain $u_s^{G.2018} = 4 = 5\dot{\gamma}_{core}a_1$, showing a greater slip velocity in our simulations.

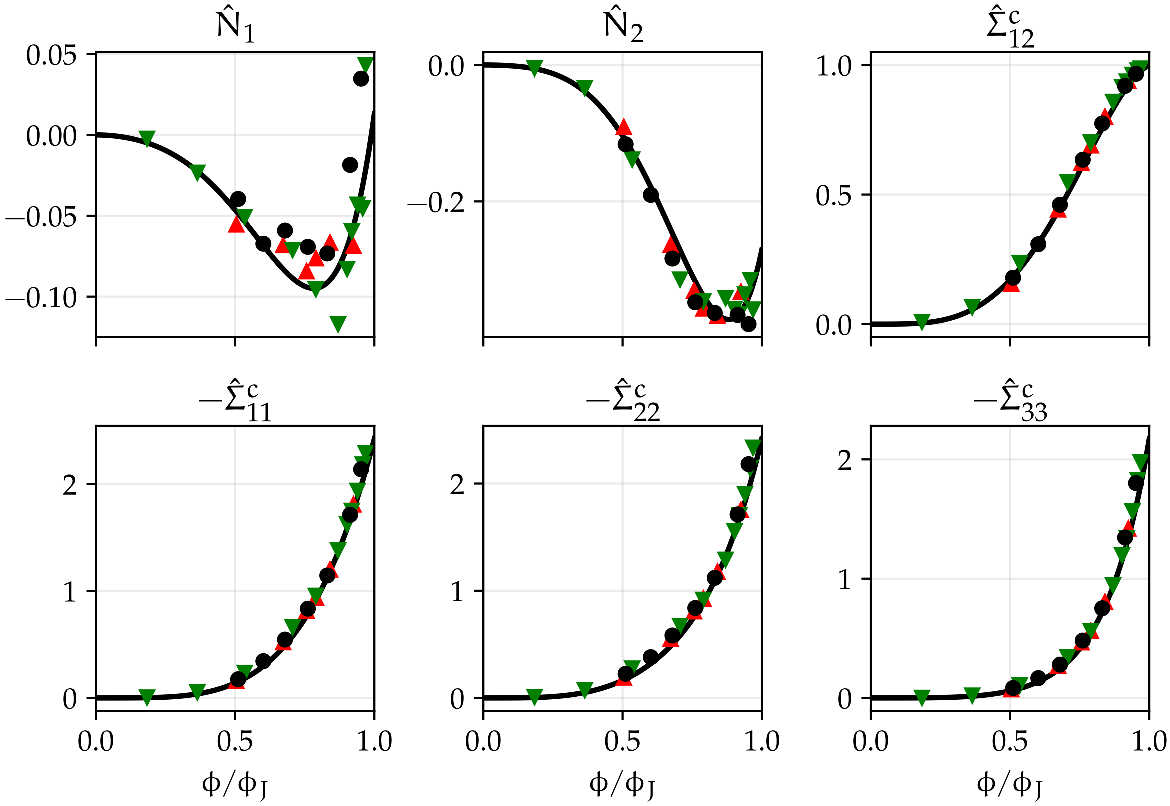

Figure 4.17
(top) Normal stress differences, and contact contribution to the total shear stress. (bottom) Contact contribution to the normal stresses. The normalized quantities (Eq. (4.13)) are displayed as a function of ϕ/ϕ_J. Symbols: simulation data from: the present work (●), Gallier et al. (2018) (▼), and Lobry et al. (2019) (▲). Plain line: correlation law from Badia et al. (2022).

4.2.3 MECHANICAL CONSISTENCY

Let us now check the mechanical consistency of the forces acting in the system. Here we want to check that the coupling of the momentum equations for the fluid and the particles is conveniently tackled. This is one of the most important characteristic features of the Fictitious Domain Method: as the fluid flow is completely solved, we have access to all the hydrodynamic forces acting on and generated by the fluid, in addition to all the quantities related to the particles.

We propose to check one of the suspensions treated in the current section: the one with $\phi_0 = 0.42$ (see Section 4.2). However, it should be kept in mind that we rigorously checked the mechanical consistency for every single case presented in the whole current work.

First, integration of Eq. (2.1) (without inertia and gravity) over the whole simulation domain, and taking into account that $\boldsymbol{\lambda}$ is zero outside the particles domain $\cup_p \mathcal{D}_p$, yields:

$$\int_{\partial_w} \boldsymbol{\sigma} \cdot \mathbf{n} \, d\mathcal{S} + \rho_f \int_{\cup_p \mathcal{D}_p} \boldsymbol{\lambda} \, d\mathcal{V} = 0 \tag{4.14}$$

In addition, integration of the same equation only on the particle domain yields:

$$\int_{\cup_p \partial \mathcal{D}_p} \boldsymbol{\sigma} \cdot \mathbf{n} \, d\mathcal{S} + \rho_f \int_{\cup_p \mathcal{D}_p} \boldsymbol{\lambda} \, d\mathcal{V} = 0 \tag{4.15}$$

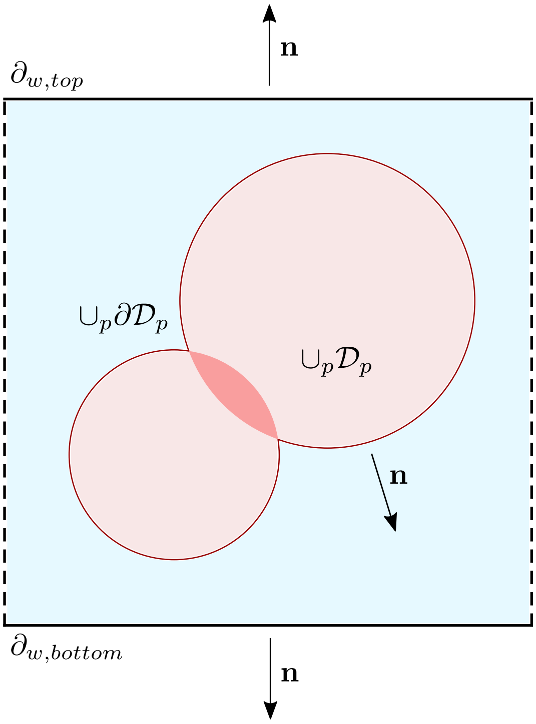

Figure 4.18
Qualitative representation of the indicator functions $\mathcal{I}_\lambda$: the particles cannot overlap, but the indicator functions can; in the overlapping positions (dark red region), $\mathcal{I}_\lambda$ is given the value 0.5 to avoid the force density to be counted twice. $\mathbf{n}$ is the outward normal to the boundaries ∂_w or to the particle surface $\partial \mathcal{D}_p$, and $\cup_p \mathcal{D}_p$ is the particles domain.

where $\mathbf{n}$ is the outward normal to the wall boundaries ∂_w or to the particle surface $\partial\mathcal{D}_p$ (see Fig. 4.18). It should also be noted that the net contribution of the periodic boundaries is equal to zero.

Eq. (4.15) means that the opposite of the integral of the force density equals the hydrodynamic force exerted on the solid domain as computed by the solver (see Eq. (2.6)). As a consequence, Eq. (4.14) means that the force exerted by the boundaries on the fluid is transmitted to the particle domain. Thus, checking Eq. (4.14) is equivalent to checking that the integral momentum equation accurately holds.

The hydrodynamic forces produced by the fluid (second term in RHS of Eqs. (4.14) and (4.15)) can be computed in two ways: either by integrating the force density field $\boldsymbol{\lambda}$ directly in the whole volume without the need of indicator functions or by integrating it in each particle using the corresponding indicator function $\mathcal{I}_\lambda$ and then summing over the particles (see Section 2.5.4). Clearly, as $\boldsymbol{\lambda}$ is itself defined equal to zero outside $\mathcal{I}_\lambda$, the two procedures should exactly give the same result. However, this is very useful and meaningful: as the indicator function is bigger than the particle size, they can overlap when two particles are at close distance, and that is why we decided in Section 2.5.4 to set $\mathcal{I}_\lambda$ equal to 0.5 in the overlapping positions: as a consequence, even though particles overlap, the force density in the overlapping region is not counted twice. Then, comparing the hydrodynamics forces produced by the fluid computed in the two proposed manners verifies the correct implementation and behavior of the indicator functions.

This is particularly important, since the fluid equations, and consequently the computed flow, account for the force density with no indicator function, while the particle momentum equation (Eq. (2.4)) is based on the hydrodynamic forces computed using the indicator functions. It is thus mandatory that the total force exerted by the fluid on the particles be the same with and without the use of indicator functions.

Therefore, let us define the following quantities:

$$\begin{aligned}
\mathbf{F}^{w} &= \int_{\partial_w} \boldsymbol{\sigma}\cdot\mathbf{n}\,\mathrm{d}\mathcal{S} \\
\mathbf{F}^{\mathrm{FDM,V}} &= -\rho_f \int_{\cup_p \mathcal{D}_p} \boldsymbol{\lambda}\,\mathrm{d}\mathcal{V} \\
\mathbf{F}^{\mathrm{FDM,parts}} &= -\rho_f \sum_p \int_{\partial\mathcal{D}_p} \boldsymbol{\sigma}\cdot\mathbf{n}\,\mathrm{d}\mathcal{S} = \sum_p \mathbf{F}_p^{\mathrm{FDM}}
\end{aligned} \tag{4.16}$$

which are respectively the force exerted by the whole domain boundaries on the fluid, the force exerted by the fluid on the particle domain, and the sum of the forces exerted by the fluid on the particles.

Finally, let us compare them in Fig. 4.19 in the three directions (x, y, z), where a zoom at the beginning of the simulation ($0 \leqslant \dot{\gamma}_0 t \leqslant 5$) is proposed. As we can see, Eq. (4.14) is extremely well satisfied for the three components, proving also the right implementation of the indicator functions.

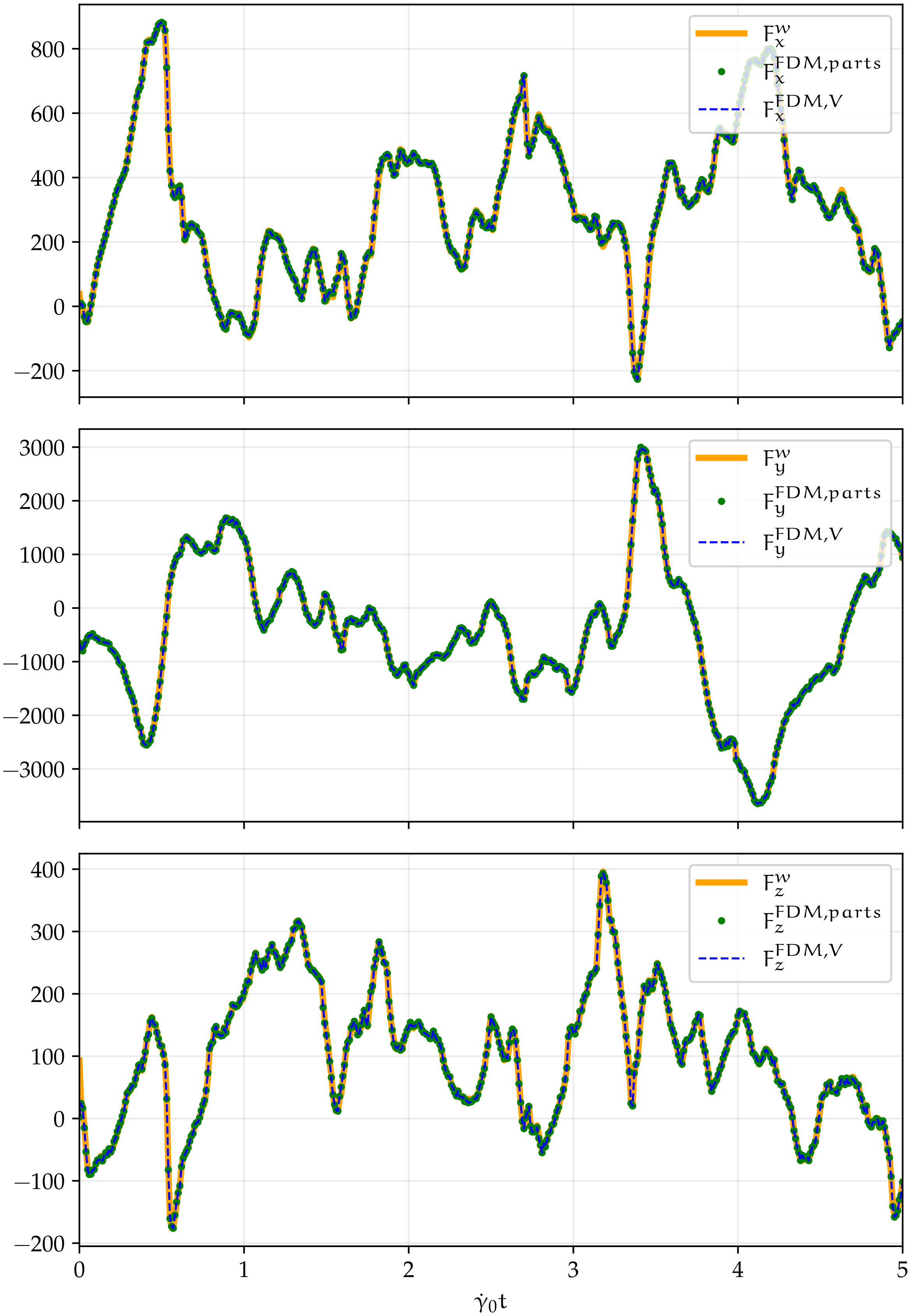

Figure 4.19
Comparison between the total force exerted by the boundaries on the fluid, and the sum of the hydrodynamic forces acting of each particle computed in two different manners, along the three directions (i.e., check of Eqs. (4.14) and (4.15)). Only a zoom at the beginning of the simulation ($0 \leqslant \dot{\gamma}_0 t \leqslant 5$) is given as an example.

Let us now turn our attention to the mechanical consistency of each particle, and let us check that the hydrodynamic forces (and torques) acting on the particles (both the ones computed by the solver and the ones coming from the sub-grid corrections) are counterbalanced by the contact ones, i.e. that on each particle and for each time step the following equations, which follow from Eq. (2.4) without inertia and gravity, hold:

$$\mathbf{F}_p^h + \mathbf{F}_p^c = 0 \,, \qquad \mathbf{T}_p^h + \mathbf{T}_p^c = 0 \tag{4.17}$$

with $\mathbf{F}_p^h = \mathbf{F}_p^{FDM} + \mathbf{F}_p^{SG}$, being $\mathbf{F}_p^{FDM}$ and $\mathbf{F}_p^{SG}$ the hydrodynamic forces as seen by the solver and the ones coming from the sub-grid corrections, respectively (see Section 2.1), and the contact forces and torques $\mathbf{F}_p^c$ and $\mathbf{T}_p^c$ as defined in Section 2.6.

As we can see in Fig. 4.20, where the three components (normalized by $N_p \eta \dot{\gamma}_0 a_1^2$ for the forces and by $N_p \eta \dot{\gamma}_0 a_1^3$ for the torques) are investigated, Eq. (4.17) is very well satisfied by each particle at each time step (just to be precise, on each subplot there are [# time steps] × [# particles] $= 10001 \times 547 = 5470547$ points), demonstrating that the contact forces and torques acting on each particle are perfectly counterbalanced by the hydrodynamic ones, recalling and stressing out that the hydrodynamic forces and torques have been corrected using the sub-grid corrections proposed in Chapter 3.

In Table 4.8, the comparisons shown in both Figs. 4.19 and 4.20 are re-proposed by displaying the error, which has been computed by averaging over the time steps, and also over the particles when necessary. As we can see, the agreement is very good for all the quantities and in the three directions, in particular when comparing $F^{FDM,parts}$ with $F^{FDM,V}$: $F^{FDM,V}$ was computed during the run so that one single number was written in the file for each vector component, while each component of $F^{FDM,parts}$ is the sum of $N_p = 547$ numbers, each of which was written in a file, and the sum was performed in post-processing so that the difference between the two is related to the writing precision. This demonstrates again the correct implementation and behavior of the indicator functions.

This quantitatively proves that the mechanical consistency is very well satisfied in the whole system, for each particle, and at each time step of the simulation.

Table 4.8
Quantitatively comparing the quantities displayed in Fig. 4.19 and Fig. 4.20. The notation $\overline{(\cdot)}$ stands for the averaging over the time steps (and an additional averaging over the particles when necessary, i.e. for $F_p^{c,h}$ and $T_p^{c,h}$).

	$\sqrt{\dfrac{\left(\overline{F}^w - \overline{F}^{FDM,parts}\right)^2}{\left(\overline{F}^w\right)^2}}$	$\sqrt{\dfrac{\left(\overline{F}^{FDM,V} - \overline{F}^{FDM,parts}\right)^2}{\left(\overline{F}^{FDM,V}\right)^2}}$	$\sqrt{\dfrac{\left(\overline{F}_p^c + \overline{F}_p^h\right)^2}{\left(\overline{F}_p^c\right)^2}}$	$\sqrt{\dfrac{\left(\overline{T}_p^c + \overline{T}_p^h\right)^2}{\left(\overline{T}_p^c\right)^2}}$
x	0.0229	$0.82 \cdot 10^{-7}$	0.0019	0.0062
y	0.0016	$1.46 \cdot 10^{-7}$	0.0020	0.0224
z	0.0225	$1.42 \cdot 10^{-7}$	0.0017	0.0117

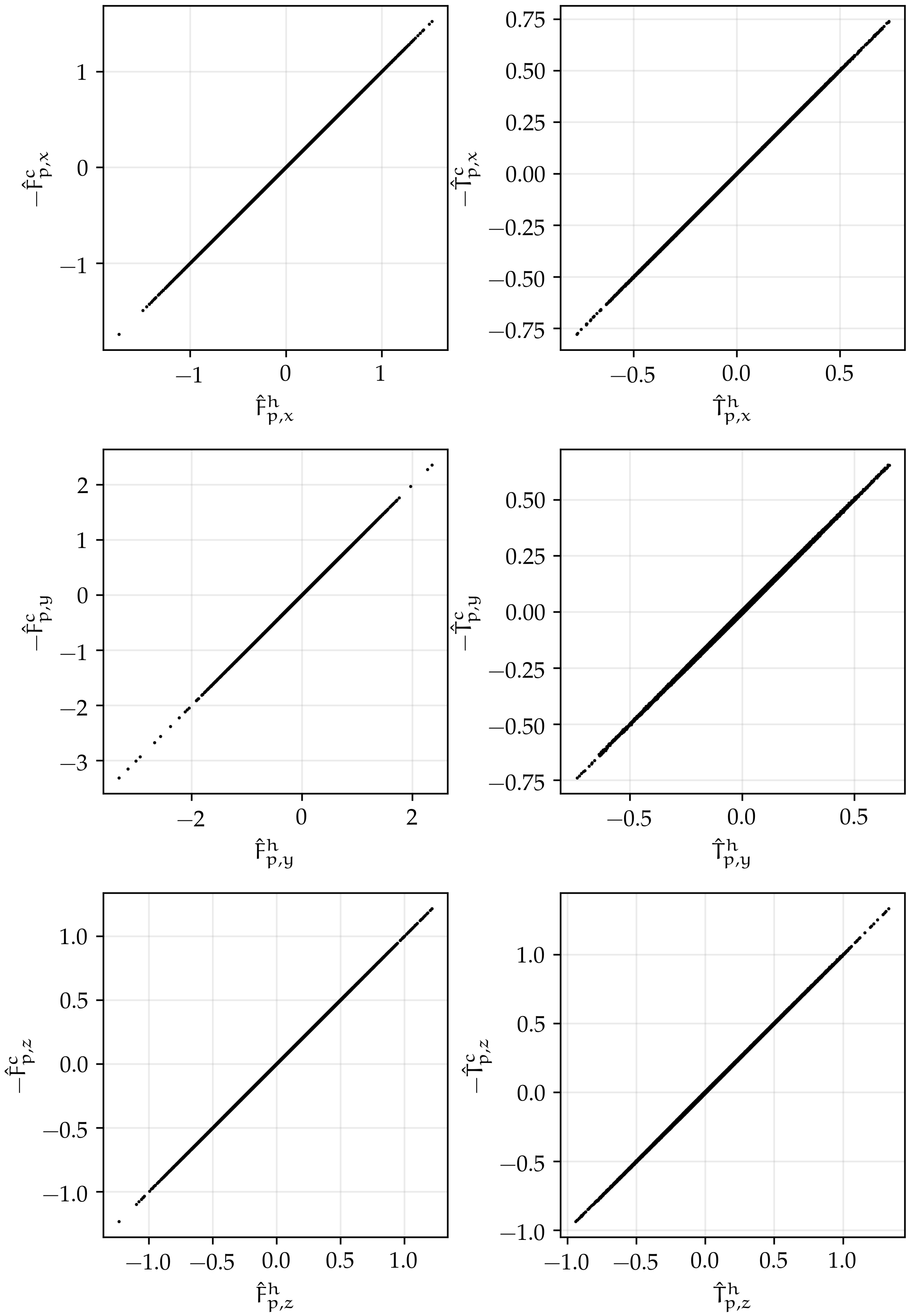

Figure 4.20
Comparison between the normalized hydrodynamic forces (and torques) acting on the particles (the sum of the forces computed by the solver and the sub-grid ones) and the contact forces, along the three directions and for each particle at each time step (i.e., check of Eq. (4.17)), where $\hat{\mathbf{F}} = \mathbf{F}/\left(N_p \eta \dot{\gamma}_0 a_1^2\right)$ and $\hat{\mathbf{T}} = \mathbf{T}/\left(N_p \eta \dot{\gamma}_0 a_1^3\right)$.

4.2.4 COMPUTATIONAL PERFORMANCES

In Table 4.9 we present the relative computational times of the flow resolution (fluid velocity and pressure fields) and of the computation of the velocities of the particles (inversion of the linear system of Eq. (2.43)) with respect to the total time step, varying the number of particles N_P. The sum of these two computational times does not make the totality, as the writing of the results files and the setup of the time step (moving the particles, building the resistance matrix, etc.) are not shown here. As we can observe, the computation of the velocities of the particles takes more and more time with respect to the total time step as we increase the number of particles. We did not test the optimization of this step, however, we easily could try to reduce it by coupling OpenMP with MPI (OpenMP is already implemented in the Eigen library, which is used to solve the linear system associated with the velocities of the particles). We also present the wall times for the different simulations; we employed two different partitions: one with Intel Xeon Gold 6428 @2.5GHz cores and the other with AMD Epyc 7302 @3GHz cores (see the technical presentation of the Université Côte d'Azur cluster Azzurra for more information about the nodes). In Figs. 4.21 and 4.22 and Table 4.9 the strong scaling is tested for three different domain sizes:

- $(L_x \times L_y \times L_z) = (20a_1 \times 20a_1 \times 20a_1)$, i.e. 10^6 mesh cells (size S);
- $(L_x \times L_y \times L_z) = (40a_1 \times 40a_1 \times 20a_1)$, i.e. $4 \cdot 10^6$ mesh cells (size M);
- $(L_x \times L_y \times L_z) = (40a_1 \times 40a_1 \times 40a_1)$, i.e. $8 \cdot 10^6$ mesh cells (size L).

As we can see, the ideal speedup is rapidly abandoned: this is a known limit in OpenFOAM. However, we notice that a better speedup is achieved for the domain sizes M and L: indeed, the number of mesh cells per core seems to be an important factor. There exists a minimum number of mesh cells per core below which there is no speedup achievable. We also observe a significant difference between the AMD and the Intel cores: in the cluster, we employed for the benchmarks (Azzurra, mentioned above) each AMD core has ≈ 1.7 times the memory of the Intel ones and 4 times the bandwidth.

Table 4.9
Computational times for suspensions in a simple shear flow.

ϕ_0	N_P	$\frac{L_{x,y}}{a_1}$	$\frac{L_z}{a_1}$	flow res. [%]	parts. vels. [%]	N_{cores}	wall time [s]
0.27	350	20	20	80	7	96	0.40
0.32	416	20	20	77	8	96	0.42
0.37	481	20	20	72	10	96	0.45
0.42	547	20	20	76	9	64	0.66
0.47	956	25	20	48	20	128	0.58
0.52	1057	25	20	40	30	92	0.91

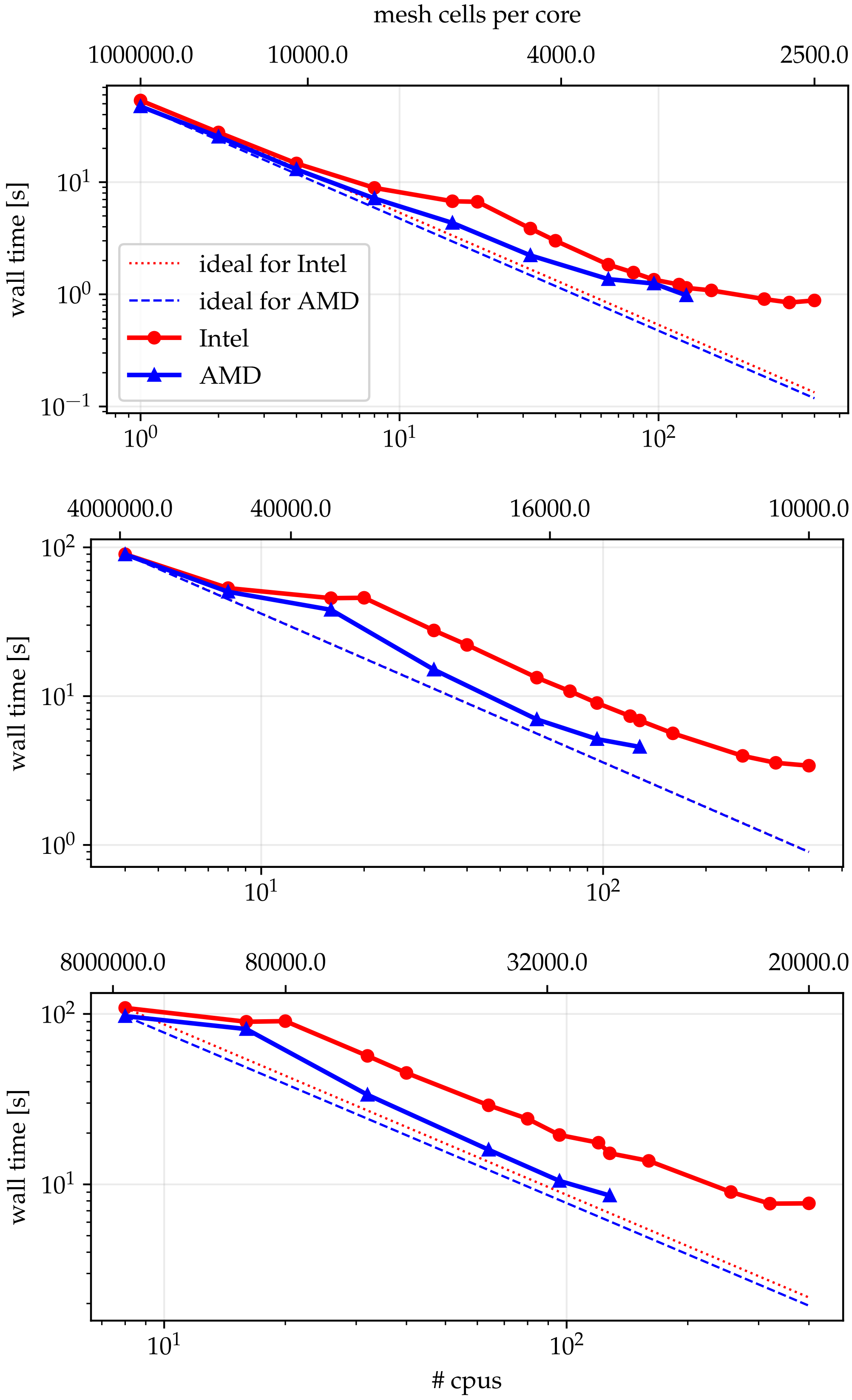

Figure 4.21
Wall times testing the strong scaling performances for three different domain sizes: (top) $(L_x \times L_y \times L_x) = (20 \times 20 \times 20)a_1^3$, i.e. 10^6 mesh cells; (center) $(L_x \times L_y \times L_x) = (40 \times 40 \times 20)a_1^3$, i.e. $4 \cdot 10^6$ mesh cells; (bottom) $(L_x \times L_y \times L_x) = (40 \times 40 \times 40)a_1^3$, i.e. $8 \cdot 10^6$ mesh cells.

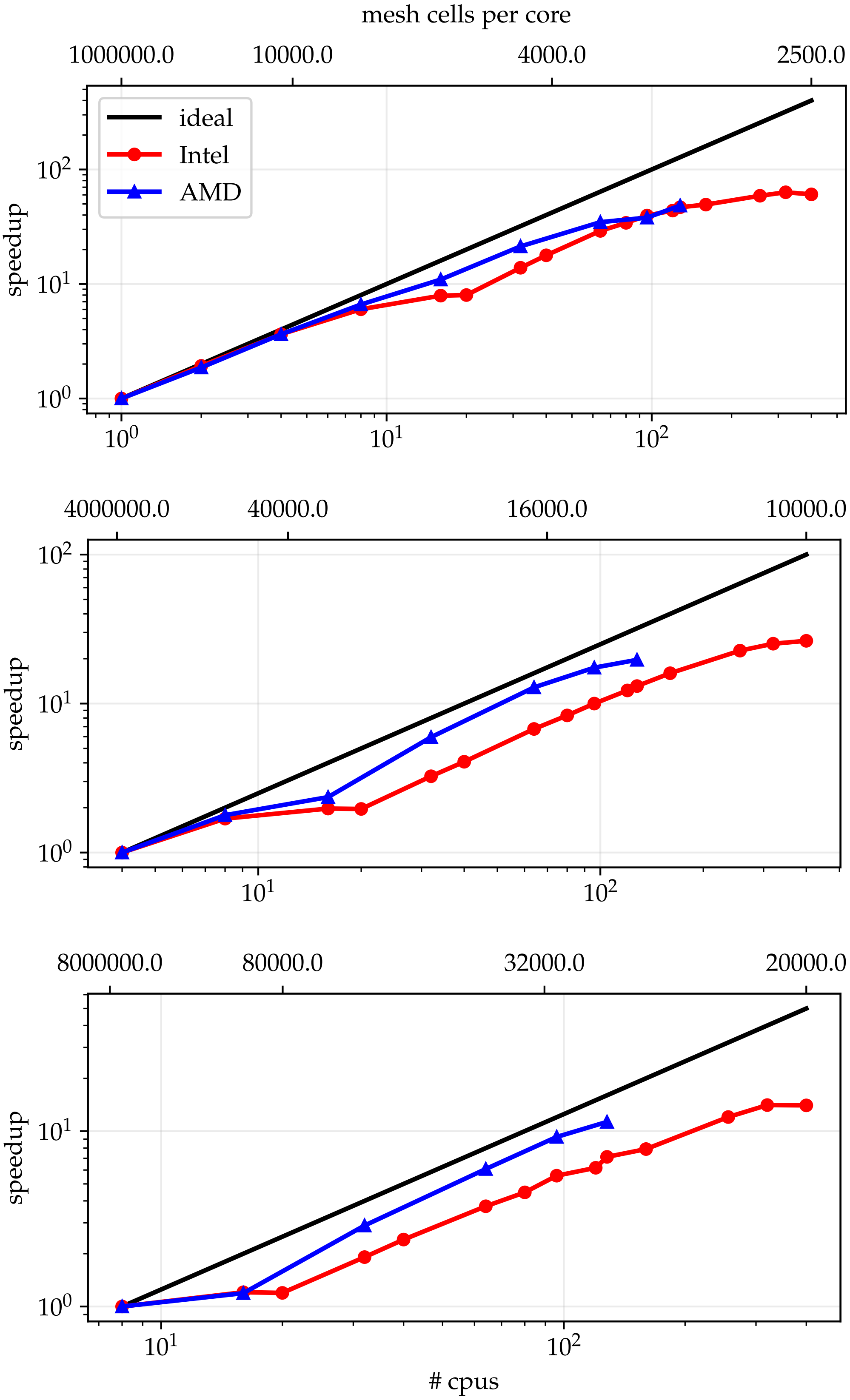

Figure 4.22
Speedup obtained testing the strong scaling performances for three different domain sizes: (top) $(L_x \times L_y \times L_z) = (20a_1 \times 20a_1 \times 20a_1)$, i.e. 10^6 mesh cells; (center) $(L_x \times L_y \times L_z) = (40a_1 \times 40a_1 \times 20a_1)$, i.e. $4 \cdot 10^6$ mesh cells; (bottom) $(L_x \times L_y \times L_z) = (40a_1 \times 40a_1 \times 40a_1)$, i.e. $8 \cdot 10^6$ mesh cells.

5

THE ROLE OF ADHESION IN FRICTIONAL SUSPENSIONS

We investigate the effect of adhesive forces in frictional suspensions. We start by presenting the current relevant literature: different experimental studies have been done, but only a few numerical studies are present. Then, we introduce and justify the contact model employed here: we choose a very simple but still realistic model. To proceed, we will have to define all the dimensionless parameters of interest.

After introducing the simulation setup, we present a cartography of the difficulties encountered. Finally, we display the results and propose a discussion.

5.1 STATE OF THE ART

ADHESION AND YIELD STRESS

Following Larson (1999), two yields stresses can be defined. At high shear stresses the relation between the shear rate and the stress is more or less linear, while at zero shear rate, a positive stress is extrapolated. This defines the "Bingham" yield stress, which differs from the "real" yield stress, measured by finding the minimum stress required to induce flow.

There has been a long controversy about the existence of a "real" yield stress: Barnes (1999) claimed that this is a fiction, and gave various illustrations of materials that apparently tended to limit shear stress at low shear rates but that nevertheless did still flow at lower shear rates or shear stresses. The statement that a material does not flow is of course always associated with a particular time scale. Reiner (1959) would argue that even the mountains flow if you wait long enough. The concept of yielding can be compared with that of glass transition, which is also based on a kinetic rather than a thermodynamic argument. Unfortunately, there is no unique experimental procedure to determine the yield stress. Nevertheless, the *yield stress* remains a useful and commonly used rheological concept.

In the present study, the yielding mechanism is related to attractive forces between the particles. Indeed, adhesion can have a significant effect on the microstructure and rheological properties and has been widely investigated mainly in Brownian colloidal suspensions (Larson, 1999; Mewis & Wagner, 2011): in most real systems there are often interparticle forces causing neighboring particles to attract each other and generate clusters.

THE ROLE OF THE VOLUME FRACTION ON THE MICROSTRUCTURE

In this framework, the volume fraction plays a central role. At low concentrations, increasing the intensity of adhesive forces results in floc formation, i.e. dynamic clusters more or less independent from each other. The instantaneous structure of the flocs is affected by and has an effect on the flow: the flow accelerates the rate of aggregation as it brings particles together more quickly, but it also pulls particles apart possibly breaking the aggregates. The size of these clusters depends on the shear rate: the higher the shear rate the smaller the flocs (Doi & Chen, 1989; Boromand et al., 2017; Papadopoulou et al., 2020). However, very low values of the jamming volume fractions may be found at high shear stresses, seemingly indicating that not all the clusters are destroyed even at high stresses (Papadopoulou et al., 2020). The strong influence of the clusters on rheology, together with the different length scales at play (particles and clusters), make the experimental and numerical study of adhesive suspensions a difficult matter.

Increasing the concentration leads to an increase in the size of the flocs. This also increases the probability for different flocs to interact; depending on the shear stress, this can either cause percolation and yielding or flocs breaking and reforming quickly (Larson, 1999).

At very high concentrations, yielding and shear-thinning behaviors may alter the shear-thickening transition from lubricated to frictional contact (Pednekar et al., 2017; Abhinendra Singh et al., 2019; Richards, 2021), leading to particular microstructure (Edens et al., 2021).

THE EFFECT ON RHEOLOGY

The complex interplay between microstructure and flow results in strongly-non-Newtonian behaviors and induces pronounced rheological changes. In semi-dilute regimes, increasing the interparticle attraction changes the rheological behavior quite suddenly from that of a liquid to that of a weak solid or gel, as Agbangla et al. (2014) observed in their numerical investigation of microchannel clogging. While increasing, even more, the concentration of particles leads to percolation, gelation, and glass formation. In general, an increase of the adhesive forces can lead to enormous increases in the low-shear viscosity, possibly evolving into a yield stress below which the suspension does not flow (Mewis & Wagner, 2011).

At low shear stresses, a strong shear-thinning behavior of the viscosity has been observed in the 2D numerical simulations of non-Brownian suspensions by Doi & Chen (1989). This is also confirmed by Koumakis et al. (2015), who investigated colloids both experimentally in a large range of Péclet's numbers and numerically neglecting hydrodynamic interactions, at fixed volume fraction $\phi = 0.44$: while increasing the shear rate, they observed a transition from yielding to Newtonian behavior, and they defined a modified Péclet's number Pe_{dep} which reflects the ratio of shear to attracting forces and found the limit between the two above-mentioned behaviors at $Pe_{dep} = 1$. They also observed a very heterogeneous structure of the particles, evidencing the presence of flocs with very different behaviors at $Pe_{dep} < 1$. It should be noted that the transition $Pe_{dep} = 1$ occurs at quite a high standard Péclet's number (~ 100) suggesting a limited influence of Brownian motion in the transition.

Yielding is also observed for larger particles for which Brownian motion is negligible (Zhou et al., 1995; Richards et al., 2020), and it strongly increases with the volume fraction.

OUR RESEARCH

Surely, adhesion has a strong appeal, also because a lot of questions are still unanswered and a clear and shared framework has not been established yet. Here, we want to numerically investigate the role of adhesion in frictional non-Brownian particles, for moderately concentrated and concentrated suspensions undergoing simple shear flow. It will be shown that more dilute systems may be more difficult to tackle. The results are compared to earlier data obtained with the Force Coupling Method (FCM) and have not been published yet.

The central quantity of interest here is the ratio between the shear stress and the adhesive force $\Sigma_{12}a^2/F^{adh}$ (it should be noted that this ratio is equivalent to the definition of Pe_{dep} by Koumakis et al. (2015)); combining this quantity with the idea of a stress-dependent jamming volume fraction, we propose to search for the behavior of the latter while varying adhesion, i.e. we want to study $\phi_J = f\left(\Sigma_{12}a^2/F^{adh}\right)$. This stress-dependent jamming volume fraction has already allowed rationalizing experimental measurements using modeling (Zhou et al., 1995; Barnes, 1999; Guy et al., 2018; Richards et al., 2020; Richards, 2021) as well as numerical simulations (Koumakis et al., 2015), in particular in the field of shear-thickening transition of adhesive suspensions (Abhinendra Singh et al., 2019; Richards, 2021). As explained in these papers, this stress-dependent jamming volume fraction is equivalent to a volume-fraction-dependent yield stress $\sigma_y a^2/F^{adh} = f(\phi)$.

5.2 CONTACT MODEL: ELASTICITY AND ADHESION

In Section 2.6 we already presented the model employed for elastic contact, and we have seen that this comes from the hypothesis that contact between particles (and between particles and walls) occurs between asperities present on the particle surface. Now, let us see how the contact model is modified to introduce an adhesive force.

Contact between two elastic bodies is a very complex mechanism and, as shown by Johnson (1985) when closely investigating the edge of contact the model proposed by Hertz (1882) becomes too restrictive. The JKR theory of elastic contact recalled in Appendix E, has the same validity domain as Hertz theory and is well suited to spherical smooth bodies or for mono-asperity contacts. In this case, the dependence of normal load and contact area on compression is complex, and the maximum value of the tangential (frictional) force is expected to be proportional to the square of the contact area and nonlinear with the normal load. Also, as explained below, in JKR theory, when the normal load is zero the contact area is finite, and, consequently, friction is finite too.

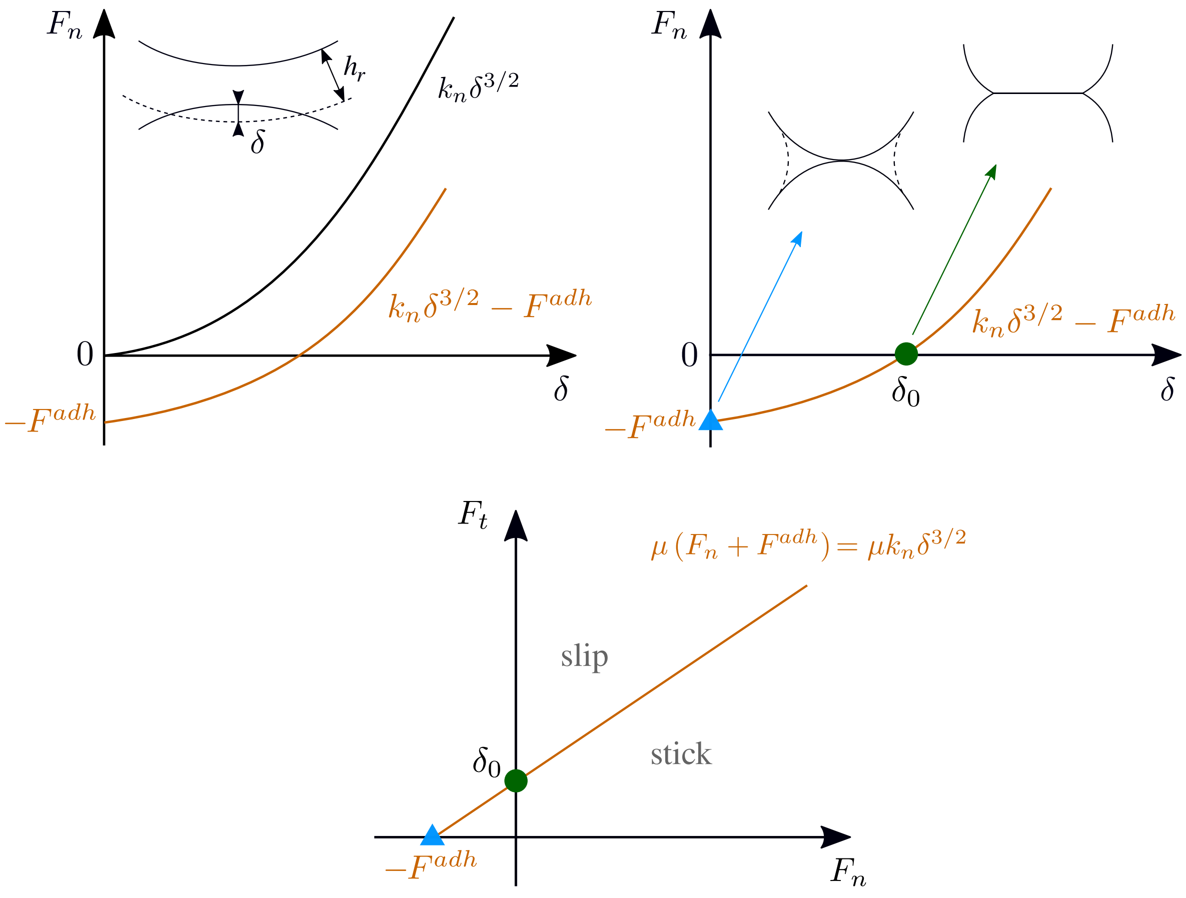

Figure 5.1
Contact model: (top) normal force, and (bottom) maximum value of the tangential force. $F_n = 0$ is reached at a positive compression δ_0, and a positive tangential force is still present (●). At $\delta = 0$ (▲), the tangential force vanishes and the normal one is equal to the (negative) adhesive force.

It should be stressed that in the situation of real rough surfaces where contact occurs via numerous asperities, the contact area is lower than the apparent one, and the tribology is very complicated and system-dependent. However, an in-depth discussion of this subject is out of the scope of the present study.

The model chosen here is a simplified version of the more complete model presented by Johnson et al. (1971): we add a constant (negative) adhesive force to the normal elastic force (the latter coming from the Hertz Law), as represented in Fig. 5.1 [top left] and of the form:

$$F_n = k_n \delta^{3/2} - F^{adh} \tag{5.1}$$

As previously, contact occurs when the distance between the particle surfaces is smaller than the roughness height h_r, i.e. the compression δ is positive. The normal contact force is equal to the (negative) adhesive one when $\delta = 0$ (▲ in Fig. 5.1), and it is zero at a positive compression δ_0, where the compression force balances the attractive one (● in Fig. 5.1). As a consequence, the normal force is attractive for $\delta < \delta_0$ and repulsive otherwise.

The friction force is assumed to be related to the contact area, which is connected to the elastic contribution of the force, i.e.:

$$F_t = \mu \left(F_n + F^{adh} \right) \tag{5.2}$$

This idea is explained in detail in Appendix E, where a comparison with the JKR's theory is proposed. In particular, we note here that the vanishing of the tangential force at $\delta = 0$ is expected to be unrealistic since the contact area is not expected to vanish. However, an important point is that a finite tangential force may occur for zero normal force (●), as expected. We note also that, in the same way as previously, the relation between F_n and δ is made steeper for $\delta \rightarrow h_r$ (Eq. (2.57)).

5.3 NUMERICAL DETAILS

Before proceeding, it should be noted that high adhesive forces need smaller time steps. Hopefully, decreasing the time-step allows decreasing the number of SIMPLEC loops to be done in the algorithm over the fields U, p and λ and the velocities of the particles $(\mathbf{U}_p, \mathbf{\Omega}_p)$ while keeping a low tolerance for the convergence of the force density field. However, in general, the computational cost increases when high adhesive forces are employed. The choices of Δt and the number of loops have been done using previously obtained non-adhesive suspension simulation results and by checking the overall particle momentum balance and force density residuals. In conclusion, we employ $\dot{\gamma}_0 \Delta t = 10^{-5}$ and $\dot{\gamma}_0 \Delta t = 5 \cdot 10^{-6}$ with only 1 SIMPLEC loop for the most adhesive cases, and $\dot{\gamma}_0 \Delta t = 10^{-4}$ with 10 SIMPLEC loops for all the others.

5.3.1 NUMERICAL SETUP AND DIMENSIONAL ANALYSIS

Time, length, and forces are made dimensionless using respectively $1/\dot{\gamma}_0$, a_1, and $\eta\dot{\gamma}_0 a_1^2$. Then, the dimensionless parameters used in the simulations are:

- **cubic domain** → $(L_x \times L_y \times L_z)/a_1^3 = (20 \times 20 \times 20)$: a cubic domain is employed, which size (kept fixed) leads to a number of particles N_p typically between 300 and 900; walls are orthogonal to the y-direction with the same but opposite velocity imposing a shear rate $\dot{\gamma}_0 = 1/t$;

- **volume fraction** → ϕ_0: various values of the mean volume fraction are investigated;

- **particles radii** → $a_2/a_1 = 1.4$: bidisperse suspensions with two particle radius lengths a_1 and a_2 are considered, with equal volume fraction $\phi_1 = \phi_2 = \phi_0/2$;

- **friction coefficient** → $\mu = [0.0,\ 0.1,\ 0.5]$: for each considered system, the value of the friction coefficient is kept constant; however, three values are investigated here, for which adhesion is varied;

- **roughness height** → $h_r/a_1 = 0.005$: as previously mentioned, contact occurs through asperities present on the particle surface, which height h_r is kept fixed; this is the typical value found in experiments for model spherical particles (Blanc et al., 2011b);

- **elastic parameter** → $6\pi\eta a_1^2\dot{\gamma}_0/\left(k_n\left(\bar{\epsilon}h_r\right)^{3/2}\right) = \dot{\Gamma} = 1$: the typical hydrodynamic stress between two particles in a simple shear flow (in dilute suspensions) is $6\pi\eta a_1^2\dot{\gamma}_0$, and its ratio to the elastic normal force $k_n\left(\bar{\epsilon}h_r\right)^{3/2}$ is set to 1 and kept fixed, leading to a typical compression of the asperity in dilute suspensions of about 5% ($\bar{\delta} \approx 0.05h_r$, see Section 2.6 and Eq. (2.58));

- **adhesion parameter** → $G_0^{adh} = F^{adh}/\left(6\pi\eta a_1^2\dot{\gamma}_0\right)$: this is the ratio of the intensity of the adhesive force to the typical hydrodynamic force in a dilute suspension; we are going to vary this parameter to vary the adhesion between the particles and between the particles and the walls, or equivalently to vary the shear stress for a constant adhesion force between particles; we note that G_0^{adh} does not involve the suspension viscosity, but only the solvent viscosity and, as a consequence, its inverse is actually to be considered a reduced shear rate in a concentrated suspension.

In experiments, the shear rate is varied for given properties of the particles (stiffness, adhesive force). In that frame, both $\dot{\Gamma}$ and G_0^{adh} would vary, such that $\dot{\Gamma} \times G_0^{adh}$ is constant. This is not done here and, as said above, $\dot{\Gamma}$ is kept constant. This should not be of importance in the present work: without adhesion, this should have no effect if $\dot{\Gamma}$ is kept high enough (Section 2.6), and in previous simulations performed using the FCM with $\dot{\Gamma} \times G_0^{adh} = \text{const}$ this showed no effect (as it will be presented in the following).

5.3.2 NUMERICAL PARAMETERS

For each of the three considered values of the friction coefficient μ, sequences of equal or similar volume fractions ϕ_0 are chosen, for which the adhesion parameter G_0^{adh} is varied.

In Table 5.1 the parameters used in the simulations for the three friction coefficients $\mu = [0.0,\ 0.1,\ 0.5]$ are shown. In general, the main idea is to choose such parameters to obtain results that fill a grid with more or less constant core volume fractions and shear stresses. Then, for each value of the volume fraction (or a list of similar volume fractions, as for $\mu = 0.0$ and $\mu = 0.1$), the adhesion parameter G_0^{adh} is let vary from high values (strong adhesive forces) to low ones (weak adhesive forces).

It has to be specified that the campaign for $\mu = 0.5$ was first performed. In that case, the volume fraction ϕ_0 is kept constant for multiple values of G_0^{adh}; this is slightly different for $\mu = 0.0$ and $\mu = 0.1$, for which each value of ϕ_0 has a specific associated value of G_0^{adh}. Also, the volume fractions employed for $\mu = 0.0$ and $\mu = 0.1$ are in general higher, because we expect higher jamming volume fractions for lower friction coefficients. The other reasons why for $\mu = 0.0$ and $\mu = 0.1$ higher volume fractions ϕ_0 have been chosen and why they have been varied more often will be clearer after discussing the results.

Table 5.1
Numerical parameters for the three values of the friction coefficient $\mu = [0.0,\ 0.1,\ 0.5]$: chosen volume fractions ϕ_0 and associated adhesive coefficients G_0^{adh}.

$\mu = 0.5$	
ϕ_0 [%]	G_0^{adh}
27	97, 29, 14, 4.4, 2.66, 1.6, 0.66, 0.29
32	184, 92, 37, 7.3, 4.44, 2.3, 0.96, 0.37
37	435, 104, 17.4, 9, 4.4, 1.67, 0.65
42	405, 53, 22.12, 11, 3.63, 1.2
45	377, 226, 44.72, 23, 6.54, 2.5

$\mu = 0.1$	
ϕ_0 [%]	G_0^{adh}
36, 36, 37, 37	9.34, 4.05, 1.9, 0.9
41, 41, 42, 42	17.9, 7.2, 3.27, 1.5
45, 45, 47, 47	30, 11.3, 6.92, 3
49, 50, 51, 52	84, 33, 17.1, 8.83
52, 54, 55, 56	336, 180, 93, 48

$\mu = 0.0$	
ϕ_0 [%]	G_0^{adh}
36, 36, 37, 37	4.71, 2.95, 1.72, 0.74
41, 41, 42, 42	13.5, 6.2, 2.85, 1.32
46, 46, 47, 47	24, 10.6, 5.46, 2.43
50, 51, 52, 53	54, 28, 14.4, 7.44
54, 56, 57, 58	216, 199, 103, 53

5.3.3 SIMULATION DOMAIN

As already mentioned, in all the results presented in the current chapter the domain size is $(L_x \times L_y \times L_z) = (20a_1 \times 20a_1 \times 20a_1)$, and a simple shear flow as in Fig. 5.2 [left] is imposed with a shear rate equal to $\dot{\gamma}_0 = 1$.

In an attempt to limit wall-depletion and shear-banding (Section 5.4.1), for $\mu = 0.0$ and $\mu = 0.1$ particles have been "attached" to the walls (i.e., they have the same velocity as the walls: this choice has been done aiming at better shearing the suspension. Numerically, the particles are attached to the walls by simply considering a bigger domain size in the direction of the walls when initially filling the domain with the specified volume fraction. For the cases presented here, the domain size is increased by a length equal to $1.4a_1$ for each wall during the filling.

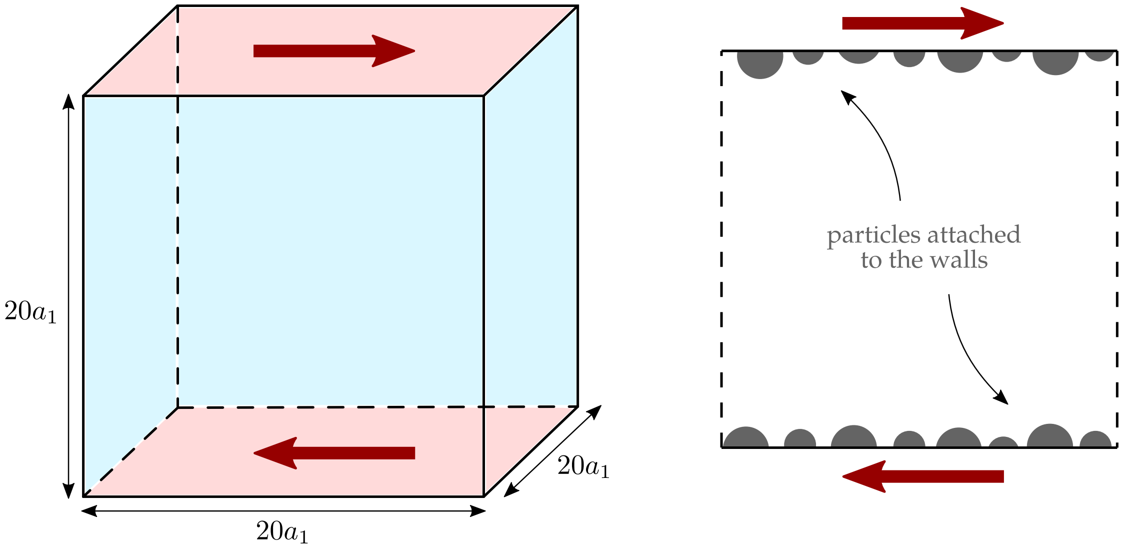

Figure 5.2
(left) Numerical domain employed for all the simulations presented in the current chapter. (right) For $\mu = 0.0$ and $\mu = 0.1$, particles have been attached to the walls to better shear the suspension.

5.3.4 RHEOLOGY

The mean stress and the volume fraction, as well as their profiles, are computed as in Section 2.7 (see Eqs. (2.70) to (2.75)). Also, the adhesive part of the stresses can be easily isolated from the elastic one. Generally speaking, this separation of the two contributions may be a bit arbitrary, but in the frame of our model, it should be recalled that only the elastic part affects friction, and therefore it may make sense to separate it from the adhesive contribution. The volume fraction and particle velocity profiles $\phi(y)$ and $\mathbf{u}_{p,x}(y)$, respectively, are computed as defined in Eqs. (2.70) and (6.4).

5.4 RESULTS

We present in this section the simulation results obtained with the FDM. We investigate three values of the friction coefficient: $\mu = [0.0;\ 0.1;\ 0.5]$. For each of them, we vary the adhesive forces, i.e. we vary the adhesive parameter G_0^{adh}, and we study the typical rheological quantities. To have a wider view, we integrate also some results earlier obtained with the Force Coupling Method.

We will show how to analyze the results and exploit them to obtain the desired quantities: in particular, data will need to be interpolated. But first, the shear-banding and wall-depletion observed at low volume fractions and high adhesion are displayed. To this purpose, different quantities may be defined upon averaging either in the core homogeneous suspension, where the walls exert no influence (*core* quantities), or in the whole simulation domain (*apparent* quantities). In more detail, the apparent relative viscosity reads:

$$\frac{\Sigma_{12}}{\eta\dot{\gamma}_0} = \eta^s_{app} \tag{5.3}$$

where Σ_{12} is the mean shear stress averaged over the whole simulation domain and over time (in the stationary regime).

Let us now define quantities in the suspension core, where no wall-layering is observed. The shear rate $\dot{\gamma}_{core}$ is computed from the linear regression of the particle velocity profile and is then time-averaged over the stationary regime. Since particle layering in the vicinity of the walls induces wall slip, the core shear rate is smaller than the imposed one $\dot{\gamma}_0$, at least when the walls are not roughened using attached particles. In addition, the volume fraction in the wall area is smaller than its counterpart in the core region, so that $\phi_{core} > \phi_0$. This leads to a measured core adhesive parameter G^{adh}_{core} and a core reduced shear stress:

$$\begin{gathered}\frac{F^{adh}}{6\pi\eta\dot{\gamma}_{core}a_1^2} = G^{adh}_{core}\\ \frac{6\pi\Sigma_{12,core}a_1^2}{F^{adh}} = \sigma^* = \frac{\eta^s_{core}}{G^{adh}_{core}}\end{gathered} \tag{5.4}$$

where the core relative viscosity η^s_{core} is computed from the time-averaged core shear stress and shear rate as:

$$\frac{\Sigma_{12,core}}{\eta\dot{\gamma}_{core}} = \eta^s_{core} \tag{5.5}$$

It should be noted that, given a specific system in experiments, keeping a constant σ^* corresponds to keeping a constant shear stress. Thus, σ^* is the ratio of the shear stress to the stress $F^{adh}/\left(6\pi a_1^2\right)$, which is the typical stress needed to separate two particles at contact.

5.4.1 WALL-DEPLETION AND SHEAR-BANDING

In the cases of moderately concentrated suspensions and high adhesive forces, the particles may form a single cluster, or sometimes two clusters, which do not deform, most of the time due to a clear layer in the vicinity of the walls that results in a strong wall-slip: this behavior is called *wall-depletion*. In such cases, the core shear rate $\dot{\gamma}_{core}$ drops to very low values, sometimes exactly zero: this behavior is called *shear-banding*.

To better understand these mechanisms, an example is given in Fig. 5.3: the results for two mean volume fractions $\phi_0 = 0.27$ (blue lines, upper three rows) and $\phi_0 = 0.45$ (green lines, lower three rows), with same friction coefficient $\mu = 0.5$, and multiple adhesion parameters G_0^{adh} (increasing from left to right) are given.

As we can observe, for the cases with low mean volume fraction and high adhesive forces (on the right of the upper three rows), agglomerations of particles arise, leading to volume fraction profiles (time-averaged in the stationary regime) that are not constant in the core region, contrarily to the non-agglomerated cases with low adhesive forces (on the left of the upper three rows). Also, in the agglomerated cases the core shear rate decreases during the simulation run and it can reach very low values, sometimes exactly zero, showing that the suspension is no longer deformed and agglomerates are only translated. We note that, in general, the agglomerated cases exhibit a long transient, so it is very important to wait for the stationary regime to be able to see such behavior.

The above-mentioned behavior is not observed in suspensions with high volume fractions, not even in the cases with high adhesive forces, as we observe in the lower three rows of Fig. 5.3 (i.e., for $\phi_0 = 0.45$), where the suspension always shows a finite shear rate $\dot{\gamma}_{core}$ and the corresponding volume fraction profiles (time-averaged in the stationary regime) show a constant region in the core.

The quantities in Fig. 5.3 for $\phi_0 = 0.45$ also present strong oscillations, showing the importance of performing long-lasting simulations. All the simulations have been launched for a deformation of the core region during the stationary regime of at least $\approx 25t\dot{\gamma}_{core}$.

In the cases where $\dot{\gamma}_{core} \approx 0$, the core relative viscosity η^s_{core} cannot be defined. In Fig. 5.4 the results for $\mu = 0.5$ are shown, where the computed apparent relative viscosity is also displayed. We notice that in the agglomerated cases η^s_{app} levels off: this is only a side effect of shear-banding (*"apparent"*, indeed). We note that in the context of experimental measurements in the presence of shear-banding, a viscosity close to η^s_{app} is expected.

Fig. 5.4 displays the trends that have been explained above: at high mean volume fraction ϕ_0, reducing the stress induces a slight increase of the volume fraction, and a decrease of the core-shear rate, which keeps finite though. The viscosity seems to diverge, suggesting the existence of a yield stress. At a lower mean volume fraction, the viscosity increases too as the stress is decreased, but the conclusions are blurred by the concomitant increase of the core volume fraction. In that case, low-stress measurements are impeded due to shear-banding.

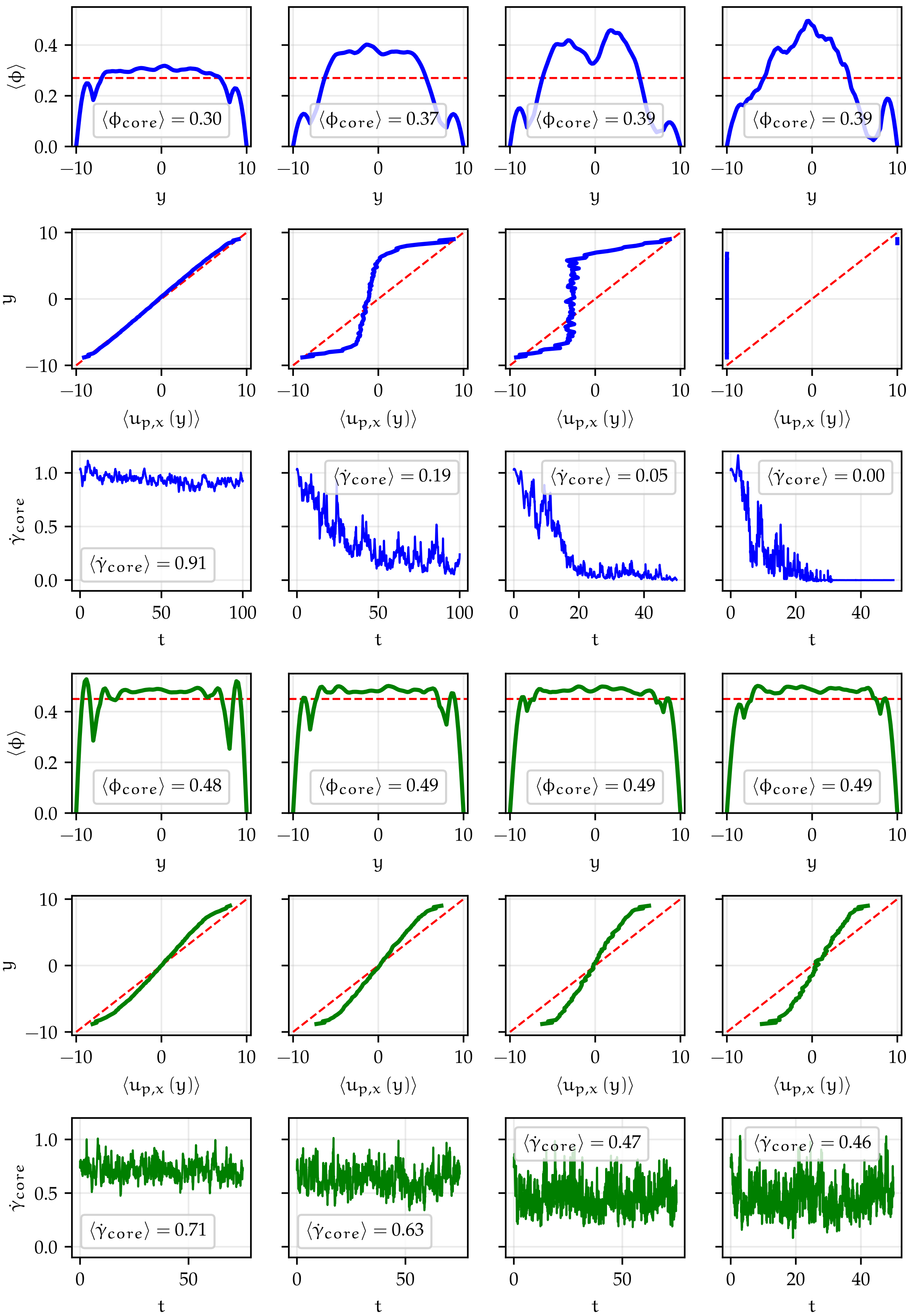

Figure 5.3
Volume fraction profiles $\langle\phi\rangle$ and particle velocity profiles $\langle u_{p,x}(y)\rangle$ (both time-averaged in the stationary regime), and evolution in time of the core shear rate $\dot\gamma_{core}$, for $\mu = 0.5$ and different adhesion parameters G_0^{adh} (increasing from left to right): (blue lines, upper three rows) results for $\phi_0 = 0.27$ ($\sigma^* = [10.59,\ 0.4,\ 0.21,\ 0.07]$), and (green lines, lower three rows) results for $\phi_0 = 0.45$ ($\sigma^* = [7.84,\ 2,\ 0.9,\ 0.82]$).

Finally, in both volume fraction ranges, homogeneous straining of the suspension is only possible for reduced stress larger than typically 1. This suggests that the yield stress satisfies the following intuitive relation:

$$\sigma_c^* \sim \frac{F^{adh}}{6\pi a_1^2} \tag{5.6}$$

meaning that the stress needs to be high enough for the induced force between the particles to break adhesive bonds between particles. We finally recover the qualitative definition of a yield fluid: if the shear stress is too weak, the material does not flow.

To conclude, it is very difficult to simulate systems with $\sigma^* \lesssim 1$, and the exact critical value (the yield stress) depends on the mean volume fraction ϕ_0: for $\phi_0 \gtrsim 0.4$, the core volume fraction slightly increases and the relative viscosity diverges, leading to prohibitive computational costs while approaching the yield stress; for $\phi_0 \lesssim 0.4$, the relative viscosity increases too, but now the core volume fraction strongly increases, leading to very low values of the core shear rate (often exactly zero) and results become unclear or unusable.

We recall that $\mu = 0.5$ has been the first simulations campaign, and we have seen that in some cases, shear-banding and wall-depletion were observed. For $\mu = 0.0$ and $\mu = 0.1$, we tried to avoid these behaviors: this is why, as previously introduced, we decided to attach particles to the walls (as shown in Fig. 5.2 [right]), aiming at better shearing the suspension. In Fig. 5.5, the volume fraction and particle velocity profiles as well as the

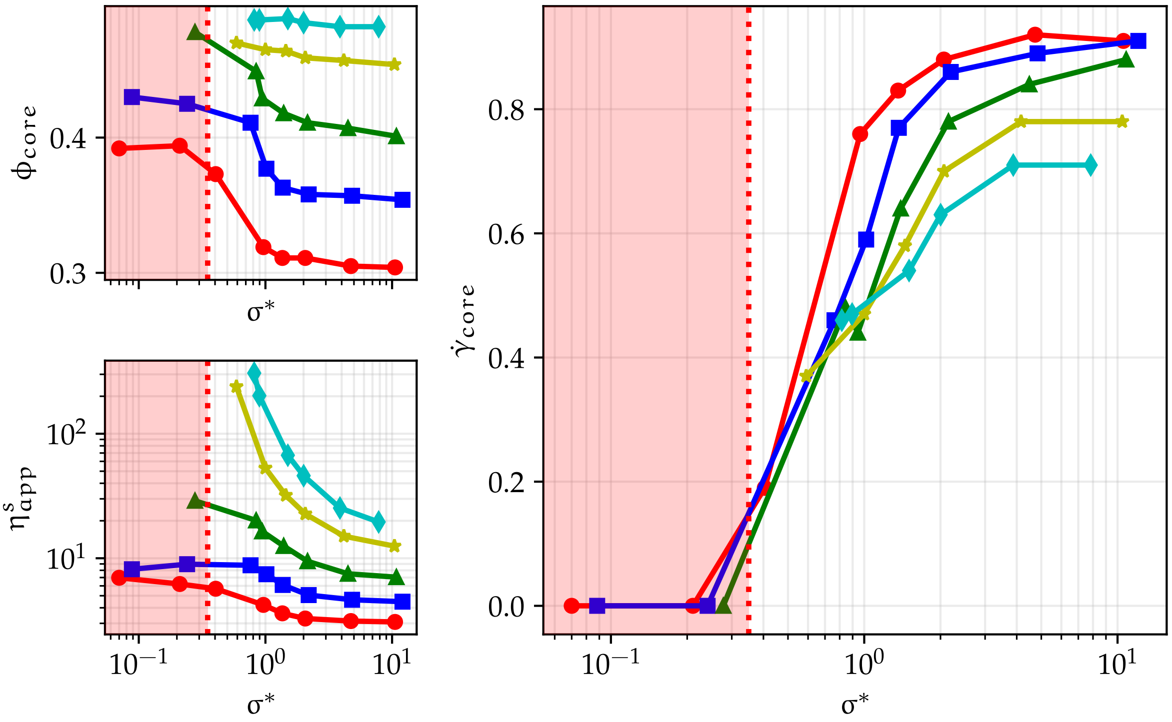

Figure 5.4
Time-averaged (upper left) core volume fraction ϕ_{core}, (lower left) apparent relative viscosity η^s_{app}, and (right) core shear rate $\dot{\gamma}_{core}$, as a function of the reduced shear stress σ^*, for different values of ϕ_0 and with $\mu = 0.5$. Symbols: (●) $\phi_0 = 0.27$, (■) $\phi_0 = 0.32$, (▲) $\phi_0 = 0.37$, (★) $\phi_0 = 0.42$, (♦) $\phi_0 = 0.45$. The lines are a guide to the eye. Red region: shear-banding regime.

temporal evolution of the shear rate for $\mu = 0.1$, $\phi_0 = 0.36 - 0.37$, and varying the adhesion parameter (increasing from left to right), are shown. Observing the results, we notice that the shear rate never reaches values close to zero (the results for $\mu = 0.0$, although not shown here, are analogous). Therefore, we have the feeling that the suspension is indeed better sheared in cases with high adhesion when particles are attached to the walls.

However, a definitive conclusion about the effect of attaching particles to the walls cannot be done at this point, as a systematic comparison of simulations with smooth (but still frictional) and rough walls and with otherwise same parameters should be done. Also, we expect this stratagem not to be completely sufficient to avoid shear-banding. Indeed, we tried to attach particles to the walls in one of the cases with $\mu = 0.5$ showing shear-banding, but the results showed no difference when compared to the ones obtained without using this stratagem. Therefore, we expect this expedient to work only – and partially – for moderately concentrated and concentrated suspensions. Moreover, we note that the volume fraction at the walls is always larger than the mean volume fraction, meaning that, as the particles at the walls were frozen, some layering still occurred. Increasing the size of the box used in the preparation of the roughened wall (Section 5.3.3) may improve this point.

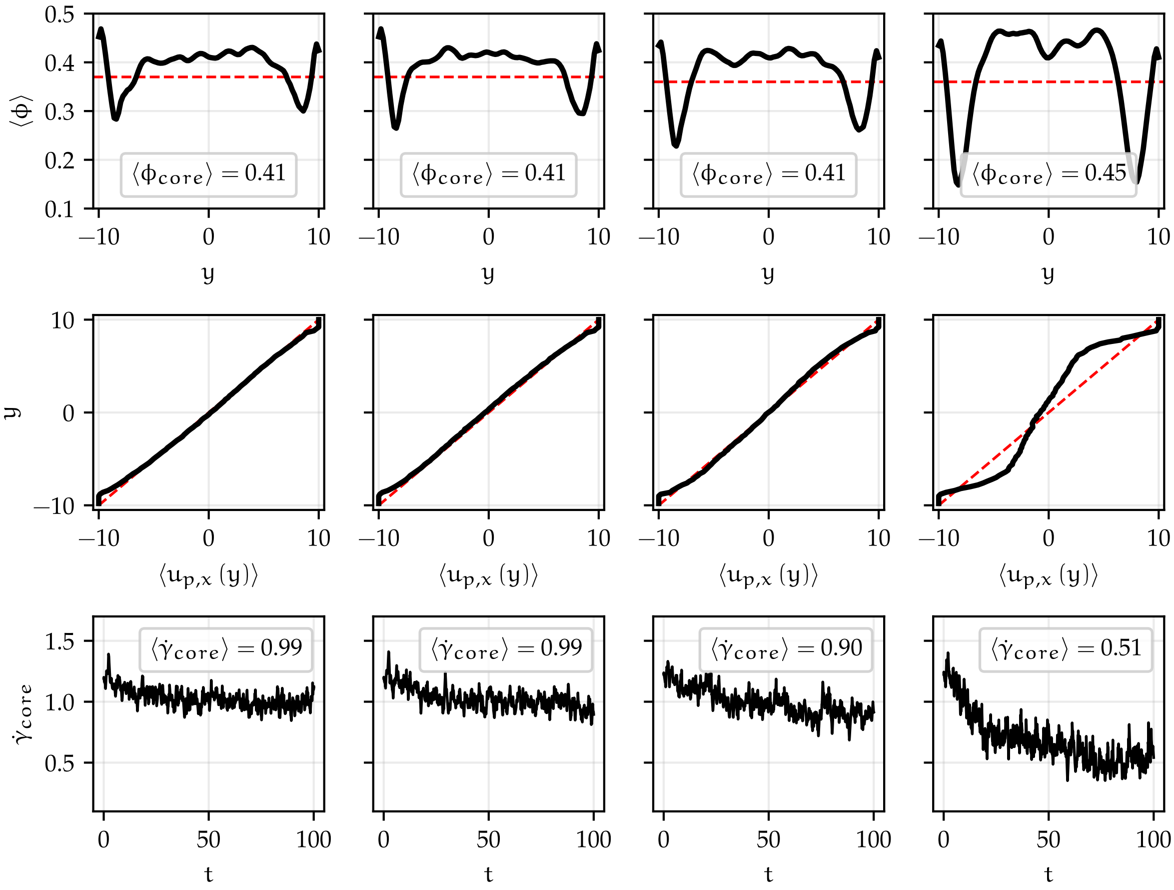

Figure 5.5
(top row) volume fraction and (center row) particle velocity profiles $\langle \phi (y) \rangle$ and $\langle u_{p,x} (y) \rangle$, respectively, time-averaged in the stationary regime, and (bottom row) temporal evolution of the core shear rate $\dot{\gamma}_{core}$, for $\mu = 0.1$ and different adhesion parameters G_0^{adh} (increasing from left to right): results for $\phi_0 = [0.37,\ 0.37,\ 0.36,\ 0.36]$, $\sigma^* = [7.71,\ 3.74,\ 1.84,\ 0.98]$).

5.4.2 MATERIAL FUNCTIONS: RAW DATA

Let us now investigate the reduced shear stress σ^* and the core volume fraction ϕ_{core}, shear rate $\dot{\gamma}_{\text{core}}$, and relative viscosity η^s_{core}, for the three values of the friction coefficient $\mu = [0.0;\ 0.1;\ 0.5]$ and while varying the adhesion parameter G^{adh}, i.e. while varying the reduced shear stress σ^*.

In Fig. 5.6, the shear stress is shown as a function of the shear rate: yield stresses are quite visible for the two curves for $\mu = 0.5$ with the highest volume fractions ($\phi_{\text{core}} \approx 0.47$ and $\phi_{\text{core}} \approx 0.48$), for which the stress seems to level off at low shear rate. For lower values of the friction coefficient the results are more difficult to interpret because, as already pointed out, the core volume fraction is not constant when varying the shear stress.

As we can see in Fig. 5.7 [top], and as we already explained for $\mu = 0.5$, the core volume fraction ϕ_{core} is rarely constant when decreasing the shear stress. For $\mu = 0.0$ and $\mu = 0.1$ we even tried to decrease ϕ_0 when increasing G_0^{adh} (recall Table 5.1) aiming at obtaining a more or less constant ϕ_{core}: however, we notice that we still got an increase of ϕ_{core} for the low volume fractions (indicating that a stronger decrease is needed, or equivalently that we are approaching the shear-banding regime), and for the high ones we got a decrease of ϕ_{core} (indicating that a weaker or no preventive decrease should be needed). Also, the relative viscosity η^s_{core} increases when decreasing the shear stress and approaching $\sigma^*_c \sim 1$: the effect is more pronounced for $\mu = 0.5$, and less visible for the other friction coefficients, due to the decrease of ϕ_{core}, which shades the increase of the viscosity.

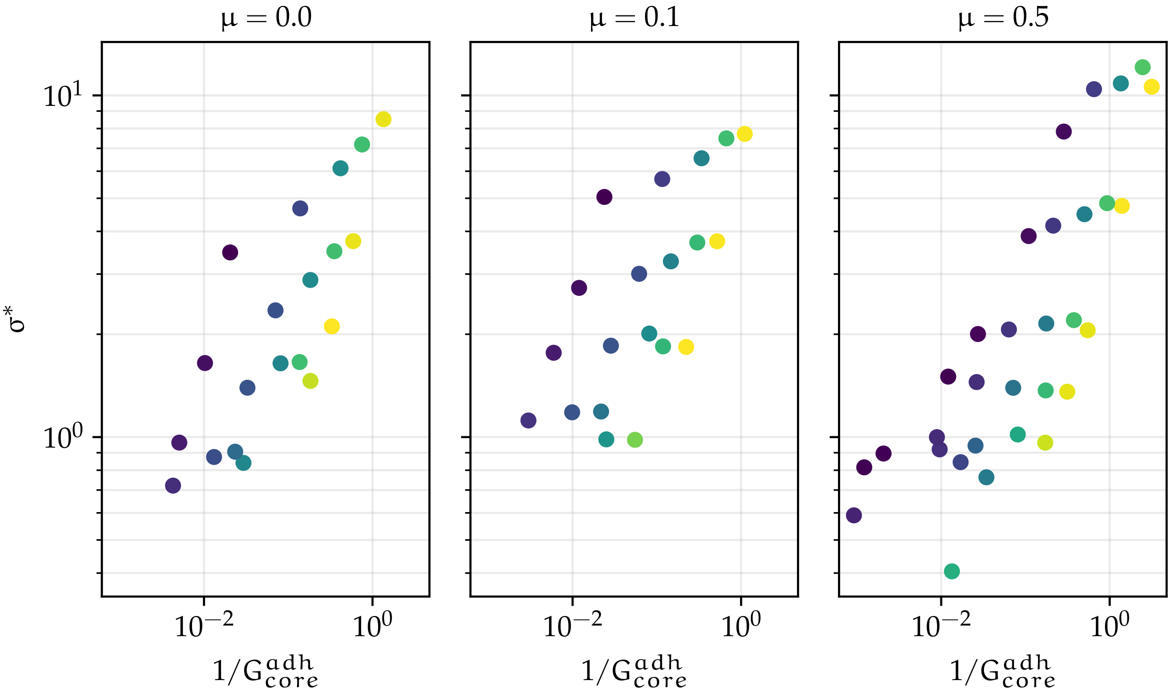

Figure 5.6
Reduced shear stress as a function of the reduced shear rate, for the three friction coefficients. The color of the points is related to the core volume fraction (the darker the color, the higher ϕ_{core}).

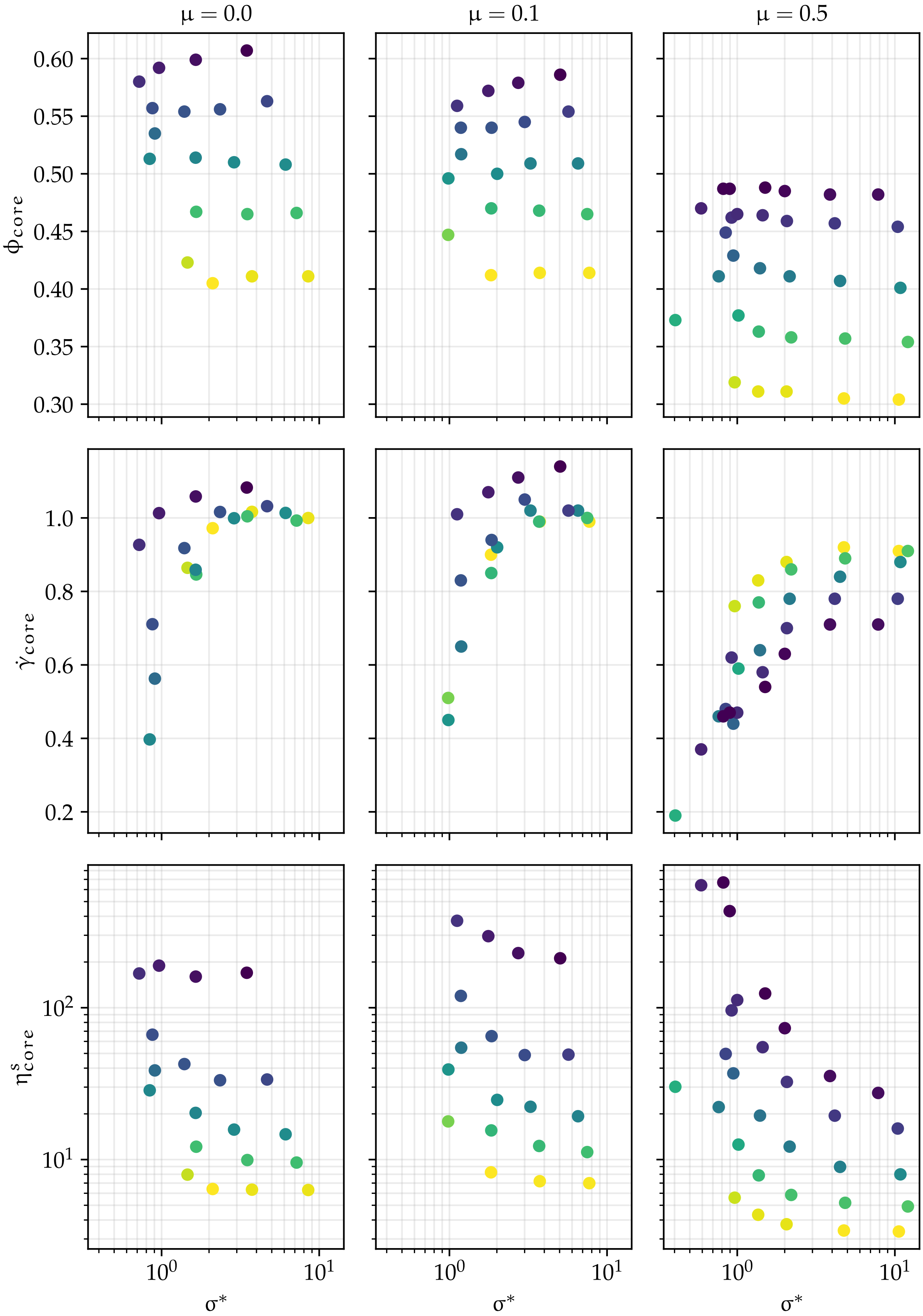

Figure 5.7
Core material functions for (left column) $\mu = 0.0$, (central column) $\mu = 0.1$, and (right column) $\mu = 0.5$: (top row) core volume fraction, (central row) core shear rate, and (bottom row) core relative viscosity, as functions of the reduced shear stress. The color of the points is related to the core volume fraction (the darker the color, the higher ϕ_{core}).

5.4.3 MATERIAL FUNCTIONS: INTERPOLATED DATA

All the quantities considered from now on refer to the core region. Therefore, for the sake of simplicity, the "core" notation is dropped in the text (but kept in the figures).

We have previously explained that the relative viscosity η^s depends on two parameters: the volume fraction ϕ and the shear stress σ^*. However, only the apparent adhesion parameter G_0^{adh} is imposed, and not the reduced stress. In addition, the core volume fraction is not controlled either but only measured. To have a better understanding of the dependence the quantities show with respect to adhesion, the data need to be interpolated.

Let us start by taking the case $\mu = 0.5$ as an example, and let us interpolate the relative viscosity at selected values of the volume fraction and shear stress. This has been done by performing a cubic 2D interpolation and using a logarithmic scale for both η^s and σ^*. In Fig. 5.8, as an example, an interpolation of η^s over a very fine grid (ϕ, σ^*) is shown to evidence the double dependence of the relative viscosity on the volume fraction and the shear stress. For quantitative processing, to guarantee the accuracy of the interpolated data, values of ϕ and σ^* have been selected close to the raw ones. The interpolated values are displayed in Fig. 5.9 and are compared to the raw data. As we can see, the yielding behavior previously shown in Fig. 5.6 is now clearer (Fig. 5.9 [left]). We can also appreciate the effect of the volume fraction: for the same shear rate $\dot{\gamma}$, a higher shear stress σ^* is obtained for a higher volume fraction ϕ; also, we can foresee that the extrapolated value of the shear stress (i.e., the yield stress) increases with ϕ. In Fig. 5.9 [right], the relative viscosity is displayed

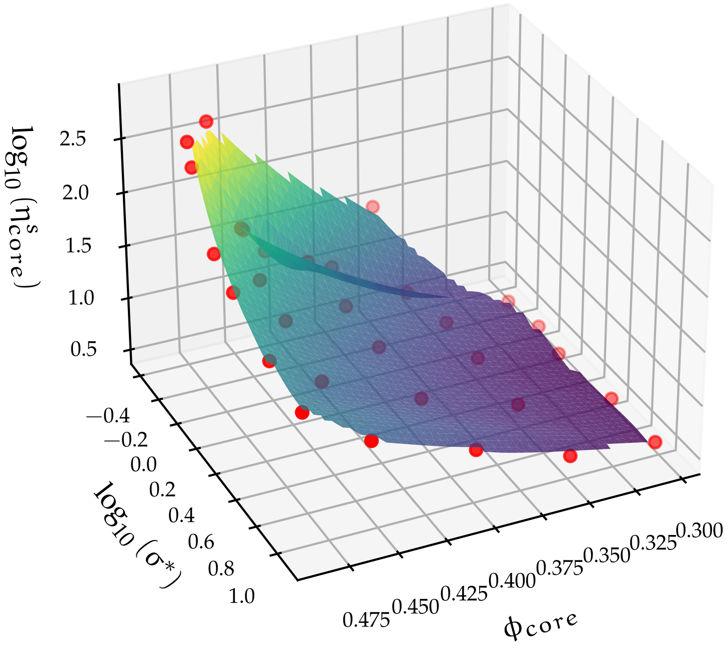

Figure 5.8
Three-dimensional plot of the core relative viscosity η^s_{core} as a function of both the core volume fraction ϕ_{core} and the reduced shear stress σ^*, for $\mu = 0.5$. The raw data (●) have been interpolated along both ϕ_{core} and σ^* with a high number of interpolation points to obtain a smooth fine grid (surface).

for different values of the shear stress as a function of the volume fraction: in this case, too, the jamming mechanism previously shown in Fig. 5.7 is now clearer, evidencing that the jamming volume fraction ϕ_J decreases with σ^*.

The above-described procedure would be less accurate for the cases with $\mu = 0.1$ and $\mu = 0.0$ because the raw data are more misaligned. This is why we performed a linear interpolation of both $\log(\eta^s)$ and ϕ, separately, at selected values of $\log(\sigma^*)$, the latter being chosen close to the raw data to increase the accuracy of the interpolation. For the sake of consistency, we re-interpolated the data for $\mu = 0.5$ with this procedure choosing the same values for σ^* as in Fig. 5.9. The interpolation results are proposed in Fig. 5.10, where a comparison with the raw data is shown. It should be noted that the interpolated values for $\mu = 0.5$ are indeed closer to the raw data.

Based on the obtained results, we can represent the viscosity with a function of the form: $\eta^s = f(\phi, \phi_J(\sigma^*))$. This description has already been proposed by other authors (Zhou et al., 1995; Snabre & Mills, 1996; Abhinendra Singh et al., 2019; Richards et al., 2020; Gilbert et al., 2022). Fitting the results with such a function, the jamming volume fraction ϕ_J can be obtained for each specific shear stress σ^*. This procedure is a bit tricky: as noted below, the available data, including interpolated values, are scarcer in the low-volume-fraction and low-stress range. In more detail, the data from the simulations are interpolated at constant values of σ^* by fitting a stress-dependent Maron-Pierce law:

$$\eta^s = \frac{\alpha(\sigma^*)}{\left(1 - \frac{\phi}{\phi_J(\sigma^*)}\right)^2} \tag{5.7}$$

where α and ϕ_J are free parameters. Then, the jamming volume fractions ϕ_J for different shear stress values can be obtained.

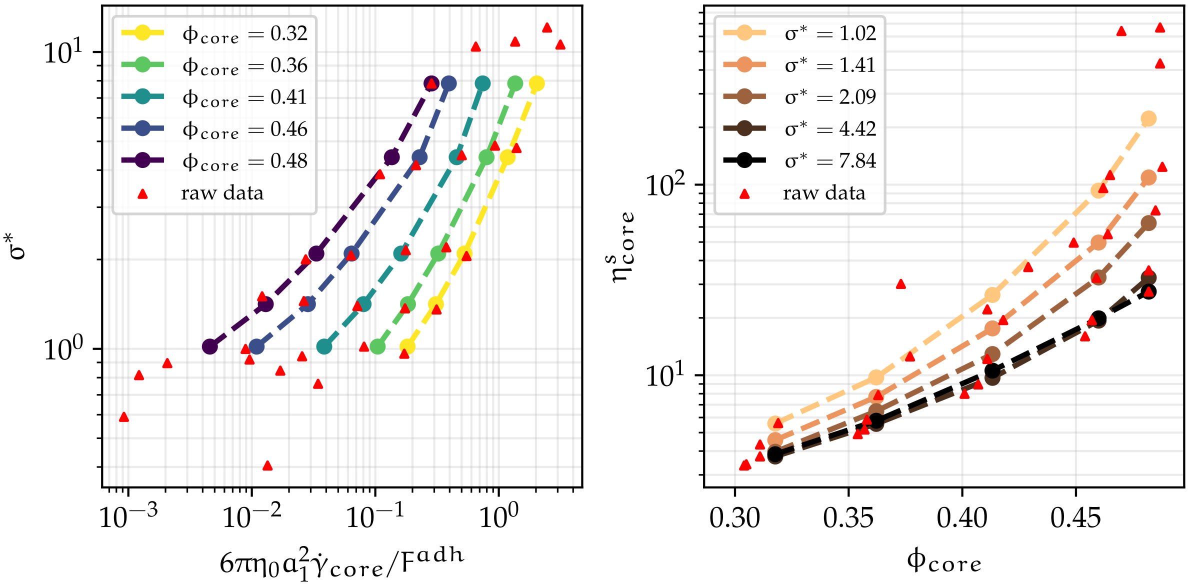

Figure 5.9
The raw data for $\mu = 0.5$ shown in Figs. 5.6 and 5.7 is interpolated at selected values of the core volume fraction and reduced shear stress.

The interpolated data together with the fitting functions from Eq. (5.7) are displayed in Fig. 5.11. The results without adhesion from Section 4.2 for $\mu = 0.5$, the ones from Gallier et al. (2018) for $\mu = 0.0$, together with unpublished data by Stany Gallier for $\mu = 0.1$, are added. As it can be observed, at high shear stress the adhesionless viscosity is recovered, and the lower the shear stress the lower the jamming volume fraction. The latter behavior is less and less pronounced when decreasing the friction coefficient, in the limit of $\mu = 0.0$ for which the jamming volume fractions are seemingly almost the same for any of the considered shear stresses.

Another peculiar behavior can be observed for $\mu = 0.0$: we notice that at high volume fractions, the viscosity diverges more rapidly, losing the linearity of $1/\sqrt{\eta^s}$ with ϕ (it is very clear in the results without adhesion from Gallier et al. (2018)). This could indicate the presence of two different zones of viscosity: one for low-to-medium volume fractions which is conveniently described by Maron-Pierce law and one for high volume fractions with a faster divergence of the viscosity. This trend is absent for $\mu = 0.5$, for which there is a linear dependence between $1/\sqrt{\eta^s}$ and ϕ. While, in the case of $\mu = 0.1$, this double behavior of the viscosity is visible at high stresses and in the results without adhesion.

For $\mu = 0.0$, the relative viscosity varies quite slowly with the shear stress. This could suggest that σ^* has not been decreased enough. On the other hand, we already observe a strong increase in the core volume fraction suggesting the inception of shear-banding.

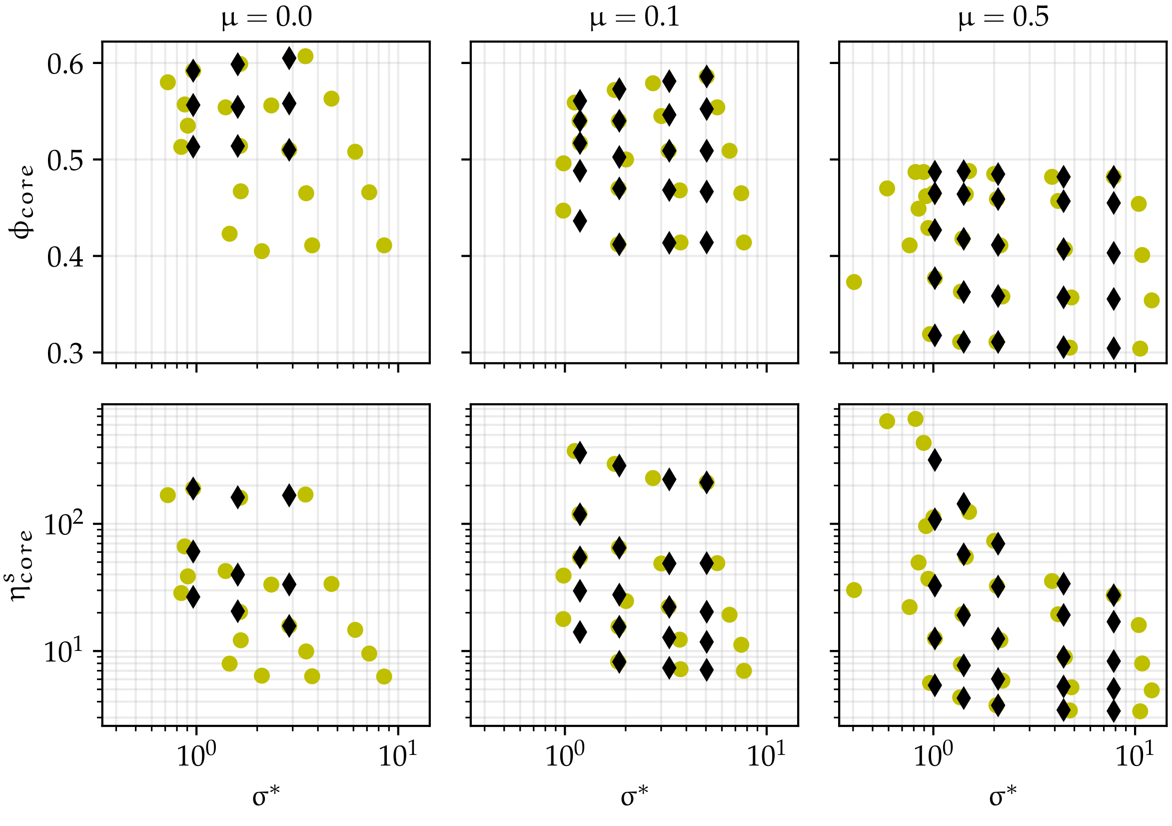

Figure 5.10
(●) same data for ϕ_{core} and η^s_{core} as in Fig. 5.7, interpolated (♦) at constant shear stresses σ^*.

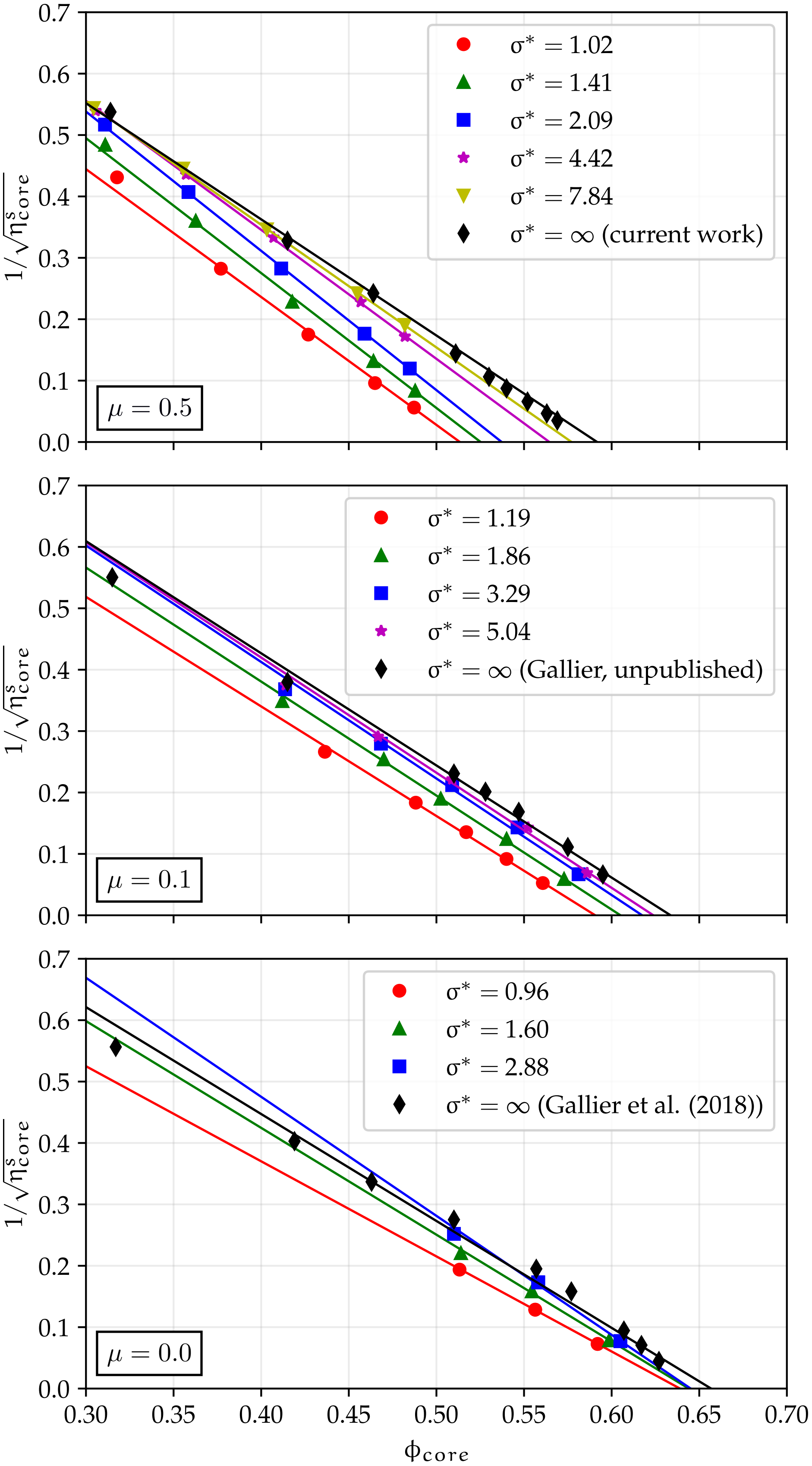

Figure 5.11
Curves obtained by fitting the interpolated data with a Maron-Pierce law (Eq. (5.7)), and comparison with the raw data: (top) $\mu = 0.5$, (center) $\mu = 0.1$, and (bottom) $\mu = 0.0$. The computations without adhesion from Section 4.2 ($\mu = 0.5$), the ones by Gallier et al. (2018) ($\mu = 0.0$) together with unpublished data by Stany Gallier ($\mu = 0.1$) are added (♦).

5.4.4 JAMMING VOLUME FRACTION AND YIELD STRESS

The obtained curves $\phi_J(\sigma^*)$ are shown in Fig. 5.12 (which can also be seen as $\sigma_y^*(\phi)$ curves), and are compared to previous results obtained with the Force Coupling Method (FCM) and not published yet. In particular, the results with the FCM have been obtained using a cubic domain, periodic in all three directions, with size $(16a_1)^3$ and including adhesive forces using the same model as the one employed in the present work. Moreover, the horizontal dotted gray lines in Fig. 5.12 are the jamming volume fractions in the adhesionless case.

We appreciate a very good agreement for $\mu = 0.5$ between FCM and FDM. This has to be considered a validation because, as already pointed out, in the simulations performed with the FCM the product $\dot{\Gamma} \times G_0^{adh}$ has been fixed: this has not been done in the present work and the same results are obtained; therefore, it can be considered that there is no influence of this choice.

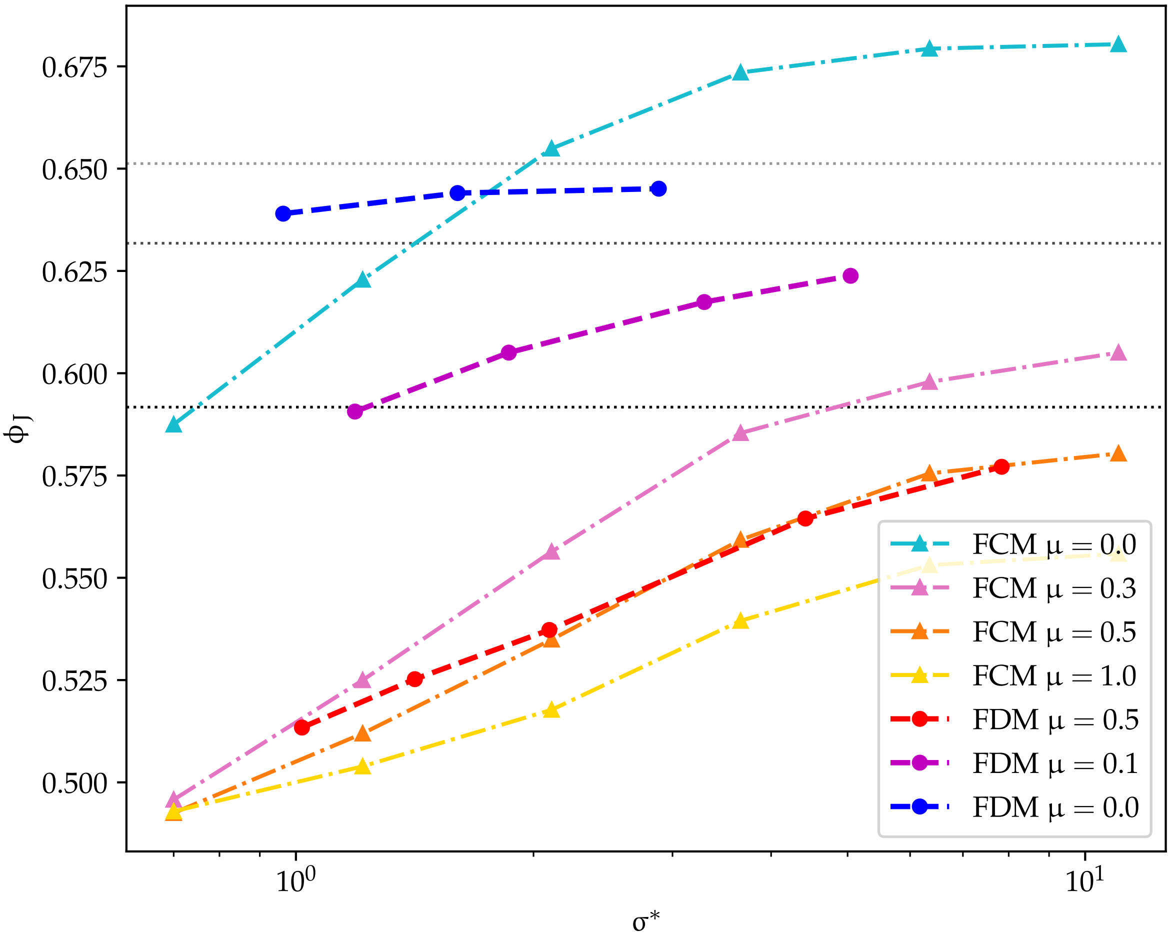

Figure 5.12
$\phi_J(\sigma^*)$: comparison between the results obtained with the FDM in the present work and previous results obtained with the FCM. The horizontal dotted gray lines are the jamming volume fractions in the adhesionless case ($\sigma^* = \infty$): (lower line) from Section 4.2 ($\mu = 0.5$, $\phi_J = 0.592$), (center line) unpublished data by Stany Gallier ($\mu = 0.1, \phi_J = 0.632$), and (upper line) Gallier et al. (2018) ($\mu = 0.0, \phi_J = 0.651$); the results by Stany Gallier have been fitted for $\phi \geqslant 0.45$.

For $\mu = 0.1$ and $\mu = 0.0$, the agreement is less satisfactory. We have already seen in Fig. 5.11 that, in these cases, at high shear stress two different ranges of the volume fraction can be noticed (more evident for $\mu = 0.0$), and that at high values of the volume fraction, the viscosity curve is not well described by Maron-Pierce law. This behavior can justify the disagreement with the results obtained with the FCM for $\mu = 0.0$ because it is fundamental to fit the viscosity at high values of the volume fraction while fitting only at low values of the volume fraction can mislead to non-reliable values of the jamming volume fraction.

This is clearly shown in Fig. 5.13. In the left and center figures, a comparison between the fitting done with the results from the FCM and with the results from the current work is proposed (the results from the FCM have been re-interpolated to perform the comparison at the same shear stress). In the simulations with the FCM, values of the volume fraction in the range $0.30 \leqslant \phi_0 \leqslant 0.45$ have been employed, while in the present work, we get core volume fractions in the range $0.40 \lesssim \phi \lesssim 0.61$. As we can see, fitting only at low values of the volume fraction has different effects depending on the shear stress: at low shear stresses this misleads to lower values of the jamming volume fraction (Fig. 5.13 [left]), while at high shear stresses this misleads to higher jamming volume fractions (Fig. 5.13 [center]). Therefore, this can justify the disagreement in the case of $\mu = 0.0$.

In Fig. 5.13 [right], only the adhesionless results from Gallier et al. (2018) are taken into account, but two different ranges of the volume fraction are used to perform the fitting: considering only $\phi < 0.45$ gives a jamming volume fraction which is considerably higher than the one obtained considering only $\phi \geqslant 0.45$. The values of ϕ_J without adhesion for $\mu = 0.0$ and $\mu = 0.1$ shown in Fig. 5.12 have been computed by fitting η^s at $\phi \geqslant 0.45$.

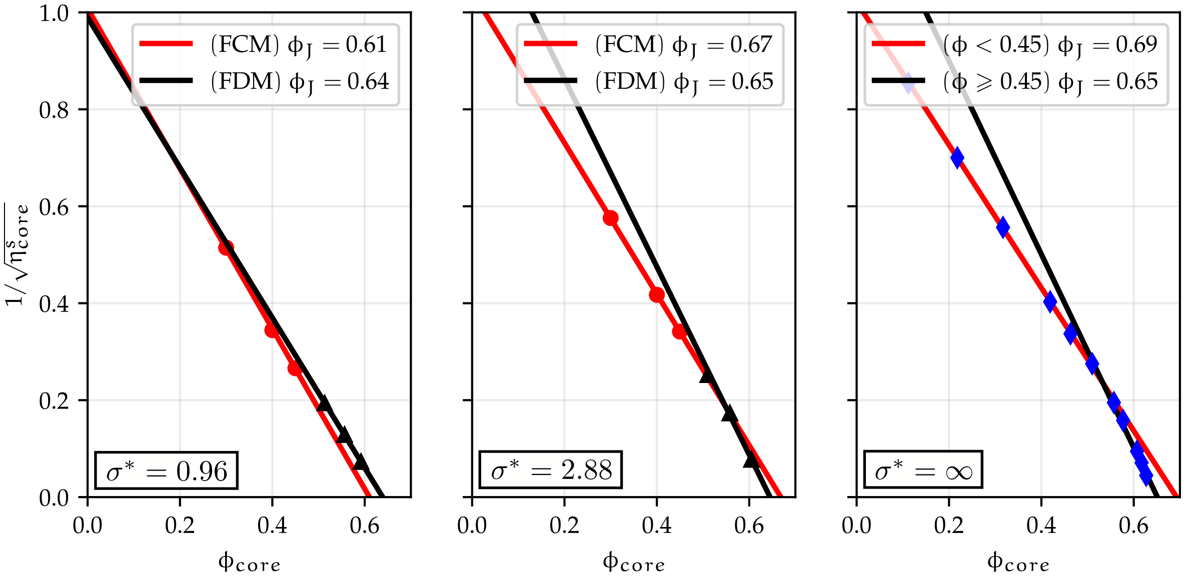

Figure 5.13
Effect of performing a fit at low or high values of the volume fraction for $\mu = 0.0$: comparison between the FCM for which only low values of ϕ_{core} are available and the current work in which higher values of ϕ_{core} are obtained, at (left) low values and (center) high values of the shear stress; (right) comparison between a fit performed only for $\phi_{core} < 0.45$ (red line) and one performed for $\phi_{core} \geqslant 0.45$ (black line), using the data from Gallier et al. (2018) without adhesion.

Finally, the jamming volume fractions proposed here should be considered more reliable, also for the case $\mu = 0.1$, for which no results with the FCM are available.

Fig. 5.12 deserves a few comments. First, the jamming volume fraction increases as the reduced stress increases, and levels off to its adhesionless value. Since the same figure displays the evolution of the yield stress as a function of the volume fraction (as implied by Eq. (5.7)), it means that the yield stress increases with the volume fraction, and diverges as the jamming volume fraction is approached.

Concerning the effect of friction, the high-stress limit of the jamming volume fraction increases as the friction coefficient increases, as already known from simulations of adhesionless suspensions. For high enough a friction coefficient ($\mu > 0.5$), the jamming volume fraction converges toward a single value at $\sigma^* \approx 0.6 - 0.7$, suggesting that the influence of friction on the jamming volume fraction decreases when increasing the adhesive forces. On the other hand, the overall effect of adhesion seems less pronounced at a lower friction coefficient. This last assertion is to be somewhat softened since shear-banding is still observed, which in addition impedes probing the low-stress range.

5.5 DISCUSSION AND PERSPECTIVES

We have seen that adhesion is indeed a really attractive topic. We are starting to understand the effect that adhesive forces have on the rheological properties of dense non-Brownian suspensions in the presence of frictional contact (and in the frictionless case too, for $\mu = 0.0$).

The definition of a jamming volume fraction as a function of the shear stress, i.e. $\phi_J(\sigma^*)$, has already been proposed to describe the yield stress of adhesive suspensions (Zhou et al., 1995; Snabre & Mills, 1996). More recently, Richards et al. (2020) were able to interpret experimental data regarding the viscosity of an adhesive suspension by adapting the so-called "constraint rheology" model proposed by Guy et al. (2015). The authors were able, in a phase space (ϕ, σ^*), to define a flow region and a jamming region, separated by a $\phi_J(\sigma^*)$ curve similar to those we have calculated. In their case, they reach much lower volume fractions, of the order of ≈ 0.35 (≈ 0.20 for Richards (2021)). We stress out that this $\phi_J(\sigma^*)$ curve can also be interpreted as a $\sigma_y^*(\phi)$ curve, identifying the two just mentioned regions where the suspension is either jammed or flowing (see Fig. 5.14). What would be the results at low volume fractions when $\sigma^* \to 1$ is still an open question for us.

From the point of view of the simulations, this same interpretation is implicit in Abhinendra Singh et al. (2019), where the viscosity law of an adhesive suspension is described as the superposition of a Herschel-Buckley law and the viscosity of a suspension with discontinuous shear-thickening (DST). The result is the definition of a phase space (ϕ, σ^*) where the flow area is bounded at low stresses by the yield stress and high stresses by the DST threshold. In our case, only the low-stress threshold line is present since we do not consider shear-thickening suspensions.

An important result of our study is the dependence of the jamming volume fraction (or equivalently of the threshold stress) on friction. We recall that for $\mu > 0.3$, ϕ_J decreases from the adhesionless value, which depends on μ, to a value that is independent of it at low stress. For lower friction coefficients, the decrease is weaker. This result can be related to the model proposed by Richards et al. (2020), which defines a stress-dependent jamming volume fraction for an adhesive suspension, as a weighted average between the jamming volume fraction without adhesion ($\phi_\mu = 0.53$ in their case) and a volume fraction for an adhesive suspension (adhesive loose packing 0.35). The weighting coefficient depends on the stress, as a fraction of particles in adhesive contact.

In our case, we do not manage to decrease the reduced shear stress below $\approx 0.7 - 0.8$, and for $\mu > 0.3$ all the curves $\phi_J(\sigma^*)$ meet in $\phi_J \approx 0.5$. This suggests that the jamming volume fraction for these values of σ^* would be independent of μ and would be ≈ 0.5. For lower friction coefficients, our data are a bit too patchy, yet it appears that the jamming volume fraction is larger, which is consistent with the literature (see Richards et al. (2020) and references therein). Further investigation of our data against the model proposed by Richards et al. (2020) would be interesting, although not straightforward since we cannot decrease σ^* too much.

However, these conclusions should be qualified by the difficulties we had in obtaining measurements at low reduced shear stress. Indeed, it is likely that the too-small size of our simulation volume is at the origin of the wall depletion and the shear-banding that we observe at medium concentrations. Multiple studies, especially for Brownian suspensions, show the appearance of aggregates of various sizes which make the flow heterogeneous

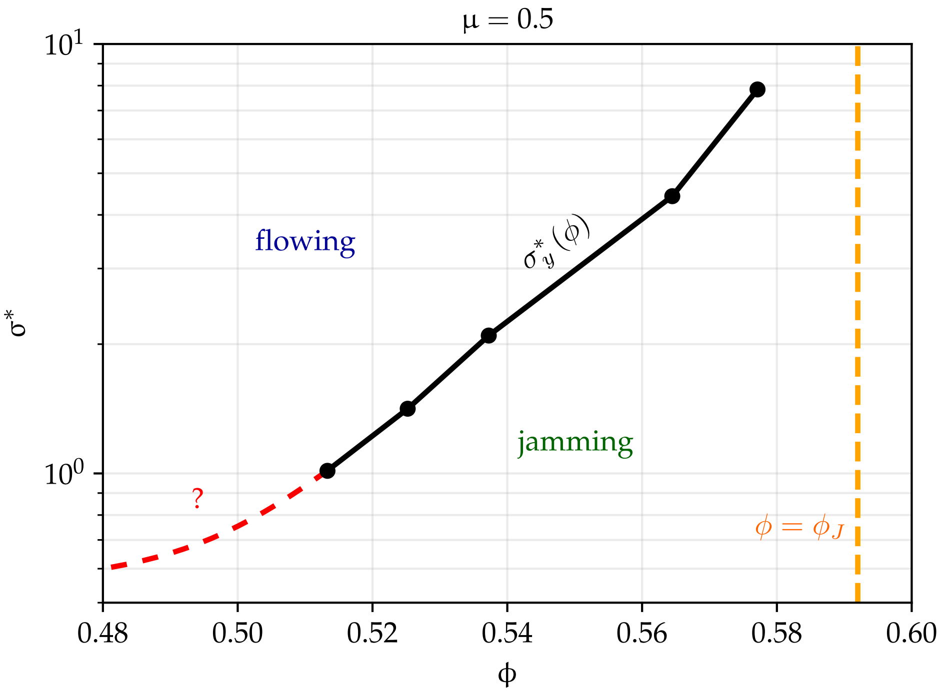

Figure 5.14
The results for $\mu = 0.5$ are displayed as a $\sigma^*_y(\phi)$ curve. What would be the results at low values of ϕ when $\sigma^* = 1$ is approached is still an open question for us.

and modify the rheology of the suspension, and this all the more as the shear stress is low (Koumakis et al., 2015). These aggregates, as soon as they develop with a size of a few particle diameters, would quickly reach the size of our simulation domain. In this case, this would probably lead to a modification of the measured rheology, and possibly to the shear-banding that we observe. It would therefore be essential to continue with larger volume simulations to study the influence of this parameter on the rheology of adhesive suspensions. In the same vein, a detailed study of the suspension microstructure would be useful, for example by measuring the aggregates' size. The pair distribution function of particles at contact would probably be informative.

In particular, we recall that in concentrated regimes the microstructure loses isotropy, establishing a preferred direction for finding the close-contact pairs (see Fig. 1.2 in Section 1.2.2). Increasing adhesion at medium-to-high volume fractions, we observed that this isotropy is more and more recovered for particles at contact while decreasing the shear stress, indicating that the particles remain attached to each other in the dilatation axis. This behavior is also illustrated by the distribution of the normal contact forces on the surface of the particles in Fig. 5.15, showing still-existing adhesive forces in the dilatation axis that counter-balance the elastic forces, keeping together the particles in such a direction in which particles are pulled away from each other. This could be associated with the formation of clusters. At low volume fractions, the investigation becomes complicated due to the formation of aggregates that do not deform (the so-called flocs).

Peculiar results are found when representing the ratio between the contact (elastic + adhesive) contribution to the total shear stress against the viscous number computed only with the elastic normal stress at $\mu = 0.5$: in this case, a master curve can be found. In Fig. 5.16 a comparison between the results from the current chapter, the adhesionless results presented in Section 4.2, and the adhesionless results from Gallier et al. (2018), is proposed. As we can observe, all the results collapse on the same curve. Although not shown here, the agreement with the adhesionless case is more and more lost when decreasing the friction coefficient. The reasons for this disagreement still have to be cleared out, but it suggests that the effect of adhesion might be significant up to larger stresses in the case of frictionless particles. As already pointed out, the size of the simulation domain could have an impact.

We have started to work on these last points, and we will see what comes of it in the future. However, regarding the effect of the size of the simulation domain, it is likely that our numerical method is not the best suited for a parametric study (i.e. systematically varying σ^*, ϕ and μ) for large domain sizes because even though it allows to take into account short and long-range hydrodynamic interactions, as well as complex contact interactions, the counterpart is a relatively long computation time, which makes at the moment difficult the systematic study of systems of more than a few thousands of particles. In the next chapter, we will turn to an application that better matches the advantages of our numerical method, i.e. the study of shear-induced particle migration in a pressure-driven flow.

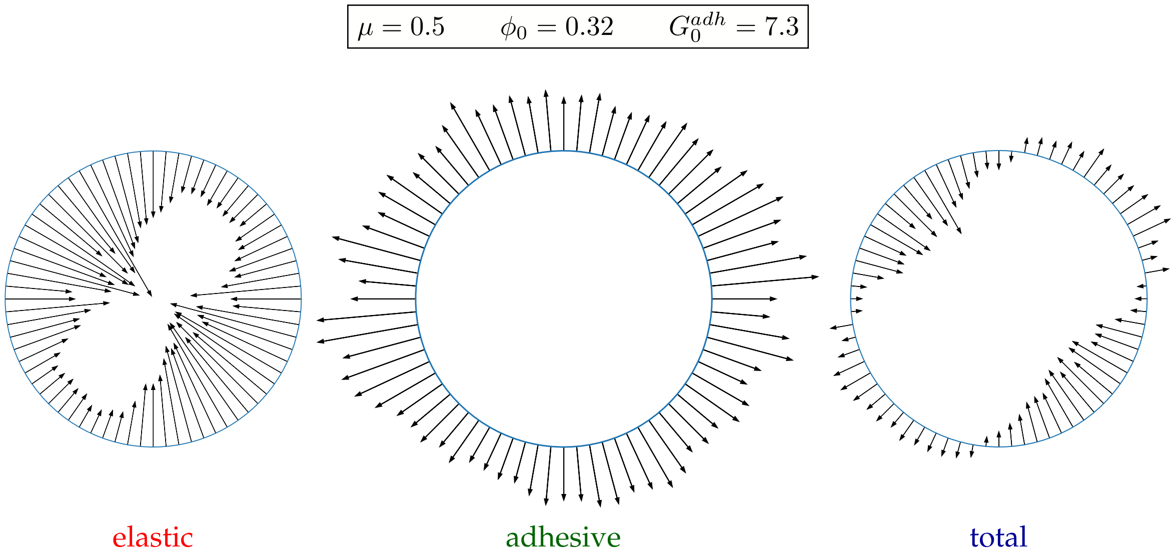

Figure 5.15
Distribution of the normal contact forces on the surface of the particles for a moderately concentrated case at relatively low reduced shear stress ($\sigma^* = 2.2$): comparison between the distribution of the elastic (left) and adhesive (center) contributions to the total elastic normal force (right). The length of the arrows is qualitative.

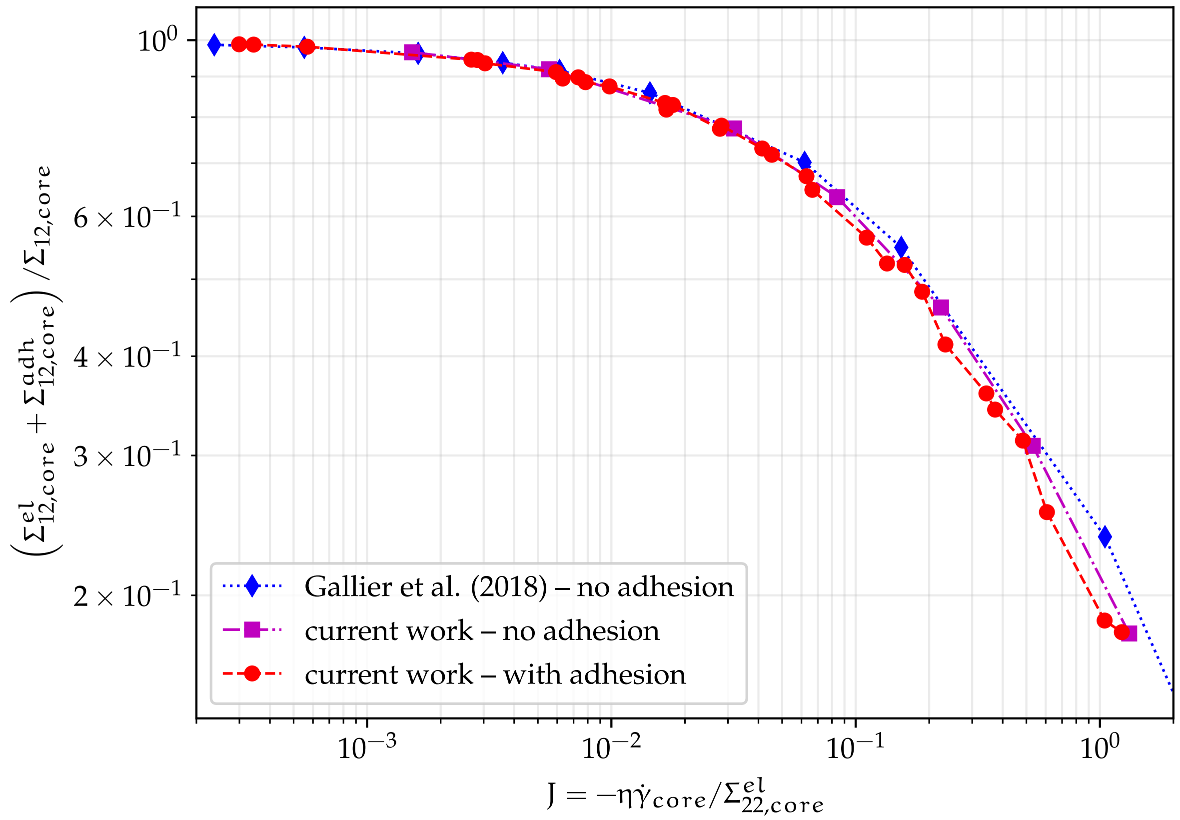

Figure 5.16
Ratio between the contact (elastic + adhesive = total contact) contribution to the total shear stress against the viscous number computed only with the elastic contribution to the normal stress at $\mu = 0.5$: comparison between the results with adhesion presented in this chapter, the ones without adhesion presented in Section 4.2, and the ones without adhesion from Gallier et al. (2018). The lines are a guide to the eye.

6

PRESSURE-DRIVEN FLOWS

A particulate suspension in a nonlinear flow shows shear-induced particle migration. In the present chapter, we simulate the pressure-driven flow of a bidisperse three-dimensional frictional suspension, for three values of the volume fraction. After displaying the chosen numerical setup, we start by investigating the transient volume fraction and particle velocity profiles. Then, we concentrate on the steady-state profiles and we compare the results to a modified version of the Suspension Balance Model (SBM) as proposed by Badia et al. (2022) and recalled in Appendix F. We finish the chapter by studying the various contributions to the local stress balance (in particular, we investigate the shear stress and the second normal stress parallel to the velocity gradient), and by proposing a discussion.

6.1 STATE OF THE ART

PARTICLE MIGRATION

A particulate suspension in a nonlinear flow shows particle migration. The first observations have been made by Karnis et al. (1966) in a pressure-driven tube flow, who found the development of a "plug" at the channel center showing high volume fraction, in which the translational velocity of the particles is almost uniform. Many other experimental studies on Poiseuille-flow suspensions have been made since then (Koh et al., 1994; Hampton et al., 1997; Lyon & Leal, 1998; Gao et al., 2009, 2010), all revealing a gradient in the local concentration. As a result, the suspension velocity develops a blunted profile.

The theoretical development of this kind of suspension flow has been slow due to the complex hydrodynamic interactions and lack of detailed data about the dynamics of the particles. Having direct access to information otherwise unreachable in experiments is where numerical simulations come into play. Many numerical investigations have been performed in this framework, the first being by Nott & Brady (1994), who employed the Stokesian Dynamics approach to study the pressure-driven flow of a single-layer of monodisperse non-Brownian particles at zero Reynolds number: they showed that starting from a homogeneous concentration, particles migrate toward the channel center. They demonstrated that particle migration is a different phenomenon than the migration due to inertial forces first observed by Segré & Silberberg (1962). Nott & Brady (1994) also studied the effect of the volume fraction: at low concentration, particles are separated from the walls by a zone of clear fluid, while increasing the volume fraction causes a decrease of the velocity at the channel center. Moreover, they introduced the concept of "suspension temperature": this quantity measures the fluctuating motion of particles arising from their chaotic dynamics.

The phenomena have been confirmed and the associated knowledge enriched by later three-dimensional numerical studies with different methods, simulating monodisperse (Yeo & Maxey, 2011; Chun et al., 2017), bidisperse (Chun et al., 2019), and polydisperse (Di Vaira et al., 2022) suspensions in pressure-driven flow. In their study of monodisperse suspension, Yeo & Maxey (2011) identified three zones in the flow: layering occurs close to the walls, while a plug forms at the center of the channel, where the averaged quantities vary abruptly with the distance in the wall-normal direction. In the intermediate zone between the mentioned zones, volume fraction, stresses, and velocity fluctuations vary evenly, and the authors found it possible to extract constitutive laws in overall qualitative agreement with data from the literature concerning homogeneous shear flow.

Migration and segregation have been studied in bidisperse suspensions. Chun et al. (2019) showed the typical migration time in bidisperse suspensions to be comparable to monodisperse suspensions. However, they evidenced particle segregation, meaning that the large particles preferably migrate toward the center of the channel, while depletion of small particles is observed there. Segregation is 5-8 times slower than overall migration.

The plug zone has received special attention in the literature. Nott & Brady (1994) observed that the granular temperature (i.e., velocity fluctuations) is lower at the channel center, where the concentration is large, while the local shear rate is zero. This has been confirmed by Yeo & Maxey (2011) in 3D simulations, who also evidenced that the particle microstructure turns more isotropic at the center of the channel and that the plug extension increases with the bulk volume fraction. In addition, Oh et al. (2015) showed in their experimental work concerning the pressure-driven flow of concentrated non-Brownian suspensions that the volume fraction in the plug zone could exceed the jamming volume fraction as measured in homogeneous shear flow, up to the random close packing fraction 0.64 at the pipe center. This was recently also observed by Gillissen & Ness (2020) in 2D simulations of a Kolmogorov suspension flow, where the ambient shear flow is given a sine shape. They showed that the $\mu(J)$ rheology (Boyer et al., 2011) was significantly altered at the positions where the local shear rate vanishes, meaning that the macroscopic friction coefficient μ falls under its usual value at jamming for $J > 0$ (i.e., before jamming). They also found that, at the same position, the volume fraction could exceed the jamming volume fraction as measured in a homogeneous shear flow. They proposed an explanation based on the fluctuations of the shear rate tensor, extending a recent constitutive tensor model for the suspension stress.

More generally, the precise local measurement of the whole stress tensors in heterogeneous flows is of great interest due to its connection with shear-induced migration (see below) and is a difficult matter, both in experiments and in numerical simulations. In experiments, such local measurements have been performed in rheometrical flows, such as parallel-plate geometry using pressure sensors (Anugrah Singh & Nott, 2003; Dbouk et al., 2013). Particle resuspension in a rotating Couette device allows particle normal stress measurements as well, either through measurement of resuspension height (Acrivos, 1993) or in a more local way through measurement of volume fraction fields (Saint-Michel et al., 2019; d'Ambrosio et al., 2021). In the latter works, normal stress determination requires theoretical modeling (the so-called Suspension Balance Model, which will be explained in the following). Direct measurement of the particle normal stress is also possible using a pressure sensor in the same geometry (Deboeuf et al., 2009), or in parallel plate rheometry (Dbouk et al., 2013) as well as in the frame of pressure controlled rheometry (Boyer et al., 2011).

Direct measurements of local stress are quite scarce in discrete simulations. As mentioned above, Yeo & Maxey (2011) measured the particle stresses in steady Poiseuille flow. They found that the measured stresses in the intermediate zone qualitatively agreed with experimental and numerical measurements in homogeneous shear flow. More recently, in their study of bedload transport in relation to experiments (Aussillous et al., 2013) using Immersed Boundary Method, Vowinckel et al. (2021) performed precise local stress balance. They determined velocity, volume fraction, and stress profiles, showing qualitative agreement with material functions from homogeneous flow measurement, both in volume-controlled and pressure-controlled rheology. Finally, Rahmani et al. (2018) studied the homogeneous shear flow of suspensions at finite particle Reynolds number. They did not measure local stresses, but they instead integrated the momentum equation for each phase, solid and fluid, over the whole simulation domain. They could determine the contribution of inertia to the mean suspension stress.

CONTINUUM MODELS

Leighton & Acrivos (1987b) first proposed a phenomenological model to explain their observation of long-time decrease and short-time increase in the effective viscosity of a suspension in a Couette viscometer. They proposed that the net flux of particles consists of two contributions: a diffusive flux driven by a gradient in the shear rate, and diffusion due to a gradient in the volume fraction. The predictions of this model are in reasonable agreement with both experimental measurements (Phillips et al., 1992) and numerical simulations (Chun et al., 2019).

The diffusive flux model has been very useful to open the path to phenomenological models. A widely accepted model is nowadays the Suspension Balance Model (SBM), first proposed by Nott & Brady (1994). In this approach, there is no diffusion, but rather mass, momentum, and energy balances are written for the particulate phase. Then, these balances are solved simultaneously for concentration, particle velocity, and suspension temperature. The macroscopic statement that, in a steady state, there is no pressure variation in the direction perpendicular to the mean motion of the suspension (later confirmed also by Yeo & Maxey (2011)) gives an equation for the final volume fraction profile.

The basic idea is that the dynamics of the particles are described by Newton's laws of motion just as molecules, with the difference that the forces acting on the particles are given by rather complex configuration-dependent expressions. The local momentum balance equation inside the particles is averaged at the suspension scale to yield an equation for the transport of particles. Then, particle migration occurs due to non-uniformity of the normal stresses (Morris & Brady, 1998; Morris & Boulay, 1999).

In the original SBM, the particle contribution to the stress is supposed to be responsible for particle migration. Lhuillier (2009) performed a complete derivation of the particle phase momentum balance, showing that the divergence of the contact contribution to the stress is balanced by the interphase force density, but shifting the issue to the formulation of a constitutive law for each term of the equation. He proposed in particular a more systematic description of the non-drag part of the hydrodynamic force, debating that in the SBM the only stress involved in stress-induced migration is that from direct interactions only. In the same line, Nott et al. (2011) proposed to split the interphase force into the drag component and the divergence of a stress, hydrodynamic in nature, so that the original form of the SBM is recovered.

We finally note that the SBM implementation classically assumes a locally-plane shear flow. It has been extended to a form suitable to general flows, either in 2D (Miller et al., 2009) or 3D (Badia et al., 2022).

In this framework, as mentioned above, numerical simulations are eagerly needed to test the relevance of phenomenology and to complete the understanding of shear-induced particle migration in viscous suspensions.

6.2 NUMERICAL SETUP

To simulate the pressure-driven flow of a suspension in a channel, the numerical setup displayed in Fig. 6.1 is employed. In particular, a homogeneous pressure gradient is applied at each point of the simulation volume:

$$\nabla P_0 = \frac{dP_0}{dx}\mathbf{e}_x \tag{6.1}$$

We recall that this pressure gradient, should it be applied to the pure suspending fluid with viscosity η, would produce the following velocity and shear rate profiles:

$$\mathbf{u}_0 = -\frac{L_y^2}{8\eta}\frac{dP_0}{dx}\left(1-\frac{4y^2}{L_y^2}\right)\mathbf{e}_x\,, \qquad \dot{\gamma}_0\left(y\right) = \left|\frac{d\mathbf{u}_0}{dx}\right| = \frac{1}{\eta}\left|\frac{dP_0}{dx}y\right| \quad \rightarrow \quad \bar{\dot{\gamma}}_0 = \frac{L_y}{4\eta}\left|\frac{dP_0}{dx}\right| \tag{6.2}$$

where $\bar{\dot{\gamma}}_0$ is the mean shear rate in such a pure fluid flow. In the present case, where the viscosity of the suspension is larger and depends on the position due to shear-induced particle migration, a different velocity profile is expected. In the following, length, time, velocity, and stresses are made dimensionless as follows:

$$y^* = \frac{y}{L_y}\,, \qquad \dot{\gamma}^* = \frac{\dot{\gamma}}{\bar{\dot{\gamma}}_0}\,, \qquad t^* = \bar{\dot{\gamma}}_0 t\,, \qquad \mathbf{u}^* = \frac{\mathbf{u}}{\bar{\dot{\gamma}}_0 L_y}\,, \qquad \Sigma^* = \frac{\Sigma}{\eta\bar{\dot{\gamma}}_0} \tag{6.3}$$

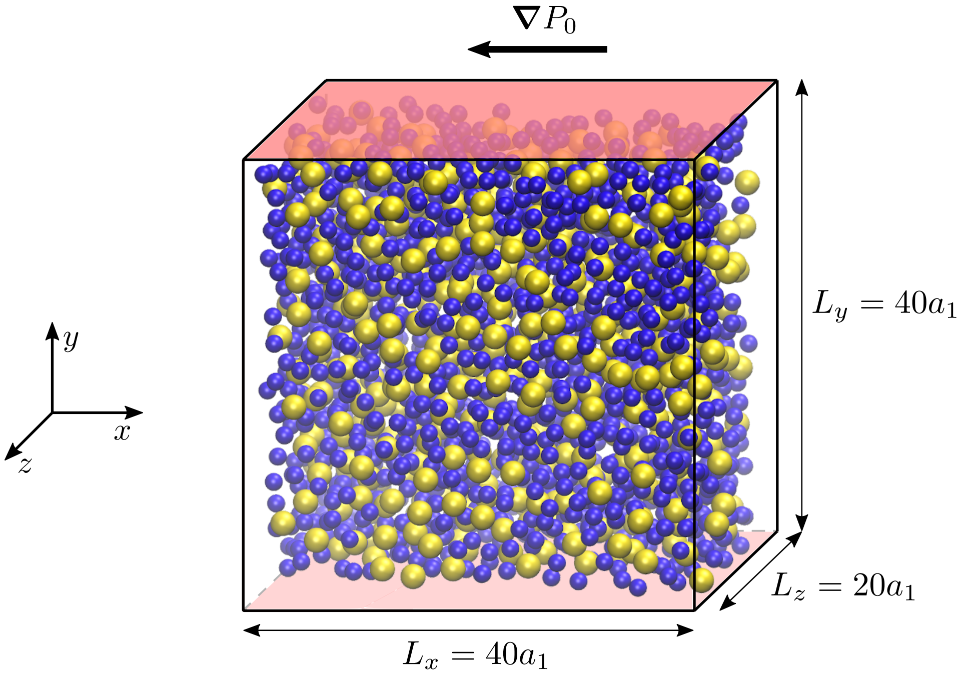

Figure 6.1
Numerical setup for the simulation of a pressure-driven particulate flow in a channel: a pressure gradient is imposed, generating a flow in the opposite direction. Frictional walls are present in y direction, while periodic boundary conditions are imposed in both x and z directions.

We simulate bidisperse ($a_2 = 1.4a_1$, $\phi_1 = \phi_2 = \phi_0/2$) suspensions with three values of the mean volume fraction $\phi_0 = [0.3,\ 0.4,\ 0.5]$. The particles and the walls are frictional with a constant friction coefficient $\mu = 0.5$, with roughness height $h_r = 0.005a_1$ (see Section 2.6 for more details concerning contact forces between particles). The particles are initially placed at random positions.

Particle migration is a slow process and, therefore, long-lasting simulation runs are necessary: for the three values of the volume fraction, the simulations ran until $t_f^* = 2000$. We employed a time-step sufficiently small for the dynamics of the particles to be conveniently computed: $\overline{\dot{\gamma}}_0 \Delta t^* = 10^{-3}$ with 10 SIMPLEC loops, checking that the residual of $\boldsymbol{\lambda}$ (Eq. (2.54)) was always of the order of $\approx 10^{-4}$. As for the tolerances, we used the same ones as in Section 4.2.1 and Section 5.3, i.e. $tol_p = 10^{-3}$ and $tol_u = 10^{-5}$.

DATA RE-SAMPLING

The volume fraction profile is computed as defined in Eq. (2.70), and following Yeo & Maxey (2011) the particle velocity profile $\mathbf{u}_p(y)$ is computed from the velocities of the particles:

$$\phi(y)\,\mathbf{u}_p(y) = \frac{1}{L_x L_z} \iint_{\{plane\ y\}} \sum_p \mathbf{U}_p \chi_p(\mathbf{x})\, dx\, dz \tag{6.4}$$

For the moment, we are not interested in variations at a scale smaller than a particle radius. As a consequence, the different profiles are re-sampled at positions y_n such as $y_{n+1} - y_n = \Delta y = a_1$ (see Fig. 6.2). For this purpose, the fine-scale profiles are averaged over each position bin, e.g. for the volume fraction:

$$\phi^{coarse}(y_n) = \frac{1}{\Delta y} \int_{y_n - \Delta y/2}^{y_n + \Delta y/2} \phi(y)\, dy \tag{6.5}$$

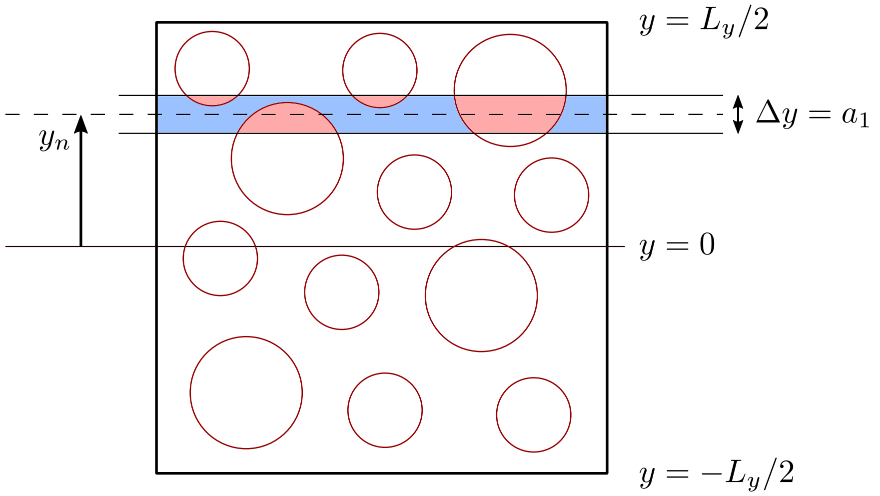

Figure 6.2
The profiles of the different quantities are re-sampled and averaged over each position bin.

6.3 RESULTS: VOLUME FRACTION, VELOCITY, AND SHEAR RATE

6.3.1 TRANSIENT PARTICLE MIGRATION

To start investigating the results, let us first take the case $\phi_0 = 0.40$ as an example. To seek the steady state, let us take five vertical positions between the channel center and the top wall $y^* = [0.0125,\ 0.1125,\ 0.2125,\ 0.3125,\ 0.4125]$ (being the first point close to the channel center and the last one close to the top wall), and let us study the evolution in time of the local (coarse-grained) volume fraction at such positions.

The results are displayed in Fig. 6.3. We can already appreciate particle migration. Indeed, the volume fraction at the channel center (blue line, $y^* = 0.0125$) strongly increases from ≈ 0.45 to over 0.60, while close to the wall (green line, $y^* = 0.4125$) the volume fraction decreases from ≈ 0.40 to ≈ 0.31. We can also notice that the variation of the volume fraction (i.e., particle migration) is slower at the channel center than close to the wall: in the latter region, the volume fraction reaches its stationary value at $t^* \approx 750$, while at the channel center we have to wait until $t^* \approx 1600$.

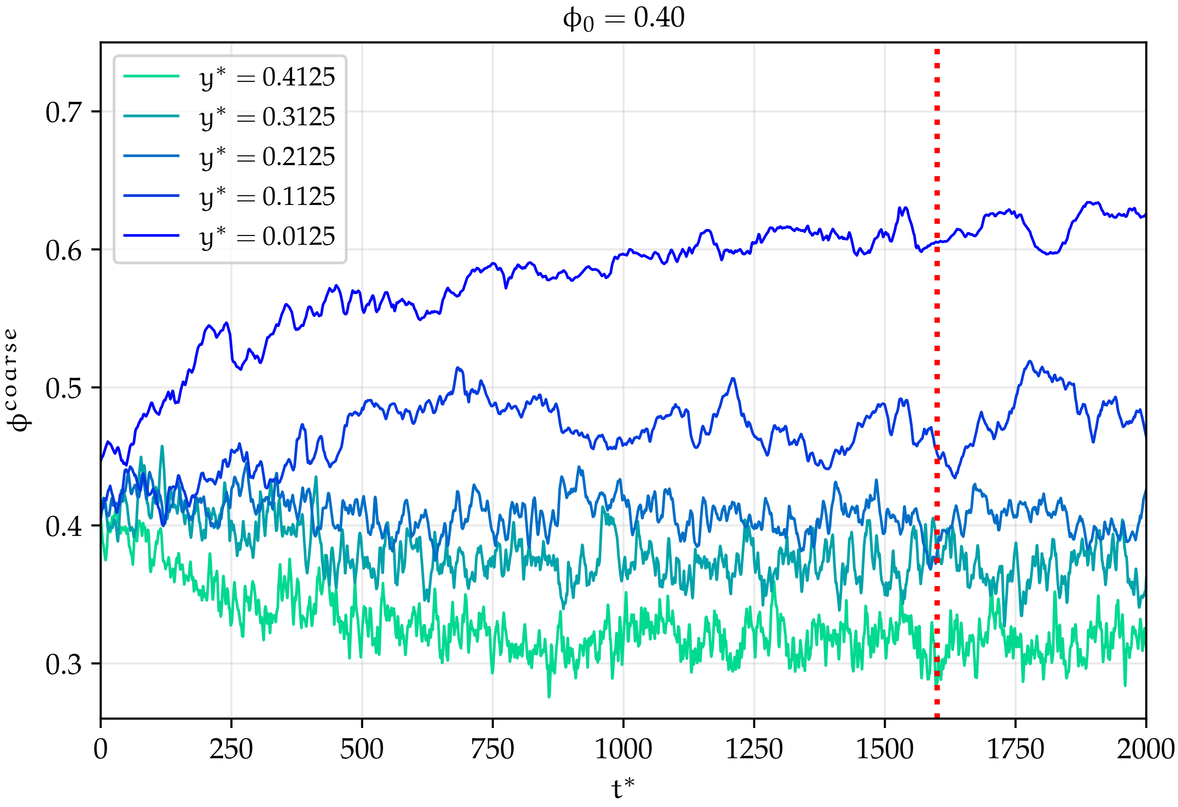

Figure 6.3
Evolution in time of the volume fraction at different vertical positions, being $y^* = 0.0125$ close to the channel center (blue line) and $y^* = 0.4125$ close to the top wall (green line). The dotted red vertical line at $t^* = 1600$ is the time at which all the points reach the steady state.

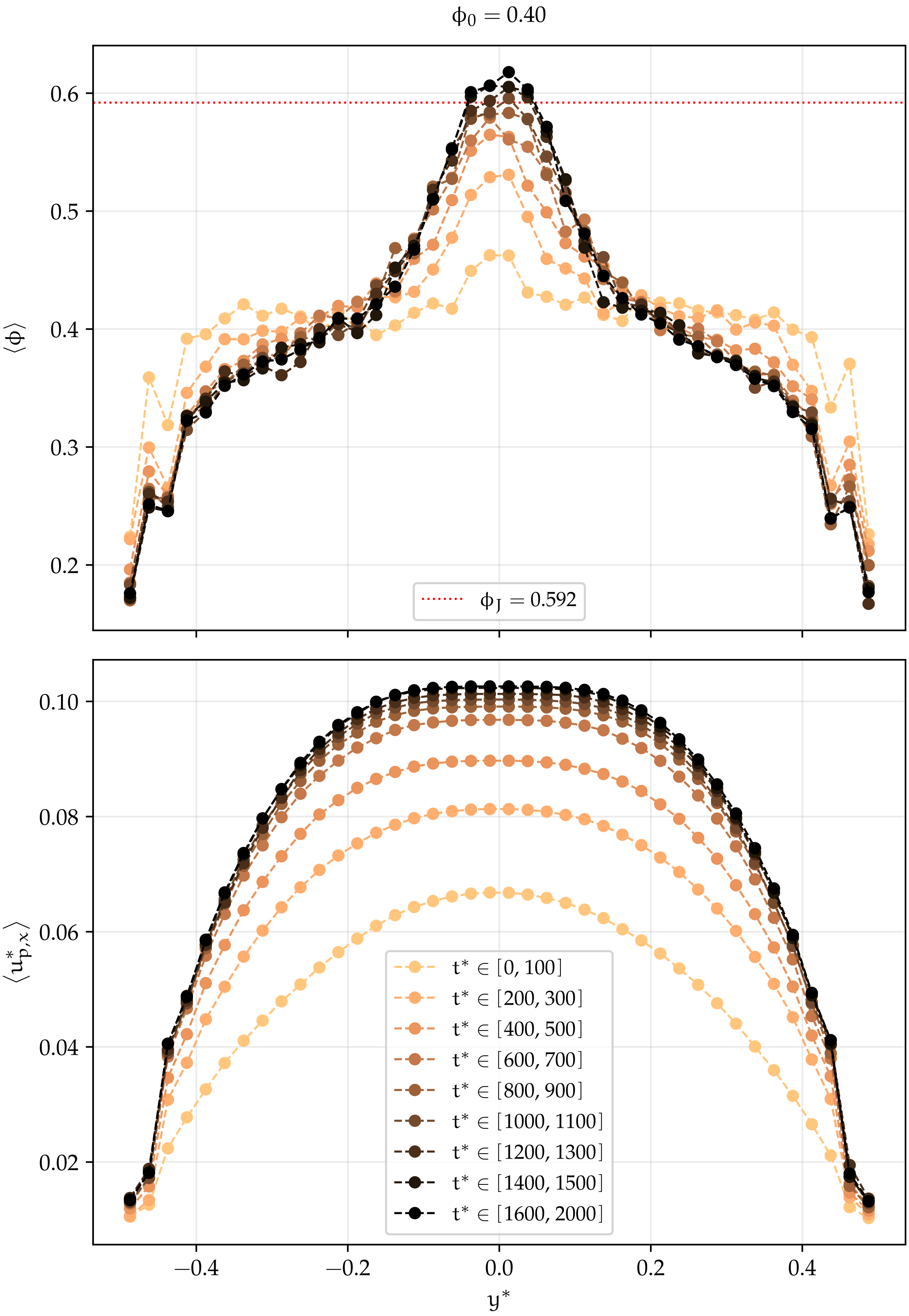

Figure 6.4
(top) volume fraction and (bottom) particle velocity profiles in time (from light to dark lines). The profiles are averaged in temporal intervals $\Delta t^* = 100$, except for the last one (black line) which has been averaged over the steady state ($\Delta t^* = 400$).

We can now turn the attention to the volume fraction and particle velocity profiles, displayed in Fig. 6.4. Each profile has been averaged in a temporal interval $\Delta t^* = 100$ (observing in Fig. 6.3 that in such an interval the overall variation is indeed small), except for the last one which has been averaged over the steady state ($\Delta t^* = 400$). Also, in the computation of the particle velocity profile, the contributions of the rotational velocities are not accounted for in Eq. (6.4). We have checked that these contributions may be completely neglected, meaning that they vanish when averaging over multiple particles in the same planar bin (see Fig. 6.2), with a slightly larger intensity in the wall layer.

Particle migration is now perfectly observable: particles have migrated toward the channel center, starting from an almost uniform volume fraction profile (lightest line, noticing that, having averaged for $t^* \in [0,\ 100]$, a slight migration has already occurred) to a non-uniform profile (darkest line, $t^* \in [1600,\ 2000]$, i.e. the steady state), with low values close to the walls and high values at the channel center. We note that the local volume fraction at the channel center slightly exceeds the jamming volume fraction $\phi_J = 0.592$ that was estimated from the homogeneous suspension viscosity (Fig. 4.16). This occurs over a quite narrow area, approximately $4a_1$ in width (we are going to refer to this zone as "the plug"). The numerical derivative of the stationary particle velocity profile $d\left\langle u^*_{p,x}\right\rangle/dy^*$ is displayed in Fig. 6.5. We can notice that at the channel center, where the local volume fraction exceeds the jamming volume fraction, the actual shear rate is close to zero, with a mean value $\overline{\dot{\gamma}}^*_{\mathrm{plug}} \approx 7 \cdot 10^{-4}$,

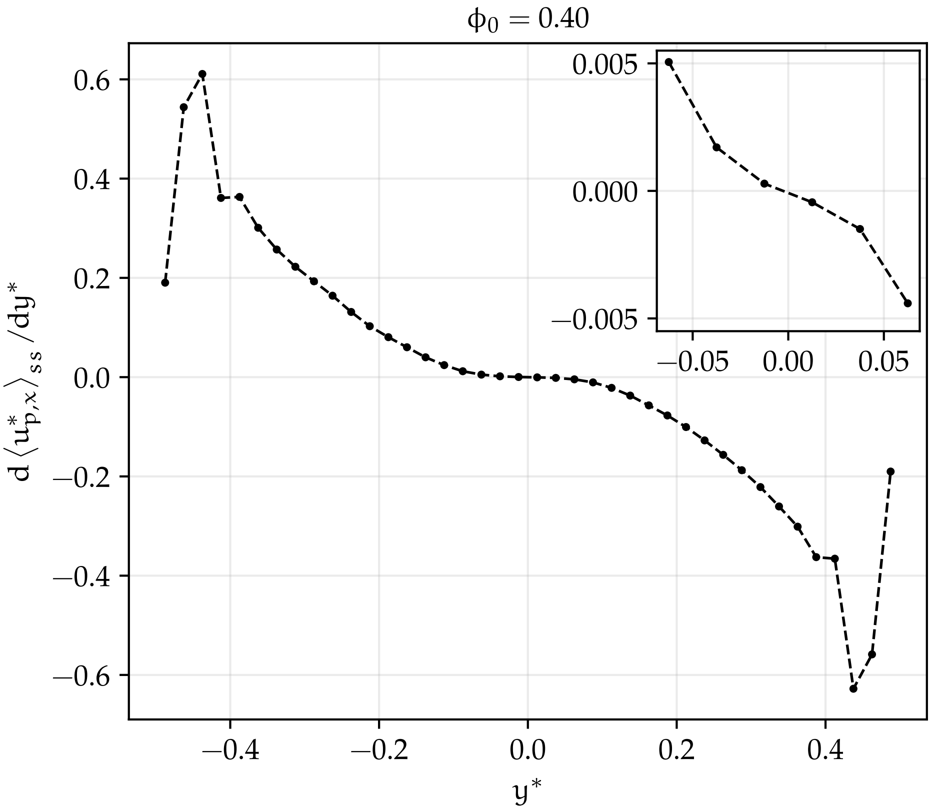

Figure 6.5
Numerical derivative of the stationary particle velocity profile (the line is a guide to the eye). The inset is a zoom at the channel center region.

to be compared to the maximum value at the walls $\dot{\gamma}^*_{max} \approx 0.4$. The suspension is thus not completely jammed in this area, even though the shear rate is very low. We can also clearly observe particle ordering close to the walls, which extends over $\approx 4a_1$ at each side, despite the precaution of mixing particles of two different sizes.

Since the volume fraction at the channel center increases, while it decreases at the walls, the particle velocity profile (Fig. 6.4) evolves from the usual parabolic profile observed in pressure-driven flows (lightest line) to one characterized by a blunted region at the channel center (darkest line, steady state), in agreement with Fig. 6.5. We also note that the particle velocity does not vanish at the walls: the rapid variation of the particle velocity close to the walls (i.e., in the first layer at the wall) and the finite value at the walls may be termed as "wall-slip", and is classically observed in experiments (Jana et al., 1995).

In Fig. 6.6, the coarse profiles from Eq. (6.5) and presented in Fig. 6.4 are compared to finer profiles discretized with $\Delta y = 0.01a_1$ (referred as "dense" profiles), in the steady state only. Clearly, in the dense profiles particle ordering close to the walls is more evident, and the effect of the wall is shown to fade out for distances from the wall larger than $\approx 4 - 5a_1$.

In Fig. 6.7 [left], the particle velocity profile and the suspension velocity profile as computed by the solver in OpenFOAM averaged in the steady state regime are compared. In particular, the suspension velocity profile as computed by the solver takes into account both the fluid and the particle domains. Two different OpenFOAM velocity profiles are shown: the raw profile (mesh size $\Delta = 0.2a_1 = L_y/200$) and the re-sampled profile with the same sample rate as the coarse-grained particle velocity profile. We can observe that the two profiles are very close to each other, showing that the suspension velocity field has almost

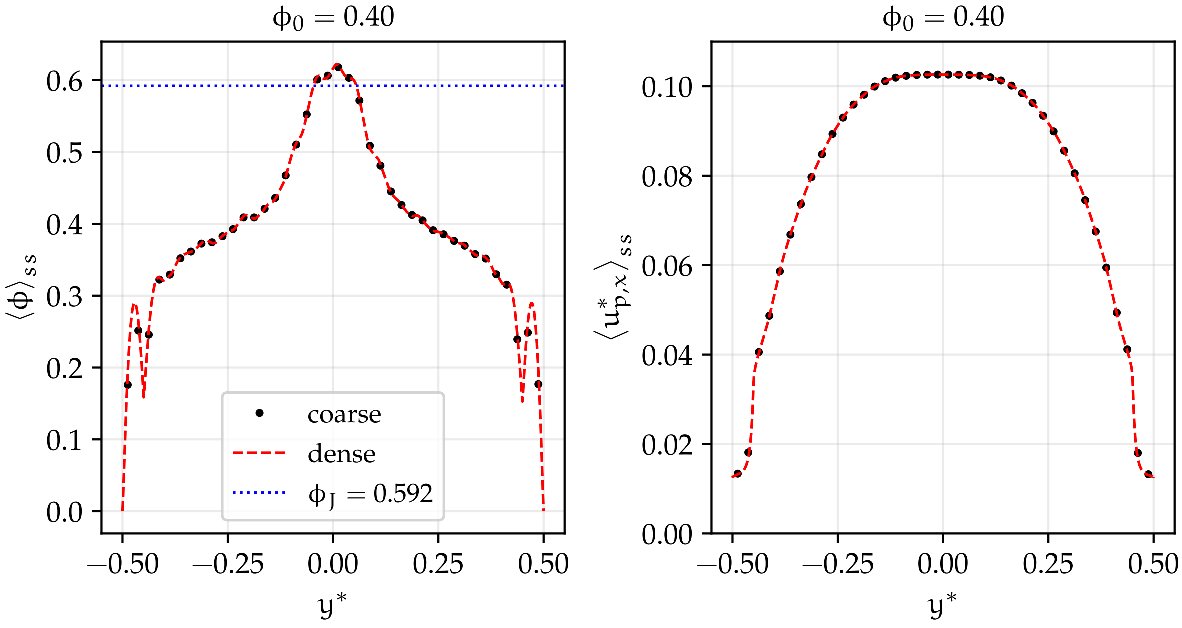

Figure 6.6
Comparison between coarse ($\Delta y = a_1$, see Eq. (6.5)) and dense ($\Delta y = 0.01a_1$) profiles for the steady state (left) volume fraction and (right) particle velocity. The blue dotted horizontal line indicates the jamming volume fraction for this suspension as measured in a simple shear flow, computed in Section 4.2.2 to be $\phi_J = 0.592$.

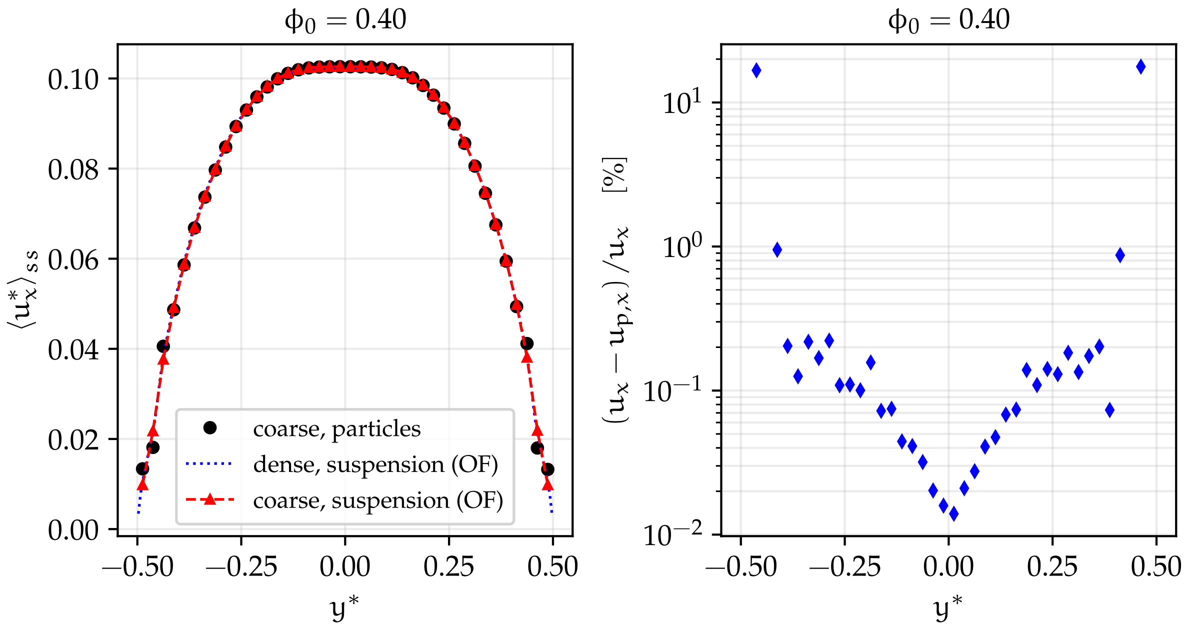

Figure 6.7
Comparison between the particle velocity profile and the suspension velocity profile as computed by the solver in OpenFOAM (both dense and coarse), in the steady state regime.

the same horizontal component as the particles. However, a slight difference can be observed even far from the walls in Fig. 6.7 [right], where the normalized difference between the data from OpenFOAM and the particle velocity is displayed. We also note that, as expected, the dense velocity profile goes to zero at the walls, in agreement with the no-slip boundary condition imposed by the finite volume solver.

6.3.2 STEADY PROFILES: COMPARISON WITH THE SBM

Let us now compare the steady volume fraction and particle velocity profiles to theoretical computations using the *Suspension Balance Model* (SBM) (Nott & Brady, 1994; Mills & Snabre, 1995; Morris & Boulay, 1999; Lhuillier, 2009; Nott et al., 2011).

The main trends of the SBM as used in the current work (see also Badia et al. (2022)) are recalled here. This model mainly considers the suspension as a continuum undergoing incompressible flow. The governing equations are the momentum balance equation together with the mass balance equation:

$$\nabla \cdot \mathbf{u} = 0 \tag{6.6}$$

$$\nabla \cdot \boldsymbol{\Sigma} - \nabla P_0 = 0 \tag{6.7}$$

where $\mathbf{u}$ denotes the suspension velocity field, and $\boldsymbol{\Sigma}$ is the bulk suspension stress. The latter is computed from the suspension velocity gradient and the solid volume fraction using the material functions defined in Section 4.2.2.

In the frame of this model, particle migration is induced by stress gradients. When inertia and gravity forces are not relevant, the SBM describes the transport of momentum and particles using the suspension and particle phase velocity fields $\mathbf{u}$ and $\mathbf{u}_p$:

$$\frac{\partial \phi}{\partial t} + \boldsymbol{\nabla} \cdot (\phi \mathbf{u}) + \boldsymbol{\nabla} \cdot \phi \left(\mathbf{u}_p - \mathbf{u}\right) = 0 \tag{6.8}$$

In the simplest version of the SBM, which we use here, the particle velocity may be computed from the following relation, which originates from the momentum balance equation of the particle phase (Lhuillier, 2009; Nott et al., 2011):

$$\frac{9}{2} \frac{\eta}{\overline{a}^2} \frac{\phi}{f(\phi)} \left(\mathbf{u} - \mathbf{u}_p\right) + \boldsymbol{\nabla} \cdot \boldsymbol{\Sigma}^c = 0 \tag{6.9}$$

where $f(\phi) = (1-\phi)^{5.1}$ is the hindered settling function, and $\overline{a}$ is the relevant particle size, which can be chosen as $\overline{a} = (a_1 + a_2)/2$. $\boldsymbol{\Sigma}^c$ is the contact contribution to the bulk suspension stress $\boldsymbol{\Sigma}$, as defined in Section 2.7.2 and recalled in Section 4.2.2.

In Eq. (6.9), the first term denotes the hydrodynamic force density exerted on the particle phase by the liquid phase (interphase force), while the second term is the force density exerted on the particle phase due to contacting neighbors, i.e. inside the particle phase. Writing Eq. (6.9) involves quite a strong assumption, namely that the hydrodynamic force density only originates in the difference between the suspension velocity as a whole and the particle phase velocity, which is still a largely open question (Lhuillier, 2009; Nott et al., 2011). Nevertheless, in the present study, Eq. (6.9) is employed as is.

We note that this version of the SBM has been extensively studied by Badia (2021) and Badia et al. (2022) in various flow geometries including pressure-driven flow using finite volume element modeling. The SBM equations in the present flow geometry are derived in Appendix F. They involve the material functions that were determined from the discrete simulations and mentioned in Section 4.2.2. The dimensionless steady particle velocity and volume fraction profiles obey the following equations:

$$\frac{du_x^*}{dy^*} = -\frac{4}{\eta^s\left(\phi_r\left(y^*\right)\right)} y^* \tag{6.10a}$$

$$\frac{d\phi_r}{dy^*} = -\frac{\hat{\Sigma}_{22}^c}{y^* \dfrac{d\hat{\Sigma}_{22}^c}{d\phi_r}} \tag{6.10b}$$

with the constraint that the total particle volume is kept constant, i.e.:

$$\int_{-1/2}^{+1/2} \phi_r \, dy^* = \frac{\phi_0}{\phi_J} \tag{6.11}$$

where $\phi_r = \phi/\phi_J$. Eq. (6.10a) states that the shear stress is driven by the pressure gradient, while Eq. (6.10b) controls the steady volume fraction profile.

Once Eqs. (6.10b) and (6.11) are solved, the velocity profile is simply determined by integration of Eq. (6.10a). It should be noted that the SBM as presented here suffers important drawbacks (see Snook et al. (2016) for a discussion). In particular, the steady-state volume fraction is allowed to exceed the jamming volume fraction ϕ_J, which is easily understood by inspection of Eq. (6.10b): the multiplying factor of $1/y^*$ in the RHS is negative so that ϕ increases as $|y^*|$ decreases; in addition, this factor does not vanish as $\phi/\phi_J \to 1$ so that the volume fraction gradient diverges as $|y^*| \to 0$, and ϕ exceeds ϕ_J. To avoid this divergence, it has been proposed to slightly modify the expression of the particle flux with a non-local stress. This non-local stress may be induced by a suspension "temperature" (Nott & Brady, 1994), a force network (Mills & Snabre, 1995), or the finite size of the particles (Miller & Morris, 2006). These approaches deserve to be examined against the present data. However, as a first approximation, we follow here a simple empirical idea: we postulate that the particle flux vanishes as soon as ϕ reaches ϕ_J. As a consequence, a jammed zone where $\phi = \phi_J$ develops in the vicinity of the channel center plane. Finally, to avoid the difficulties associated with particle layering and wall slip on the one hand, and with the central plug region, on the other hand, Eqs. (6.10a), (6.10b) and (6.11) are solved outside the layering region, i.e. at a distance from the bounding walls larger than $\approx 2.5a_1$ (it is fine-tuned for each value of ϕ_0), and outside the plug region. As a consequence, only the mean volume fraction inside this region is considered while solving Eqs. (6.10a), (6.10b) and (6.11).

The steady-state volume fraction and particle velocity profiles are displayed in Fig. 6.8 for the three values of the volume fraction investigated here, together with the shear rate, the latter computed by performing the numerical derivative of the steady-state particle velocity profile. Having verified in Fig. 6.7 that the particle velocity and the velocity of the suspension as a whole are very similar, and having checked that the difference between the two profiles predicted by Eq. (6.9) is indeed small in the x-direction, we compare the particle velocity from the simulations with the predictions of the SBM for the suspension velocity. The simulation results and the SBM predictions are in close agreement for the three quantities, except in the direct vicinity of the walls and at the channel center. As mentioned above, the discrepancies at the walls are related to particle layering.

For the highest concentrations, i.e. $\phi_0 = 0.40$ and $\phi_0 = 0.50$, in the jammed region, the volume fraction from the simulations is larger than the jamming volume fraction ϕ_J, as also experimentally observed by Oh et al. (2015), and reaches approximately the value 0.62 for $\phi_0 = 0.40$ and 0.64 for $\phi_0 = 0.50$. This may appear surprising, since the shear rate from the average velocity profile does not vanish, except at the exact center plane. However, it is very low, and, as already noted by Yeo & Maxey (2011) in their simulations of monosized suspensions in Poiseuille flow, velocity fluctuations never vanish, so they may play a significant role in the central region, as also confirmed by the 2D simulations performed by Gillissen & Ness (2020) of a Kolmogorov suspension flow, in particular, they may help particle rearrangement and induce this concentration increase. We can also observe that the plug region width increases from $\approx 4a_1$ for $\phi_0 = 0.40$ to $\approx 10a_1$ for $\phi_0 = 0.50$. It should be noted that the case with $\phi_0 = 0.30$ never reaches the jamming volume fraction, so also in this case the volume fraction profile at the channel center is not correctly accounted for by the SBM. This last observation is in qualitative agreement with previous experimental measurements (Lyon & Leal, 1998; Snook et al., 2016) and numerical simulations (Nott & Brady, 1994; Yeo & Maxey, 2011; Chun et al., 2019; Di Vaira et al., 2022) from the literature. We note here that the agreement between the simulated profiles and the predictions of the SBM is somewhat less good for the less concentrated case.

Concerning the shear rate, we observe that the higher the volume fraction the lower the shear rate. Indeed, its minimum value in the plug region is $\dot{\gamma}^*_{\mathtt{plug}} \approx 10^{-5}$ for $\phi_0 = 0.50$, $\dot{\gamma}^*_{\mathtt{plug}} \approx 2 \cdot 10^{-4}$ for $\phi_0 = 0.40$, and $\dot{\gamma}^*_{\mathtt{plug}} \approx 4 \cdot 10^{-3}$ for $\phi_0 = 0.30$. The version of the SBM employed here clearly miscalculates the shear rate in this region, being the velocity uniform, and, therefore, the associated shear rate is perfectly zero.

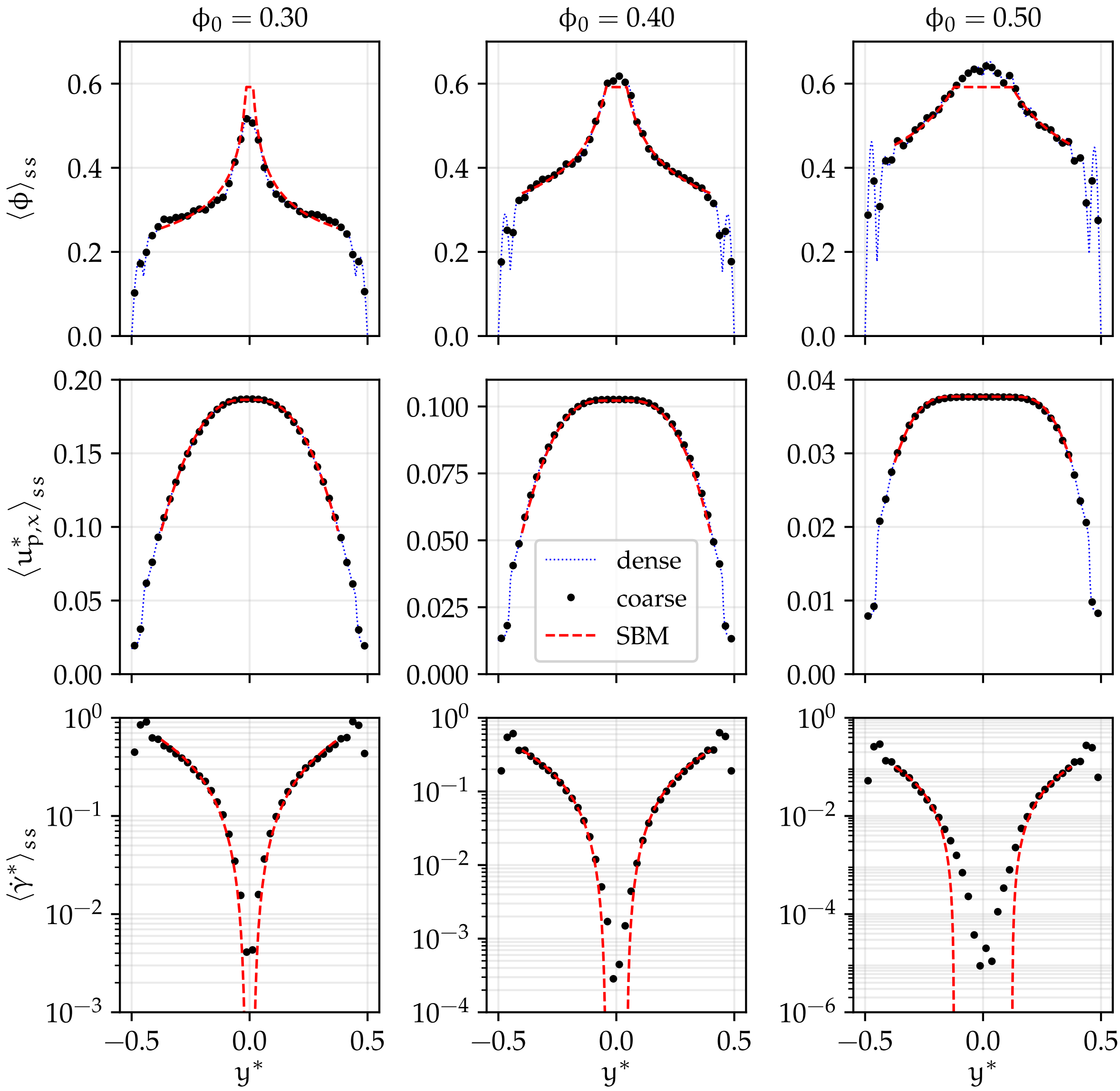

Figure 6.8
Comparison of the steady-state (top row) volume fraction, (central row) particle velocity, and (bottom row) shear rate profiles between (black bullets) the simulation data and (red-dashed lines) the predictions of the modified version of the SBM employed in the current work, for the three values of the volume fraction: (left column) $\phi_0 = 0.30$, (center column) $\phi_0 = 0.40$, (right column) $\phi_0 = 0.50$.

6.4 SUSPENSION STRESS BALANCE

6.4.1 LOCAL STRESS COMPUTATION

We observed in the previous section the spatial and temporal behavior of volume fraction, particle velocity, and shear rate. Let us now investigate the profiles of both the shear stress Σ_{12} and the second normal stress Σ_{22}. But first, let us recall the expression of the stress in the suspension, which is usually defined as:

$$\mathbf{\Sigma} = -P\delta + \eta\dot{\gamma}\left(\mathbf{e}_x \otimes \mathbf{e}_y + \mathbf{e}_y \otimes \mathbf{e}_x\right) + \mathbf{\Sigma}^{h_p} + \mathbf{\Sigma}^{c} \tag{6.12}$$

where the first term of the RHS is the contribution of the mean pressure in the liquid to the suspension stress (Batchelor, 1970). It should be recalled that in an incompressible flow, the overall pressure level is arbitrary so a reference pressure must be defined. This reference pressure is chosen at each time-step as the mean pressure p, as computed by the finite volume solver Eq. (2.11a), in the simulation domain, and the relevant pressure is the difference between the pressure and this reference value.

Let us re-write a local version of Eq. (6.12) inside the particles. For each vertical position y_n:

$$\mathbf{\Sigma}_{y_n} = -\left[1-\phi_{y_n}\right]\langle p\rangle^{f}_{y_n}\,\delta + \eta\dot{\gamma}_{y_n}\left(\mathbf{e}_x \otimes \mathbf{e}_y + \mathbf{e}_y \otimes \mathbf{e}_x\right) + \mathbf{\Sigma}^{h_p}_{y_n} + \mathbf{\Sigma}^{c}_{y_n} \tag{6.13}$$

where ϕ_{y_n}, $\dot{\gamma}_{y_n}$, and $\langle p\rangle^{f}_{y_n}$ are the local volume fraction, shear rate, and fluid pressure (outside the particles domain), respectively, averaged over the position bin of interest. It should be noted that the pressure P_0 from Eq. (6.1) should contribute to the equation above; however, we make the hypothesis that it can be neglected by horizontal (in x-direction) translation indifference of the volume fraction and, therefore, it is omitted in the following (see also the last comment at the end of the current section).

Being χ_p the indicator function delimiting the particle domain (i.e., this corresponds to $\mathcal{I}_\lambda$ as defined by Eq. (2.51)), the term $\left[1-\phi_{y_n}\right]\langle p\rangle^{f}_{y_n}$ is computed as:

$$\left[1-\phi_{y_n}\right]\langle p\rangle^{f}_{y_n} = \frac{1}{\Delta y\ L_x\ L_z}\iint_{\{\text{plane } y_n\}}\int_{y_n-\Delta y/2}^{y_n+\Delta y/2} p\left(\mathbf{x}\right)\left[1-\chi_p\left(\mathbf{x}\right)\right]\,dy\,dx\,dz \tag{6.14}$$

The last two terms of Eq. (6.13) stand respectively for the hydrodynamic and contact contributions to the particle stress. We recall here the definition of the hydrodynamic stresslet of a particle (p) and its trace as computed by the solver (see Section 2.7):

$$\begin{aligned}\mathbf{S}^{FDM}_p &= -\rho_f\int_{\mathcal{D}_p}\left\{\frac{1}{2}\left[\boldsymbol{\lambda}\otimes\left(\mathbf{x}-\mathbf{x}_p\right)+\left(\mathbf{x}-\mathbf{x}_p\right)\otimes\boldsymbol{\lambda}\right]-\frac{1}{3}\boldsymbol{\lambda}\cdot\left(\mathbf{x}-\mathbf{x}_p\right)\delta\right\}\,d\mathcal{V}\\ s^{FDM}_p &= -\int_{\mathcal{D}_p}\left[\rho_f\boldsymbol{\lambda}\cdot\left(\mathbf{x}-\mathbf{x}_p\right)+3p\right]\,d\mathcal{V}\end{aligned} \tag{6.15}$$

to which a sub-grid correction must be added, so that:

$$\begin{aligned} \mathbf{S}_p^h &= \mathbf{S}_p^{FDM} + \mathbf{S}_p^{SG} \\ s_p^h &= s_p^{FDM} + s_p^{SG} \end{aligned} \tag{6.16}$$

As for the contact stresslet, it reads:

$$\mathbf{S}_p^c = \sum_{p' \in \mathcal{D}_p} \frac{1}{2} \frac{a_p}{a_p + a'_p} \left(\mathbf{F}^{p' \to p} \otimes \mathbf{x}^{(pp')} + \mathbf{x}^{(pp')} \otimes \mathbf{F}^{p' \to p} \right) \tag{6.17}$$

The contact stresslet as defined in Eq. (6.17) is not traceless, while the hydrodynamic one is. Finally, the local hydrodynamic and contact contributions to the suspension stress are:

$$\begin{aligned} \Sigma_{y_n}^h = & - [1 - \phi_{y_n}] \langle p \rangle_{y_n}^f \delta + \eta \dot{\gamma}_{y_n} (\mathbf{e}_x \otimes \mathbf{e}_y + \mathbf{e}_y \otimes \mathbf{e}_x) + \\ & + \frac{1}{\Delta y \, L_x \, L_z} \iint_{\{\text{plane } y_n\}} \int_{y_n - \Delta y/2}^{y_n + \Delta y/2} \sum_p \frac{\mathbf{S}_p^h + \frac{1}{3} s_p^h \delta}{\frac{4}{3} \pi a_p^3} \chi_p(\mathbf{x}) \, dy \, dx \, dz \end{aligned} \tag{6.18}$$

$$\Sigma_{y_n}^c = \frac{1}{\Delta y \, L_x \, L_z} \iint_{\{\text{plane } y_n\}} \int_{y_n - \Delta y/2}^{y_n + \Delta y/2} \sum_p \frac{\mathbf{S}_p^c}{\frac{4}{3} \pi a_p^3} \chi_p(\mathbf{x}) \, dy \, dx \, dz \tag{6.19}$$

The equations above deserve a few comments concerning the influence of the pressure as computed by the solver:

- pressure is involved in two different contributions to the stress, namely the mean fluid pressure (Eq. (6.14)) and the trace of the hydrodynamic stress (Eqs. (6.15) and (6.18)); in both cases, the mean pressure is involved, either in the fluid or in the particles;
- a close look at those terms reveals that their sum should yield the local mean pressure over fluid and particles; this has been checked to quantitatively hold;
- one of the consequences of this is that the pressure $P_0 = (dP_0/dx)\, x$, whose average along x-direction is zero, does not contribute to the total stress profile since variations are examined against y position; in addition, the influence of P_0 on each of the two terms, fluid and particle stress, is expected to be small, due to statistical indifference of the suspension volume fraction along the x-direction.

All profiles are averaged over time to lower statistical fluctuations. The shear rate profile is computed as the numerical derivative of the time-averaged velocity profile, which is computed according to Eq. (6.4), and re-sampled according to Eq. (6.5).

6.4.2 LOCAL STRESS BALANCE

In Fig. 6.9, the steady state profile of the shear stress $\Sigma_{12} = \Sigma_{xy}$ is displayed for the three values of the mean volume fraction. The results are compared to the theoretical values (black line), and the hydrodynamic (▼) and contact (▲) contributions to the total shear stress (●) are evidenced. The theoretical expression of Σ_{12} (Eq. (F.6a)), whose dimensionless expression (Eq. (6.3)) is $\Sigma^*_{12} = -4y^*$, classically shows that, in a pressure-driven flow, the tangential stress is driven by the pressure gradient. As we can see, there is a very good agreement with the theory. In particular, the shear stress vanishes at the channel center. We note that the pure fluid term $\eta\dot{\gamma}_{y_n}$ must be accounted for to recover this good agreement, at least for the two lowest values of the mean volume fraction. Also, we can notice that the contact contribution increases with volume fraction. This is in agreement, at least outside the walls and plug regions, with Fig. 4.17, where the ratio $\hat{\Sigma}^c_{12} = \Sigma^c_{12}/\Sigma_{12}$ is displayed. It can be observed that the contact contribution is larger than the hydrodynamic contribution for $\phi/\phi_J \gtrsim 0.70$, i.e. $\phi \gtrsim 0.42$. This is indeed observed for all values of the mean volume fraction ϕ_0 in Fig. 6.9.

However, the relative level of contact and hydrodynamic stresses seems not to obey Fig. 4.17 in the central region. Considering the lowest concentration $\phi_0 = 0.30$, even though the volume fraction remains smaller than ϕ_J, it significantly exceeds 0.42. Despite this, the contact contribution hardly reaches the hydrodynamic contribution. In the more concentrated cases, the volume fraction in the plug is larger than ϕ_J, so that the correlation laws displayed in Fig. 4.17 cannot be used anymore. It is clear though that the hydrodynamic contribution may be completely neglected and that the shear stress is completely and exclusively dominated by contact forces.

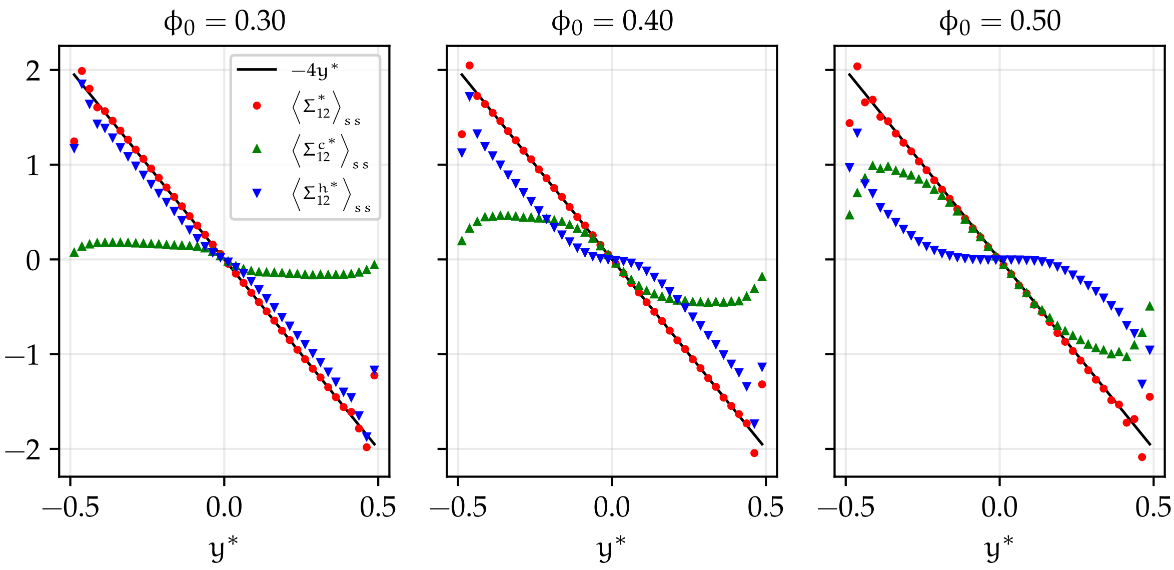

Figure 6.9
Time-averaged steady-state shear stress profiles: total shear stress Σ^*_{12} (●), theoretical expression $-4y^*$ (black line), contact contribution Σ^{c*}_{12} (▲), and hydrodynamic contribution Σ^{h*}_{12} (▼).

Finally, the evolution of the second normal stress $\Sigma_{22} = \Sigma_{yy}$ and its hydrodynamic and contact contributions are displayed over time in Fig. 6.10. It should be stressed that, although the contact and hydrodynamic contributions significantly vary over the channel, the total stress Σ_{22} does not, in agreement with the standard momentum balance in y-direction. This first check validates the numerical method and allows us to consider testing the SBM in the future with confidence.

As already mentioned, a gradient of the contact contribution to the stress, as well as of its hydrodynamic counterpart, is evidenced. In more detail, the gradient of contact stress denotes the force density on the particle phase originating from contacting neighbors (Lhuillier, 2009; Nott et al., 2011; Andreotti et al., 2013):

$$\langle \mathbf{f}^c \rangle = \boldsymbol{\nabla} \cdot \boldsymbol{\Sigma}^c \tag{6.20}$$

In the present case, the force $\langle \mathbf{f}^c \rangle = \partial_y \Sigma^c_{yy}$ drives the particles toward the channel center. In addition, in agreement with the SBM, the stress gradient fades out as particle migration occurs. However, we note that a significant stress gradient persists at the end of the simulation, more pronounced in the central region, but not limited to it, especially in the less concentrated case ($\phi_0 = 0.30$). It is now difficult to ascertain that the steady volume fraction profile has been reached due to significant temporal fluctuations of the volume fraction. Longer simulations would probably be required.

The statements above surely deserve a comment. Since the total stress is uniform, it means that this contact force density is balanced by the hydrodynamic stress gradient, as evidenced in Fig. 6.10. It should be stressed here that, since no inertia is accounted for in the simulations, the total force on each particle, i.e. the sum of the contact and hydrodynamic contributions, is zero at each time, as shown in Section 4.2.3. As a consequence, the hydrodynamic force density exerted on the particle phase in the y-direction is:

$$\langle f^h_y \rangle = -\partial_y \Sigma^c_{yy} = \partial_y \Sigma^h_{yy} \tag{6.21}$$

where the last equality follows from the uniformity of Σ_{yy}. The hydrodynamic force density is thus related to the hydrodynamic stress gradient, in the same way as the contact force density to the contact stress gradient. We note that simulations allow us to compute both sides of Eqs. (6.20) and (6.21). We checked that both equations, if properly time-averaged to lower statistical fluctuations, quantitatively hold.

Another striking feature in Fig. 6.10 is that the contact stress does not vanish at the center of the channel, while the shear rate does. This is another hint that the suspension behavior at this point seems quite different from the usual viscous constitutive equation, where the normal stresses are proportional to the tangential stress.

Nevertheless, this assertion should be softened by the following remarks. First, care should be taken while analyzing time-averaged values: since the tangential stress is not instantaneously the same at the two walls, the linear stress profile fluctuates with time, meaning that the position where it vanishes changes too. Due to the linearity of the profile, this does not affect the mean tangential stress profile. However, since the contact normal stress is not sensitive to the sign of the tangential stress, fluctuations will not be averaged out. In the same line, the instantaneous velocity profile is a spatial average too, meaning that velocity and velocity gradient fluctuations are expected to occur at the particle level, even at the channel center, possibly generating stresses. The effect of such fluctuations is expected to play a role at the channel center, where the mean value of the tangential stress is zero.

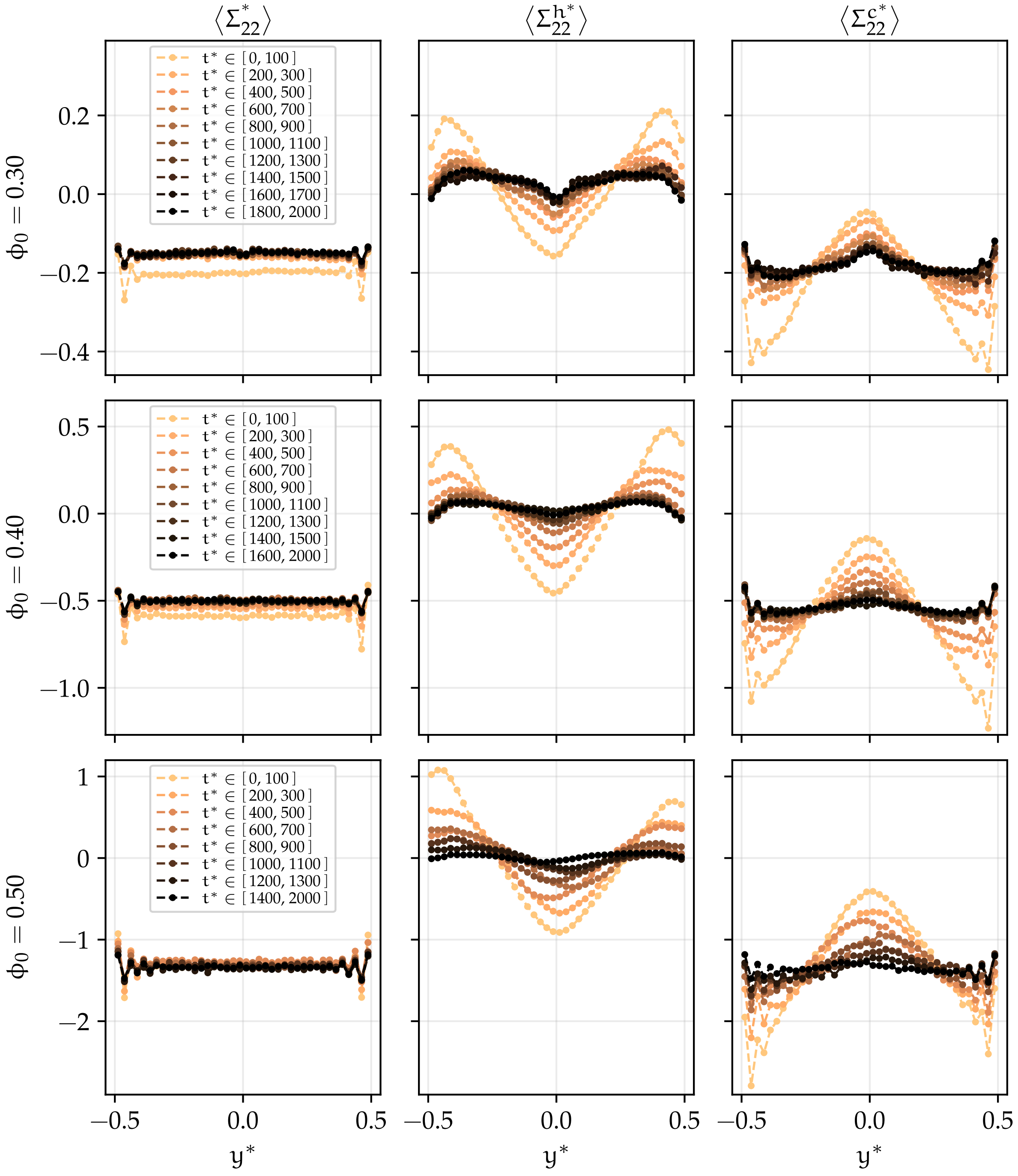

Figure 6.10
Second normal stress profiles: evolution in time (from lightest to darkest), averaged over temporal intervals $\Delta t^* = 100$, except for the steady state. Comparison between (left column) the total stress Σ^*_{22}, (center column) the hydrodynamic contribution $\Sigma^{h^*}_{22}$, and the contact contribution $\Sigma^{c^*}_{22}$.

Finally, as evidenced in Eqs. (6.18) and (6.19), the computation of stresses is not itself a perfectly local operation, since stresslet is an integral quantity over each particle, which is further re-scattered over the particle (Eq. (6.19)). As a consequence, it is expected to probe stresses with a smoothing length scale of at least one particle diameter. In other words, a continuum modeling of the suspension is not expected to hold at a length scale smaller than a few particle diameters at positions where the local quantities abruptly vary, such as the near-wall and plug areas regions.

6.5 DISCUSSION AND PERSPECTIVES

In this last chapter, we were able to calculate transient and steady-state velocity, volume fraction, and stress profiles in a pressure-driven suspension flow in a channel. In particular, the volume fraction and velocity profiles in the steady state have been studied and compared with a modified version of the SBM for which migration is artificially blocked for volume fractions higher than the jamming volume fraction measured in simple shear flow. An important point in this regard is that the material functions that were used for the SBM were determined by the same discrete numerical method used in the present study.

Three different zones have been highlighted, in agreement with Yeo & Maxey (2011): a zone close to the walls, where particle layering develops over a width of about two particle diameters and strong wall-slip is observed; a second zone, located between the structured zone and the central zone, is reasonably well described by the SBM as implemented here in steady state; finally, a third, central zone, where the observed rheology seems quite different from the usual behavior in shear flow. In the central zone, the SBM does not correctly describe the observed volume fraction and velocity distributions: at low mean concentration, the volume fraction does not reach the jamming volume fraction in the center, which is rather a confirmation that this version of the SBM is not adapted to the description of this region of the suspension flow where the shear stress cancels out. A more important point is the appearance, for mean volume fractions higher than 0.40, of a central region where the volume fraction exceeds the jamming volume fraction ϕ_J measured in simple shear flow. The width of this region can be as large as $4-10$ particle radii, i.e. well above the size of a particle. It is possible that velocity and stress fluctuations, in a zone where the average shear rate is very low, are the cause of an over-concentration of particles. However, questions about the relationship between stress and shear rate in this zone arise.

To go further, it will be necessary to closely examine the stresses that develop in the suspension and their relationship with the kinematic quantities that characterize the flow. The first approach, necessary, was to check the good coherence of the measured local constraints, i.e. that they obey the local momentum balance. This is perfectly achieved for stresses averaged over short time intervals during the transient regime and during the subsequent stationary flow. This verification fully validates the use of the numerical method presented here for nonlinear flows.

On the other hand, a gradient of contact stresses at each instant has been revealed, which is naturally counterbalanced by the gradient of the hydrodynamic contribution. This gradient decreases as the migration takes place, to approximately disappear once particle migration is completed and the volume fraction profile is established. The existence of this gradient, directed to push particles toward the center of the channel, and its decrease during migration, is in qualitative agreement with the SBM, which states that particle migration is driven by a particle stress gradient.

Several points remain to be clarified, which sets the direction for future work. First, it will be interesting to investigate the quantitative relationships between particle flux and transient stress gradient within this Poiseuille flow and to compare them to those prevailing in the SBM framework. This work could of course be extended by studying a resuspension flow, which adds a term to the stress balance, in addition to the contact and hydrodynamic contributions. One could also compare the local constitutive equation that relates the stresses to the velocity gradient to the one determined in simple shear. In particular, the material functions from the two types of simulations can be compared.

On the other hand, the behavior of the suspension in the central region should be clarified. In the case of the lowest mean volume fraction $\phi_0 = 0.30$, the jamming volume fraction is not reached, contrary to what is expected by the SBM as implemented here. This has already been observed in experiments and numerical simulations in the literature. One of the proposed explanations is based on the non-locality of the constitutive equation which would have as origin the velocity fluctuations (i.e., the local "temperature") (Nott & Brady, 1994), the existence of a network of forces (Mills & Snabre, 1995) or the finite size of the particles (Miller & Morris, 2006). Such non-locality would not be surprising in our case, since the area where the SBM predictions differ from simulation calculations extends over two or three particle diameters: it is not feasible to apply a continuous medium at smaller scales. However, it would be instructive to precisely determine the extension of the central zone. The measurement of the local constitutive equation would probably allow us to characterize it precisely since it is likely to differ from the law measured in simple homogeneous shear in this zone.

In the case of larger mean volume fractions, we have seen that the volume fraction could exceed ϕ_J, on a scale quite larger than one particle diameter. It seems likely that velocity and stress fluctuations, in this zone where the tangential stress is close to zero, are responsible for the densification of the suspension, in the manner of the standard tapping in granular materials. However, the nature of the stresses in this zone is also an important question. In particular, it is questionable whether a true flow is still taking place. One way to answer these questions would be to measure velocity correlations in the suspension. We can recall that Guasto et al. (2010) have experimentally demonstrated a higher spatial velocity correlation in the central zone. In the same line, Yeo & Maxey (2011), in their simulations of monodisperse suspensions, have shown a different structure, more isotropic, within the central zone.

CONCLUSION

We started this project by wanting to propose a numerical method for the simulation of three-dimensional concentrated non-Brownian suspensions in linear and nonlinear flows. We wanted a precise tool, able to correctly take into account both contact and hydrodynamic interactions between particles, i.e. we wanted to solve the Navier-Stokes equations for an incompressible Newtonian fluid and couple them with the particle dynamics.

We opted for the Fictitious Domain Method (FDM), as it has all the characteristics we were searching for. Then, we decided to implement it in the OpenFOAM toolbox, due to its large quantity of libraries useful for simulating fluid flows and to the growing number of users, making it a reference in the CFD community. Also, this makes our implementation of the FDM portable and easy to use, being OpenFOAM open-source and free.

In Chapter 2 we deeply detailed all the numerical features characterizing the method. We started by defining the governing equations for both fluid and particles and then we separated the fluid sub-problem from the particle sub-problem. The former is solved by the solver in OpenFOAM: we chose the SIMPLEC algorithm, and we fully detailed the complete numerical procedure together with the discretization of the various terms. Then, we explained how the two sub-problems are coupled: the difficulty in the numerical approach employed here is that the two sub-problems proceed consecutively, presenting a lag between the force density and the velocity and pressure fields, and, by consequence, imposing the use of an iterative approach. We then tackled all the numerical details: how to solve the involved linear systems, how to deal with the parallelization of the tasks, the boundary conditions to employ, the use of indicator functions to track the particles, and how to control convergence. We ended Chapter 2 by displaying the contact model chosen here, and defining how the rheological quantities of interest are measured.

After having chosen the numerical method and understood how to implement it, the first issue to tackle has been the sub-grid corrections. We have seen in Chapter 3 that, as the FDM uses a fixed Cartesian mesh, the solver is not able to correctly compute the lubrication flow arising between particles approaching at a distance smaller than the mesh grid size. The implementation of the sub-grid corrections is today a standard procedure, and many authors have proposed it. However, the standard implementation of such corrections involves the underlying linear flow. To appropriately expand our research to nonlinear flows, we propose an innovative modification of the sub-grid corrections, which does not need to take into account the ambient flow, and we did this for both the cases of two close particles and a particle close to a wall. We provided the reader with the full details about this matter in Chapter 3, together with even further details in Appendices A to D.

We had the numerical procedure, and we had this new version of the sub-grid corrections that opened up to nonlinear flows. The next natural step has been to verify the correct implementation of the method. Therefore, we tested several configurations: starting from one or two particles in both linear and nonlinear flows, with different boundary conditions, with or without walls, with or without contact, needing or not sub-grid corrections, to three particles in more "exotic" configurations, and finally up to concentrated bidisperse frictional suspensions in simple shear flow. All these validations are collected in Chapter 4. We compared the results to existing literature, and we definitively proved the correct implementation of the method and the proposed sub-grid corrections. Moreover, we checked the mechanical consistency of a suspension in a simple shear flow, and, again, the results confirmed the relevance of the numerical method. Finally, we wanted to check the computational performances of the method. The computational costs and the strong scaling are displayed at the end of Chapter 4.

At that point, we had a very precise and accurate tool in our hands, and it was time to take advantage of it. The first application we decided to investigate was to study the influence that adhesive forces between particles have on the rheological properties of bidisperse frictional suspensions: for three values of the friction coefficient, we performed a parametric study by varying both volume fraction and intensity of the adhesive forces. We encountered several difficulties in simulating cases with low volume fraction and high adhesion, which showed wall depletion and shear-banding. However, we were able to retrieve useful information from our simulations (displayed in Chapter 5), and we observed that the relative viscosity of the suspension is a function of both volume fraction and reduced shear stress (the latter taking into account adhesion). This led to the definition of a curve describing the jamming volume fraction as a function of shear stress, which can also be interpreted as a curve of the yield stress as a function of volume fraction. This separates the phase space (volume fraction, shear stress) into two regions: one in which the suspension flows and one in which the suspension jams.

We decided to keep the cherry on the top for the end: the investigation of the shear-induced particle migration occurring in a bidisperse frictional suspension in a planar pressure-driven flow (note: it is the "cherry on the top" simply because it is an application that perfectly matches the advantages of our numerical method). We performed the investigation for three values of the mean volume fraction, and the results are shown in Chapter 6. We observed that, as expected, particles migrate toward the center of the channel, where the shear rate fades out, and this is reflected by a blunted particle velocity profile. This behavior happens whatever the volume fraction. However, for the two higher volume fractions, in the channel center, the volume fraction locally exceeds the jamming volume fraction as measured in simple shear flow, and particles form a plug with a width of a few particle diameters. We compared the results with a modified version of the Suspension Balance Model (SBM), showing the well-known limits of this simplified model. Finally, we investigated the balance of the local stresses in the suspension, and we checked that they obeyed the conservation law of the local momentum all along the simulation run: we observed that the shear stress is driven by the pressure gradient, as expected by theory, and that the second normal stress (i.e., parallel to the velocity gradient) does not vary across the channel width, and a gradient in the contact stress (directed as to push the particles towards the center) is found, which is counter-balanced by the hydrodynamic stress.

Beyond having answered several questions about the rheological properties of the systems studied here, many further questions have arisen. Concerning the role of adhesion in frictional suspensions, further investigation of our results with recent models would be interesting (although not easy, due to the difficulties in decreasing the shear stress). Moreover, a complete investigation of the behavior of the stresses when varying adhesion together with volume fraction should be proposed. Also, the formation of aggregates should be studied, investigating the behavior and evolution of the microstructure and employing larger domain sizes to evaluate the influence of this parameter on the computed rheology. Concerning particle migration in pressure-driven flows, the peculiarities characterizing the plug region should be cleared out, and a deeper and more precise investigation of the temporal and spatial evolution of the stresses needs to be performed. A complete investigation of the microstructure is needed in this case too. More generally, the relation between particle flux and stress gradient should be precisely determined.

Finally, further developments should be performed from a numerical point of view, the most important one being the optimization of the code. Albeit it is something that has been deeply carried out all along the implementation of the method (and even after), there surely are some more features that can be added. For example, the solution of the linear system for the computation of the velocities of the particles could be parallelized with the message passing interface (MPI) standard, using already existing libraries such as PETSc. This would allow us to further increase the number of particles without reaching unmanageable computational costs.

APPENDICES

A

GENERAL FORM OF THE RESISTANCE TENSORS

The general form of the resistance tensors for a particle pair is given here, together with the symmetry relations from Lorentz's reciprocal theorem and the relations from the geometrical symmetry. As for the resistance functions for a particle close to a wall, the same reasoning can be followed with the required cautions.

A.1 PARTICLE PAIR

Considering two particles (p_1) and (p_2) and the unitary vector connecting their centers $\mathbf{d} = (\mathbf{x}_2 - \mathbf{x}_1)/\|\mathbf{x}_2 - \mathbf{x}_1\|$, the general forms of the resistance tensors in Eq. (3.5), valid for the theoretical matrices as well as for the FDM matrices and the sub-grid correction matrices, are (Kim & Karrila, 1991):

$$A_{ij}^{(\alpha\beta)} = X_{\alpha\beta}^{A} d_i d_j + Y_{\alpha\beta}^{A} \left(\delta_{ij} - d_i d_j\right)$$

$$B_{ij}^{(\alpha\beta)} = Y_{\alpha\beta}^{B} \epsilon_{ijk} d_k$$

$$\tilde{B}_{ij}^{(\alpha\beta)} = Y_{\alpha\beta}^{\tilde{B}} \epsilon_{ijk} d_k$$

$$C_{ij}^{(\alpha\beta)} = X_{\alpha\beta}^{C} d_i d_j + Y_{\alpha\beta}^{C} \left(\delta_{ij} - d_i d_j\right)$$

$$G_{ijk}^{(\alpha\beta)} = X_{\alpha\beta}^{G} \left(d_i d_j - \frac{1}{3}\delta_{ij}\right) d_k + Y_{\alpha\beta}^{G} \left(d_i \delta_{jk} + d_j \delta_{ik} - 2 d_i d_j d_k\right)$$

$$\tilde{G}_{ijk}^{(\alpha\beta)} = X_{\alpha\beta}^{\tilde{G}} \left(d_j d_k - \frac{1}{3}\delta_{jk}\right) d_i + Y_{\alpha\beta}^{\tilde{G}} \left(d_j \delta_{ki} + d_k \delta_{ij} - 2 d_i d_j d_k\right)$$

$$H_{ijk}^{(\alpha\beta)} = Y_{\alpha\beta}^{H} \left(d_i \varepsilon_{jkm} d_m + d_j \varepsilon_{ikm} d_m\right)$$

$$\tilde{H}_{ijk}^{(\alpha\beta)} = Y_{\alpha\beta}^{\tilde{H}} \left(d_j \varepsilon_{kim} d_m + d_k \varepsilon_{jim} d_m\right)$$

$$\begin{aligned} M_{ijkl}^{(\alpha\beta)} = {} & \frac{3}{2} X_{\alpha\beta}^{M} \left(d_i d_j - \frac{1}{3}\delta_{ij}\right)\left(d_k d_l - \frac{1}{3}\delta_{kl}\right) + \frac{1}{2} Y_{\alpha\beta}^{M} \left(d_i \delta_{jl} d_k + d_j \delta_{il} d_k \right. \\ & \left. + d_i \delta_{jk} d_l + d_j \delta_{ik} d_l - 4 d_i d_j d_k d_l\right) + \frac{1}{2} Z_{\alpha\beta}^{M} \left(\delta_{ik}\delta_{jl} + \delta_{jk}\delta_{il} - \delta_{ij}\delta_{kl} \right. \\ & \left. + d_i d_j \delta_{kl} + \delta_{ij} d_k d_l + d_i d_j d_k d_l - d_i \delta_{jl} d_k - d_j \delta_{il} d_k - d_i \delta_{jk} d_l - d_j \delta_{ik} d_l\right) \end{aligned}$$

$$P_{i}^{(\alpha\beta)} = X_{\alpha\beta}^{P} d_i$$

$$Q_{ij}^{(\alpha\beta)} = X_{\alpha\beta}^{Q} \left(d_i d_j - \frac{1}{3}\delta_{ij}\right)$$

where the scalar resistance functions $X_{\alpha\beta}^{A}$, ldots, depend on a_1, a_2 and on the reduced distance between the particles surfaces $\xi = 2\|\mathbf{x}_2 - \mathbf{x}_1\|/(a_1 + a_2) - 2$.

The resistance matrix obeys symmetry relations from Lorentz reciprocal theorem:

$$\begin{aligned} A_{ij}^{\alpha\beta} &= A_{ji}^{\beta\alpha} & \tilde{B}_{ij}^{\alpha\beta} &= B_{ji}^{\beta\alpha} & C_{ij}^{\alpha\beta} &= C_{ji}^{\beta\alpha} \\ \tilde{G}_{ijk}^{\alpha\beta} &= G_{jki}^{\beta\alpha} & \tilde{H}_{ijk}^{\alpha\beta} &= H_{jki}^{\beta\alpha} & M_{ijkl}^{\alpha\beta} &= M_{lkij}^{\beta\alpha} \end{aligned}$$

Then, from the definition of the terms, we obtain:

$$
\begin{array}{lll}
X^{A}_{\alpha\beta} = X^{A}_{\beta\alpha} & Y^{A}_{\alpha\beta} = Y^{A}_{\beta\alpha} & X^{C}_{\alpha\beta} = X^{C}_{\beta\alpha} \\
X^{M}_{\alpha\beta} = X^{M}_{\beta\alpha} & Y^{M}_{\alpha\beta} = Y^{M}_{\beta\alpha} & Y^{C}_{\alpha\beta} = Y^{C}_{\beta\alpha} \\
Y^{\tilde{B}}_{\alpha\beta} = -Y^{B}_{\beta\alpha} & X^{\tilde{G}}_{\alpha\beta} = X^{G}_{\beta\alpha} & Z^{M}_{\alpha\beta} = Z^{M}_{\beta\alpha} \\
Y^{\tilde{G}}_{\alpha\beta} = Y^{G}_{\beta\alpha} & Y^{\tilde{H}}_{\alpha\beta} = Y^{H}_{\beta\alpha} &
\end{array}
$$

Moreover, the relations for $\lambda = \frac{a_2}{a_1}$ and λ^{-1} originating from geometrical symmetry read, for the dimensionless functions (Jeffrey & Onishi, 1984; Jeffrey, 1989; Jeffrey et al., 1993):

$$
\begin{array}{ll}
\hat{X}^{A}_{\alpha\beta}(s,\lambda) = \hat{X}^{A}_{(3-\alpha)(3-\beta)}(s,\lambda^{-1}) & \hat{Y}^{A}_{\alpha\beta}(s,\lambda) = \hat{Y}^{A}_{(3-\alpha)(3-\beta)}(s,\lambda^{-1}) \\
\hat{Y}^{B}_{\alpha\beta}(s,\lambda) = -\hat{Y}^{B}_{(3-\alpha)(3-\beta)}(s,\lambda^{-1}) & \hat{X}^{C}_{\alpha\beta}(s,\lambda) = \hat{X}^{C}_{(3-\alpha)(3-\beta)}(s,\lambda^{-1}) \\
\hat{Y}^{C}_{\alpha\beta}(s,\lambda) = \hat{Y}^{C}_{(3-\alpha)(3-\beta)}(s,\lambda^{-1}) & \hat{X}^{G}_{\alpha\beta}(s,\lambda) = -\hat{X}^{G}_{(3-\alpha)(3-\beta)}(s,\lambda^{-1}) \\
\hat{Y}^{G}_{\alpha\beta}(s,\lambda) = -\hat{Y}^{G}_{(3-\alpha)(3-\beta)}(s,\lambda^{-1}) & \hat{Y}^{H}_{\alpha\beta}(s,\lambda) = \hat{Y}^{H}_{(3-\alpha)(3-\beta)}(s,\lambda^{-1}) \\
\hat{X}^{M}_{\alpha\beta}(s,\lambda) = \hat{X}^{M}_{(3-\alpha)(3-\beta)}(s,\lambda^{-1}) & \hat{Y}^{M}_{\alpha\beta}(s,\lambda) = \hat{Y}^{M}_{(3-\alpha)(3-\beta)}(s,\lambda^{-1}) \\
\hat{Z}^{M}_{\alpha\beta}(s,\lambda) = \hat{Z}^{M}_{(3-\alpha)(3-\beta)}(s,\lambda^{-1}) & \hat{X}^{P}_{\alpha\beta}(s,\lambda) = -\hat{X}^{P}_{(3-\alpha)(3-\beta)}(s,\lambda^{-1}) \\
\hat{X}^{Q}_{\alpha\beta}(s,\lambda) = \hat{X}^{Q}_{(3-\alpha)(3-\beta)}(s,\lambda^{-1}) &
\end{array}
$$

A.2 PARTICLE-WALL

The same general forms hold for the particle-wall interaction matrices $\mathbf{Mat}_w$ as for their two-particle counterpart $\mathbf{Mat}_{11}$ provided that $\mathbf{d}$ is now the unit vector normal to the wall into the wall. The scalar resistance functions depend on the radius of the particle a and the reduced distance of the particle surface to the wall $\varepsilon = [(\mathbf{x}_w - \mathbf{x}_p) \cdot \mathbf{d}] / a - 1$, where $\mathbf{x}_w$ is the position of the wall.

B

THE THEORETICAL RESISTANCE MATRICES

Here, the theoretical expressions of the resistance functions are collected. In the case of a particle close to a wall, the expressions proposed by Chaoui & Feuillebois (2003) are found to be preferable to the expressions from the lubrication approximation.

B.1 TWO-PARTICLE RESISTANCE MATRIX

Depending on the reduced distance $\xi = 2\|\mathbf{x}_2 - \mathbf{x}_1\| / (a_1 + a_2) - 2$ between the particles' surfaces, the theoretical resistance functions are computed either from expressions obtained in the frame of the lubrication approximation (Jeffrey & Onishi, 1984; Jeffrey, 1992; Jeffrey et al., 1993) ($\xi \leqslant 0.01$) or by interpolation of tabulated values ($\xi > 0.01$). The tabulated values were computed using the programs made available on the web by Jeffrey (2021). The expressions are quoted below for the particular coefficients that are needed in the frame-invariant sub-grid correction matrix (see Section 3.3), as a function of ξ and the particles' radii ratio $\lambda = a_2/a_1$. They are made dimensionless according to Appendix A.

The constants at the end of each expression, such as $A^X_{21}(\lambda)$, $A^Y_{21}(\lambda)$, etc., may be computed using programs available on the same web page. We note here that the resistance functions in the sub-grid correction matrix diverge as $\xi \to 0$. To keep the linear system in Eq. (2.43) reasonably well conditioned, a threshold (10^{-5}) is imposed on the reduced distance ξ, below which the resistance functions are kept constant.

$$\begin{aligned}\frac{X^A_{21}}{3\pi(a_1+a_2)} = &-\frac{4\lambda^2}{(1+\lambda)^4}\xi^{-1} - \frac{2\lambda\left(1+7\lambda+\lambda^2\right)}{5(1+\lambda)^4}\ln\xi^{-1} \\ &-\frac{2\left(1+18\lambda-29\lambda^2+18\lambda^3+\lambda^4\right)}{42(1+\lambda)^4}\xi\ln\xi^{-1} + A^X_{21}(\lambda)\end{aligned}$$

$$\frac{Y^A_{21}}{3\pi(a_1+a_2)} = -\frac{8\lambda\left(2+\lambda+2\lambda^2\right)}{15(1+\lambda)^4}\ln\xi^{-1} - \frac{4\left(16-45\lambda+58\lambda^2-45\lambda^3+16\lambda^4\right)}{375(1+\lambda)^4}\xi\ln\xi^{-1} + A^Y_{21}(\lambda)$$

$$\frac{X^C_{21}}{\pi(a_1+a_2)^3} = \frac{2\lambda^2}{(1+\lambda)^4}\xi\ln\xi^{-1} + C^X_{21}(\lambda)$$

$$\frac{Y^C_{11}}{8\pi a_1^3} = \frac{2}{5}\lambda(1+\lambda)^{-1}\ln\xi^{-1} + \frac{1}{125}\left(8+6\lambda+33\lambda^2\right)(1+\lambda)^{-1}\xi\ln\xi^{-1} + C^Y_{11}(\lambda)$$

$$\frac{Y^B_{21}}{\pi(a_1+a_2)^2} = -\frac{4\lambda^{-1}\left(4+\lambda^{-1}\right)}{5\left(1+\lambda^{-1}\right)^4}\ln\xi^{-1} - \frac{4\left(32-33\lambda^{-1}+83\lambda^{-2}+43\lambda^{-3}\right)}{250\left(1+\lambda^{-1}\right)^4}\xi\ln\xi^{-1} + B^Y_{21}(\lambda)$$

$$\begin{aligned}\frac{X^G_{11}}{4\pi a_1^2} = &\frac{3\lambda^2}{(1+\lambda)^3}\xi^{-1} + \frac{3\left(\lambda+12\lambda^2-4\lambda^3\right)}{10(1+\lambda)^3}\ln\xi^{-1} \\ &+\frac{5+181\lambda-453\lambda^2+566\lambda^3-65\lambda^4}{140(1+\lambda)^3}\xi\ln\xi^{-1} + G^X_{11}(\lambda)\end{aligned}$$

$$\frac{Y_{11}^{G}}{4\pi a_1^2} = \frac{4\lambda - \lambda^2 + 7\lambda^3}{10\left(1+\lambda\right)^3}\ln\xi^{-1} + \frac{32 - 179\lambda + 532\lambda^2 - 356\lambda^3 + 221\lambda^4}{500\left(1+\lambda\right)^3}\xi\ln\xi^{-1} + G_{11}^{Y}\left(\lambda\right)$$

$$\frac{Y_{21}^{H}}{\pi\left(a_1+a_2\right)^3} = \frac{8\left(\lambda^{-2} + 7\lambda^{-3}\right)}{20\left(1+\lambda^{-1}\right)^5}\ln\xi^{-1} + \frac{8\left(43\lambda^{-1} + 147\lambda^{-2} - 185\lambda^{-3} + 221\lambda^{-4}\right)}{1000\left(1+\lambda^{-1}\right)^5}\xi\ln\xi^{-1} + H_{21}^{Y}\left(\lambda\right)$$

$$\begin{aligned}\frac{X_{12}^{P}}{\pi\left(a_1+a_2\right)^2} &= -\frac{12\lambda^2}{\left(1+\lambda\right)^5}\xi^{-1} - \frac{12\left(\lambda - 4\lambda^2\right)}{10\left(1+\lambda\right)^4}\ln\xi^{-1} \\ &\quad - \frac{4\left(5 - 97\lambda + 64\lambda^2 - 44\lambda^3 + \lambda^4\right)}{140\left(1+\lambda\right)^4}\xi\ln\xi^{-1} + P_{12}^{X}\left(\lambda\right)\end{aligned}$$

$$\begin{aligned}\frac{X_{21}^{P}}{\pi\left(a_1+a_2\right)^2} &= \frac{12\lambda^{-2}}{\left(1+\lambda^{-1}\right)^5}\xi^{-1} + \frac{12\left(\lambda^{-1} - 4\lambda^{-2}\right)}{10\left(1+\lambda^{-1}\right)^4}\ln\xi^{-1} \\ &\quad + \frac{4\left(5 - 97\lambda^{-1} + 64\lambda^{-2} - 44\lambda^{-3} + \lambda^{-4}\right)}{140\left(1+\lambda^{-1}\right)^4}\xi\ln\xi^{-1} + P_{21}^{X}\left(\lambda\right)\end{aligned}$$

B.2 PARTICLE-WALL RESISTANCE MATRIX

Concerning the lubrication between a particle and a wall, no tabulated values are available. Therefore, we have to use the theoretical expressions as soon as we need the sub-grid correction. Yeo & Maxey (2010b) propose a compilation from the literature for X^A, Y^A, Y^B, X^C, Y^C, Y^G and Y^H that is quoted below for the sake of completeness. As to the remaining functions, following Gallier et al. (2014a) we compute X^G and X^P starting from the expressions for two particles with radii a and λa and we compute the limit for $\lambda \to \infty$. Finally, the term $\mathcal{O}(1)$ is taken from Jeffrey (1992) for $\lambda = 100$, which is the maximum value that we considered.

However, these theoretical expressions should be used in principle only for $\varepsilon \leqslant 0.01$ (with $\varepsilon = \left[\left(\mathbf{x}_w - \mathbf{x}_p\right) \cdot \mathbf{d}\right]/a - 1$, where $\mathbf{x}_w$ is the position of the wall), because they are less and less accurate for larger distances. Chaoui & Feuillebois (2003) investigated the flow of a particle close to a wall in a shear flow, and they slightly modified some of the lubrication expressions and proposed some expansions for further distances for the force friction factor and the torque friction factor for translation along a wall (Y^A and Y^B), and for the torque friction factor for rotation close to a wall (Y^C). We finally use these latter expressions to compute the sub-grid correction matrix.

As in the two-particle case, the resistance functions in the sub-grid correction matrix diverge as the distance between the particle surface and a wall tends to zero. Following the same reasoning, a threshold (10^{-5}) is imposed on the reduced distance ε, below which the resistance functions are kept constant.

The expressions gathered by Yeo & Maxey (2010b) and the ones obtained following Gallier (2014) and Jeffrey (1992) are:

$$
\begin{aligned}
\frac{X^A}{6\pi a} &= \varepsilon^{-1} + \frac{1}{5}\ln\varepsilon^{-1} + \frac{1}{21}\varepsilon\ln\varepsilon^{-1} + 0.8193\\
\frac{X^C}{8\pi a^3} &= -\frac{1}{2}\varepsilon\ln\varepsilon^{-1} + 1.2021\\
\frac{X^G}{4\pi a^2} &= \frac{3}{2}\varepsilon^{-1} - \frac{6}{5}\ln\varepsilon^{-1} + 0.3912\\
\frac{Y^B}{4\pi a^2} &= -\frac{3}{15}\ln\varepsilon^{-1} - \frac{43}{125}\varepsilon\ln\varepsilon^{-1} + 0.3852\\
\frac{X^P}{4\pi a^2} &= \frac{3}{2}\varepsilon^{-1} - \frac{6}{5}\ln\varepsilon^{-1} - 0.552\\
\frac{Y^A}{6\pi a} &= \frac{8}{15}\ln\varepsilon^{-1} + \frac{64}{375}\varepsilon\ln\varepsilon^{-1} + 0.9557\\
\frac{Y^C}{8\pi a^3} &= \frac{2}{5}\ln\varepsilon^{-1} + \frac{66}{125}\varepsilon\ln\varepsilon^{-1} + 0.3720\\
\frac{Y^G}{4\pi a^2} &= \frac{7}{10}\ln\varepsilon^{-1} + \frac{221}{250}\varepsilon\ln\varepsilon^{-1} - 0.923\\
\frac{Y^H}{8\pi a^3} &= -\frac{1}{10}\ln\varepsilon^{-1} + \frac{2}{250}\varepsilon\ln\varepsilon^{-1} + 0.0916\\
\frac{Y^M}{\frac{20}{3}\pi a^3} &= \frac{24}{25}\ln\varepsilon^{-1} + \frac{1182}{625}\varepsilon\ln\varepsilon^{-1} - 0.685
\end{aligned}
$$

It should be noted that the constant term for X^G has not the same value as the one proposed by Gallier (2014), and it is now set to 0.3912. This value has been chosen after evaluating X^G varying the particles' radii ratio λ and choosing the value for $\lambda = 100$. Also, the simulations pointed out that no sub-grid correction is needed for X^C.

Finally, the expansions for further distances for the force friction factor and the torque friction factor for translation along a wall (Y^A and Y^B), and for the torque friction factor for rotation close to a wall (Y^C) proposed by Chaoui & Feuillebois (2003) – preferred to the expressions from the lubrication approximation mentioned above – are quoted below:

$$
\begin{aligned}
\frac{Y^A_{CF}}{6\pi a} &= \sum_{j=0}^{5}\left[\phi^t_j\varepsilon^j\ln\varepsilon + f^t_j\varepsilon^j\right]\\
\frac{Y^B_{CF}}{-8\pi a^2} &= \sum_{j=0}^{5}\left[\gamma^t_j\varepsilon^j\ln\varepsilon + c^t_j\varepsilon^j\right] \qquad \text{(B.1)}\\
\frac{Y^C_{CF}}{8\pi a^3} &= \sum_{j=0}^{5}\left[\gamma^r_j\varepsilon^j\ln\varepsilon + c^r_j\varepsilon^j\right]
\end{aligned}
$$

where:

$$\phi_0^t = -8/15$$

$$\phi_1^t = -64/375$$

$$\phi_2^t = 0.011595712294862$$

$$\phi_3^t = -0.002559314461340$$

$$\phi_4^t = 0.002165777707452$$

$$\phi_5^t = 0.000351260314552$$

$$f_0^t = 0.954293724783876$$

$$f_1^t = 0.429450132564500$$

$$f_2^t = -0.001897844702304$$

$$f_3^t = 0.002058408405495$$

$$f_4^t = 0.000096108639584$$

$$f_5^t = -0.001248147281379$$

$$\gamma_0^t = -1/10$$

$$\gamma_1^t = -43/250$$

$$\gamma_2^t = -0.036913066460225$$

$$\gamma_3^t = 0.001486892317125$$

$$\gamma_4^t = 0.000012689734456$$

$$\gamma_5^t = 0.000103798994187$$

$$c_0^t = -0.192952745666190$$

$$c_1^t = 0.100579155700110$$

$$c_2^t = 0.094493729126963$$

$$c_3^t = 0.003821112414990$$

$$c_4^t = -0.000819028830091$$

$$c_5^t = -0.000097511506358$$

$$\gamma_0^r = -2/5$$

$$\gamma_1^r = -0.528001276176667$$

$$\gamma_2^r = -0.212879560114862$$

$$\gamma_3^r = -0.035965644690736$$

$$\gamma_4^r = -0.006385459746252$$

$$\gamma_5^r = 0.000167620439255$$

$$c_0^r = 0.370892565890165$$

$$c_1^r = 0.340079923061464$$

$$c_2^r = 0.225531274283815$$

$$c_3^r = 0.097897336215370$$

$$c_4^r = 0.005878696055717$$

$$c_5^r = 0.001503759398496$$

C

MEASURING THE 2P RESISTANCE MATRIX

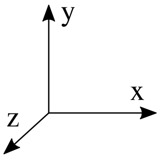

Recalling the two-particle resistance matrix in Section 3.1 and Eq. (3.5), we concentrate here on measuring the resistance functions for (p_1) (the ones for (p_2) are analogous). Each resistance function is linked to specific movements of the particles and of the flow. One has to carefully choose the right configuration to measure them separately. In all the expressions given in the following, $\mathbf{d} = (\mathbf{x}_2 - \mathbf{x}_1) / \|\mathbf{x}_2 - \mathbf{x}_1\|$ is the vector linking the centers of the two particles. Also, the practical configurations employed are shown. The same setups can be used when measuring the resistance functions for a particle close to a wall, by replacing (p_2) with the considered wall. The figure here represents the reference frame employed in the present chapter.

C.1 1^{ST} AND 2^{ND} COLUMNS: A, B, G, P

The first two columns link the resistance functions to the translational velocities of (p_1) and (p_2). So, to measure $\mathbf{A}, \mathbf{B}, \mathbf{G}$ and $\mathbf{P}$ for (p_1), everything is put at rest, and only the translational velocity of (p_1) is non-null: $\mathbf{u}^\infty = 0,\ \boldsymbol{\Omega}_1 = \boldsymbol{\Omega}_2 = 0,\ \mathbf{U}_1 \neq 0,\ \mathbf{U}_2 = 0$

$$\frac{1}{\eta}\mathbf{F}_1 = -\mathbf{A}_{11} \cdot \mathbf{U}_1 = -\left[X^A_{11} \mathbf{d} \otimes \mathbf{d} + Y^A_{11} \left(\mathbf{I} - \mathbf{d} \otimes \mathbf{d}\right)\right] \cdot \mathbf{U}_1$$

$$\frac{1}{\eta}\mathbf{T}_1 = -\mathbf{B}_{11} \cdot \mathbf{U}_1 = -Y^B_{11} \mathbf{U}_1 \wedge \mathbf{d}$$

$$\frac{1}{\eta}\mathbf{S}_1 = -\mathbf{G}_{11} \cdot \mathbf{U}_1 = -X^G_{11} \mathbf{U}_1 \cdot \mathbf{d} \left(\mathbf{d} \otimes \mathbf{d} - \frac{1}{3}\mathbf{I}\right) - Y^G_{11} \left(\mathbf{d} \otimes \mathbf{U}_1 + \mathbf{U}_1 \otimes \mathbf{d} - 2\left(\mathbf{U}_1 \cdot \mathbf{d}\right) \mathbf{d} \otimes \mathbf{d}\right)$$

$$\frac{1}{\eta}s_1 = -\mathbf{P}_{11} \cdot \mathbf{U}_1 = -X^P_{11} \mathbf{U}_1 \cdot \mathbf{d}$$

C.1.1 1ST SETUP

The two particles are aligned along x, and (p_1) has a translational velocity parallel to the vector linking the centers (i.e., towards (p_2)).

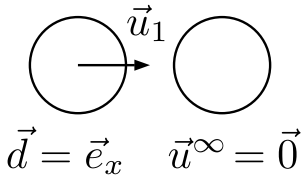

$X^A_{11} = -\dfrac{F_{1,x}}{\eta u_{1,x}}$	$X^G_{11} = -\dfrac{S_{1,xx} - S_{1,yy} - S_{1,zz}}{\frac{4}{3}\eta u_{1,x}}$
$X^A_{21} = -\dfrac{F_{2,x}}{\eta u_{1,x}}$	$X^G_{21} = -\dfrac{S_{2,xx} - S_{2,yy} - S_{2,zz}}{\frac{4}{3}\eta u_{1,x}}$
$X^P_{11} = -\dfrac{s_1}{\eta u_{1,x}}$	$X^P_{21} = -\dfrac{s_2}{\eta u_{1,x}}$

C.1.2 2ND SETUP

The two particles are aligned along x, and (p_1) has a translational velocity orthogonal to the vector linking the centers.

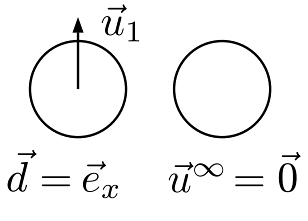

$Y^A_{11} = -\dfrac{F_{1,y}}{\eta u_{1,y}}$	$Y^G_{11} = -\dfrac{S_{1,xy} + S_{1,yx}}{2\eta u_{1,y}}$
$Y^A_{21} = -\dfrac{F_{2,y}}{\eta u_{1,y}}$	$Y^G_{21} = -\dfrac{S_{2,xy} + S_{2,yx}}{2\eta u_{1,y}}$
$Y^B_{11} = +\dfrac{T_{1,z}}{\eta u_{1,y}}$	$Y^B_{21} = +\dfrac{T_{2,z}}{\eta u_{1,y}}$

C.2 3^{RD} AND 4^{TH} COLUMNS: $\tilde{\mathbf{B}}$, C, H

The third and fourth columns are linked to the rotational velocities of (p_1) and (p_2). So, to measure $\tilde{\mathbf{B}}, \mathbf{C}$ and $\mathbf{H}$ for (p_1), everything is put at rest, and only the rotational velocity of (p_1) is non-null: $\mathbf{u}^\infty = 0,\ \mathbf{U}_1 = \mathbf{U}_2 = 0,\ \boldsymbol{\Omega}_1 \neq 0,\ \boldsymbol{\Omega}_2 = 0$

$$\frac{1}{\eta}\mathbf{F}_1 = -\tilde{\mathbf{B}}_{11}\cdot\boldsymbol{\Omega}_1 = -Y^{\tilde{B}}_{11}\boldsymbol{\Omega}_1 \wedge \mathbf{d}$$

$$\frac{1}{\eta}\mathbf{T}_1 = -\mathbf{C}_{11}\cdot\boldsymbol{\Omega}_1 = -X^{C}_{11}\left(\mathbf{d}\otimes\mathbf{d}\right)\cdot\boldsymbol{\Omega}_1 - Y^{C}_{11}\left(\mathbf{I}-\mathbf{d}\otimes\mathbf{d}\right)\cdot\boldsymbol{\Omega}_1$$

$$\frac{1}{\eta}\mathbf{S}_1 = -\mathbf{H}_{11}\cdot\boldsymbol{\Omega}_1 = -Y^{H}_{11}\left[\mathbf{d}\otimes\left(\boldsymbol{\Omega}_1\wedge\mathbf{d}\right) + \left(\boldsymbol{\Omega}_1\wedge\mathbf{d}\right)\otimes\mathbf{d}\right]$$

C.2.1 3RD SETUP

The two particles are aligned along x, and (p_1) has a non-null rotational velocity $\boldsymbol{\Omega}_y$.

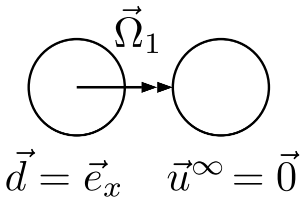

$$\boxed{\begin{aligned} X^{C}_{11} &= -\frac{T_{1,x}}{\eta\Omega_{1,x}} \\ X^{C}_{21} &= -\frac{T_{2,x}}{\eta\Omega_{1,x}} \end{aligned}}$$

C.2.2 4TH SETUP

The two particles are again aligned along x, and (p_1) has a non-null rotational velocity $\boldsymbol{\Omega}_z$.

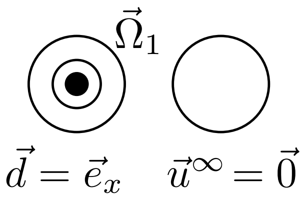

$$\boxed{\begin{aligned} Y^{\tilde{B}}_{11} &= -\frac{F_{1,y}}{\eta\Omega_{1,z}} & \qquad Y^{H}_{11} &= -\frac{S_{1,xy}+S_{1,yx}}{2\eta\Omega_{1,z}} \\ Y^{\tilde{B}}_{21} &= -\frac{F_{2,y}}{\eta\Omega_{1,z}} & \qquad Y^{H}_{21} &= -\frac{S_{2,xy}+S_{2,yx}}{2\eta\Omega_{1,z}} \\ Y^{C}_{11} &= -\frac{T_{1,z}}{\eta\Omega_{1,z}} & \qquad Y^{C}_{21} &= -\frac{T_{2,z}}{\eta\Omega_{1,z}} \end{aligned}}$$

C.3 5TH AND 6TH COLUMNS: $\tilde{\mathbf{G}}$, $\tilde{\mathbf{H}}$, M, Q

The last two columns are linked to the strain tensor. So, to measure $\tilde{\mathbf{G}}, \tilde{\mathbf{H}}, \mathbf{M}$ and $\mathbf{Q}$, the strain tensor has to be non-null, leading non-null translational velocities of both (p_1) and (p_2): $\mathbf{u}^\infty = \mathbf{E}^\infty \cdot \mathbf{x},\ \mathbf{U}_1 = \mathbf{E}^\infty \cdot \mathbf{x}_1,\ \mathbf{U}_2 = \mathbf{E}^\infty \cdot \mathbf{x}_2,\ \boldsymbol{\Omega}_1 = \boldsymbol{\Omega}_2 = 0$

$$\begin{aligned}\frac{1}{\eta}\mathbf{F}_1 = \left(\tilde{\mathbf{G}}_{11} + \tilde{\mathbf{G}}_{12}\right) \cdot \mathbf{E}^\infty &= \left(X^{\tilde{G}}_{11} + X^{\tilde{G}}_{12}\right) \left[\mathbf{E}^\infty : (\mathbf{d} \otimes \mathbf{d})\right] \mathbf{d} \\ &+ 2\left(Y^{\tilde{G}}_{11} + Y^{\tilde{G}}_{12}\right) \left[\mathbf{E}^\infty \cdot \mathbf{d} - \left(\mathbf{E}^\infty : (\mathbf{d} \otimes \mathbf{d})\right) \mathbf{d}\right]\end{aligned}$$

$$\frac{1}{\eta}\mathbf{T}_1 = \left(\tilde{\mathbf{H}}_{11} + \tilde{\mathbf{H}}_{12}\right) \cdot \mathbf{E}^\infty = 2\left(Y^{\tilde{H}}_{11} + Y^{\tilde{H}}_{12}\right) \mathbf{d} \wedge \left(\mathbf{E}^\infty \cdot \mathbf{d}\right)$$

$$\begin{aligned}\frac{1}{\eta}\mathbf{S}_1 = \left(\mathbf{M}_{11} + \mathbf{M}_{12}\right) \cdot \mathbf{E}^\infty &= \frac{3}{2}\left(X^{M}_{11} + X^{M}_{12}\right) \left(\mathbf{E}^\infty : (\mathbf{d} \otimes \mathbf{d})\right) \left(\mathbf{d} \otimes \mathbf{d} - \frac{1}{3}\mathbf{I}\right) \\ &+ \left(Y^{M}_{11} + Y^{M}_{12}\right) \left[\mathbf{d} \otimes (\mathbf{E}^\infty \cdot \mathbf{d}) + (\mathbf{E}^\infty \cdot \mathbf{d}) \otimes \mathbf{d} - 2\left(\mathbf{E}^\infty : (\mathbf{d} \otimes \mathbf{d})\right)(\mathbf{d} \otimes \mathbf{d})\right] \\ &+ \left(Z^{M}_{11} + Z^{M}_{12}\right) \left[\mathbf{E}^\infty + \frac{1}{2}\left(\mathbf{E}^\infty : (\mathbf{d} \otimes \mathbf{d})\right)(\mathbf{I} + \mathbf{d} \otimes \mathbf{d}) - \mathbf{d} \otimes (\mathbf{E}^\infty \cdot \mathbf{d}) - (\mathbf{E}^\infty \cdot \mathbf{d}) \otimes \mathbf{d}\right]\end{aligned}$$

$$\frac{1}{\eta}s_1 = \left(\mathbf{Q}_{11} + \mathbf{Q}_{12}\right) \cdot \mathbf{E}^\infty = \left(X^{Q}_{11} + X^{Q}_{12}\right) \left(\mathbf{d} \otimes \mathbf{d} - \frac{1}{3}\mathbf{I}\right) : \mathbf{E}^\infty$$

C.3.1 5TH SETUP

A pure straining flow is imposed, and the two particles are aligned along x.

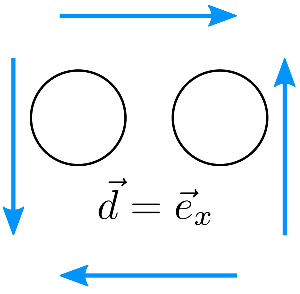

$$\mathbf{E}^\infty = \frac{\dot{\gamma}}{2}\begin{pmatrix} 0 & 1 & 0 \\ 1 & 0 & 0 \\ 0 & 0 & 0 \end{pmatrix}$$

$$\mathbf{U}_1 = \frac{\dot{\gamma}}{2}\left(y_1\mathbf{e}_x + x_1\mathbf{e}_y\right)$$

$$\mathbf{U}_2 = \frac{\dot{\gamma}}{2}\left(y_2\mathbf{e}_x + x_2\mathbf{e}_y\right)$$

$$Y^{\tilde{G}}_{11} + Y^{\tilde{G}}_{12} = \frac{F_{1,y}}{\eta\dot{\gamma}}$$

$$Y^{\tilde{H}}_{11} + Y^{\tilde{H}}_{12} = \frac{T_{1,z}}{\eta\dot{\gamma}}$$

$$Y^{M}_{11} + Y^{M}_{12} = \frac{S_{1,xy} + S_{1,yx}}{\eta\dot{\gamma}}$$

C.3.2 6TH SETUP

A pure straining flow (different from the one in setup 5) is imposed, and the two particles are aligned along x.

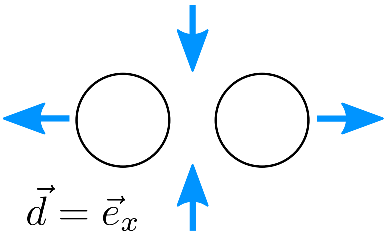

$$\mathbf{E}^{\infty} = \frac{\dot{\gamma}}{2}\begin{pmatrix} 1 & 0 & 0 \\ 0 & -1 & 0 \\ 0 & 0 & 0 \end{pmatrix}$$

$$\mathbf{U}_1 = \frac{\dot{\gamma}}{2}\left(x_1\mathbf{e}_x - y_1\mathbf{e}_y\right)$$

$$\mathbf{U}_2 = \frac{\dot{\gamma}}{2}\left(x_2\mathbf{e}_x - y_2\mathbf{e}_y\right)$$

$$\boxed{X_{11}^{\tilde{G}} + X_{12}^{\tilde{G}} = \frac{2F_{1,x}}{\eta\dot{\gamma}}}$$

C.3.3 7TH SETUP

A pure straining flow as in setup 5 is imposed, and the two particles are aligned along z.

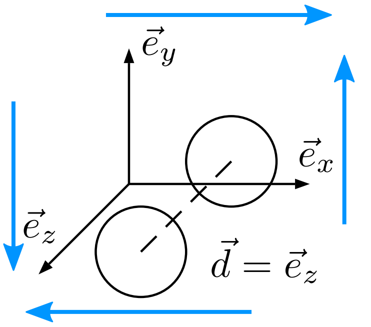

$$\mathbf{E}^{\infty} = \frac{\dot{\gamma}}{2}\begin{pmatrix} 0 & 1 & 0 \\ 1 & 0 & 0 \\ 0 & 0 & 0 \end{pmatrix}$$

$$\mathbf{U}_1 = \frac{\dot{\gamma}}{2}\left(y_1\mathbf{e}_x + x_1\mathbf{e}_y\right)$$

$$\mathbf{U}_2 = \frac{\dot{\gamma}}{2}\left(y_2\mathbf{e}_x + x_2\mathbf{e}_y\right)$$

$$\boxed{Z_{11}^{M} + Z_{12}^{M} = \frac{S_{1,xy} + S_{1,yx}}{\eta\dot{\gamma}}}$$

C.3.4 8TH SETUP

An elongational flow is imposed, and the two particles are aligned along x.

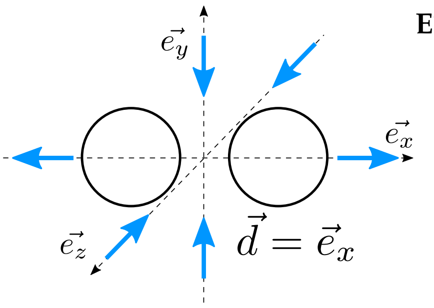

$$\mathbf{E}^{\infty} = \frac{\dot{\gamma}}{3}\begin{pmatrix} 2 & 0 & 0 \\ 0 & -1 & 0 \\ 0 & 0 & -1 \end{pmatrix}$$

$$\mathbf{U}_1 = \frac{\dot{\gamma}}{3}\left(2x_1\mathbf{e}_x - y_1\mathbf{e}_y - z_1\mathbf{e}_z\right)$$

$$\mathbf{U}_2 = \frac{\dot{\gamma}}{3}\left(2x_2\mathbf{e}_x - y_2\mathbf{e}_y - z_2\mathbf{e}_z\right)$$

$$\boxed{\begin{aligned} X_{11}^{M} + X_{12}^{M} &= \frac{S_{1,xx} - \frac{1}{2}S_{1,yy} - \frac{1}{2}S_{1,zz}}{\eta\dot{\gamma}} \\ X_{11}^{Q} + X_{12}^{Q} &= \frac{s_1}{\frac{2}{3}\eta\dot{\gamma}} \end{aligned}}$$

D

IMPOSING THE FRAME INDIFFERENCE OF THE 2P RESISTANCE MATRIX

We show here how the constraints quoted in Section 3.3.3 are obtained. We recall that to obtain them, the second and third terms in the RHS of Eq. (3.9) have to be put exactly equal to zero: this means that no sub-grid correction is wanted in both the cases of a particle pair with a rigid body motion in a liquid at rest and a particle pair at rest in a pure straining flow, respectively.

The superscript SG has been removed for the sake of simplicity.

D.1 A PARTICLE PAIR WITH A RIGID BODY MOTION IN A LIQUID AT REST

Imposing the first and second terms of Eq. (3.14) to be zero leads to the following relations:

$$\begin{aligned}\frac{\mathbf{F}_1}{\eta} = &- \left(X^A_{11} + X^A_{12}\right)\left(\mathbf{U}_0' \cdot \mathbf{d}\right) \cdot \mathbf{d} - \left(Y^A_{11} + Y^A_{12}\right)\left(\mathbf{I} - \mathbf{d} \otimes \mathbf{d}\right) \cdot \mathbf{U}_0' \\ &+ \left[\frac{r}{2}\left(Y^A_{11} - Y^A_{12}\right) - \left(Y^{\tilde{B}}_{11} + Y^{\tilde{B}}_{12}\right)\right]\left(\mathbf{\Omega}_\infty \times \mathbf{d}\right) = 0\end{aligned}$$

$$\Rightarrow \boxed{\begin{aligned}&X^A_{11} + X^A_{12} = 0 \\ &Y^A_{11} + Y^A_{12} = 0 \\ &\frac{r}{2}\left(Y^A_{11} - Y^A_{12}\right) - \left(Y^{\tilde{B}}_{11} + Y^{\tilde{B}}_{12}\right) = 0\end{aligned}}$$

$$\begin{aligned}\frac{\mathbf{T}_1}{\eta} = &- \left(Y^B_{11} + Y^B_{12}\right)\left(\mathbf{U}_0' \times \mathbf{d}\right) - \left[\frac{r}{2}\left(Y^B_{11} - Y^B_{12}\right) + \left(Y^C_{11} + Y^C_{12}\right)\right]\left(\mathbf{I} - \mathbf{d} \otimes \mathbf{d}\right) \cdot \mathbf{\Omega}_\infty \\ &- \left(X^C_{11} + X^C_{12}\right)\left(\mathbf{\Omega}_\infty \cdot \mathbf{d}\right)\mathbf{d} = 0\end{aligned}$$

$$\Rightarrow \boxed{\begin{aligned}&Y^B_{11} + Y^B_{12} = 0 \\ &X^C_{11} + X^C_{12} = 0 \\ &\frac{r}{2}\left(Y^B_{11} - Y^B_{12}\right) + \left(Y^C_{11} + Y^C_{12}\right) = 0\end{aligned}}$$

$$\begin{aligned}\frac{\mathbf{S}_1}{\eta} = &- \left(X^G_{11} + X^G_{12}\right)\mathbf{U}_0' \cdot \mathbf{d}\left(\mathbf{d} \otimes \mathbf{d} - \frac{1}{3}\mathbf{I}\right) - \left(Y^G_{11} + Y^G_{12}\right)\left(\mathbf{d} \otimes \mathbf{U}_0' + \mathbf{U}_0' \otimes \mathbf{d} - 2\mathbf{U}_0' \cdot \mathbf{d}\left(\mathbf{d} \otimes \mathbf{d}\right)\right) \\ &+ \left[\frac{r}{2}\left(Y^G_{11} - Y^G_{12}\right) - \left(Y^H_{11} + Y^H_{12}\right)\right]\left(\mathbf{d} \otimes \left(\mathbf{\Omega}_\infty \times \mathbf{d}\right) + \left(\mathbf{\Omega}_\infty \times \mathbf{d}\right) \otimes \mathbf{d}\right) = 0\end{aligned}$$

$$\Rightarrow \boxed{\begin{aligned}&X^G_{11} + X^G_{12} = 0 \\ &Y^G_{11} + Y^G_{12} = 0 \\ &\frac{r}{2}\left(Y^G_{11} - Y^G_{12}\right) - \left(Y^H_{11} + Y^H_{12}\right) = 0\end{aligned}}$$

$$\frac{s_1}{\eta} = - \left(X^P_{11} + X^P_{12}\right)\mathbf{U}_0' \cdot \mathbf{d} = 0$$

$$\Rightarrow \boxed{X^P_{11} + X^P_{12} = 0}$$

D.2 A PARTICLE PAIR AT REST IN A PURE STRAINING FLOW

Imposing the third term of Eq. (3.14) to be exactly zero leads to the following relations:

$$\begin{aligned}\frac{\mathbf{F}_1}{\eta} &= \left[\frac{r}{2}\left(-X_{11}^{A}+X_{12}^{A}\right)+\left(X_{11}^{\tilde{G}}+X_{12}^{\tilde{G}}\right)\right]\cdot\left(\mathbf{E}^{\infty}:(\mathbf{d}\otimes\mathbf{d})\right)\mathbf{d}\\ &\quad+\left[\frac{r}{2}\left(-Y_{11}^{A}+Y_{12}^{A}\right)+2\left(Y_{11}^{\tilde{G}}+Y_{12}^{\tilde{G}}\right)\right]\left(\mathbf{E}^{\infty}\cdot\mathbf{d}-\left(\mathbf{E}^{\infty}:(\mathbf{d}\otimes\mathbf{d})\right)\mathbf{d}\right)=0\end{aligned}$$

$$\Rightarrow\quad\boxed{\begin{aligned}&\frac{r}{2}\left(-X_{11}^{A}+X_{12}^{A}\right)+\left(X_{11}^{\tilde{G}}+X_{12}^{\tilde{G}}\right)=0\\ &\frac{r}{2}\left(-Y_{11}^{A}+Y_{12}^{A}\right)+2\left(Y_{11}^{\tilde{G}}+Y_{12}^{\tilde{G}}\right)=0\end{aligned}}$$

$$\frac{\mathbf{T}_1}{\eta}=\left[\frac{r}{2}\left(-Y_{11}^{B}+Y_{12}^{B}\right)-2\left(Y_{11}^{\tilde{H}}+Y_{12}^{\tilde{H}}\right)\right]\left(\mathbf{E}^{\infty}\cdot\mathbf{d}\right)\times\mathbf{d}=0$$

$$\Rightarrow\quad\boxed{\frac{r}{2}\left(-Y_{11}^{B}+Y_{12}^{B}\right)-2\left(Y_{11}^{\tilde{H}}+Y_{12}^{\tilde{H}}\right)=0}$$

$$\begin{aligned}\frac{\mathbf{S}_1}{\eta} &= \left[\frac{r}{2}\left(-X_{11}^{G}+X_{12}^{G}\right)+\frac{3}{2}\left(X_{11}^{M}+X_{12}^{M}\right)\right]\left(\mathbf{E}^{\infty}:\mathbf{d}\otimes\mathbf{d}\right)\left(\mathbf{d}\otimes\mathbf{d}-\frac{1}{3}\mathbf{I}\right)\\ &\quad+\left[\frac{r}{2}\left(-Y_{11}^{G}+Y_{12}^{G}\right)+\left(Y_{11}^{M}+Y_{12}^{M}\right)\right]\left[\mathbf{d}\otimes\left(\mathbf{E}^{\infty}\cdot\mathbf{d}\right)+\left(\mathbf{E}^{\infty}\cdot\mathbf{d}\right)\otimes\mathbf{d}-\left[2\mathbf{E}^{\infty}:(\mathbf{d}\otimes\mathbf{d})\right](\mathbf{d}\otimes\mathbf{d})\right]\\ &\quad+\frac{1}{2}\left(Z_{11}^{M}+Z_{12}^{M}\right)\left[\mathbf{E}^{\infty}-\left(\mathbf{d}\otimes\left(\mathbf{E}^{\infty}\cdot\mathbf{d}\right)+\left(\mathbf{E}^{\infty}\cdot\mathbf{d}\right)\otimes\mathbf{d}\right)+\frac{1}{2}\mathbf{E}^{\infty}:(\mathbf{d}\otimes\mathbf{d})\left(\mathbf{I}+\mathbf{d}\otimes\mathbf{d}\right)\right]=0\end{aligned}$$

$$\Rightarrow\quad\boxed{\begin{aligned}&\frac{r}{2}\left(-X_{11}^{G}+X_{12}^{G}\right)+\frac{3}{2}\left(X_{11}^{M}+X_{12}^{M}\right)=0\\ &\frac{r}{2}\left(-Y_{11}^{G}+Y_{12}^{G}\right)+\left(Y_{11}^{M}+Y_{12}^{M}\right)=0\\ &\frac{1}{2}\left(Z_{11}^{M}+Z_{12}^{M}\right)=0\end{aligned}}$$

$$\frac{s_1}{\eta}=\left[\frac{r}{2}\left(-X_{11}^{P}+X_{12}^{P}\right)+\left(X_{11}^{Q}+X_{12}^{Q}\right)\right]\mathbf{E}^{\infty}:(\mathbf{d}\otimes\mathbf{d})=0$$

$$\Rightarrow\quad\boxed{\frac{r}{2}\left(-X_{11}^{P}+X_{12}^{P}\right)+\left(X_{11}^{Q}+X_{12}^{Q}\right)=0}$$

E

JKR CONTACT THEORY

The first satisfactory analysis of the stresses at the contact of two elastic solids is due to Hertz (1882). He first made the hypothesis that the contact area generally is elliptical. He then introduced the simplification that each body can be regarded as an elastic half-space loaded over a small elliptical region of its surface. This simplification is justifiable if the significant dimensions of the contact are small compared to the dimensions of each body and the radius of curvature of the surfaces. Finally, the surfaces are assumed to be frictionless so that only a normal load is transmitted between them. However, the assumptions made in this theory can become too restricting when closely investigating the edge of contact.

Even though in the current study we are not interested in deeply investigating the tribology of two rigid spheres and we accept the assumptions made by Hertz, when considering adhesive forces questions arise on how to implement them. As it is presented in Section 5.2, we decided to opt for a very simple but easily employable model. Nevertheless, other models can be found in the literature, and one that has to be mentioned is the theory proposed by Johnson et al. (1971). We present their model and we show the differences with the model employed here.

E.1 THE CONTACT OF ELASTIC SOLIDS

In Section 5.2 we present the contact model employed in the current work. Let us now recall the contact theory for the normal force developed by Johnson et al. (1971) and let us see the differences with the model chosen here.

Following Johnson (1985), two ideally flat surfaces have an equilibrium separation distance z_0: for $z < z_0$ they will repel each other, while for $z > z_0$ they will attract. The variation of force per unit area as a function of separation z is usually represented by a law of the following form (displayed in Fig. E.1):

$$p\left(z\right) = -Az^{-n} + Bz^{-m} \qquad \text{with} \quad m > n \tag{E.1}$$

In these circumstances, a tensile (negative) force – the force of adhesion – has to be exerted to separate the two surfaces. It is usual to measure the work 2γ required to separate the surfaces (see Fig. E.1) and to ascribe a surface energy γ to each newly created free surface.

To study the effect of adhesive forces in the absence of surface roughness, we shall consider two spheres of radii R_1 and R_2 which make contact over a circular area of radius a, as represented in Fig. E.2. The normal elastic displacement in the contact circle must satisfy:

$$\overline{u}_{z_1} + \overline{u}_{z_2} = \delta - \frac{r^2}{2R} \tag{E.2}$$

where $\overline{u}_{z_1}$ and $\overline{u}_{z_2}$ are the vertical (i.e., parallel to the normal force, see Fig. E.2) displacement of the surface of each body toward their respective centers of curvature due to contact pressure, r is the position inside the contact circle, and $1/R = (1/R_1 + 1/R_2)$ is the relative

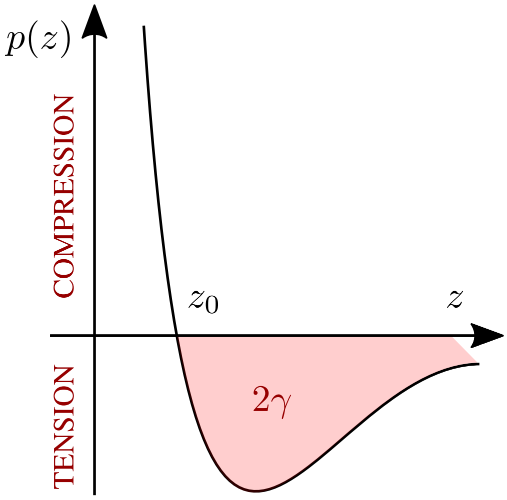

Figure E.1
Force-separation curve and the positive shaded area is the energy that must be provided to separate the surfaces (Eq. (E.1)).

curvature (this comes directly from the Hertz's theory of elastic contact), and δ is the compression. This condition is satisfied by a pressure distribution of the form:

$$p(r) = p_0 \left(1 - \frac{r^2}{a^2}\right)^{1/2} + p_0' \left(1 - \frac{r^2}{a^2}\right)^{-1/2} \tag{E.3}$$

where:

$$p_0 = \frac{2aE^*}{\pi R} \tag{E.4}$$

and:

$$E^* = \left(\frac{1-\nu_1^2}{E_1} + \frac{1-\nu_2^2}{E_2}\right)^{-1} \tag{E.5}$$

being E and ν Young's modulus and Poisson's coefficient, respectively.
In the presence of attractive forces we cannot exclude the possibility of a negative p_0'. Considering the work done in compression, the elastic strain energy stored in the bodies is:

$$U_E = \frac{\pi^2 a^3}{E^*} \left(\frac{2}{15} p_0^2 + \frac{2}{3} p_0 p_0' + (p_0')^2\right) \tag{E.6}$$

The total compression is:

$$\delta = \frac{\pi a}{2E^*} (p_0 + 2p_0') = \frac{a^2}{R} + \frac{\pi a p_0'}{E^*} \tag{E.7}$$

where the definition of p_0 has been used. The variation in strain energy U_E with contact radius a, keeping the overall relative displacement of the two bodies δ constant is (after a few lines of calculus):

$$\left[\frac{\partial U_E}{\partial a}\right]_\delta = \frac{\pi^2 a^2}{E^*} (p_0')^2 \tag{E.8}$$

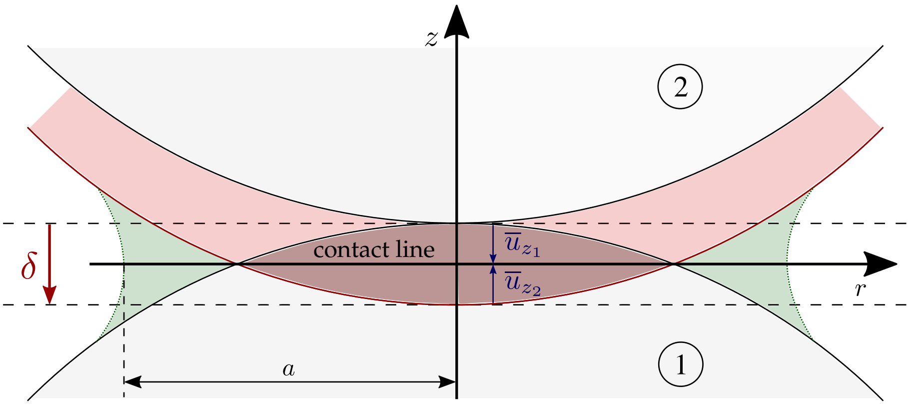

Figure E.2
Two elastic spheres at contact: from an initial position at which $\delta = 0$, sphere 2 moves towards sphere 1 with a displacement $\delta > 0$. $\overline{u}_{z_1}$ and $\overline{u}_{z_2}$ are the vertical displacement of the surface of each body due to contact pressure. Eq. (E.2) can be deduced.

Since δ is kept constant, no external work is done, therefore, for equilibrium, we would expect $\partial U_E/\partial a$ to vanish, giving $p_0' = 0$, as indeed it is in Hertz theory.
In the present problem, adhesive forces introduce a surface energy that decreases when the surfaces come into intimate contact and increases when they separate:

$$U_S = -2\gamma\pi a^2 \tag{E.9}$$

The total free energy of the system is now $U_T = U_E + U_S$. For equilibrium, $[\partial U_T/\partial a]_\delta$ vanishes giving:

$$\frac{\pi^2 a^2}{E^*}\left(p_0'\right)^2 = -\frac{\partial U_S}{\partial a} = 4\pi\gamma a \tag{E.10}$$

leading to:

$$p_0' = -\left(\frac{4\gamma E^*}{\pi a}\right)^{1/2} \tag{E.11}$$

where the positive sign has been voluntarily omitted because it would have the wrong implication (contact outside the circle with radius a). We recall here that negative p_0' implies a tensile contribution to the contact force (Eq. (E.3)). Then, substituting for p_0 and p_0', the net contact force is given by:

$$\begin{aligned} P &= \int_0^a \pi r p(r)\,dr = \left(\frac{2}{3}p_0 + 2p_0'\right)\pi a^2 = 2\pi a^2\left(\frac{2aE^*}{3\pi R} - \left(\frac{4\gamma E^*}{\pi a}\right)^{1/2}\right) \\ \Rightarrow \quad P(a) &= \frac{4E^* a^3}{3R} - \sqrt{16\pi\gamma E^* a^3} \end{aligned} \tag{E.12}$$

Replacing p_0' in Eq. (E.7) leads to:

$$\delta(a) = \frac{a^2}{R} - \left(\frac{\pi\gamma a}{E^*}\right)^{1/2} \tag{E.13}$$

Eqs. (E.12) and (E.13) define the JKR adhesive contact law. Before explaining these equations in some detail, they are made dimensionless. By searching for the minimum net contact force with respect to the contact area, we can define the corresponding contact area a_c:

$$\frac{dP}{da} = 0 \tag{E.14}$$

After some derivatives, it finally leads to:

$$a_c = \left(\frac{9}{4}\frac{\pi R^2\gamma}{E^*}\right)^{1/3} \tag{E.15}$$

We can define the associated critical load as:

$$P_c = P(a_c) = -3\pi R\gamma \tag{E.16}$$

Let us now introduce the following dimensionless expressions, represented in Fig. E.3:

$$\begin{aligned} \frac{P}{P_c} &= f\left(\frac{a}{a_c}\right) = \left(\frac{a}{a_c}\right)^3 - 2\left(\frac{a}{a_c}\right)^{3/2} \\ \frac{R\delta}{a_c^2} &= f\left(\frac{a}{a_c}\right) = \left(\frac{a}{a_c}\right)^2 - \frac{4}{3}\left(\frac{a}{a_c}\right)^{1/2} \end{aligned} \tag{E.17}$$

We note that in both equations in Eq. (E.17), the first term of the RHS corresponds to Hertz law without adhesion. When the two bodies are loaded by a compressive force, the adhesive forces pull the surfaces into contact over an area that exceeds the one given by Hertz theory (see Fig. E.3 [a]); zero load leaves the surfaces adhering together with a finite area and a positive compression δ; a tensile (negative) load causes the contact area to shrink further; beyond the (▲) point ($P = -P_c$, and $a = a_c$), the situation becomes unstable and they separate. The latter is true only when the load is imposed; if we impose the separation distance, this part of the curve is stable and the point (●) can be reached without separation, meaning that the (negative) compression δ can be further decreased (Fig. E.3 [center]).

Before proceeding, it should be noted that Johnson et al. (1971) also propose in their paper an approximated theory in which Hertz relation between the contact area and the compression holds $a^2 = R\delta$, and surface energy is added to Hertz elastic energy:

$$U_T^{approx} = \frac{8}{15}E^*\left(R\delta^5\right)^{1/2} - 2\gamma\pi R\delta \tag{E.18}$$

In this case, the normal load becomes:

$$P^{approx} = \frac{dU_S}{d\delta} = \frac{dU_E}{d\delta} - 2\gamma\pi R = \frac{4}{3}E^*\left(R\delta^3\right)^{1/2} - 2\gamma\pi R = F^{el} - F^{adh} \tag{E.19}$$

with $F^{adh} = 2P_c/3$, leading to:

$$\begin{aligned} \left(\frac{P}{P_c}\right)^{approx} &= \left(\frac{a}{a_c}\right)^3 - \frac{2}{3} \\ \left(\frac{R\delta}{a_c^2}\right)^{approx} &= \left(\frac{a}{a_c}\right)^2 \end{aligned} \tag{E.20}$$

We note that the relation between the load P and the compression δ in Eq. (E.19) is formally identical to the modeling that is used in the present work (Eq. (5.1)). This approximate approach is compared to the complete JKR theory in Fig. E.3, where the corresponding relations in the frame of non-adhesive Hertz contact are displayed as well for the sake of completeness.

In Fig. E.3 [a] and [b] the reduced contact area radius is represented as a function of both the reduced load and the reduced compression, while in Fig. E.3 [c] the reduced normal load is represented as a function of the reduced compression. In the JKR theory, the contact area decreases with the compression δ until separation (point (●), $\delta_{min} < 0$), but after reaching a_c (▲) the load slightly increases again. As we can see, for both the JKR model and the approximated theory a tensile (i.e., adhesive) force can exist even without separation of the surfaces for positive compression (contact inception, point ▼ at $\delta = 0$). Moreover, at zero load there exists a positive compression (point ■), at which the associated elastic force counterbalances the attractive one. Additionally, the area of contact is an increasing function of the load for $P > -P_c$. However, the approximate theory does not allow contact for $\delta < 0$, and the area of contact is zero at maximum traction ($\delta = 0$), which is not true for the JKR model. Indeed, in the frame of the JKR model, contact is maintained for negative displacement. We suppose that the slight difference in the force at small positive values of δ does not have a qualitative effect on suspensions; anyway, this difference quickly vanishes for higher values of δ. The latter discrepancy ($a = 0$ for $P = -F_{adh}$) is important for frictional contact as explained in the following.

In Fig. E.4 the maximum value of the tangential force against the normal load is shown. The most natural way of including friction in the JKR model would be to assume that the largest friction force that the contact can bear before sliding is proportional to the contact area. Considering the curve for $P \geqslant -P_c$ and $a \geqslant a_c$ (otherwise the situation may be unstable): $\max(F_t)$ is never zero, as $a_c \neq 0$, meaning that friction is maintained as the particles detach (which is not the same for our model, in which we can have zero tangential force); the dependence of the normal force on the tangential one in such a frictional JKR model is not linear, as displayed in Fig. E.4.

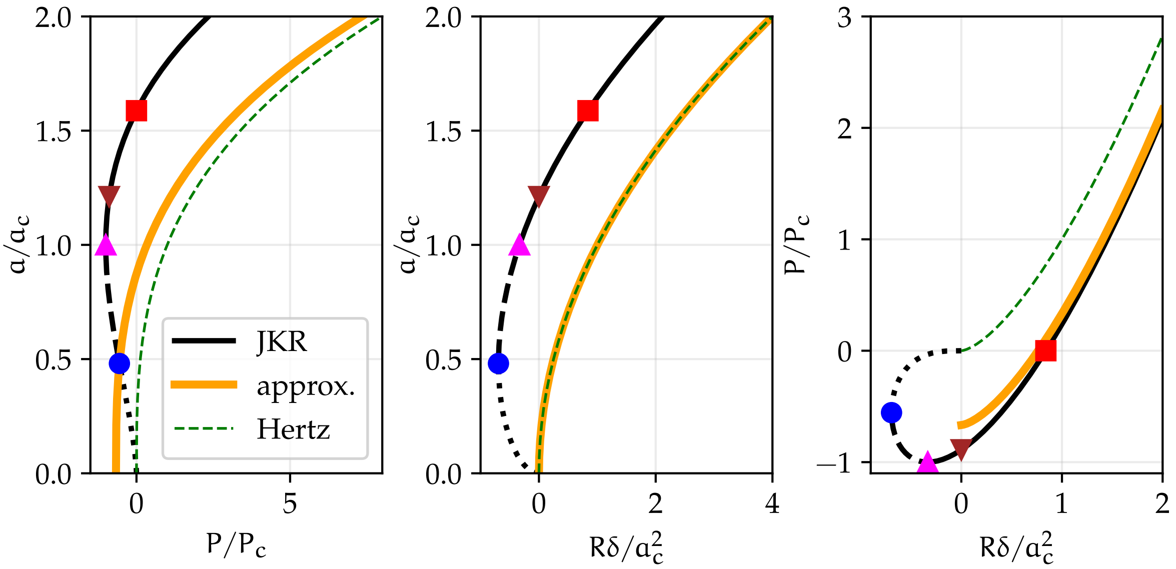

Figure E.3
(a) normalized contact area radius a/a_c over the normalized load P/P_c, (b) normalized contact area radius a/a_c over the normalized compression $\delta/\left(a_c^2/R\right)$, and (c) normalized load P/P_c over the normalized compression $\delta/\left(a_c^2/R\right)$. (■) point at which the load is zero; (▼) point at which the compression (and thus the separation distance) is zero; (▲) point at which $a = a_c$ and $P = -P_c$, point after which the situation becomes unstable and surfaces separate when the load is imposed (stable when compression is imposed); (●) point of minimum compression at which the situation becomes unstable and the surfaces separate.

If the same relation $F_t \propto a^2$ is assumed in the simplified approach, the relation between F_t and P is not linear either, and in that case, it vanishes for the largest traction. The influence of the precise relation between friction force and load surely deserves a specific study. We note that in the field of non-adhesive particle suspensions, this issue has been tackled. In more detail, in most of the computational work, a constant friction coefficient has been used ($F_t \propto P$), yielding rate-independent rheology. However, if a mono-contact is assumed, the friction coefficient decreases with load, and shear-thinning behavior is observed (Lobry et al., 2019). This question is out of the scope of the present study since we do not want to precisely conclude on the nature of adhesive contact in a specific suspension, but rather to evaluate the influence of coupled friction and adhesion in the frame of a simple contact model. As a consequence, we choose a simple constant friction coefficient, using the following relation between F_t and P:

$$F_t = \mu \left(P + \frac{2}{3} P_c \right) \tag{E.21}$$

Such a relation is qualitatively displayed in Fig. E.4.

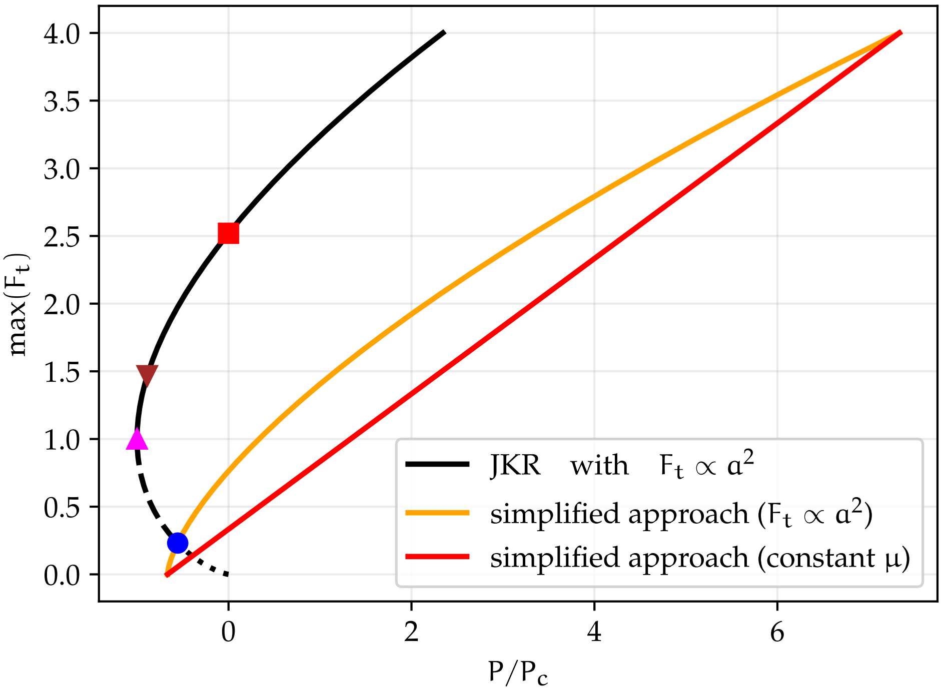

Figure E.4
Qualitative maximum value of the frictional force as a function of the normalized normal load: comparison between a frictional JKR model, a simplified approach with a variable friction coefficient, and a simplified approach with constant friction coefficient (employed in the current work). The evidenced points are the same as in Fig. E.3. We recall that below point (▲), the situation is unstable.

F

THE SUSPENSION BALANCE MODEL FOR A PLANAR POISEUILLE FLOW

We recall here the modified version of the Suspension Balance Model (SBM) as proposed by (Badia et al., 2022), and we derive the governing equations in the case of a planar pressure-driven flow. This is useful for comparing the results in Chapter 6.

F.1 THE SBM IN A PLANAR POISEUILLE FLOW

The governing equations are:

$$\begin{aligned} &\boldsymbol{\nabla} \cdot \mathbf{u} = 0 \\ &\boldsymbol{\nabla} \cdot \boldsymbol{\Sigma} - \boldsymbol{\nabla} P_0 = 0 \\ &\frac{\partial \phi}{\partial t} + \boldsymbol{\nabla} \cdot (\phi \mathbf{u}) + \boldsymbol{\nabla} \cdot \left(\frac{2\bar{a}^2}{9\eta} f(\phi) \boldsymbol{\nabla} \cdot \boldsymbol{\Sigma}^c \right) = 0 \end{aligned} \tag{F.1}$$

where $\mathbf{u}$ denotes the suspension velocity field, $\boldsymbol{\Sigma}$ the bulk suspension stress tensor, $\boldsymbol{\Sigma}^c$ the contact contribution to the stress, $f(\phi) = (1-\phi)^{5.1}$ (Badia et al., 2022) is the hindered settling function, and $\bar{a}$ is the relevant particle size, which can be chosen as $\bar{a} = (a_1 + a_2)/2$. The last equation governs particle transport, while the first two equations govern the flow of the suspension as a continuous medium. In general flow geometry, the expression of the stresses is a quite involved task (Miller et al., 2009; Badia et al., 2022). In the present case, the velocity and volume fraction fields are assumed to only depend on the y-coordinate:

$$\mathbf{u} = u(y,t)\, \mathbf{e}_x \, , \qquad \phi = \phi(y,t) \tag{F.2}$$

In such a plane shear flow, the stresses are given simple expressions (Badia et al., 2022):

$$\operatorname{dev}(\boldsymbol{\Sigma}) = 2\eta\eta^s(\phi)\, \mathbf{E} + \eta\eta^s(\phi)\, \dot{\gamma} \begin{pmatrix} \frac{1}{3}(2\hat{N}_1 + \hat{N}_2) & 0 & 0 \\ 0 & \frac{1}{3}(-\hat{N}_1 + \hat{N}_2) & 0 \\ 0 & 0 & \frac{1}{3}(-\hat{N}_1 - 2\hat{N}_2) \end{pmatrix} \tag{F.3}$$

$$\boldsymbol{\Sigma}^c = 2\eta_c \eta \mathbf{E} + \eta\eta^s(\phi)\, \dot{\gamma} \begin{pmatrix} \hat{\Sigma}^c_{11} & 0 & 0 \\ 0 & \hat{\Sigma}^c_{22} & 0 \\ 0 & 0 & \hat{\Sigma}^c_{33} \end{pmatrix} \tag{F.4}$$

where the normalized quantities η^c, $\hat{N}_i$, $\hat{\Sigma}^c_{ii}$ only depend on the reduced volume fraction ϕ/ϕ_J, and the shear rate tensor and shear rate read:

$$\mathbf{E} = \frac{\partial u}{\partial y} \begin{pmatrix} 0 & \frac{1}{2} & 0 \\ \frac{1}{2} & 0 & 0 \\ 0 & 0 & 0 \end{pmatrix} \, , \qquad \dot{\gamma} = \left| \frac{\partial u}{\partial y} \right| \tag{F.5}$$

Eq. (F.1) may be simplified using Eqs. (F.3) and (F.4) in a standard way (Snook et al., 2016; Badia et al., 2022) to obtain the equations that govern the volume fraction and velocity profiles in the channel:

$$\Sigma_{xy} = \eta\eta^s(\phi) \frac{\partial u}{\partial y} = \frac{dP_0}{dx} y \tag{F.6a}$$

$$\frac{\partial \phi}{\partial t} + \frac{2\bar{a}^2}{9\eta} \frac{\partial}{\partial y} \left(f(\phi) \frac{\partial}{\partial y} \left(\left| \frac{dP_0}{dx} \right| |y|\, \hat{\Sigma}^c_{22} \right) \right) = 0 \tag{F.6b}$$

Eq. (F.6a) states as usual that the shear stress is controlled by the pressure gradient, while Eq. (F.6b) is a kind of diffusion equation, with boundary conditions on the walls such that the particle flux vanishes:

$$J_{y=\pm L_y/2} = f(\phi)\frac{\partial}{\partial y}\left(\left|\frac{dP_0}{dx}\right||y|\,\hat{\Sigma}^c_{22}\right) = 0 \tag{F.7}$$

Eqs. (F.6a) and (F.6b) may be made dimensionless using the shear rate $\dot{\gamma}_0 = \frac{L_y}{4\eta}\left|\frac{dP_0}{dx}\right|$ and the length L_y. Switching to dimensionless unknown functions, we obtain:

$$\frac{\partial u^*}{\partial y^*} = -\frac{4}{\eta^s\left(\phi_r\left(y^*\right)\right)}y^* \tag{F.8a}$$

$$\frac{\partial \phi}{\partial t^*} + \frac{8}{9}\left(\frac{\bar{a}}{L_y}\right)^2\frac{\partial}{\partial y^*}\left(f(\phi)\frac{\partial}{\partial y^*}\left(|y^*|\,\hat{\Sigma}^c_{22}\right)\right) = 0 \tag{F.8b}$$

The transient variations are not tackled in the present work. However, the typical dimensionless transient duration may be estimated from Eq. (F.8a):

$$\tau_m \sim \frac{9}{8}\left(\frac{L_y}{\bar{a}}\right)^2 \approx 300 \tag{F.9}$$

which is in roughly qualitative agreement with the transient time mentioned in the article ($t^* \approx 1500$). In steady state, the reduced volume $\phi_r = \phi/\phi_J$ profile obeys the following ordinary differential equation:

$$\frac{d\phi_r}{dy^*} = -\frac{\hat{\Sigma}^c_{22}}{y^*\dfrac{d\hat{\Sigma}^c_{22}}{d\phi_r}} \tag{F.10}$$

with the constraint that the total particle volume is kept constant, i.e.:

$$\int_{-1/2}^{+1/2}\phi_r\,dy^* = \frac{\phi}{\phi_J} \tag{F.11}$$

Once Eqs. (F.10) and (F.11) are solved, the velocity profile is simply determined by integration of Eq. (F.8a). It should be noted that the SBM as presented here suffers important drawbacks (see Snook et al. (2016) for a discussion). In particular, the steady-state volume fraction is allowed to exceed the jamming volume fraction ϕ_J, which is easily understood by inspection of Eq. (6.10b): the multiplying factor of $1/y^*$ in the RHS is negative so that ϕ increases as $|y^*|$ decreases; in addition, this factor does not vanish as $\phi/\phi_J \to 1$ so that the volume fraction gradient diverges as $|y^*| \to 0$, and ϕ exceeds ϕ_J. To avoid this divergence, it has been proposed to slightly modify the expression of the particle flux with a non-local stress. This non-local stress may be induced by a suspension "temperature" (Nott & Brady, 1994), a force network (Mills & Snabre, 1995), or the finite size of the particles (Miller & Morris, 2006). These approaches deserve to be examined against the present data. However, as a first approximation, we follow here a simple empirical idea: we postulate that the particle flux vanishes as soon as ϕ reaches ϕ_J. As a consequence, a jammed zone where $\phi = \phi_J$ develops in the vicinity of the channel center plane.

G

ESTIMATING MEASUREMENT ERRORS

Numerical results may be subject to systematic errors, and it is essential to obtain an estimate of their statistical significance. Following Allen & Tildesley (2017), we assume that the quantities of interest are Gaussian processes, which is a reasonable assumption if the quantity is essentially the sum of a large number of "random" quantities (statistically independent or not). Our problem, then, is to estimate the mean and the variance on a long (but finite) simulation run.

G.1 ESTIMATING SYSTEMATIC ERRORS

The data points are usually not independent, as we normally store configurations sufficiently frequently and, therefore, they are correlated with each other. The main idea is to break the signal into several blocks, and then compute the error in the simulation run average of these blocks. As an example, let us consider the quantity $\mathcal{A}$. Its signal has τ_{run} time-steps and its average is simply:

$$\langle \mathcal{A} \rangle_{run} = \frac{\sum_{\tau=1}^{\tau_{run}} \mathcal{A}(t)}{\tau_{run}} \tag{G.1}$$

The first thing to do is to estimate the number of steps for which the correlations persist. Let us break the signal into n_b blocks of size τ_b, whose average is:

$$\langle \mathcal{A} \rangle_{b} = \frac{\sum_{\tau=1}^{\tau_{b}} \mathcal{A}(t)}{\tau_{b}} \tag{G.2}$$

the mean values for all the blocks may then be used to estimate the variance:

$$\sigma^2 (\langle \mathcal{A} \rangle_b) = \frac{1}{n_b} \sum_{b=1}^{n_b} (\langle \mathcal{A} \rangle_b - \langle \mathcal{A} \rangle_{run})^2 \tag{G.3}$$

We expect this quantity to be inversely proportional to τ_b at large τ_b, as the blocks become large enough to be statistically uncorrelated, which allows us to estimate the variance for the entire run.

To estimate τ_b, we can define the statistical efficiency as the limiting ratio of the observed variance of an average to the limit expected on the assumption of uncorrelated Gaussian statistics:

$$s = \lim_{\tau_b \to \infty} \frac{\tau_b \sigma^2 (\langle \mathcal{A} \rangle_b)}{\sigma^2 (\mathcal{A})} \tag{G.4}$$

where:

$$\sigma^2 (\langle \mathcal{A} \rangle_b) = \frac{\sum_{b=1}^{n_b} (\langle \mathcal{A} \rangle_b - \langle \mathcal{A} \rangle_{run})^2}{n_b} \tag{G.5}$$

The above quantity increases with τ_b until it reaches a plateau, which gives the number of configurations to wait for them to be uncorrelated.

The error bars showed in the current work are obtained by computing the statistical efficiency on the signal of the considered quantity and by using Eq. (G.3).

BIBLIOGRAPHY

Abbas M., Climent E., & Simonin O. (2007). *Fully Coupled Simulations of Non-Colloidal Monodisperse Sheared Suspensions*. Chemical Engineering Research and Design, *85*(6), 778–791. https://doi.org/10.1205/cherd06114 (cit. on p. 14)

Abbas M., Magaud P., Gao Y., & Geoffroy S. (2014). *Migration of finite sized particles in a laminar square channel flow from low to high Reynolds numbers*. Physics of Fluids, *26*(12), 123301. https://doi.org/10.1063/1.4902952 (cit. on pp. 17, 20)

Acrivos A. (1993). *Shear-induced resuspension in a Couette device*. https://doi.org/10.1016/0301-9322(93)90043-T (cit. on pp. 16, 133)

Agbangla G. C., Climent É., & Bacchin P. (2014). *Numerical investigation of channel blockage by flowing microparticles*. Computers & Fluids, *94*, 69–83. https://doi.org/10.1016/j.compfluid.2014.01.018 (cit. on p. 107)

Allen M. P., & Tildesley D. J. (2017). *Computer simulation of liquids* (Second edition). Oxford University Press. https://doi.org/10.1093/oso/9780198803195.001.0001. (Cit. on p. 191)

Andreotti B., Forterre Y., & Pouliquen O. (2013). *Granular Media: Between Fluid and Solid* (First). Cambridge University Press. https://doi.org/10.1017/CBO9781139541008. (Cit. on p. 148)

Arshad M., Maali A., Claudet C., Lobry L., Peters F., & Lemaire E. (2021). *An experimental study on the role of inter-particle friction in the shear-thinning behavior of non-Brownian suspensions*. Soft Matter, *17*(25), 6088–6097. https://doi.org/10.1039/D1SM00254F (cit. on p. 15)

Aussillous P., Chauchat J., Pailha M., Médale M., & Guazzelli É. (2013). *Investigation of the mobile granular layer in bedload transport by laminar shearing flows*. Journal of Fluid Mechanics, *736*, 594–615. https://doi.org/10.1017/jfm.2013.546 (cit. on p. 133)

Badia A. (2021). *Modélisation numérique de suspensions non-browniennes concentrées en écoulement rhéométrique ou général* (Doctoral dissertation). Université Côte d'Azur. https://www.theses.fr/2021COAZ4093. (Cit. on p. 142)

Badia A., D'Angelo Y., Peters F., & Lobry L. (2022). *Frame-invariant modeling for non-Brownian suspension flows*. Journal of Non-Newtonian Fluid Mechanics, *309*, 104904. https://doi.org/10.1016/j.jnnfm.2022.104904 (cit. on pp. 3, 7, 94, 95, 131, 134, 141, 142, 187, 188)

Ball R., & Melrose J. (1997). *A simulation technique for many spheres in quasi-static motion under frame-invariant pair drag and Brownian forces*. Physica A: Statistical Mechanics and its Applications, *247*(1-4), 444–472. https://doi.org/10.1016/S0378-4371(97)00412-3 (cit. on pp. 67, 68)

Barnes H. A. (1999). *The yield stress — a review or 'panta rei' — everything flows?* 46. https://doi.org/10.1016/S0377-0257(98)00094-9 (cit. on pp. 106, 107)

Batchelor G. K. (1970). *The stress system in a suspension of force-free particles*. Journal of Fluid Mechanics, *41*(3), 545–570. https://doi.org/10.1017/S0022112070000745 (cit. on pp. 52, 55, 145)

Bhattacharya S., Bławzdziewicz J., & Wajnryb E. (2006). *Hydrodynamic interactions of spherical particles in Poiseuille flow between two parallel walls*. Physics of Fluids, *18*(5), 053301. https://doi.org/10.1063/1.2195992 (cit. on pp. 85–87)

Bian X., Litvinov S., Qian R., Ellero M., & Adams N. A. (2012). *Multiscale modeling of particle in suspension with smoothed dissipative particle dynamics*. Physics of Fluids, *24*(1), 012002. https://doi.org/10.1063/1.3676244 (cit. on p. 19)

Blanc F., Lemaire E., Meunier A., & Peters F. (2013). *Microstructure in sheared non-Brownian concentrated suspensions*. Journal of Rheology, *57*(1), 273–292. https://doi.org/10.1122/1.4766597 (cit. on pp. 13, 93)

Blanc F., Peters F., & Lemaire E. (2011a). *Experimental Signature of the Pair Trajectories of Rough Spheres in the Shear-Induced Microstructure in Noncolloidal Suspensions*. Physical Review Letters, *107*(20), 208302. https://doi.org/10.1103/PhysRevLett.107.208302 (cit. on pp. 13, 49)

Blanc F., Peters F., & Lemaire E. (2011b). *Local transient rheological behavior of concentrated suspensions*. Journal of Rheology, *55*(4), 835–854. https://doi.org/10.1122/1.3582848 (cit. on p. 110)

Blazek J. (2001). *Computational fluid dynamics: principles and applications* (1st ed). Elsevier. https://doi.org/10.1016/B978-0-08-044506-9.X5000-0. (Cit. on p. 28)

Boromand A., Jamali S., & Maia J. M. (2017). *Structural fingerprints of yielding mechanisms in attractive colloidal gels*. Soft Matter, *13*(2), 458–473. https://doi.org/10.1039/C6SM00750C (cit. on p. 106)

Bossis G., & Brady J. F. (1984). *Dynamic simulation of sheared suspensions. I. General method*. The Journal of Chemical Physics, *80*(10), 5141–5154. https://doi.org/10.1063/1.446585 (cit. on p. 18)

Boyer F., Guazzelli É., & Pouliquen O. (2011). *Unifying Suspension and Granular Rheology*. Physical Review Letters, *107*(18), 188301. https://doi.org/10.1103/PhysRevLett.107.188301 (cit. on pp. 12, 133)

Brady J. F. (1988). *Stokesian Dynamics*. Annual Review of Fluid Mechanics, *20*(111-57), 47. https://doi.org/10.1146/annurev.fl.20.010188.000551 (cit. on pp. 18, 67)

Brady J. F. (2001). *Computer simulation of viscous suspensions*. Chemical Engineering Science, *56*(9), 2921–2926. https://doi.org/10.1016/S0009-2509(00)00475-9 (cit. on p. 18)

Breugem W.-P. (2012). *A second-order accurate immersed boundary method for fully resolved simulations of particle-laden flows*. Journal of Computational Physics, *231*(13), 4469–4498. https://doi.org/10.1016/j.jcp.2012.02.026 (cit. on p. 20)

Catalano E., Chareyre B., & Barthélémy E. (2014). *Pore-scale modeling of fluid-particles interaction and emerging poromechanical effects: pore-scaling modeling of fluid-particles interactions*. International Journal for Numerical and Analytical Methods in Geomechanics, *38*(1), 51–71. https://doi.org/10.1002/nag.2198 (cit. on p. 21)

Chaoui M., & Feuillebois F. (2003). *Creeping flow around a sphere in a shear flow close to a wall*. The Quarterly Journal of Mechanics and Applied Mathematics, *56*, 381–410. https://doi.org/10.1093/qjmam/2F56.3.381 (cit. on pp. 61, 70, 71, 77, 78, 163, 165, 166)

Cheal O., & Ness C. (2018). *Rheology of dense granular suspensions under extensional flow*. Journal of Rheology, *62*(2), 501–512. https://doi.org/10.1122/1.5004007 (cit. on p. 21)

Chèvremont W., Chareyre B., & Bodiguel H. (2019). *Quantitative study of the rheology of frictional suspensions: Influence of friction coefficient in a large range of viscous numbers*. Physical Review Fluids, *4*(6), 064302. https://doi.org/10.1103/PhysRevFluids.4.064302 (cit. on p. 51)

Chun B., Kwon I., Jung H. W., & Hyun J. C. (2017). *Lattice Boltzmann simulation of shear-induced particle migration in plane Couette-Poiseuille flow: Local ordering of suspension*. Physics of Fluids, *29*(12), 121605. https://doi.org/10.1063/1.4991428 (cit. on p. 132)

Chun B., Park J. S., Jung H. W., & Won Y.-Y. (2019). *Shear-induced particle migration and segregation in non-Brownian bidisperse suspensions under planar Poiseuille flow*. Journal of Rheology, *63*(3), 437–453. https://doi.org/10.1122/1.5065406 (cit. on pp. 132, 134, 144)

Cichocki B., Ekiel-Jeżewska M. L., & Wajnryb E. (1999). *Lubrication corrections for three-particle contribution to short-time self-diffusion coefficients in colloidal dispersions*. The Journal of Chemical Physics, *111*(7), 3265–3273. https://doi.org/10.1063/1.479605 (cit. on pp. 67, 68)

Claeys I. L., & Brady J. F. (1993). *Suspensions of prolate spheroids in Stokes flow. Part 1. Dynamics of a finite number of particles in an unbounded fluid*. Journal of Fluid Mechanics, *251*, 411–442. https://doi.org/10.1017/S0022112093003465 (cit. on p. 19)

Da Cunha F. R., & Hinch E. J. (1996). *Shear-induced dispersion in a dilute suspension of rough spheres*. Journal of Fluid Mechanics, *309*, 211–223. https://doi.org/10.1017/S0022112096001619 (cit. on pp. 83, 84)

d'Ambrosio E., Blanc F., & Lemaire E. (2021). *Viscous resuspension of non-Brownian particles: determination of the concentration profiles and particle normal stresses*. Journal of Fluid Mechanics, *911*, A22. https://doi.org/10.1017/jfm.2020.1074 (cit. on pp. 16, 93, 133)

Dbouk T., Lobry L., & Lemaire E. (2013). *Normal stresses in concentrated non-Brownian suspensions*. Journal of Fluid Mechanics, *715*, 239–272. https://doi.org/10.1017/jfm.2012.516 (cit. on pp. 14, 133)

Deboeuf A., Gauthier G., Martin J., Yurkovetsky Y., & Morris J. F. (2009). *Particle Pressure in a Sheared Suspension: A Bridge from Osmosis to Granular Dilatancy*. Physical Review Letters, *102*(10), 108301. https://doi.org/10.1103/PhysRevLett.102.108301 (cit. on p. 133)

Denn M. M., & Morris J. F. (2014). *Rheology of Non-Brownian Suspensions*. Annual Review of Chemical and Biomolecular Engineering, *5*(1), 203–228. https://doi.org/10.1146/annurev-chembioeng-060713-040221 (cit. on p. 9)

Di Vaira N. J., Łaniewski-Wołłk Ł., Johnson R. L., Aminossadati S. M., & Leonardi C. R. (2022). *Influence of particle polydispersity on bulk migration and size segregation in channel flows*. Journal of Fluid Mechanics, *939*, A30. https://doi.org/10.1017/jfm.2022.166 (cit. on pp. 132, 144)

Doi M., & Chen D. (1989). *Simulation of aggregating colloids in shear flow*. The Journal of Chemical Physics, *90*(10), 5271–5279. https://doi.org/10.1063/1.456430 (cit. on pp. 106, 107)

Drazer G., Koplik J., Khusid B., & Acrivos A. (2004). *Microstructure and velocity fluctuations in sheared suspensions*. Journal of Fluid Mechanics, *511*, 237–263. https://doi.org/10.1017/S0022112004009577 (cit. on p. 13)

Durlofsky L., Brady J. F., & Bossis G. (1987). *Dynamic simulation of hydrodynamically interacting particles*. Journal of Fluid Mechanics, *180*(-1), 21. https://doi.org/10.1017/S002211208700171X (cit. on p. 18)

Edens L. E., Alvarado E. G., Singh A., Morris J. F., Schenter G. K., Chun J., & Clark A. E. (2021). *Shear stress dependence of force networks in 3D dense suspensions*. Soft Matter, *17*(32), 7476–7486. https://doi.org/10.1039/D1SM00184A (cit. on p. 106)

Einstein A. (1909). *Eine neue Bestimmung der Moleküldimensionen*. Annalen der Physik, *19*, 289–306. https://einsteinpapers.press.princeton.edu/vol2-doc/219 (cit. on pp. 1, 5, 11)

Einstein A. (1911). *Berichtigung zu meiner Arbeit: "Eine neue Bestimmung der Moleküldimensionen"*. Annalen der Physik, *34*, 591–592. https://www.academia.edu/8638726/Berichtigung_zu_meiner_Arbeit_Eine_neue_Bestimmung_der_Molek%C3%BCldimensionen (cit. on pp. 1, 5, 11)

Ferziger J. H., & Perić M. (2002). *Computational Methods for Fluid Dynamics*. Springer Berlin Heidelberg. https://doi.org/10.1007/978-3-642-56026-2. (Cit. on p. 28)

Gadala-Maria F., & Acrivos A. (1980). *Shear-Induced Structure in a Concentrated Suspension of Solid Spheres*. Journal of Rheology, *24*(6), 799–814. https://doi.org/10.1122/1.549584 (cit. on pp. 12, 16, 17)

Gallier S. (2014). *Simulation numérique de suspensions frictionnelles: application aux supergols solides* (Doctoral dissertation). Université de Nice-Sophia Antipolis. https://tel.archives-ouvertes.fr/tel-01127088. (Cit. on pp. 14, 20, 21, 49, 90, 91, 93, 166)

Gallier S., Lemaire E., Lobry L., & Peters F. (2014a). *A fictitious domain approach for the simulation of dense suspensions*. Journal of Computational Physics, *256*, 367–387. https://doi.org/10.1016/j.jcp.2013.09.015 (cit. on pp. 13, 19, 21, 27, 36, 42, 45, 165)

Gallier S., Lemaire E., Lobry L., & Peters F. (2016). *Effect of confinement in wall-bounded non-colloidal suspensions*. Journal of Fluid Mechanics, *799*, 100–127. https://doi.org/10.1017/jfm.2016.368 (cit. on pp. 21, 42, 93)

Gallier S., Lemaire E., Peters F., & Lobry L. (2014b). *Rheology of sheared suspensions of rough frictional particles*. Journal of Fluid Mechanics, *757*, 514–549. https://doi.org/10.1017/jfm.2014.507 (cit. on pp. 14, 15, 21, 50, 84)

Gallier S., Peters F., & Lobry L. (2018). *Simulations of sheared dense noncolloidal suspensions: Evaluation of the role of long-range hydrodynamics*. Physical Review Fluids, *3*(4), 042301. https://doi.org/10.1103/PhysRevFluids.3.042301 (cit. on pp. 21, 93–95, 122–125, 128, 129)

Gao C., Kulkarni S. D., Morris J. F., & Gilchrist J. F. (2010). *Direct investigation of anisotropic suspension structure in pressure-driven flow*. Physical Review E, *81*(4), 041403. https://doi.org/10.1103/PhysRevE.81.041403 (cit. on p. 132)

Gao C., Xu B., & Gilchrist J. F. (2009). *Mixing and segregation of microspheres in microchannel flows of mono- and bidispersed suspensions*. Physical Review E, *79*(3), 036311. https://doi.org/10.1103/PhysRevE.79.036311 (cit. on p. 132)

Ghalya N., Sellier A., Ekiel-Jeżewska M. L., & Feuillebois F. (2020). *Effective viscosity of a dilute homogeneous suspension of spheres in Poiseuille flow between parallel slip walls*. Journal of Fluid Mechanics, *899*, A13. https://doi.org/10.1017/jfm.2020.429 (cit. on pp. 81, 82)

Gilbert D., Valette R., & Lemaire E. (2022). *Impact of particle stiffness on shear-thinning of non-Brownian suspensions*. Journal of Rheology, *66*(1), 161–176. https://doi.org/10.1122/8.0000338 (cit. on p. 121)

Gillissen J. J. J., & Ness C. (2020). *Modeling the Microstructure and Stress in Dense Suspensions under Inhomogeneous Flow*. Physical Review Letters, *125*(18), 184503. https://doi.org/10.1103/PhysRevLett.125.184503 (cit. on pp. 133, 143)

Glowinski R. (1999). *A distributed Lagrange multiplier/fictitious domain method for particulate flows*. International Journal of Multiphase Flow, *184*(2-4), 241–267. https://doi.org/http://dx.doi.org/10.1016/S0045-7825(99)00230-3 (cit. on p. 19)

Glowinski R., Pan T. W., Hesla T., Joseph D., & Périaux J. (2001). *A Fictitious Domain Approach to the Direct Numerical Simulation of Incompressible Viscous Flow past Moving Rigid Bodies: Application to Particulate Flow*. Journal of Computational Physics, *169*(2), 363–426. https://doi.org/10.1006/jcph.2000.6542 (cit. on p. 19)

Guasto J. S., Ross A. S., & Gollub J. P. (2010). *Hydrodynamic irreversibility in particle suspensions with nonuniform strain*. Physical Review E, *81*(6), 061401. https://doi.org/10.1103/PhysRevE.81.061401 (cit. on p. 151)

Guazzelli E., Morris J. F., & Pic S. (2011). *A Physical Introduction to Suspension Dynamics*. Cambridge University Press. https://doi.org/10.1017/CBO9780511894671. (Cit. on p. 21)

Guazzelli É., & Pouliquen O. (2018). *Rheology of dense granular suspensions*. Journal of Fluid Mechanics, *852*. https://doi.org/10.1017/jfm.2018.548 (cit. on pp. 9, 12, 15)

Guy B. M., Hermes M., & Poon W. C. K. (2015). *Towards a Unified Description of the Rheology of Hard-Particle Suspensions*. Physical Review Letters, *115*(8), 088304. https://doi.org/10.1103/PhysRevLett.115.088304 (cit. on p. 126)

Guy B. M., Richards J. A., Hodgson D. J. M., Blanco E., & Poon W. C. K. (2018). *Constraint-Based Approach to Granular Dispersion Rheology*. Physical Review Letters, *121*(12), 128001. https://doi.org/10.1103/PhysRevLett.121.128001 (cit. on p. 107)

Hampton R. E., Mammoli A. A., & Graham A. L. (1997). *Migration of particles undergoing pressure-driven flow in a circular conduit*. Journal of Rheology, *41*(3), 21. https://doi.org/10.1122/1.550863 (cit. on p. 132)

Hasimoto H. (1959). *On the periodic fundamental solutions of the Stokes equations and their application to viscous flow past a cubic array of spheres*. Journal of Fluid Mechanics, *5*(02), 317. https://doi.org/10.1017/S0022112059000222 (cit. on pp. 74–76)

Hertz H. (1882). *On the contact of rigid elastic solids and on hardness*. Macmillan and Co., New York. https://doi.org/10.1515/crll.1882.92.156 (cit. on pp. 108, 179)

Hughes T. J., Liu W. K., & Zimmermann T. K. (1981). *Lagrangian-Eulerian finite element formulation for incompressible viscous flows*. Computer Methods in Applied Mechanics and Engineering, *29*(3), 329–349. https://doi.org/10.1016/0045-7825(81)90049-9 (cit. on p. 18)

Jana S. C., Kapoor B., & Acrivos A. (1995). *Apparent wall slip velocity coefficients in concentrated suspensions of noncolloidal particles*. Journal of Rheology, *39*(6), 1123–1132. https://doi.org/10.1122/1.550631 (cit. on p. 140)

Jasak H. (1996). *Error Analysis and Estimation for the Finite Volume Method with Applications to Fluid Flows* (Doctoral dissertation). http://hdl.handle.net/10044/1/8335. (Cit. on p. 30)

Jeffrey D. J. (1989). *Stresslet resistance functions for low Reynolds number flow using deforming spheres*. Journal of Applied Mathematics and Physics, *40*(2), 163–171. https://doi.org/10.1007/BF00944996 (cit. on p. 161)

Jeffrey D. J. (1992). *The calculation of the low Reynolds number resistance functions for two unequal spheres*. Physics of Fluids A: Fluid Dynamics, *4*(1), 16–29. https://doi.org/10.1063/1.858494 (cit. on pp. 59, 164–166)

Jeffrey D. J. (2021). *Programs for Stokes resistance functions*. https://www.uwo.ca/apmaths/faculty/jeffrey/research/Resistance.html. (Cit. on p. 164)

Jeffrey D. J., Morris J. F., & Brady J. F. (1993). *The pressure moments for two rigid spheres in low-Reynolds-number flow*. Physics of Fluids A: Fluid Dynamics, *5*(10), 2317–2325. https://doi.org/10.1063/1.858795 (cit. on pp. 52, 59, 161, 164)

Jeffrey D. J., & Onishi Y. (1984). *Calculation of the resistance and mobility functions for two unequal rigid spheres in low-Reynolds-number flow*. Journal of Fluid Mechanics, *139*, 261–290. https://doi.org/10.1017/S0022112084000355 (cit. on pp. 59, 161, 164)

Johnson K. L. (1985). *Contact mechanics*. https://doi.org/10.1017/CBO9781139171731. (Cit. on pp. 108, 180)

Johnson K. L., Kendall K., & Roberts A. D. (1971). *Surface energy and the contact of elastic solids*, 13. https://doi.org/10.1098/rspa.1971.0141 (cit. on pp. 109, 179, 180, 183)

Jones M. A., & Ness C. (2018). *Linking attractive interactions and confinement to the rheological response of suspended particles close to jamming*. Granular Matter, *20*(1), 3. https://doi.org/10.1007/s10035-017-0770-1 (cit. on p. 21)

Karnis A., Goldsmith H. L., & Mason S. G. (1966). *The Kinectics of Flowing Dispersions, I: Concentrated Suspensions of Rigid Particles*. Journal of Colloid and Interface Science, *22*, 531–553. https://doi.org/10.1016/0021-9797(66)90048-8 (cit. on p. 132)

Kim S., & Karrila S. J. (1991). *Microhydrodynamics: principles and selected applications*. Butterworth-Heinemann. https://doi.org/10.1016/C2013-0-04644-0. (Cit. on pp. 58, 59, 160)

Koh C. J., Hookham P., & Leal L. G. (1994). *An experimental investigation of concentrated suspension flows in a rectangular channel*. Journal of Fluid Mechanics, *266*, 1–32. https://doi.org/10.1017/S0022112094000911 (cit. on p. 132)

Koumakis N., Moghimi E., Besseling R., Poon W. C. K., Brady J. F., & Petekidis G. (2015). *Tuning colloidal gels by shear*. Soft Matter, *11*(23), 4640–4648. https://doi.org/10.1039/C5SM00411J (cit. on pp. 107, 128)

Ladd A. J. C. (1994). *Numerical simulations of particulate suspensions via a discretized Boltzmann equation. Part 1. Theoretical foundation*. Journal of Fluid Mechanics, *271*, 285–309. https://doi.org/10.1017/S0022112094001771 (cit. on p. 19)

Larson R. G. (1999). *The structure and rheology of complex fluids*. Oxford University Press. https://www.eng.uc.edu/~beaucag/Classes/Properties/Books/The%20structure%20and%20rheology%20of%20complex%20fluids-RG%20Larson.pdf. (Cit. on p. 106)

Lefebvre A., & Maury B. (2005). *Apparent viscosity of a mixture of a Newtonian fluid and interacting particles*. Comptes Rendus Mécanique, *333*(12), 923–933. https://doi.org/10.1016/j.crme.2005.10.007 (cit. on p. 19)

Leighton D. T., & Acrivos A. (1987a). *Measurement of shear-induced self-diffusion in concentrated suspensions of spheres*. Journal of Fluid Mechanics, *177*, 109–131. https://doi.org/10.1017/S0022112087000880 (cit. on p. 17)

Leighton D. T., & Acrivos A. (1987b). *The shear-induced migration of particles in concentrated suspensions*. Journal of Fluid Mechanics, *181*(-1), 415. https://doi.org/10.1017/S0022112087002155 (cit. on pp. 16, 17, 134)

Lhuillier D. (2009). *Migration of rigid particles in non-Brownian viscous suspensions*. Physics of Fluids, *21*(2), 023302. https://doi.org/10.1063/1.3079672 (cit. on pp. 2, 6, 17, 95, 134, 141, 142, 148)

Liu D., Keaveny E., Maxey M. R., & Karniadakis G. (2009). *Force-coupling method for flows with ellipsoidal particles*. Journal of Computational Physics, *228*(10), 3559–3581. https://doi.org/10.1016/j.jcp.2009.01.020 (cit. on p. 20)

Lobry L., Lemaire E., Blanc F., Gallier S., & Peters F. (2019). *Shear thinning in non-Brownian suspensions explained by variable friction between particles*. Journal of Fluid Mechanics, *860*, 682–710. https://doi.org/10.1017/jfm.2018.881 (cit. on pp. 15, 93–95, 185)

Lyon M. K., & Leal L. G. (1998). *An experimental study of the motion of concentrated suspensions in two-dimensional channel flow. Part 1. Monodisperse systems*. Journal of Fluid Mechanics, *363*, 25–56. https://doi.org/10.1017/S0022112098008817 (cit. on pp. 132, 144)

Mari R., Seto R., Morris J. F., & Denn M. M. (2014). *Shear thickening, frictionless and frictional rheologies in non-Brownian suspensions*. Journal of Rheology, *58*(6), 1693–1724. https://doi.org/10.1122/1.4890747 (cit. on pp. 14, 20, 50, 94)

Maxey M. R. (2017). *Simulation Methods for Particulate Flows and Concentrated Suspensions*. Annual Review of Fluid Mechanics, *49*(1), 171–193. https://doi.org/10.1146/annurev-fluid-122414-034408 (cit. on pp. 9, 17)

Maxey M. R., & Patel B. K. (2001). *Localized force representations for particles sedimenting in Stokes flow*. International Journal of Multiphase Flow, *27*(9), 1603–1626. https://doi.org/10.1016/S0301-9322(01)00014-3 (cit. on p. 20)

Mewis J., & Wagner N. J. (2011). *Colloidal Suspension Rheology* (First). Cambridge University Press. https://doi.org/10.1017/CBO9780511977978. (Cit. on pp. 106, 107)

Miller R. M., & Morris J. F. (2006). *Normal stress-driven migration and axial development in pressure-driven flow of concentrated suspensions*. Journal of Non-Newtonian Fluid Mechanics, *135*(2-3), 149–165. https://doi.org/10.1016/j.jnnfm.2005.11.009 (cit. on pp. 17, 143, 151, 189)

Miller R. M., Singh J. P., & Morris J. F. (2009). *Suspension flow modeling for general geometries*. Chemical Engineering Science, *64*(22), 4597–4610. https://doi.org/10.1016/j.ces.2009.04.033 (cit. on pp. 134, 188)

Mills P., & Snabre P. (1995). *Rheology and Structure of Concentrated Suspensions of Hard Spheres. Shear Induced Particle Migration*. Journal de Physique II, *5*(10), 1597–1608. https://doi.org/10.1051/jp2:1995201 (cit. on pp. 17, 141, 143, 151, 189)

Morris J. F. (2018). *Lubricated-to-frictional shear thickening scenario in dense suspensions*. Physical Review Fluids, *3*(11), 110508. https://doi.org/10.1103/PhysRevFluids.3.110508 (cit. on pp. 15, 20)

Morris J. F., & Boulay F. (1999). *Curvilinear flows of noncolloidal suspensions: The role of normal stresses*. Journal of Rheology, *43*(5), 1213–1237. https://doi.org/10.1122/1.551021 (cit. on pp. 2, 6, 11, 134, 141)

Morris J. F., & Brady J. F. (1998). *Pressure-driven flow of a suspension: Buoyancy effects*. International Journal of Multiphase Flow, *24*(1), 105–130. https://doi.org/10.1016/S0301-9322(97)00035-9 (cit. on p. 134)

Moukalled F., Mangani L., & Darwish M. (2016). *The Finite Volume Method in Computational Fluid Dynamics: An Advanced Introduction with OpenFOAM® and Matlab* (Vol. 113). Springer International Publishing. https://doi.org/10.1007/978-3-319-16874-6. (Cit. on pp. 28, 30)

Ness C., Seto R., & Mari R. (2021). *The physics of dense suspensions*. Annual Review of Condensed Matter Physics, *13*, 97–117. https://doi.org/10.1146/annurev-conmatphys-031620-105938 (cit. on p. 9)

Ness C., & Sun J. (2015). *Flow regime transitions in dense non-Brownian suspensions: Rheology, microstructural characterization, and constitutive modeling*. Physical Review E, *91*(1), 012201. https://doi.org/10.1103/PhysRevE.91.012201 (cit. on p. 67)

Nguyen N. Q., & Ladd A. J. C. (2002). *Lubrication corrections for lattice-Boltzmann simulations of particle suspensions*. Physical Review E, *66*(4), 046708. https://doi.org/10.1103/PhysRevE.66.046708 (cit. on p. 19)

Nott P. R., & Brady J. F. (1994). *Pressure-driven flow of suspensions: simulation and theory*. Journal of Fluid Mechanics, *275*, 157–199. https://doi.org/10.1017/S0022112094002326 (cit. on pp. 17, 132, 134, 141, 143, 144, 151, 189)

Nott P. R., Guazzelli E., & Pouliquen O. (2011). *The suspension balance model revisited*. Physics of Fluids, *23*(4), 043304. https://doi.org/10.1063/1.3570921 (cit. on pp. 2, 6, 95, 134, 141, 142, 148)

Oh S., Song Y.-q., Garagash D. I., Lecampion B., & Desroches J. (2015). *Pressure-Driven Suspension Flow near Jamming*. Physical Review Letters, *114*(8), 088301. https://doi.org/10.1103/PhysRevLett.114.088301 (cit. on pp. 133, 143)

Ouaknin G. Y., Su Y., & Zia R. N. (2021). *Parallel accelerated Stokesian dynamics with Brownian motion*. Journal of Computational Physics, *442*, 110447. https://doi.org/10.1016/j.jcp.2021.110447 (cit. on p. 18)

Papadopoulou A., Gillissen J. J., Wilson H. J., Tiwari M. K., & Balabani S. (2020). *On the shear thinning of non-Brownian suspensions: Friction or adhesion?* Journal of Non-Newtonian Fluid Mechanics, *281*, 104298. https://doi.org/10.1016/j.jnnfm.2020.104298 (cit. on p. 106)

Parsi F., & Gadala-Maria F. (1987). *Fore-and-Aft Asymmetry in a Concentrated Suspension of Solid Spheres*. Journal of Rheology, *31*(8), 725–732. https://doi.org/10.1122/1.549944 (cit. on p. 13)

Patankar N., Singh P., Joseph D., Glowinski R., & Pan T. W. (2000). *A new formulation of the distributed Lagrange multiplier/fictitious domain method for particulate flows*. International Journal of Multiphase Flow, *26*(9), 1509–1524. https://doi.org/10.1016/S0301-9322(99)00100-7 (cit. on p. 19)

Patankar S. V. (1980). *Numerical Heat Transfer and Fluid Flow*. CRC Press. https://catatanstudi.files.wordpress.com/2010/02/numerical-heat-transfer-and-fluid-flow.pdf. (Cit. on p. 30)

Patankar S. V. (1981). *A calculation procedure for two-dimensional elliptic situations*. Numerical Heat Transfer, *4*(4), 409–425. https://doi.org/10.1080/01495728108961801 (cit. on p. 30)

Patankar S. V., & Spalding D. B. (1972). *A calculation procedure for heat, mass and momentum transfer in three-dimensional parabolic flows*. International Journal of Heat and Mass Transfer, *15*, 1787–1806. https://doi.org/10.1016/0017-9310(72)90054-3 (cit. on p. 30)

Pednekar S., Chun J., & Morris J. F. (2017). *Simulation of shear thickening in attractive colloidal suspensions*. Soft Matter, *13*(9), 1773–1779. https://doi.org/10.1039/C6SM02553F (cit. on p. 106)

Peters F., Ghigliotti G., Gallier S., Blanc F., Lemaire E., & Lobry L. (2016). *Rheology of non-Brownian suspensions of rough frictional particles under shear reversal: A numerical study*. Journal of Rheology, *60*(4), 715–732. https://doi.org/10.1122/1.4954250 (cit. on pp. 14, 15, 49–51, 94)

Pham P., Metzger B., & Butler J. E. (2015). *Particle dispersion in sheared suspensions: Crucial role of solid-solid contacts*. Physics of Fluids, *27*, 051701. https://doi.org/10.1063/1.4919728 (cit. on pp. 13, 49)

Phillips R. J., Armstrong R. C., Brown R. A., Graham A. L., & Abbott J. R. (1992). *A constitutive equation for concentrated suspensions that accounts for shear-induced particle migration*. Physics of Fluids A: Fluid Dynamics, *4*(1), 30–40. https://doi.org/10.1063/1.858498 (cit. on p. 134)

Plimpton S. (1995). *Fast Parallel Algorithms for Short-Range Molecular Dynamics*. Journal of Computational Physics, *117*(1), 1–19. https://doi.org/10.1006/jcph.1995.1039 (cit. on p. 67)

Pöschel T., & Schwager T. (2005). *Computational granular dynamics: models and algorithms*. Springer-Verlag. https://doi.org/10.1007/3-540-27720-X. (Cit. on p. 20)

Rahmani M., Hammouti A., & Wachs A. (2018). *Momentum balance and stresses in a suspension of spherical particles in a plane Couette flow*. Phys. Fluids, 18. https://doi.org/10.1063/1.5010989 (cit. on p. 133)

Rampall I., Smart J. R., & Leighton D. T. (1997). *The influence of surface roughness on the particle-pair distribution function of dilute suspensions of non-colloidal spheres in simple shear flow*. Journal of Fluid Mechanics, *339*, 1–24. https://doi.org/10.1017/S002211209600479X (cit. on p. 13)

Reiner M. (1959). *The Flow of Matter*. Scientific American, 19. https://www.jstor.org/stable/24941188 (cit. on p. 106)

Rhie C. M., & Chow W. L. (1983). *Numerical study of the turbulent flow past an airfoil with trailing edge separation*. AIAA Journal, *21*(11), 1525–1532. https://doi.org/10.2514/3.8284 (cit. on p. 30)

Richards J. A. (2021). *Turning a yield-stress calcite suspension into a shear-thickening one by tuning inter-particle friction*. Rheol Acta, 10. https://doi.org/10.1007/s00397-020-01247-z (cit. on pp. 106, 107, 126)

Richards J. A., Guy B. M., & Blanco E. (2020). *The role of friction in the yielding of adhesive non-Brownian suspensions*, 9. https://doi.org/10.1122/1.5132395 (cit. on pp. 107, 121, 126, 127)

Rivlin R., & Ericksen J. (1955). *Stress-deformation relations for isotropic materials*. Journal of Rational Mechanics and Analysis 4, 323–425. https://doi.org/10.1512/iumj.1955.4.54011 (cit. on p. 63)

Saint-Michel B., Manneville S., Meeker S., Ovarlez G., & Bodiguel H. (2019). *X-ray radiography of viscous resuspension*. Physics of Fluids, *31*(10), 103301. https://doi.org/10.1063/1.5103271 (cit. on p. 133)

Sangani A. S., Acrivos A., & Peyla P. (2011). *Roles of particle-wall and particle-particle interactions in highly confined suspensions of spherical particles being sheared at low Reynolds numbers*. Physics of Fluids, *23*(8), 083302. https://doi.org/10.1063/1.3613972 (cit. on pp. 78, 80)

Sarabian M., Firouznia M., Metzger B., & Hormozi S. (2019). *Fully developed and transient concentration profiles of particulate suspensions sheared in a cylindrical Couette cell*. Journal of Fluid Mechanics, *862*, 659–671. https://doi.org/10.1017/jfm.2018.982 (cit. on p. 93)

Saramito P. (2016). *Complex fluids: Modeling and Algorithms* (Vol. 79). Springer International Publishing. https://doi.org/10.1007/978-3-319-44362-1. (Cit. on p. 63)

Segré G., & Silberberg A. (1962). *Behaviour of macroscopic rigid spheres in Poiseuille flow Part 2. Experimental results and interpretation*. Journal of Fluid Mechanics, *14*(1), 136–157. https://doi.org/10.1017/S0022112062001111 (cit. on p. 132)

Seto R., Mari R., Morris J. F., & Denn M. M. (2013). *Discontinuous Shear Thickening of Frictional Hard-Sphere Suspensions*. Physical Review Letters, *111*(21), 218301. https://doi.org/10.1103/PhysRevLett.111.218301 (cit. on p. 20)

Sierou A., & Brady J. F. (2001). *Accelerated Stokesian Dynamics simulations*. Journal of Fluid Mechanics, *448*, 115–146. https://doi.org/10.1017/S0022112001005912 (cit. on pp. 18, 67)

Sierou A., & Brady J. F. (2002). *Rheology and microstructure in concentrated noncolloidal suspensions*. Journal of Rheology, *46*(5), 1031–1056. https://doi.org/10.1122/1.1501925 (cit. on pp. 13, 18)

Sierou A., & Brady J. F. (2004). *Shear-induced self-diffusion in non-colloidal suspensions*. Journal of Fluid Mechanics, *506*, 285–314. https://doi.org/10.1017/S0022112004008651 (cit. on p. 18)

Singh A. [Abhinendra], Mari R., Denn M. M., & Morris J. F. (2018). *A constitutive model for simple shear of dense frictional suspensions*. Journal of Rheology, *62*(2), 457–468. https://doi.org/10.1122/1.4999237 (cit. on pp. 15, 49, 94)

Singh A. [Abhinendra], Ness C., Seto R., de Pablo J. J., & Jaeger H. M. (2020). *Shear Thickening and Jamming of Dense Suspensions: The "Roll" of Friction*. Physical Review Letters, *124*(24), 248005. https://doi.org/10.1103/PhysRevLett.124.248005 (cit. on p. 21)

Singh A. [Abhinendra], Pednekar S., Chun J., Denn M. M., & Morris J. F. (2019). *From yielding to shear jamming in a cohesive frictional suspension*. Physical Review Letters, *122*(9), 098004. https://doi.org/10.1103/PhysRevLett.122.098004 (cit. on pp. 106, 107, 121, 126)

Singh A. [Anugrah], & Nott P. R. (2003). *Experimental measurements of the normal stresses in sheared Stokesian suspensions*. Journal of Fluid Mechanics, *490*, 293–320. https://doi.org/10.1017/S0022112003005366 (cit. on p. 133)

Snabre P., & Mills P. (1996). *Rheology of Weakly Flocculated Suspensions of Rigid Particles*. https://doi.org/10.1051/jp3:1996215 (cit. on pp. 121, 126)

Snook B., Butler J. E., & Guazzelli É. (2016). *Dynamics of shear-induced migration of spherical particles in oscillatory pipe flow*. Journal of Fluid Mechanics, *786*, 128–153. https://doi.org/10.1017/jfm.2015.645 (cit. on pp. 143, 144, 188, 189)

Squires K. (2007). *Point-particle methods for disperse flows*. In A. Prosperetti & G. Tryggvason (Eds.), *Computational Methods for Multiphase Flow* (pp. 282–319). Cambridge University Press. https://doi.org/10.1017/CBO9780511607486.010. (Cit. on pp. 17, 18)

Staben M. E., Zinchenko A. Z., & Davis R. H. (2003). *Motion of a particle between two parallel plane walls in low-Reynolds-number Poiseuille flow*. Physics of Fluids, *15*(6), 1711. https://doi.org/10.1063/1.1568341 (cit. on pp. 81, 82)

Swan J. W., & Brady J. F. (2011). *The hydrodynamics of confined dispersions*. Journal of Fluid Mechanics, *687*, 254–299. https://doi.org/10.1017/jfm.2011.351 (cit. on p. 19)

Uhlmann M. (2005). *An immersed boundary method with direct forcing for the simulation of particulate flows*. Journal of Computational Physics, *209*(2), 448–476. https://doi.org/10.1016/j.jcp.2005.03.017 (cit. on p. 20)

Van Doormaal J. P., & Raithby G. D. (1984). *Enhancements of the SIMPLE method for predicting incompressible flows*. Numerical Heat Transfer, *7*(2), 147–163. https://doi.org/10.1080/01495728408961817 (cit. on p. 30)

Vázquez-Quesada A., & Ellero M. (2016). *Rheology and microstructure of non-colloidal suspensions under shear studied with Smoothed Particle Hydrodynamics*. Journal of Non-Newtonian Fluid Mechanics, *233*, 37–47. https://doi.org/10.1016/j.jnnfm.2015.12.009 (cit. on p. 19)

Vázquez-Quesada A., & Ellero M. (2017). *SPH modeling and simulation of spherical particles interacting in a viscoelastic matrix*. Physics of Fluids, *29*(12), 121609. https://doi.org/10.1063/1.4993610 (cit. on p. 19)

Vowinckel B., Biegert E., Meiburg E., Aussillous P., & Guazzelli É. (2021). *Rheology of mobile sediment beds sheared by viscous, pressure-driven flows*. Journal of Fluid Mechanics, *921*, A20. https://doi.org/10.1017/jfm.2021.457 (cit. on p. 133)

Wilson H. J. (2013). *Stokes flow past three spheres*. Journal of Computational Physics, *245*, 302–316. https://doi.org/10.1016/j.jcp.2013.03.020 (cit. on pp. 88, 89)

Wu M., Peters B., Rosemann T., & Kruggel-Emden H. (2020). *A forcing fictitious domain method to simulate fluid-particle interaction of particles with super-quadric shape*. Powder Technology, *360*, 264–277. https://doi.org/10.1016/j.powtec.2019.09.088 (cit. on p. 19)

Wyart M., & Cates M. (2014). *Discontinuous shear thickening without inertia in dense non-Brownian suspensions*. Physical Review Letters, *112*(9), 098302. https://doi.org/10.1103/PhysRevLett.112.098302 (cit. on p. 15)

Yeo K., Dong S., Climent E., & Maxey M. R. (2010). *Modulation of homogeneous turbulence seeded with finite size bubbles or particles*. International Journal of Multiphase Flow, *36*(3), 221–233. https://doi.org/10.1016/j.ijmultiphaseflow.2009.11.001 (cit. on pp. 13, 20)

Yeo K., & Maxey M. R. (2010a). *Ordering transition of non-Brownian suspensions in confined steady shear flow*. Physical Review E, *81*(5), 051502. https://doi.org/10.1103/PhysRevE.81.051502 (cit. on p. 20)

Yeo K., & Maxey M. R. (2010b). *Simulation of concentrated suspensions using the force-coupling method*. Journal of Computational Physics, *229*(6), 2401–2421. https://doi.org/10.1016/j.jcp.2009.11.041 (cit. on pp. 20, 61, 93, 165, 166)

Yeo K., & Maxey M. R. (2011). *Numerical simulations of concentrated suspensions of monodisperse particles in a Poiseuille flow*. Journal of Fluid Mechanics, *682*, 491–518. https://doi.org/10.1017/jfm.2011.241 (cit. on pp. 17, 54, 55, 132–134, 136, 143, 144, 150, 151)

Yeo K., & Maxey M. R. (2013). *Dynamics and rheology of concentrated, finite-Reynolds-number suspensions in a homogeneous shear flow*. Physics of Fluids, *25*(5), 053303. https://doi.org/10.1063/1.4802844 (cit. on p. 20)

Zarraga I. E., Hill D. A., & Leighton D. T. (2000). *The characterization of the total stress of concentrated suspensions of noncolloidal spheres in Newtonian fluids*. Journal of Rheology, *44*(2), 185–220. https://doi.org/10.1122/1.551083 (cit. on p. 14)

Zarraga I. E., & Leighton D. T. (2001). *Shear-Induced Diffusivity in a Dilute Bidisperse Suspension of Hard Spheres*. Journal of Colloid and Interface Science, *243*(2), 503–514. https://doi.org/10.1006/jcis.2001.7854 (cit. on pp. 83, 84)

Zhou J. Z. Q., Uhlherr R. H. T., & Luo F. T. (1995). *Yield stress and maximum packing fraction of concentrated suspensions*, 18. https://doi.org/10.1007/BF00712315 (cit. on pp. 107, 121, 126)

Zick A. A., & Homsy G. M. (1982). *Stokes flow through periodic arrays of spheres*. Journal of Fluid Mechanics, *115*(-1), 13. https://doi.org/10.1017/S0022112082000627 (cit. on p. 74)

RÉSUMÉ

Nous présentons une méthode de simulation à l'échelle des particules pour les écoulements de suspensions non-Browniennes à faible nombre de Reynolds, basée sur la méthode des domaines fictifs et complétée par des corrections de lubrification de sous-maille. Dans leur forme habituelle, ces corrections font intervenir l'écoulement linéaire ambiant. Dans ce travail, nous déterminons les conditions requises pour éviter de considérer cet écoulement ambiant tout en conservant l'invariance par changement de référentiel, et nous construisons une matrice de correction de sorte que ces conditions soient intrinsèquement présentes. Cette procédure étend l'utilisation correcte de ces corrections aux écoulements non-linéaires. La méthode est validée pour diverses configurations d'écoulement de particules, impliquant quelques particules dans des écoulements linéaires et non-linéaires avec diverses conditions aux limites, ou des suspensions concentrées dans un écoulement de cisaillement simple. Ensuite, nous étudions le rôle des forces d'adhésion dans les suspensions frictionnelles, en faisant varier à la fois l'intensité de l'adhésion et la fraction volumique : après avoir présenté les difficultés liées à la déplétion aux parois et aux bandes de cisaillement, nous montrons que la viscosité relative de la suspension est fonction à la fois de la fraction volumique ϕ et de la contrainte de cisaillement Σ_{12}. La variation de la viscosité en fonction de ces deux paramètres est bien décrite via une fraction volumique de blocage à condition que celle-ci dépende de la contrainte sans dimension σ^* qui s'exprime en fonction de la force d'adhésion entre les particules. La variation de la fraction volumique de blocage en fonction de la contrainte peut être interprétée comme la variation de la contrainte seuil en fonction de la fraction volumique. Cette courbe sépare le plan (ϕ, σ^*) en deux régions : une dans laquelle la suspension s'écoule et l'autre dans laquelle elle est bloquée. Dans une dernière partie, nous étudions la migration des particules induite par le cisaillement dans un écoulement de Poiseuille. Dans un tel système, les particules migrent vers le centre du canal, ce qui entraîne le développement d'un gradient de concentration avec l'apparition d'une région centrale où la fraction volumique de blocage, mesurée dans un écoulement de cisaillement simple, peut être dépassée. Le profil de vitesse est donc hautement non-linéaire, à la fois en raison du gradient de pression et du gradient de concentration variant dans le temps, ce qui justifie l'utilisation de la méthode numérique présentée. Nous comparons les résultats à une version modifiée du *Suspension Balance Model*, confirmant les limites bien connues de ce modèle dans la région centrale. Enfin, nous montrons que les contraintes calculées obéissent à la loi de conservation de quantité de mouvement dans le canal. Ceci confirme le bon comportement de la méthode numérique pour des écoulements non-linéaires.

Mots-clés :

RHÉOLOGIE – SUSPENSIONS – SIMULATIONS – OPENFOAM – ADHÉSION – ÉCOULEMENTS NON-LINÉAIRES – CORRECTIONS DE SOUS-MAILLE – LUBRIFICATION – MIGRATION – MÉTHODE DE DOMAINE FICTIF